LBNL–59449
Cockroft–06–04

Configuration Studies and Recommendations for the ILC Damping Rings

Editors:

A. Wolski
Lawrence Berkeley National Laboratory, Berkeley, CA 94720, USA.

J. Gao
IHEP, Beijing, China.

S. Guiducci
INFN LNF, Frascati, Italy.

February 4, 2006

Contributors

K.L. Bane[1], D.P. Barber[2,3], Y. Cai[1], A. Dragt[4], L. Emery[5], J. Gao[6], G.D. Gollin[7], S. Guiducci[8], H. Hayano[9], S. Heifets[1], J. Jones[10], J.-Y. Jung[11], E.-S. Kim[12], M. Kuriki[9], K. Kubo[9], S. Kuroda[9], L. Malysheva[13,3], O. Malyshev[10], C. Mitchell[4], S. Mtingwa[14,15,11], T. Naito[9], J. Nelson[1], K. Ohmi[9], Y. Ohnishi[9], K. Oide[9], T. Okugi[9], M. Palmer[16], M. Pivi[1], A. Ratti[11], I. Reichel[11], M. Ross[1], D. Rubin[16], R. Schlueter[11], D. Schulte[17], G.V. Stupakov[1], N. Terunuma[9], J. Urakawa[9], J. Urban[16], M. Venturini[11], L. Wang[1], R. Wanzenberg[2], H. Weise[2], A. Wolski[11], M.D. Woodley[1], G. Xia[2], A. Xiao[5], F. Zimmermann[17].

Acknowledgements

This work was supported by the Director, Office of Science, High Energy Physics, U.S. Department of Energy under Contract No. DE-AC02-05CH11231.

[1]SLAC, Menlo Park, California, USA.
[2]DESY, Hamburg, Germany.
[3]The Cockroft Institute for Accelerator Science and Technology, Daresbury, UK.
[4]University of Maryland, College Park, Maryland, USA.
[5]ANL, Illinois, USA.
[6]IHEP, Beijing, China.
[7]University of Illinois Urbana-Champagne, Illinois, USA.
[8]LNF, Frascati, Italy.
[9]KEK, Tsukuba, Japan.
[10]CCLRC ASTeC, Daresbury, UK.
[11]LBNL, Berkeley, California, USA.
[12]POSTECH, Korea.
[13]University of Liverpool, Liverpool, UK.
[14]Harvard University, Cambridge, Massachusetts, USA.
[15]North Carolina A&T State University, Greensboro, North Carolina, USA.
[16]Cornell University, Ithaca, New York, USA.
[17]CERN, Geneva, Switzerland.

Contents

List of Tables

List of Figures

Chapter 1

Introduction

In this report, we describe the results of studies comparing different options for the baseline configuration of the ILC damping rings. The principal configuration decisions apply to the circumference, beam energy, lattice type, and technology options for key components, including the injection/extraction kickers and the damping wigglers. To arrive at our recommended configuration, we performed detailed studies of a range of lattices representing a variety of different configuration options; these lattices are described in Chapter 2. The results of the various studies are reported in chapters covering issues of beam dynamics, technical subsystems, costs, and commissioning, reliability and upgradeability. Our detailed recommendations for the baseline configuration are given in Chapter 7, where we also outline further research and development that is needed before a machine using our recommended configuration can be built and operated successfully. In the same chapter, we suggest possible alternatives to the baseline configuration.

1.1 Parameter Ranges and System Interfaces

The damping rings must accept the beams produced by the electron and positron sources, and produce beams that meet the requirements of the downstream systems (bunch compressors, main linac etc.) The injection point is the exit of the injection kickers: this is the first point at which injected bunches are nominally on the closed orbit in the damping rings. The beam parameters assumed in the configuration studies are given in Table 1.1. Note that the transverse amplitude and energy error refer to individual particles within each bunch.

Table 1.1: Nominal parameters of beams injected into the damping rings.

	Electron beam	Positron beam
Train repetition rate	5 Hz	
Number of bunches per train	2820	
Number of particles per bunch	2×10^{10}	
Max. transverse amplitude, $A_x + A_y$		0.09 m·rad
Max. energy error, δ_{max}		0.5%
Normalized injected emittance	45 μm	
RMS relative injected energy spread[1]	0.1%	
Polarization	>80%	0

The transverse amplitude of a particle in the beam is defined by:

$$\frac{A_x}{\gamma} = \gamma_x x^2 + 2\alpha_x x p_x + \beta_x p_x^2 \tag{1.1}$$

(and similarly for A_y), where γ is the relativistic factor, and α_x, β_x, γ_x are the Twiss parameters. The maximum transverse amplitude specified in Table 1.1 includes beam jitter. Note that the betatron action is given by:

$$J_x = \frac{A_x}{2\gamma} \tag{1.2}$$

in terms of which, the rms emittance is:

$$\epsilon_x = \langle J_x \rangle \tag{1.3}$$

The bunch length of the injected beam is not specified: it is expected that the injected bunch length will be much shorter than the matched bunch length for the injected energy spread, and that the bunch length will initially increase as the longitudinal phase space undergoes filamentation.

The extraction point of each damping ring is the entrance of the extraction kicker. This is the first point at which a bunch undergoing extraction is off the closed orbit. The nominal parameters of the extracted beam are given in Table 1.2. Note that the limit on the vertical jitter is given in terms of the vertical beam size, σ_y.

Alternative parameter sets are being considered for the ILC [58]. One possible parameter set calls for increasing the number of bunches per train, while reducing the bunch charge: the alternative parameters are shown in Table 1.3.

[1] Some studies for the electron source indicate that a much smaller energy spread, as low as 45 keV, can be achieved [16, 17]

Other parameter options impacting the damping rings include reduction in the extracted vertical emittance for high luminosity, and reduction in extracted horizontal emittance for operating the ILC as a $\gamma\gamma$ collider. Some of the options are considered in the damping ring configuration studies where applicable; however, most of our attention has been given to the nominal parameter sets specified in Tables 1.1 and Table 1.2.

Table 1.2: Nominal parameters of beams extracted from the damping rings.

	Electron beam	Positron beam
Number of bunches per train	2820	
Number of particles per bunch	2×10^{10}	
Bunch separation in main linac	337 ns	
Normalized horizontal emittance	8 μm·rad	
Normalized vertical emittance	0.02 μm·rad	
RMS relative energy spread	<0.15%	
RMS bunch length	6 mm	
Vertical jitter	$<0.1\sigma_y$	
Polarization	>80%	0

Table 1.3: Alternative operating parameters.

Number of bunches per train	5640
Number of particles per bunch	1×10^{10}
Bunch separation in main linac	154 ns

Chapter 2

Reference Lattices

Our recommendation for the damping rings baseline configuration is based on studies of seven lattices (the "reference lattices") covering a range of configuration options, including different circumferences, energies and lattice cell structures. Since it was not practical to study every possible combination of options, the reference lattices should be regarded as representative of the possibilities. We should emphasise that the goal of our studies was not to select one of the seven lattices as the baseline configuration, but rather to arrive at a recommendation based on an understanding of how the various choices affect the performance, cost and operability of the damping rings. This allowed the possibility of recommending a configuration not corresponding exactly to any of the seven reference lattices, but representing an optimum combination of design options.

Detailed lattice designs have been completed only for the positron damping rings. Since the beam from the electron source is likely to be much smaller than the beam from the positron source, the electron damping ring in principle is allowed longer damping times than are necessary in the positron damping ring. For example, in the TESLA TDR [72] the damping times in the positron and electron damping rings were specified to be 28 ms and 50 ms respectively. Thus, the length of the damping wiggler in the electron ring may be shorter than the wiggler in the positron ring. However, it should be noted that the wiggler acts to reduce (significantly in some cases) the natural emittance of the lattice, since the radiation damping provided by the wiggler dominates over the quantum excitation. Also, rapid radiation damping is helpful in suppressing some collective effects, including coupled-bunch instabilities and intrabeam scattering. Depending on the lattice design and the strength of the collective effects, it may therefore be desirable to use a

wiggler in the electron damping ring that provides a shorter damping time than is strictly necessary to achieve the extracted vertical emittance. This issue has not been studied in detail at this stage.

Table 2.1 lists the main parameters of the positron damping ring reference lattices. The nomenclature (PPA, OTW etc.) is designed to provide a means of referring to the lattices that is objective, and not colored by any associations. The TESLA lattice is the one used in the studies of the 2nd International Linear Collider Technical Review Committee [35], and is essentially (with some small developments) the same as the one described in the TESLA TDR [72]. The TESLA lattice is the most thoroughly studied of any of the reference lattices; its inclusion in these studies provides a useful benchmark for comparison with the other lattices.

Note that there are some cases where the nominal parameters of the lattices are different from the nominal parameters specified for the damping rings. For example, the number of bunches stored is not 2820 in every case: for the 3 km lattices (PPA and OTW), where the number of bunches is significantly less than 2820, the bunch charge is increased to provide roughly the same total number of particles in each bunch train. For two of the lattices (BRU and MCH), the natural bunch length of 9 mm is 50% larger than the nominal extracted bunch length of 6 mm. Although it would be possible in principle to reduce the bunch length by increasing the RF voltage, an unrealistically large RF voltage would be needed to achieve a bunch length of 6 mm in these lattices. While a larger bunch length in the damping rings puts pressure on the bunch compressors, it may ease operation of the damping rings by reducing the impact of collective effects (for example, space-charge) and this provides a motivation for including lattices with 9 mm bunch length in the configuration studies.

2.1 Footprints

The footprints of the reference lattices are shown in Figures 2.1 to 2.7.

2.2 Fill Patterns

With the nominal parameters shown in Tables 1.1 and 1.2, 2820 bunches must be stored in each damping ring, and bunches must be extracted individually to give the correct spacing in the linac. In the simplest scheme, the ring is uniformly filled, with n times the bunch spacing in the ring equal to the required bunch spacing in the linac, where n is *not* a factor of the total

Table 2.1: Parameters of the positron damping ring reference lattices.

Lattice	PPA [12]	OTW	OCS [26]	BRU [82]	MCH [82]	DAS [12]	TESLA [72]
Circumference [m]	2824	3223	6114	6333	15935	17014	17000
Energy [GeV]	5.0	5.0	5.066	3.74	5.0	5.0	5.0
Harmonic number	4700	7678	13256	13732	34550	28377	28200
Arc cell type	PI	TME	TME	FODO	FODO	PI	TME
Horizontal tune	47.810	45.164	50.840	65.783	75.783	83.730	76.310
Vertical tune	47.680	24.157	40.800	66.413	76.413	83.650	41.180
Natural chromaticity (x, y)	-63,-60	-88,-74	-65,-53	-79,-87	-90,-95	-105,-105	-126,-60
Momentum compaction $[10^{-4}]$	2.83	3.62	1.62	11.9	4.09	1.14	1.22
Energy loss/turn [MeV]	4.70	8.85	9.33	6.19	19.8	21.0	20.3
Transverse damping time [ms]	20.0	12.1	22.2	25.5	26.9	27.0	27.9
Longitudinal damping time [ms]	10.0	6.07	11.1	12.8	13.4	13.5	13.9
Natural emittance [nm]	0.433	0.388	0.559	0.377	0.675	0.612	0.504
Norm. natural emittance [μm]	4.24	3.80	5.54	2.76	6.60	5.99	4.93
RF voltage [MV]	17.76	21.78	19.27	23.16	53.70	48.17	50.00
RF frequency [MHz]	500	714	650	650	650	500	500
Synchrotron tune	0.0269	0.0418	0.0337	0.120	0.150	0.0668	0.071
Synchronous phase [deg]	164	156	151	164	158	154	156
RF acceptance [%]	3.2	2.1	2.0	1.3	1.5	2.8	2.9
Natural bunch length [mm]	6.00	6.00	6.00	9.00	9.00	6.00	6.00
Natural energy spread $[10^{-3}]$	1.27	1.36	1.29	0.973	1.30	1.30	1.29
Particles/bunch $[10^{10}]$	2.4	2.2	2.0	2.0	2.0	2.0	2.0
Peak current [A]	76.7	70.0	63.9	42.6	42.6	63.9	63.9
Bunch spacing $[\lambda_{RF}]$	2	3	4	4	10	10	10
Bunch spacing [ns]	4.000	4.202	6.154	6.154	15.38	20.00	20.12
Bunches per train	2350	2559	47	36	18	2820	2820
Gaps per train	0	0	8.25	8	4	0	0
Number of bunch trains	1	1	60	78	157	1	1
Average current [mA]	959	839	443	426	170	159	159
Mean horizontal beta function [m]	13.1	58.0	25.6	57.6	109	106	120
Mean vertical beta function [m]	12.5	63.8	31.0	55.4	108	106	121
Synch. radn. integral I_1 [m]	0.7986	1.158	0.9727	6.365	6.523	1.940	2.071
Synch. radn. integral I_2 $[\mathrm{m}^{-1}]$	0.5341	1.006	0.8087	2.248	2.248	2.390	2.314
Synch. radn. integral I_3 $[\mathrm{m}^{-2}]$	0.04699	0.1016	0.09992	0.2073	0.2073	0.2190	0.2113
Synch. radn. integral I_4 $[10^{-4}\mathrm{m}^{-1}]$	0.3276	1.212	1.488	3.675	3.774	1.914	2.150
Synch. radn. integral I_5 $[10^{-5}\mathrm{m}^{-1}]$	0.6342	1.104	1.424	3.043	3.112	3.883	3.206

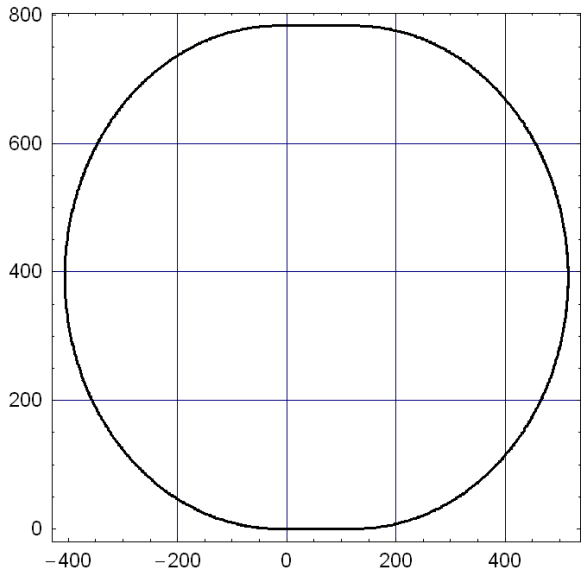

Figure 2.1: Footprint of PPA Lattice.

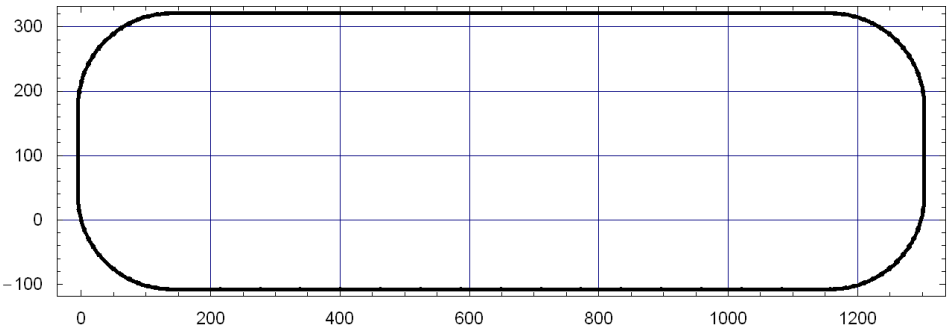

Figure 2.2: Footprint of OTW Lattice.

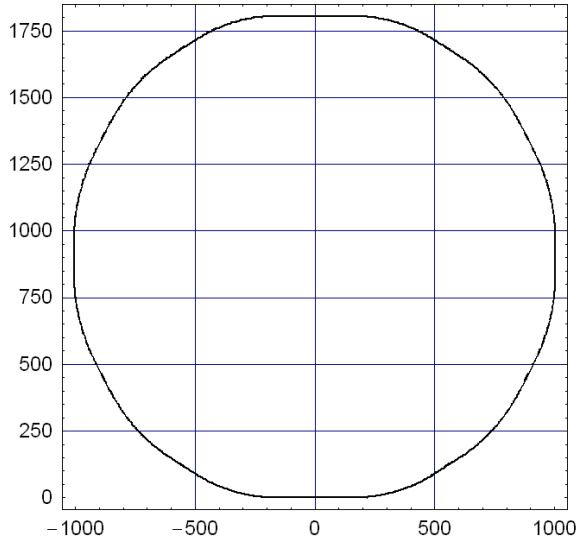

Figure 2.3: Footprint of OCS Lattice.

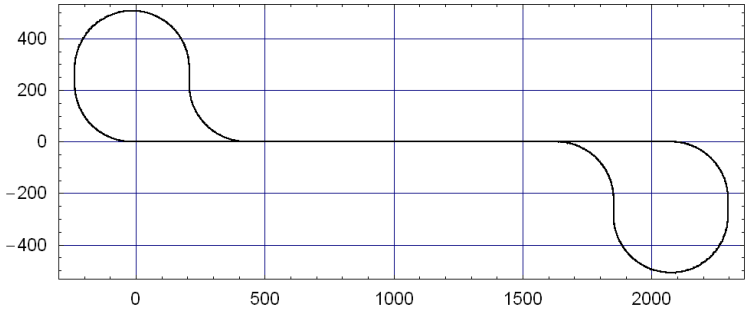

Figure 2.4: Footprint of BRU Lattice.

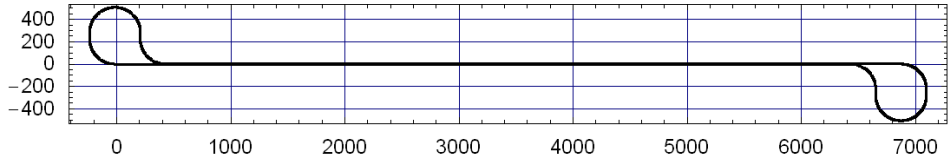

Figure 2.5: Footprint of MCH Lattice.

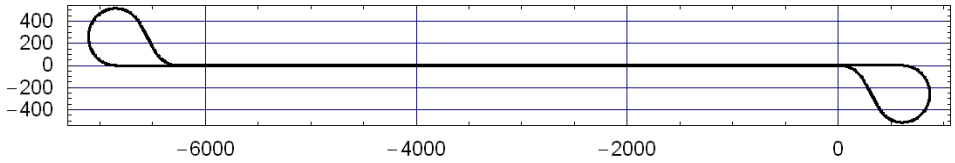

Figure 2.6: Footprint of DAS Lattice.

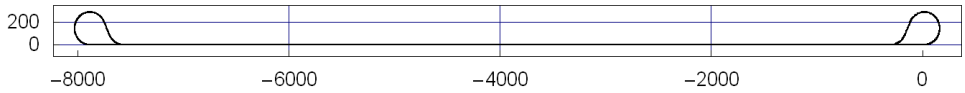

Figure 2.7: Footprint of TESLA Lattice.

number of bunches. During extraction, every nth bunch is ejected, and the ring is emptied over n turns. To avoid transients arising from variations in beam loading, the gap left by an extracted bunch is filled with a fresh bunch from the source before the gap arrives at the RF cavities.

Unfortunately, a uniform fill does not allow for gaps for clearing ions (in the electron ring) or electron cloud (in the positron ring). To meet the requirement for clearing gaps, bunches in the ring can be grouped into "mini-trains" with the spacing between corresponding bunches in successive trains equal to the required bunch separation in the linac. Let us suppose that extraction starts with the last bunch in the first mini-train. Over the course of one revolution period, the last bunch in each mini-train is extracted. The gap following the last mini-train is one bunch spacing longer than the other gaps; extraction then naturally proceeds with the last but one bunch in each mini-train (with no variation in spacing of the bunches in the linac), and so on over subsequent turns, until all the damped bunches have been extracted. As in the case of a uniform fill, the spaces left by extracted bunches must be immediately filled with fresh bunches from the source to prevent phase variations during the course of an extraction. In this scheme, the number of mini-trains in the ring is equal to the number of turns over which all the damped bunches are extracted.

The requirements for the extraction timing place constraints on the circumference of the damping ring. There is a further requirement that the ring RF frequency be a simple subharmonic of the main linac RF frequency, so that the RF systems can be phase locked, ensuring that bunches extracted from the ring always arrive at the correct phase of RF in the main linac.

Further constraints on the injection and extraction come from timing considerations of the particle sources, and the arrival times of bunches at the interaction point(s). Considering only the requirement of producing uniformly spaced bunches in the linac, however, it is possible to find solutions for different ring circumferences and RF frequencies that allow flexibility in the number of bunches per bunch train in the linac.

Table 2.2: Fill patterns in a 6.5 km ring with 500 MHz RF frequency.

Circumference [m]	6476.7163				
RF Frequency [MHz]	500				
Harmonic number	10802				
Ring bunch spacing [λ_{Ring}]	2				
Ring bunch spacing [ns]	4				
Bunches per minitrain	45				
Gaps following minitrain	45	30	22.5	15	0
Number of minitrains	60	72	80	90	120
Total number of bunches	2700	3240	3600	4050	5400
Linac bunch spacing [λ_{ML}]	468	390	351	312	234
Linac bunch spacing [ns]	360	300	270	240	180
Linac RF pulse length [ms]	0.97				

Table 2.3: Fill patterns in a 6.6 km ring with 650 MHz RF frequency.

Circumference [m]	6642.9397					
RF Frequency [MHz]	650					
Harmonic number	14403					
Ring bunch spacing [λ_{Ring}]	3					
Ring bunch spacing [ns]	4.62					
Bunches per minitrain	40					
Gaps following minitrain	40	$26\frac{2}{3}$	24	20	$13\frac{1}{3}$	0
Number of minitrains	60	72	75	80	90	120
Total number of bunches	2400	2880	3000	3200	3600	4800
Linac bunch spacing [λ_{ML}]	480	400	384	360	320	240
Linac bunch spacing [ns]	369.23	307.69	295.38	276.92	246.15	184.62
Linac RF pulse length [ms]	0.89					

An example is shown in Table 2.2, for a ring of circumference 6.5 km, and an RF frequency of 500 MHz (5/13 that of the main linac). Other examples are shown in Tables 2.3 (6.6 km, 650 MHz), 2.4 (15.8 km, 500 MHz) and

Table 2.4: Fill patterns in a 15.8 km ring with 500 MHz RF frequency.

Circumference [m]	15832.0397			
RF Frequency [MHz]	500			
Harmonic number	26405			
Ring bunch spacing [λ_{Ring}]	5			
Ring bunch spacing [ns]	10			
Bunches per minitrain	20			
Gaps following minitrain	20	12	10	0
Number of minitrains	132	165	176	264
Total number of bunches	2640	3300	3520	5280
Linac bunch spacing [λ_{ML}]	520	416	390	260
Linac bunch spacing [ns]	400	320	300	200
Linac RF pulse length [ms]	1.06			

Table 2.5: Fill patterns in a 16.6 km ring with 650 MHz RF frequency.

Circumference [m]	16606.6573				
RF Frequency [MHz]	650				
Harmonic number	36006				
Ring bunch spacing [λ_{Ring}]	6				
Ring bunch spacing [ns]	9.23				
Bunches per minitrain	20				
Gaps following minitrain	20	$13\frac{1}{3}$	10	$6\frac{2}{3}$	0
Number of minitrains	150	180	200	225	300
Total number of bunches	3000	3600	4000	4500	6000
Linac bunch spacing [λ_{ML}]	480	400	360	320	240
Linac bunch spacing [ns]	369.23	307.69	276.92	246.15	184.62
Linac RF pulse length [ms]	1.11				

2.5 (16.6 km, 650 MHz). These parameters should be regarded as examples only, which we present here to illustrate one method by which flexibility in the length of a bunch train may be achieved with a damping ring of fixed circumference and RF frequency.

The reference lattices considered in this report use a variety of different fill patterns and RF frequencies; these are shown in Table 2.1. Four of the lattices (PPA, OTW, DAS and TESLA) use a uniform fill, and three (OCS, BRU and MCH) group the bunches into mini-trains, providing gaps for clearing ions or electron cloud. It may be assumed that the design of each lattice may be modified by changing the circumference to allow different fill patterns (for example, introducing gaps in the lattices presently having uniform fills) without significantly impacting other properties of the lattice. Three of the lattices (PPA, DAS and TESLA) specify an RF system at 500 MHz, or 5/13 of the linac RF frequency; three (OCS, BRU and MCH) specify an RF system at 650 MHz, or 1/2 of the linac RF frequency. The remaining lattice, OTW, specifies an RF system at 714 MHz, which may not be an ideal choice. In general, the reference lattices do not allow flexibility in varying the number of bunches in a train.

2.3 Coupling Bumps

Early studies of beam dynamics in the TESLA damping ring led to concerns of the impact of space-charge tune shifts. Coupling the beam locally in the long straight sections of the ring was proposed as a way to reduce the impact of space-charge by reducing the charge density [18]. An appropriate local coupling can be achieved by using a pair of skew quadrupole triplets. Outside the coupled region, the vertical beam size is dominated by the vertical emittance. Within the coupled region, the vertical beam size has a signficant contribution from the horizontal emittance. Since the horizontal emittance for the damped beam is roughly 400 times larger than the vertical emittance, the vertical beam size can be increased by an order of magnitude by this technique.

Two of the 17 km lattices studied in this report (TESLA and MCH) include the necessary components for providing local coupling in the long straights. Figure 2.8 shows the lattice functions in the entrance region to one long straight section of the MCH lattice, with the coupling insertion applied.

In the notation of Figure 2.8 (and in the absence of dispersion), the beam

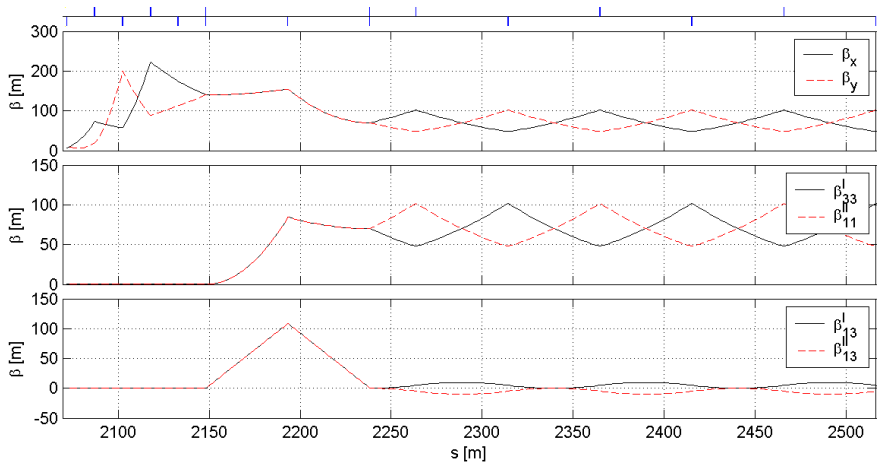

Figure 2.8: In-plane and cross-plane lattice functions at the entrance of one long straight section of the MCH lattice with the coupling insertion applied.

sizes are given by:

$$\sigma_x^2 = \beta_x \epsilon_x + \beta_{11}^{\mathrm{II}} \epsilon_y \quad (2.1)$$

$$\sigma_y^2 = \beta_y \epsilon_y + \beta_{33}^{\mathrm{I}} \epsilon_x \quad (2.2)$$

where ϵ_x and ϵ_y are the normal-mode emittances, corresponding to the horizontal and vertical emittance respectively in an uncoupled section of the lattice. The $\langle xy \rangle$ beam correlation is given by:

$$\langle xy \rangle = \beta_{13}^{\mathrm{I}} \epsilon_x + \beta_{13}^{\mathrm{II}} \epsilon_y \quad (2.3)$$

In Figure 2.8, the three skew quadrupoles forming the entrance of the coupling insertion are at s locations 2148 m, 2193 m and 2238 m. Upstream of the first skew quadrupole, there is zero coupling, and the "cross-plane" lattice functions β_{11}^{II} and β_{33}^{I} are zero. Downstream of the third skew quadrupole, the cross-plane lattice functions are of the same order of the in-plane lattice functions β_x and β_y, indicating that the horizontal and vertical emittances contribute with roughly equal weights to both the horizontal and vertical beam sizes. The beam tilt ($\langle xy \rangle$ correlation) is small, so the beam is roughly round.

The inclusion of coupling insertions in two of the reference lattices has allowed detailed studies to be performed of space-charge effects, using recently

developed tools: the results are given in section 3.4.6. Use of coupling insertions potentially has an impact on low-emittance tuning; this is disussed in section 3.2.

2.4 Vertical Bends

Various options for the geometry of the main linac are being considered. The main options are: a "laser straight" linac; a linac that smoothly follows the Earth's curvature; and a linac that has some number of vertical bends so as to stay roughly a fixed distance below ground level. The latter two options will require the inclusion of vertical bends in the (otherwise) long straight sections of the dogbone damping rings, MCH, DAS and TESLA. The simplest solution for the dogbone rings in the situation that the linac tunnel follows the Earth's curvature, is to include vertical bends in achromatic pairs, forming closed vertical dispersion bumps. The resulting vertical dispersion is small (the peak value is approximately 8 mm).

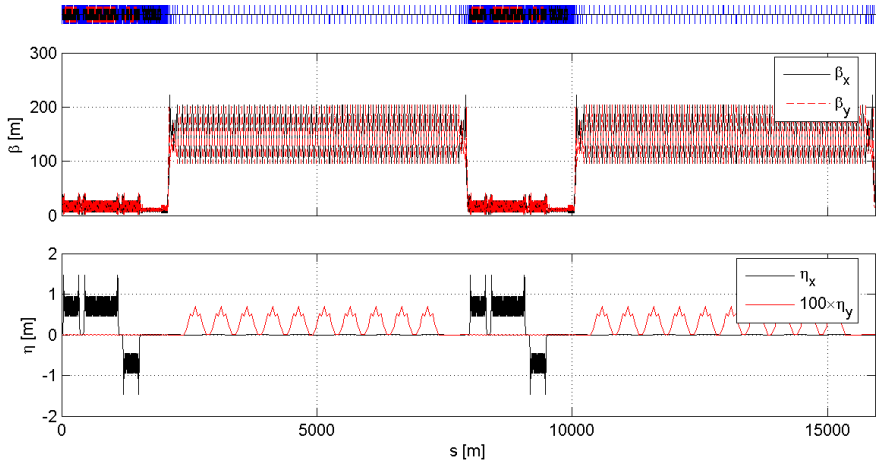

Figure 2.9: Lattice functions in the MCH lattice with vertical bends in the long "straight" sections.

Figure 2.9 shows the lattice functions in the MCH lattice, with vertical bends in the long "straight" sections, to follow approximately the curvature of the Earth. In each straight section, there are 20 vertical bending magnets distributed over a beamline length of 4987 m; the bend angle of each vertical bending magnet is 39.11 μrad, so that this section of the beamline follows

(piece-wise) an arc with radius of curvature 6378 km. Figure 2.9 shows the lattice functions in the MCH lattice with the coupling insertions turned off, but the vertical bends and the coupling insertions are not affected by each other. The vertical emittance generated by the vertical bends is negligible. A potential issue is the additional complication of low-emittance tuning in the presence of vertical dispersion that is non-zero by design.

Chapter 3

Beam Dynamics

There are three critical issues for the damping rings in which beam dynamics effects play a major role:

- Acceptance. Achieving an injection efficiency close to 100% will be essential for operating the damping rings safely, and without damaging critical components by radiation from beam losses.
- Vertical emittance. The luminosity of the ILC will depend on generating extremely small vertical emittance in the damping rings (and preserving the emittance to the interaction point).
- Beam stability. Commissioning, tuning and reliable operation of downstream systems, and producing luminosity, will depend on producing highly stable beams from the damping rings.

In this chapter, we consider all three issues, and evaluate the reference lattices in terms of the likely difficulty of achieving the necessary acceptance, beam quality and stability. In addition, it will be important to maintain beam polarization in the damping rings, at least for the electron beam; although this is regarded as somewhat less of a challenge than some of the other requirements, there are effects which could cause problems, and we present results from an evaluation of the polarization preservation.

3.1 Acceptance

The average injected beam power into the damping rings in normal operation will be more than 225 kW. As a result, an injection efficiency of very close to 100% will be needed, to avoid radiation damage to damping ring

components. Since the beam from the positron source will be much larger than that from the electron source, acceptance is principally an issue for the positron rings: assuming that the electron and positron rings are essentially the same, a solution that works for the positrons will also work for the electrons. The injected beam distribution is defined in terms of the normalized betatron amplitudes and energy errors of particles at the exit of the injection kicker. This is the first point at which the beam is nominally "on axis" and following the closed orbit.

The normalized betatron amplitude is defined as $A_x + A_y$ where:

$$\frac{A_x}{\gamma} = \gamma_x x^2 + 2\alpha_x x p_x + \beta_x p_x^2 \tag{3.1}$$

and similarly for A_y. γ is the relativistic factor; α_x, β_x and γ_x are the horizontal Twiss parameters; x and p_x are the horizontal coordinate and conjugate momentum (normalized to the reference momentum) of a particle with respect to the reference trajectory. The specification on the transverse distribution of the injected positrons is:

$$A_x + A_y < 0.09 \text{ m} \cdot \text{rad} \tag{3.2}$$

It is sometimes convenient to work with an "equivalent rms beam size". This is defined such that:

$$3\sigma_x = x_{\max} \tag{3.3}$$

and similarly for y. $x_{\max}$ is the maximum horizontal coordinate of any particle in the beam. Since, in the absence of dispersion:

$$\sigma_x = \sqrt{\beta_x \epsilon_x} \tag{3.4}$$

where ϵ_x is the rms emittance,

$$\epsilon_x = \frac{\langle A_x \rangle}{2\gamma} \tag{3.5}$$

and

$$x_{\max} = \sqrt{\beta_x \frac{A_x}{\gamma}} \tag{3.6}$$

it follows that:

$$\gamma \epsilon_x = \frac{1}{9} A_{x,\max} \tag{3.7}$$

In other words, the specification on the transverse distribution of injected positrons can be expressed as an rms normalized emittance in each plane

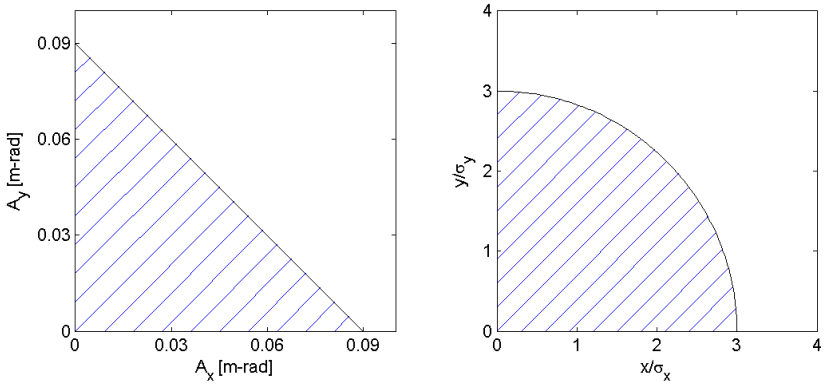

Figure 3.1: Specification on the transverse distribution of injected positrons. All particles in the injected positron beam should lie within the shaded areas. Left: specification on betatron amplitudes. Right: corresponding specification in coordinate space normalized to the rms beam size, with an equivalent rms emittance of $\gamma\epsilon = 0.01$ m·rad (only the sector with positive x and y is shown; the specification is rotationally symmetric about the origin).

$\gamma\epsilon = 0.01$ m·rad, truncated at 3σ. The specification on the transverse distribution of injected positrons is illustrated in Figure 3.1.

The specifications on the transverse amplitudes of particles in the injected bunch are independent of the longitudinal coordinates of the particles. A further specification on the injected positrons is that the energy deviations of the particles should all lie with $\pm 0.5\%$, i.e. the full-width of the energy distribution (normalized to the reference energy) is 1%. With this energy spread, the matched bunch length in the damping rings will be around 60 mm full-width. It is expected that the injected bunch length will be much less than this; however, the specification on the energy spread will be more demanding.

Note that the specifications on the transverse and longitudinal distributions include injection jitter, i.e. the centroid of the distribution may be non-zero, but all particles should still meet the specifications stated above.

The damping rings must have dynamic and physical aperture sufficient to accept a positron beam meeting the injection specifications. Generally, the acceptance of a given lattice is estimated using tracking studies. The goal of the lattice design should be to produce a lattice that has sufficient acceptance not just under ideal conditions, but also in the presence of alignment, tuning and systematic and random multipole errors. Synchrotron radiation, synchrotron oscillations and physical apertures should all be included in the tracking when determining the acceptance. Experience from operating machines is that the measured dynamic aperture can be significantly smaller than expected from tracking studies, even when all relevant effects are included. This is especially true in the early commissioning and operation stages; after careful characterization of machine errors and conditions, there can be good agreement between the measured and simulated dynamic aperture. Given the importance of good injection efficiency for operation of the damping rings, it seems prudent to aim for a design that has significant margin in the dynamic aperture beyond the bare requirements for acceptance of the specified positron distribution.

In this section, we analyze the acceptance of the reference lattices using a range of techniques and tools, under a number of different conditions. In Section 3.1.3 we consider the dynamic aperture determined by the survival of particles tracked at different amplitudes over some number of turns. The results presented include effects such as the nonlinear fields in the wiggler, and higher-order multipole errors in the main magnets. In Section 3.1.4 we present the results of Frequency Map Analysis (FMA) of the reference lattices. FMA gives more detailed information on the dynamics than a simple survival plot; however, since the technique is more computationally expen-

Table 3.1: Sytematic and random multipole errors in the dipoles used in tracking studies in the reference lattices. The reference radius is 30 mm.

n	systematic		random	
	b_n	a_n	b_n	a_n
3	1.60×10^{-4}	0	8.00×10^{-5}	0
4	-1.60×10^{-5}	0	8.00×10^{-6}	0
5	7.60×10^{-5}	0	3.80×10^{-5}	0

sive, the range of conditions investigated is not as wide as for the survival plots. In Section 3.1.6 we estimate the injection efficiency of the reference lattices using a simulated distribution of injected positrons. Finally, in Section 3.1.7 we consider the effects of the physical aperture in the wiggler (which is expected to be the limiting physical aperture in the damping rings).

3.1.1 Multipole Errors

For tracking studies with multipole errors in the main magnets, a consistent set of errors was used for all reference lattices. These errors were based on systematic and random higher-order multipole components measured in the PEP-II and SPEAR-3 magnets. The error values used in the tracking studies are shown in Table 3.1 (dipoles), Table 3.2 (quadrupoles) and Table 3.3 (sextupoles). The higher-order multipole error coefficients are defined by:

$$\frac{\Delta B_y + i\Delta B_x}{|B(r)|} = \sum_n (b_n + ia_n)\left(\frac{x}{r} + i\frac{y}{r}\right)^{n-1} \tag{3.8}$$

where ΔB_x and ΔB_y are the horizontal and vertical components of the field from the multipole error at the transverse position given by the coordinates x and y; and $|B(r)|$ is the magnitude of the field from the main magnet (dipole, quadrupole, or sextupole) at the reference radius r.

3.1.2 Wiggler Models

Wigglers have intrinsically nonlinear fields that can affect the dynamic aperture of a lattice. The damping rings will have relatively long sections of strong wigglers compared to conventional storage rings (see Table 3.4), so the effects of the wiggler need particularly careful consideration. In the studies reported here, there are four models of the wiggler commonly used. These are described below.

Table 3.2: Sytematic and random multipole errors in the quadrupoles used in tracking studies in the reference lattices. The reference radius is 50 mm.

n	systematic		random	
	b_n	a_n	b_n	a_n
3	-1.24×10^{-5}	-1.15×10^{-5}	7.61×10^{-5}	7.25×10^{-5}
4	2.30×10^{-6}	1.41×10^{-5}	1.32×10^{-4}	1.27×10^{-4}
5	-4.30×10^{-6}	6.20×10^{-7}	1.50×10^{-5}	1.62×10^{-5}
6	3.40×10^{-4}	-4.93×10^{-5}	1.65×10^{-4}	3.63×10^{-4}
7	3.00×10^{-7}	-1.02×10^{-6}	6.70×10^{-6}	6.60×10^{-6}
8	6.00×10^{-7}	3.80×10^{-7}	8.90×10^{-6}	6.60×10^{-6}
9	6.00×10^{-7}	-2.80×10^{-7}	4.60×10^{-6}	4.90×10^{-6}
10	-6.17×10^{-5}	-5.77×10^{-5}	2.46×10^{-4}	2.33×10^{-4}
11	-2.00×10^{-7}	-1.80×10^{-7}	4.20×10^{-6}	3.50×10^{-6}
12	3.60×10^{-6}	-6.53×10^{-6}	3.48×10^{-5}	3.66×10^{-5}
13	6.00×10^{-7}	1.20×10^{-6}	9.20×10^{-6}	8.60×10^{-6}
14	1.00×10^{-6}	-7.40×10^{-7}	4.76×10^{-5}	4.46×10^{-5}

Table 3.3: Sytematic and random multipole errors in the sextupoles used in tracking studies in the reference lattices. The reference radius is 32 mm.

n	systematic		random	
	b_n	a_n	b_n	a_n
4	2.00×10^{-4}	0	1.00×10^{-4}	0
5	1.00×10^{-4}	0	3.00×10^{-5}	0
6	7.00×10^{-4}	0	1.00×10^{-4}	0
7	1.00×10^{-4}	0	3.00×10^{-5}	0
8	1.00×10^{-4}	0	3.00×10^{-5}	0
9	1.00×10^{-4}	0	3.00×10^{-5}	0
10	1.00×10^{-4}	0	3.00×10^{-5}	0
11	1.00×10^{-4}	0	3.00×10^{-5}	0
12	3.20×10^{-3}	0	1.00×10^{-4}	0
13	1.00×10^{-4}	0	3.00×10^{-5}	0
14	1.00×10^{-4}	0	3.00×10^{-5}	0

Table 3.4: Parameters of the wigglers used in the reference lattices.

Lattice	Peak field $\hat{B}$ [T]	Pole length [m]	Period λ_w [m]	Section length [m]	Total length [m]
PPA	1.6	0.110	0.4	3.865	92.76
OTW	1.8	0.100	0.4	2.040	163.2
OCS	1.6	0.100	0.4	2.450	196.0
BRU	1.2	0.100	0.4	2.450	441.0
MCH	1.6	0.100	0.4	2.450	441.0
DAS	1.6	0.110	0.4	4.000	448.0
TESLA	1.6	0.110	0.4	3.865	417.42

Linear Wiggler Model

In the linear model, the wiggler is represented as a sequence of hard-edged dipoles. This is generally the model used in the lattice design, but misses significant features such as the field variation with transverse position. These features can introduce dynamic multipoles, that may significantly affect the dynamic aperture.

Fringe-Field Wiggler Model

The tracking code SAD uses a model of the wigglers in which the variation of the vertical field along the wiggler axis is represented by a trapezoid (Figure 3.2). The variation of the vertical field has a longitudinal field component associated with it, which varies with vertical position. Combined with the wiggling trajectory of a particle as it moves through the wiggler, this leads to nonlinear vertical focusing.

For a wiggler of length L_w and bending radius $\rho_w = B\rho/\hat{B}$ (where $B\rho$ is the beam rigidity and $\hat{B}$ is the peak field), the nonlinear vertical focusing may be represented by terms in the Hamiltonian given by:

$$H = \frac{L_w}{4\rho_w^2} y^2 + \frac{L_w}{12\rho_w^2} k_z^2 y^4 + \cdots \tag{3.9}$$

where $k_z = 2\pi/\lambda_w$. The dynamical map for wigglers used by SAD includes terms in the Hamiltonian up to $O(y^4)$.

From terms in the Hamiltonian of the form in Equation (3.9), we expect a tune shift from the wigglers given by:

$$\Delta\nu_y = \frac{\langle\beta_y\rangle}{4\pi} \frac{L_w}{\rho_w^2} \left(\frac{1}{2} + \frac{1}{3} k_z^2 y^2\right) \tag{3.10}$$

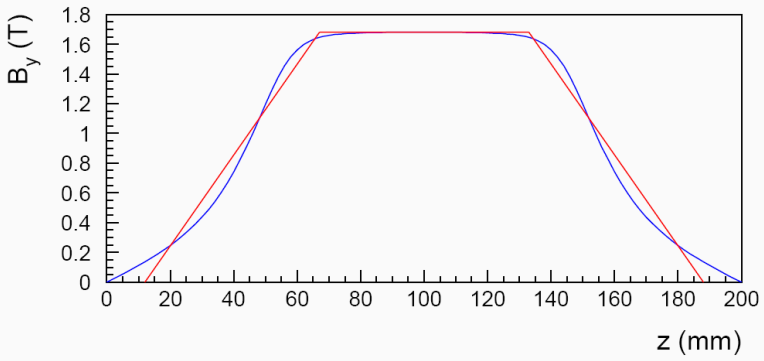

Figure 3.2: Fringe-field model of the wiggler used in SAD. The blue line shows the longitudinal variation of the vertical field in one design of a wiggler for TESLA. The red line shows the approximation made by SAD.

Defining an amplitude-dependent tune shift coefficient c_{yy}:

$$c_{yy} = \frac{1}{2}\frac{\partial \nu_y}{\partial J_y} \tag{3.11}$$

where J_y is the vertical betatron action, and making the approximation:

$$y^2 \approx 2\beta_y J_y \tag{3.12}$$

we find that the tune shift with amplitude from the wigglers is given by:

$$c_{yy} \approx \frac{\langle\beta_y\rangle^2}{12\pi}\frac{k_z^2}{\rho_w^2}L_w \tag{3.13}$$

Ideal Nonlinear Wiggler Model

In the ideal nonlinear wiggler model, the wiggler field is represented (in a periodic section of the wiggler) as:

$$B_x = 0 \tag{3.14}$$
$$B_y = \hat{B}\cos k_z z \cosh k_z y \tag{3.15}$$
$$B_z = -\hat{B}\sin k_z z \sinh k_z y \tag{3.16}$$

where $\hat{B}$ is the wiggler peak field, and $k_z = 2\pi/\lambda_w$ for wiggler of period λ_w. Note that this field satisfies Maxwell's equations, and has a pure sinusoidal

dependence along the axis of the wiggler. It is possible to derive a dynamical map for a particle moving through a field of this form. The lowest-order vertical tune shifts with amplitude in this model agree with those in the fringe-field wiggler model. Using an ideal nonlinear wiggler model in any of the reference lattices generally requires rematching, to eliminate any beta-beat and to restore the design tunes.

Modified CESR-c Wiggler Model

The ideal nonlinear wiggler model may be generalized as follows. The wiggler field can be represented, for some set of coefficients c_{mn} as:

$$B_x = -\hat{B}\sum_{m,n} c_{mn}\frac{k_{x,m}}{k_{y,mn}}\sin k_{x,m}x\cos nk_z z\sinh k_{y,mn}y \tag{3.17}$$

$$B_y = \hat{B}\sum_{m,n} c_{mn}\cos k_{x,m}x\cos nk_z z\cosh k_{y,mn}y \tag{3.18}$$

$$B_z = -\hat{B}\sum_{m,n} c_{mn}\frac{nk_z}{k_{y,mn}}\cos k_{x,m}x\sin nk_z z\sinh k_{y,mn}y \tag{3.19}$$

where the values of n are integers, and to satisfy Maxwell's equations, we have the condition:

$$k_{y,mn}^2 = k_{x,m}^2 + n^2k_z^2 \tag{3.20}$$

The coefficients c_{mn} and the values of $k_{x,m}$ may be found from some fitting procedure to a numerical field map consisting of values of the three field components on a three-dimensional grid within the wiggler. An appropriate field map may be produced by a magnetic modeling code. The ideal nonlinear wiggler model is recovered as the special case $k_{x,m} = 0$ for all m, and $c_{mn} = \delta_{n1}$.

Given a magnetic field map, a dynamical map for tracking through the wiggler may be produced by a variety of means. One technique involves integrating the equations of motion for a particle in the wiggler field using a differential algebra code, producing a dynamical map in Taylor form. Tools for this are included in BMAD [63]; other codes capable of this are also available, for example, COSY [8]. A second technique involves generating a map in Lie algebra form; this may be done, for example, with the code MARYLIE [19]. Both techniques require an analytical representation of the field map, either in the cartesian form given above, or in a form using cylindrical or elliptical coordinates.

The superferric wigglers installed to increase the radiation damping rates in CESR-c have parameters comparable to those appropriate for the damping rings. They have wide physical aperture, and good field quality. They have also been extensively studied in simulation, and in machine studies of CESR-c. A field map for a modified version of the CESR-c wigglers has been produced specifically for studies of wiggler effects in the ILC damping rings. The modifications to the original CESR-c design include an increase in the number of periods in a wiggler "section", and a reduction in the peak field. The model includes the effects of the ends of a section, which are modified from the periodic part so as to control the trajectory through the wiggler. Using a modified CESR-c wiggler model in any of the reference lattices generally requires rematching, to eliminate any beta-beat and to restore the design tunes.

3.1.3 Dynamic Aperture

Tune Shifts

Useful indications of the dynamic behavior of a lattice are provided by the tune shifts with amplitude, and by the higher-order tune shifts with energy. While it is generally not possible to determine the dynamic aperture of a lattice on the basis of the tune shifts alone, usually it is desirable (in terms of achieving a large dynamic aperture) to achieve tune shifts that are as small as possible.

The tune shifts for the seven reference lattices have been calculated with the code LEGO [11], using Taylor maps and normal form analysis; the results are shown in Tables 3.5 (tune shifts with amplitude) and 3.6 (higher-order tune shifts with energy). The chromatic sextupoles in all the lattices were tuned so that the first-order chromaticities (tune shifts with energy) were zero. We note that the higher-order tune shifts with energy in the OCS lattice are significantly smaller than in the other lattices; this is consistent with the large energy aperture in OCS that we will see in the dynamic aperture and frequency map results.

Results from BMAD

The dynamic aperture for each of the reference lattices was calculated by tracking in BMAD, for six different cases:

1. linear wiggler model, no lattice errors (Figure 3.3);

2. linear wiggler model, including lattice errors (Figure 3.4);

Table 3.5: Tune shifts with amplitude in the reference lattices.

Lattice	$\frac{\partial \nu_x}{\partial J_x}$ [m^{-1}]	$\frac{\partial \nu_y}{\partial J_y}$ [m^{-1}]	$\frac{\partial \nu_x}{\partial J_y} \approx \frac{\partial \nu_y}{\partial J_x}$ [m^{-1}]
PPA	-9806	-2306	-1232
OTW	-4090	-11518	12596
OCS	-11876	1964	-11186
BRU	-968	-2002	-6472
MCH	-1428	-2260	-8016
DAS	-3166	-1720	-640
TESLA	-15858	-5544	3834

Table 3.6: Higher-order tune shifts with energy in the reference lattices.

Lattice	$\frac{\partial^2 \nu_x}{\partial \delta^2}$	$\frac{\partial^3 \nu_x}{\partial \delta^3}$	$\frac{\partial^2 \nu_y}{\partial \delta^2}$	$\frac{\partial^3 \nu_y}{\partial \delta^3}$
PPA	233	5713	112	8912
OTW	476	25288	493	-16145
OCS	-18	-270	2	42
BRU	-37	5218	-78	2400
MCH	-78	3825	-128	3337
DAS	343	50751	358	25538
TESLA	318	12219	-68	2566

3. ideal nonlinear wiggler model, no lattice errors (Figure 3.5);

4. ideal nonlinear wiggler model, including lattice errors (Figure 3.6);

5. modified CESR-c wiggler model, no lattice errors (Figure 3.7);

6. modified CESR-c wiggler model, including lattice errors (Figure 3.8).

Synchrotron oscillations were included for off-energy tracking, but radiation and physical apertures were not included. Particles were tracked for one damping time. In Figures 3.3 – 3.8, the inner pink ellipse shows the speicified acceptance of 3σ, with an injected normalized emittance $\gamma\epsilon = 0.01$ m·rad. With linear wiggler and no multipole errors (Figure 3.3) all the reference lattices achieve the specified acceptance for energy deviations up to 0.5%. However, with the ideal nonlinear wiggler and multipole errors (Figure 3.6) only PPA, OCS and MCH have any margin over the specified acceptance for energy deviations up to 0.5%. In the case that some particles have energy errors greater than 0.5%, only the OCS lattice has any margin.

The modified CESR-c wiggler model is sufficiently close to the ideal nonlinear wiggler model that for the lattices tracked using both models, there are no significant differences in the results (Figures 3.7 and 3.8). The largest difference is seen in PPA: in this case, the difference is at least partly explained by the fact that the dynamic aperture extends beyond the wiggler field region over which the field fit was performed; particle tracking outside the known field region is not reliable.

The OCS lattice clearly has the best dynamic aperture. We note that this is also one of only two lattices with a high degree of symmetry: OTW is a racetrack lattice, and BRU, MCH, DAS and TESLA all have dogbone layouts. It is known that the dynamics of a storage ring are improved by increasing the lattice symmetry, since this reduces the number of systematic resonances that may limit the dynamic aperture. To understand better the benefits for the damping rings, we constructed a modified version of the 6 km BRU lattice, in which the arc cells were re-arranged to produce a circular, rather than a dogbone, footprint; the modified lattice has six-fold symmetry. The optics were essentially the same; for the arc cells, which comprise most of the lattice, only the dipole strength was changed, to produce the correct bending angle for the new layout. The tunes were kept the same.

The footprints of the original BRU lattice and the modified BRU lattice are shown in Figure 3.9. The corresponding dynamic apertures (with ideal nonlinear wiggler model and 15 seeds of multipole errors) are shown in Figure 3.10. With an improved symmetry, there is a very significant improvement

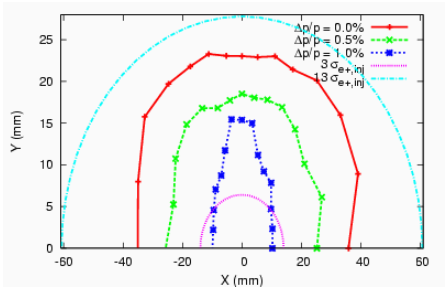

(a) PPA

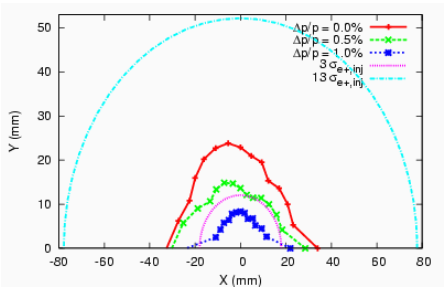

(b) OTW

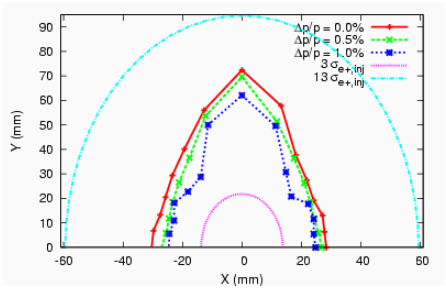

(c) OCS

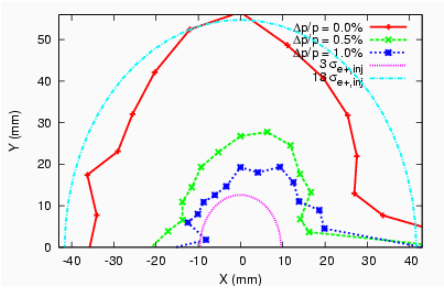

(d) BRU

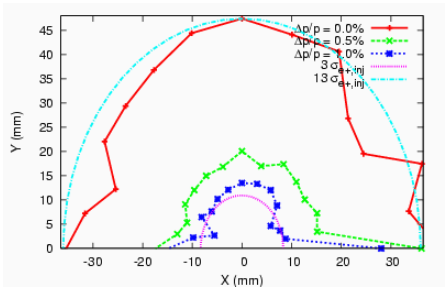

(e) MCH

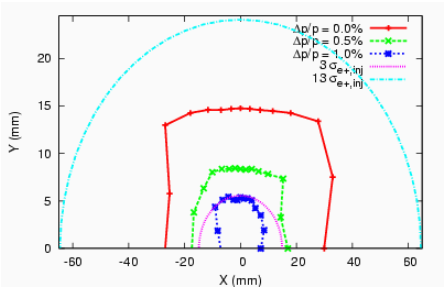

(f) DAS

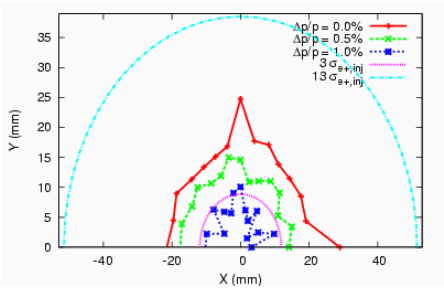

(g) TESLA

Figure 3.3: Dynamic aperture in the reference lattices with linear wiggler model and no multipole errors, computed with BMAD.

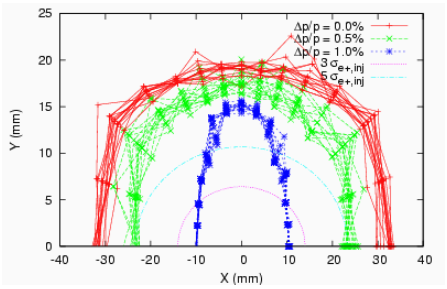

(a) PPA

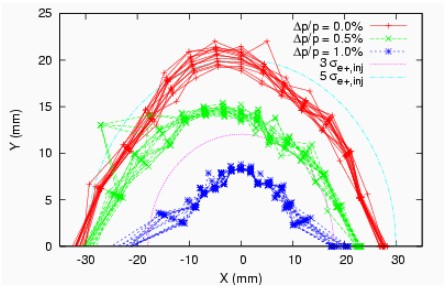

(b) OTW

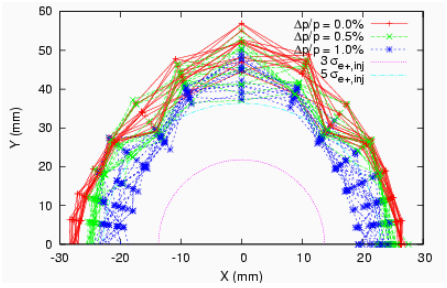

(c) OCS

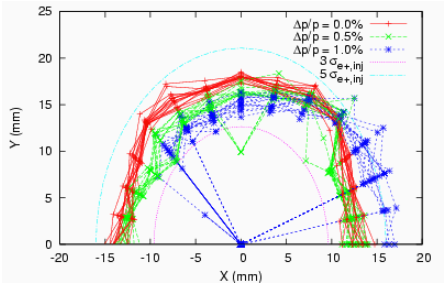

(d) BRU

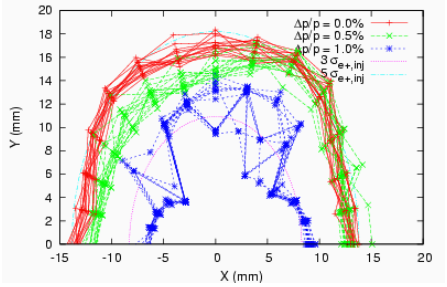

(e) MCH

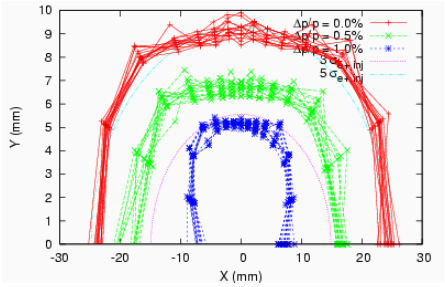

(f) DAS

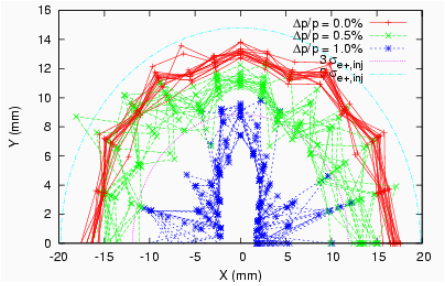

(g) TESLA

Figure 3.4: Dynamic aperture in the reference lattices with linear wiggler model and 15 seeds of multipole errors, computed with BMAD.

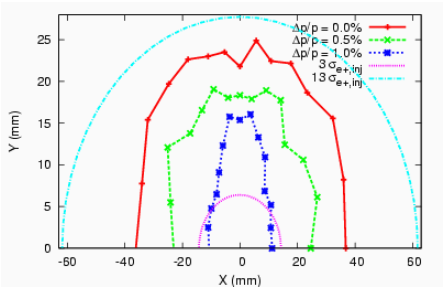

(a) PPA

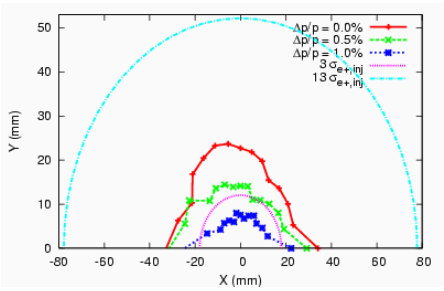

(b) OTW

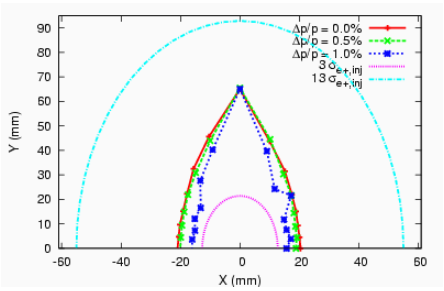

(c) OCS

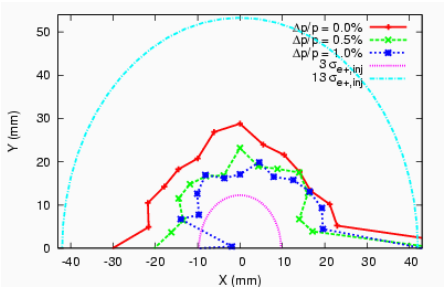

(d) BRU

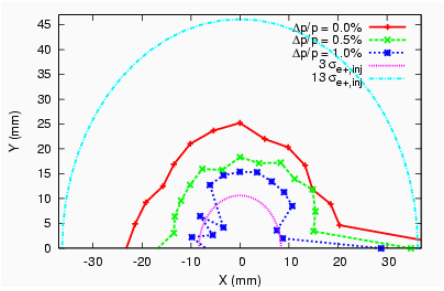

(e) MCH

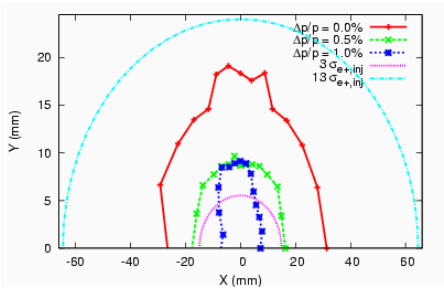

(f) DAS

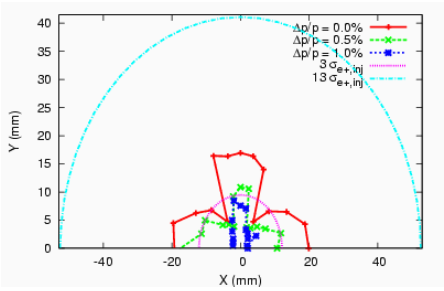

(g) TESLA

Figure 3.5: Dynamic aperture in the reference lattices with ideal nonlinear wiggler model and no multipole errors, computed with BMAD.

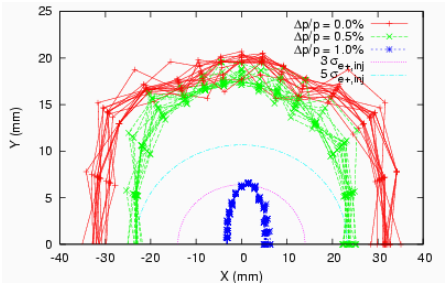

(a) PPA

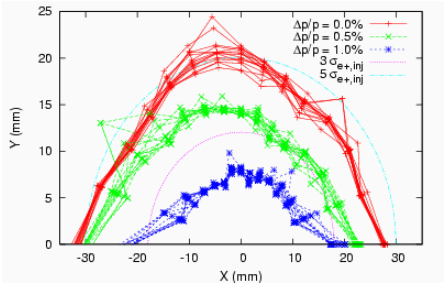

(b) OTW

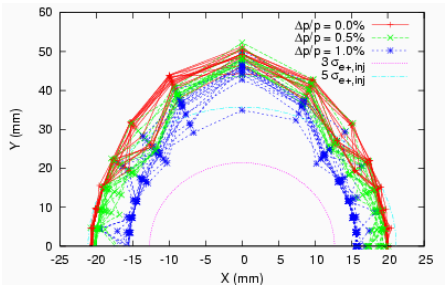

(c) OCS

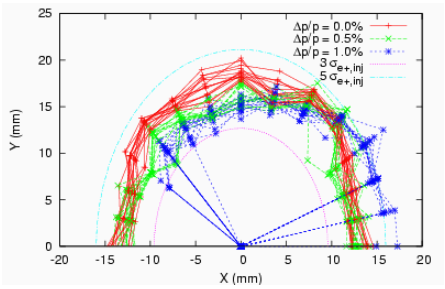

(d) BRU

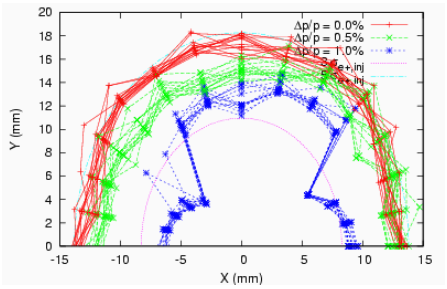

(e) MCH

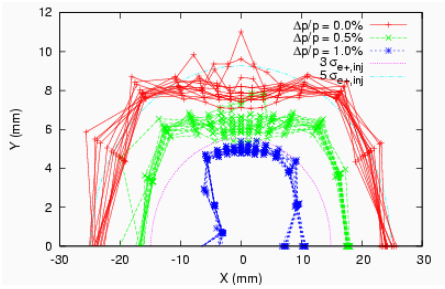

(f) DAS

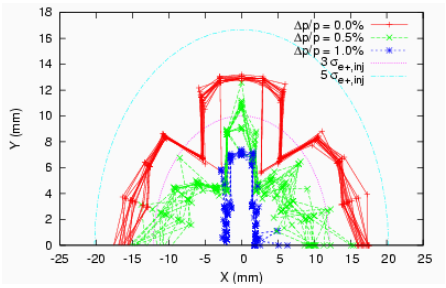

(g) TESLA

Figure 3.6: Dynamic aperture in the reference lattices with ideal nonlinear wiggler model and 15 seeds of multipole errors, computed with BMAD.

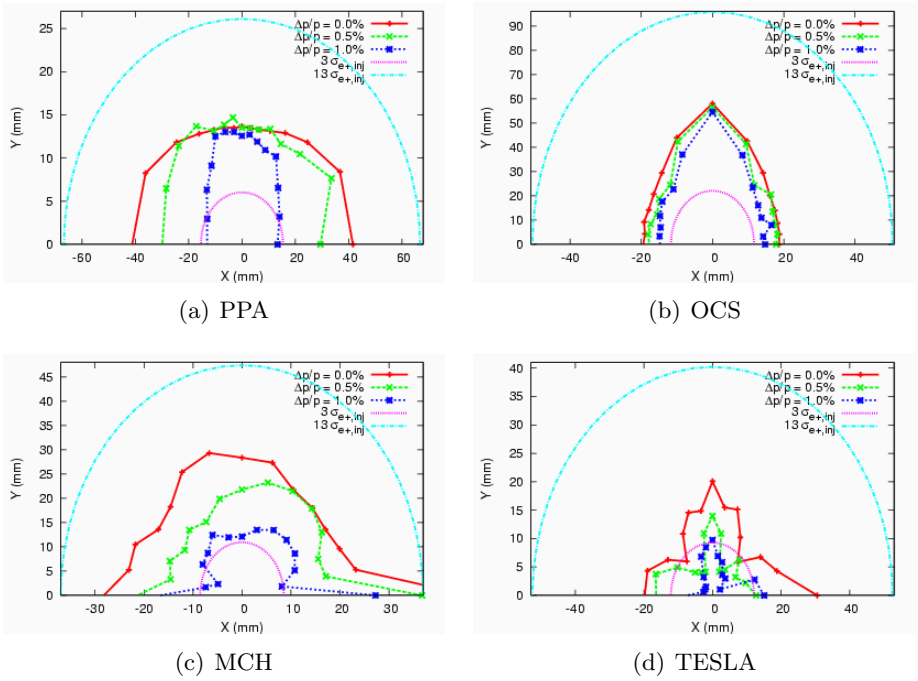

(a) PPA (b) OCS

(c) MCH (d) TESLA

Figure 3.7: Dynamic aperture in the reference lattices with modified CESR-c wiggler model and no multipole errors, computed with BMAD.

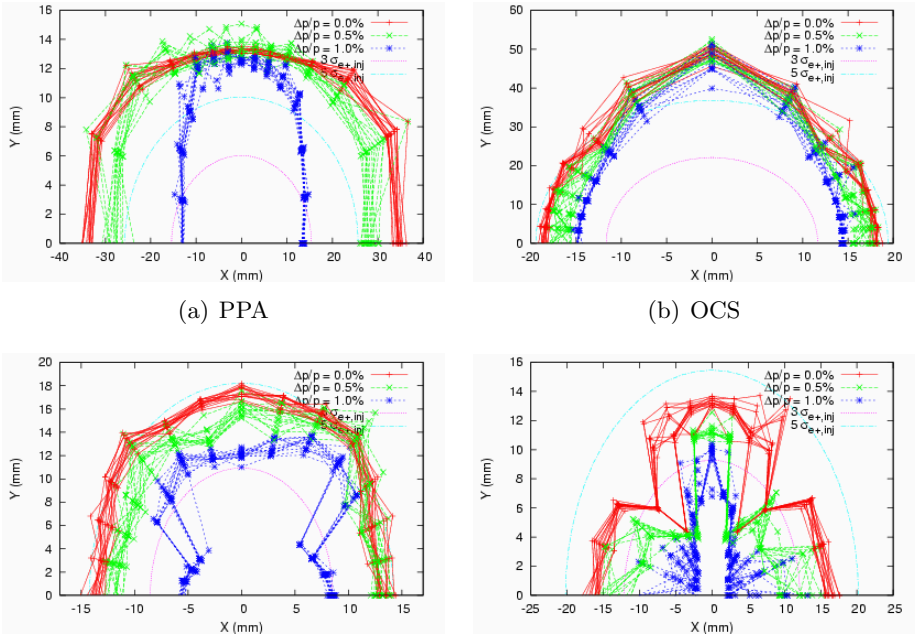

(a) PPA (b) OCS

(c) MCH (d) TESLA

Figure 3.8: Dynamic aperture in the reference lattices with modified CESR-c wiggler model and multipole errors, computed with BMAD.

in the dynamic aperture. Even for energy errors as large as 1%, the dynamic aperture with ideal nonlinear wiggler model and multipole errors is in excess of 5σ.

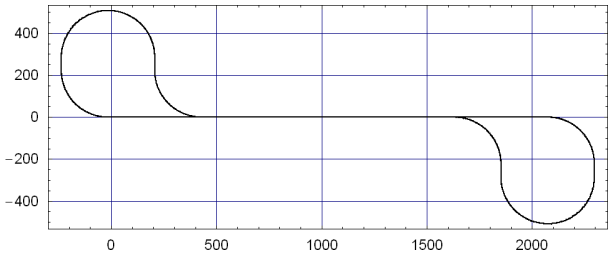

(a) BRU footprint.

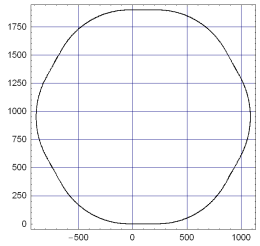

(b) Modified BRU footprint.

Figure 3.9: Footprints of (a) BRU lattice and (b) modified BRU lattice.

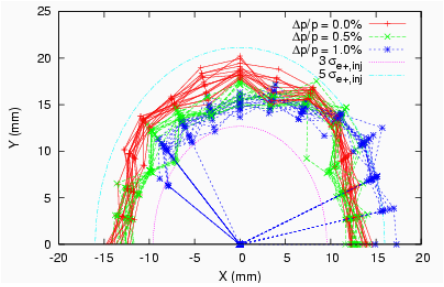

(a) BRU dynamic aperture.

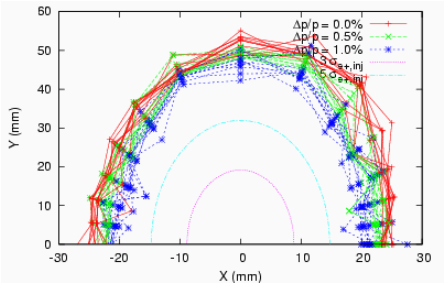

(b) Modified BRU dynamic aperture.

Figure 3.10: Dynamic apertures of (a) BRU lattice and (b) modified BRU lattice. Note the different horizontal and vertical scales in the two plots.

Results from LEGO

Simulations of the dynamic apertures of the ideal lattices and with the errors of Tables 3.1–3.3 for all seven reference lattices have been carried out using an object-oriented code, LEGO [11]. The results are essentially identical to those obtained with BMAD, and most of the results from LEGO will not be shown in this document to avoid duplication. However, the confirmation of the simulation results using different codes is an essential part of this study.

For the TESLA lattice, we studied two versions with different layouts: an "S-shaped" version, and a "C-shaped" version. The C-shaped version

is the one presented in the TESLA TDR [72], and has the layout shown in Figure 2.7. TESLA-S is a modified version of the TESLA lattice, in which the direction of bend of one of the return arcs is reversed, so that the two arcs lie on opposite sides of the straights. The layout is similar to that of MCH, shown in Figure 2.5. We found that the S-shaped lattice has a better dynamic aperture than the C-shaped lattice, because of the two-fold symmetry (compared to the one-fold symmetry of the C-shaped lattice). Tracking results of dynamic aperture with multipole errors and single-mode wiggler [12] for the C-shaped and S-shaped TESLA lattices are shown in Figure 3.11. It is clear that the effect of a resonance driven by the nonlinear wiggler field is significantly reduced by the symmetry in the S-shaped configuration.

Results from SAD

The dynamic apertures of some of the reference lattices were calculated in SAD by tracking for one damping time. The tracking included synchrotron radiation, but without quantum excitation; no machine errors were included. The linear chromaticities of the lattices were tuned (by adjusting the sextupole strengths) to be zero. Particles were tracked with equal initial amplitudes of horizontal and vertical motion, i.e. $J_{y0}/J_{x0} = 1$, and for a range of energy deviations. Trajectories for which the horizontal and vertical coordinates each remained below 10 cm during the course of the tracking were assumed to be stable. The dynamic aperture for the TESLA S-shaped lattice is shown in Figure 3.12.

Figure 3.13 shows the vertical tune shifts with amplitude under various conditions (with and without wiggler nonlinearities, and with and without sextupoles). Note that tracking is always performed with synchrotron oscillations; this means that even with sextupoles off and a linear wiggler model, there is still a large tune shift with amplitude because of the combination of the change in energy with betatron amplitude and the natural chromaticity of the lattice. As the betatron amplitude increases, the energy deviation of the particle becomes more negative so that the trajectory stays synchronous with the RF, and since the natural chromaticity of the lattice is negative, the tune increases.

We can compare the change in the tune shift with amplitude contributed from the wiggler using the results shown in Figure 3.13, with a calculation made using Equation (3.13). Specifically, we determine the effect of the wiggler in the tracking, by looking at the change in the tune shift in amplitude between the linear and nonlinear wiggler models, first with the sextupoles

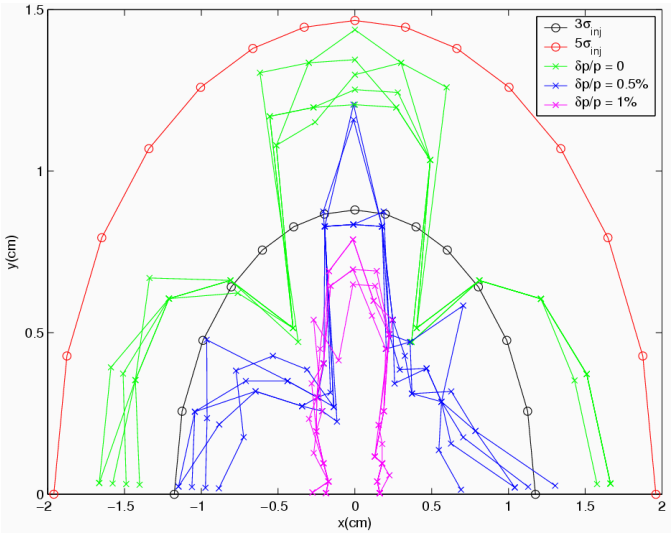

(a) TESLA-C dynamic aperture.

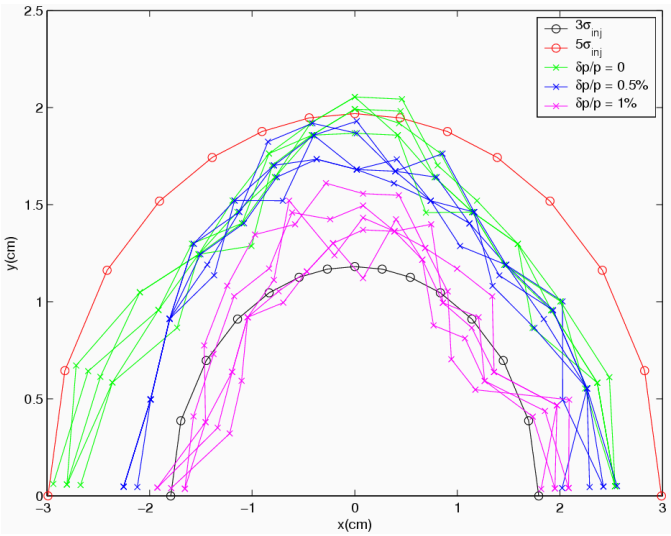

(b) TESLA-S dynamic aperture.

Figure 3.11: Dynamic aperture of (a) the the TESLA C-shaped lattice, and (b) the TESLA S-shaped lattice, computed with LEGO. The black and red ellipses show three and five times the injected beam size respectively (assuming a normalized injected emittance of 0.01 m·rad). The green, blue and purple points show the dynamic aperture for on-energy particles, and particles with initial 0.5% and 1% energy deviation respectively. Five seeds of random multipole errors were used.

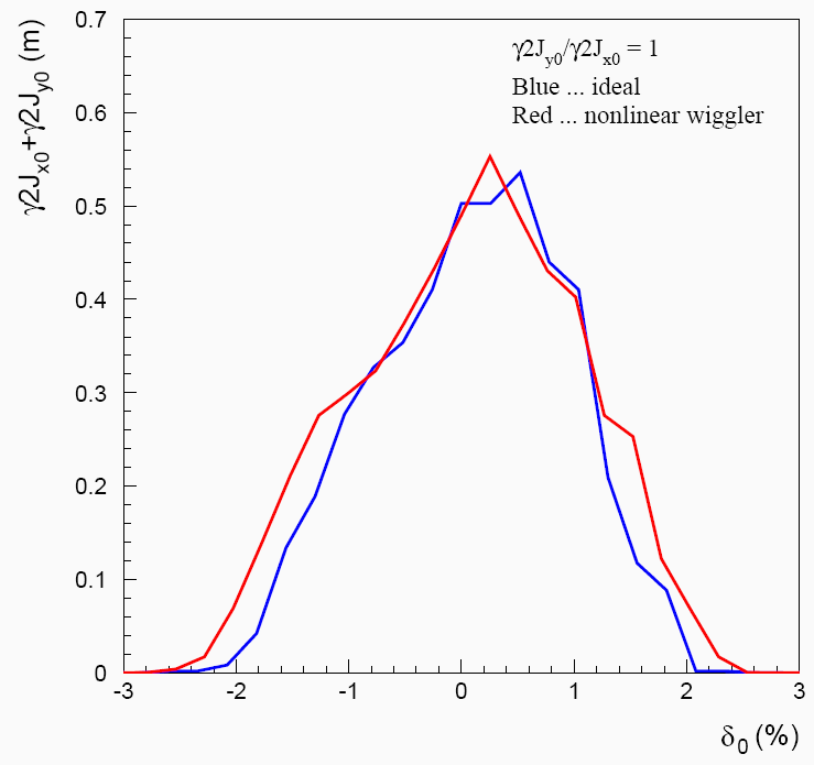

Figure 3.12: Dynamic aperture of the the TESLA S-shaped lattice computed with SAD. The blue line shows the result with a linear wiggler model; the red line shows the result with a fringe-field model for the wiggler.

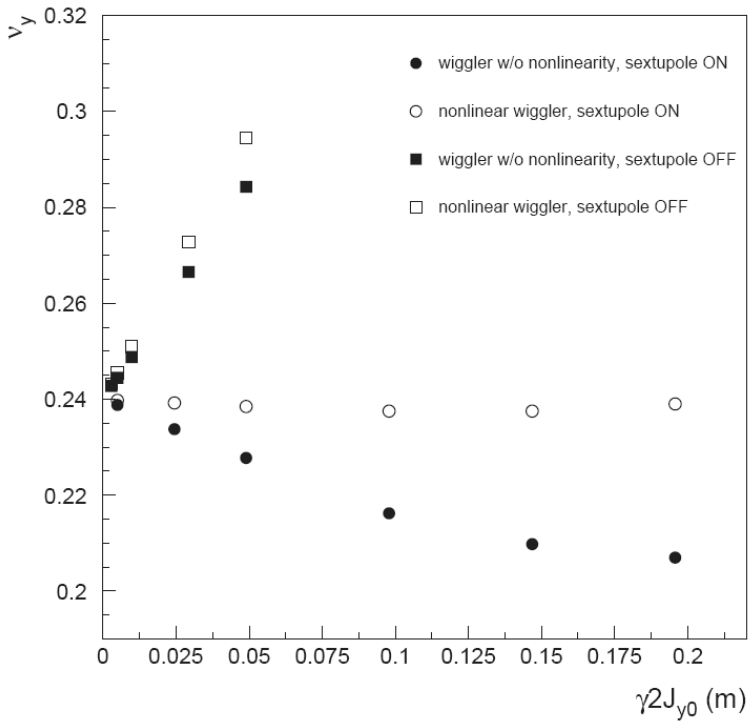

Figure 3.13: Vertical tune shifts with amplitude in the TESLA S-shaped lattice, computed with SAD. Solid circles: linear wiggler, sextupoles on. Open circles: fringe-field wiggler model, sextupoles on. Solid squares: linear wiggler, sextupoles off. Open squares: fringe-field wiggler model, sextupoles off.

Table 3.7: Effect of wiggler nonlinearities on the vertical tune shift with amplitude in the TESLA-S lattice, from analytical estimate and from tracking.

Mean beta function, $\langle\beta_y\rangle$	8.7 m
Total wiggler length, L_w	417 m
Bending radius, ρ_w	10.4 m
Wiggler period, λ_w	0.4 m
Tune shift coefficient c_{yy} from Equation (3.13)	1910 m^{-1}
Tune shift coefficient c_{yy} from tracking, sextupoles on	2123 m^{-1}
Tune shift coefficient c_{yy} from tracking, sextupoles off	2203 m^{-1}

on, and then with the sextupoles off. The results are shown in Table 3.7. There is good agreement between the tune shift with amplitude calculated using Equation (3.13) and the same quantity estimated from the tracking data.

Tune scans were performed for selected reference lattices, to find the optimal working point for achieving a large dynamic aperture. The results are shown in Figures 3.14 (PPA), 3.15 (OCS), 3.16 (MCH) and 3.17 (TESLA). The color scale indicates the smallest value of $(A_x + A_y)_{\max}$ within $-0.5\% < \delta_0 < 0.5\%$, where δ_0 is the initial energy deviation, and $(A_x + A_y)_{\max}$ is the largest amplitude of betatron amplitude (for initial conditions with $J_y/J_x = 1$) for which the particle trajectory is stable. The red contours bound acceptable working points, for which $(A_x + A_y)_{\max} > 0.09$ m·rad for all energy deviations in the range -0.5% to $+0.5\%$. Lighter colors indicate larger dynamic aperture, with white showing $(A_x + A_y)_{\max} > 0.4$ m·rad.

The tune spaces each exhibit several resonances, though the number and strength of the resonances varies widely. MCH and TESLA-S in particular show strong synchro-betatron resonances. Note that the RF voltage in the MCH lattice was set at 115 MV, to give a bunch length of 7 mm.

Following the tune scans, new working points for the lattices were chosen to optimize the dynamic aperture. The new working points are shown in Table 3.8. Note that the "optimized" tunes may not be acceptable from other considerations; for example, the proposed working points tend to be close to coupling resonances, which could make it difficult to correct the coupling sufficiently well to achieve the specified vertical emittance in the damped beam.

Dynamic apertures at the optimized working points are shown in Figure 3.18. It appears that all lattices meet the specifications in terms of the

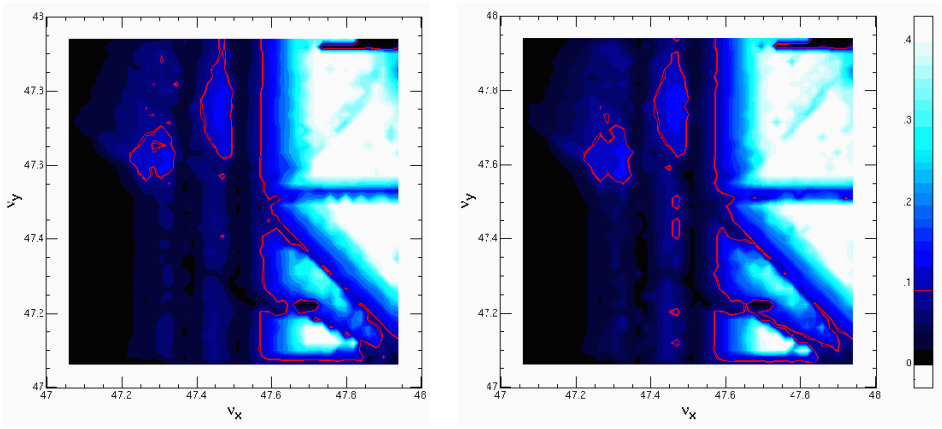

(a) No multipole errors. (b) With multipole errors.

Figure 3.14: Dynamic aperture tune scan for PPA, computed with SAD.

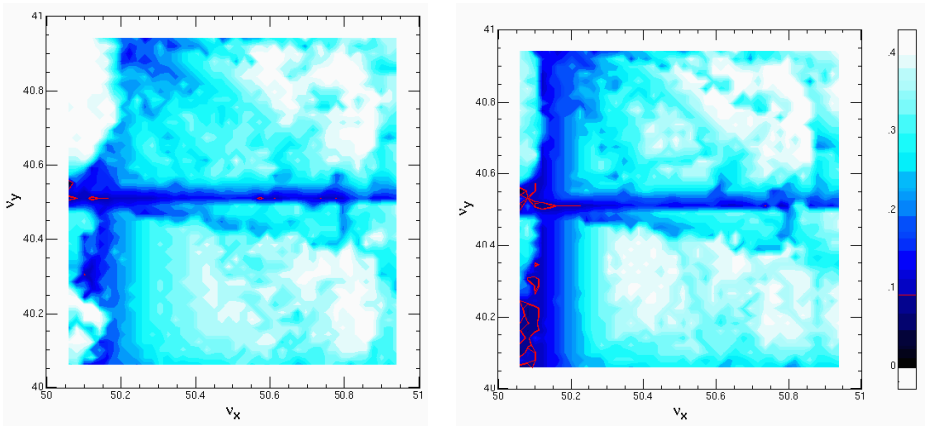

(a) No multipole errors. (b) With multipole errors.

Figure 3.15: Dynamic aperture tune scan for OCS, computed with SAD.

Table 3.8: Working points for optimized dynamic aperture.

Lattice	ν_x	ν_y
PPA	47.81	47.68
OCS	50.84	40.80
MCH	75.70	76.60
TESLA S-shaped	72.32	47.24

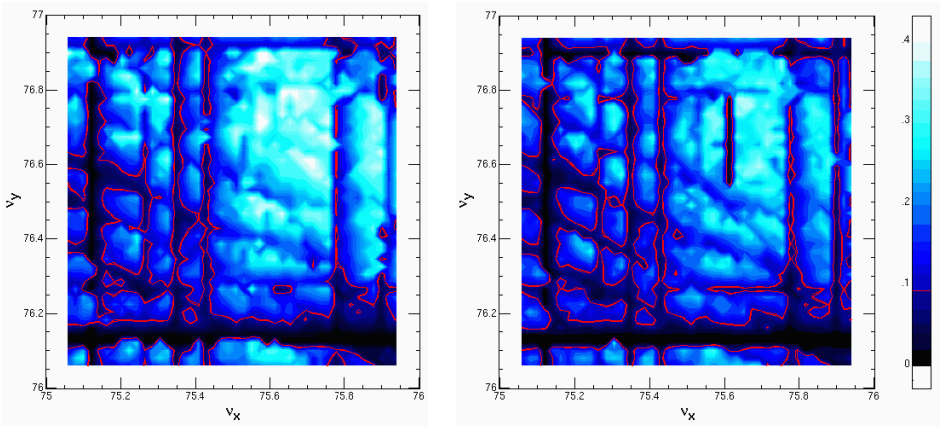

(a) No multipole errors. (b) With multipole errors.

Figure 3.16: Dynamic aperture tune scan for MCH, computed with SAD.

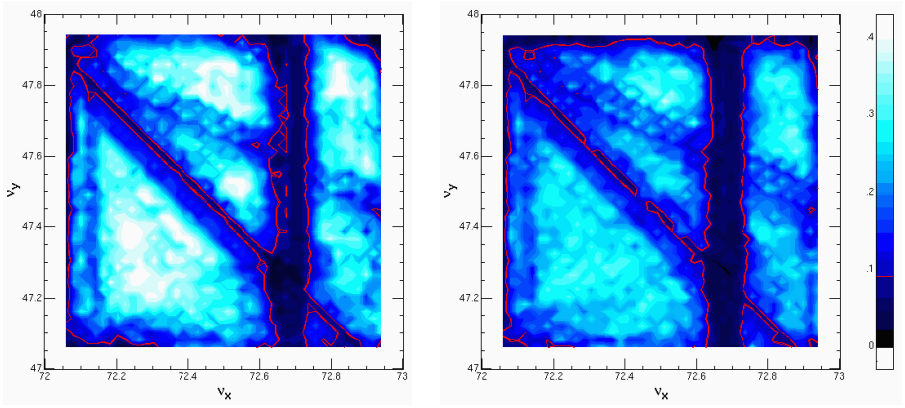

(a) No multipole errors. (b) With multipole errors.

Figure 3.17: Dynamic aperture tune scan for TESLA, computed with SAD.

dynamic aperture, even with nonlinear wiggler model and multipole errors. OCS provides the largest margin. We should emphasize that the optimized working points may not be realizable in practice.

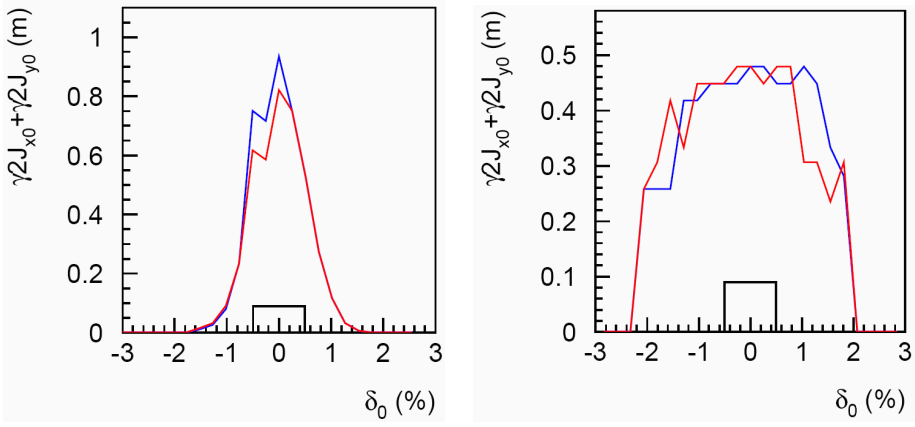

(a) PPA (b) OCS

(c) MCH (d) TESLA

Figure 3.18: Dynamic apertures at optimized working points, computed with SAD. In each plot, the blue line shows the dynamic aperture without multipole errors; the red line shows the dynamic aperture with multipole errors. The black rectangles indicated the acceptance specification.

3.1.4 Frequency Map Analysis

A more complete description of the dynamics in a storage ring than is provided by a survival plot may be obtained using frequency map analysis. In this technique, particles are tracked with a range of horizontal and vertical betatron amplitudes, and the tunes for each particle are determined numerically from the tracking data. The diffusion rate is also determined, as the rate of change of tune over the course of the tracking; in the plots shown in this section, the changes in tune between the first and second half of the tracking data are shown logarithmically on a color scale.

Frequency maps have been computed for the reference lattices with several different codes. In this section, we compare the results.

Results from MERLIN

Frequency maps were calculated in MERLIN using the ideal nonlinear wiggler model. The results are shown in Figures 3.19–3.25. No multipole errors were applied to the lattice. The tunes for different betatron amplitudes were found from an interpolated Fourier-Hanning analysis of 512 turns of tracking data. The diffusion rate in tune space, indicated on a color scale, is the sum in quadrature of the changes in horizontal and vertical tune between the first 256 and the second 256 turns.

Results from BMAD

Frequency maps were computed in BMAD for three wiggler models:

1. linear wiggler model (Figure 3.26);

2. ideal nonlinear wiggler model (Figure 3.27);

3. modified CESR-c wiggler model (Figure 3.28).

It is clear from Figures 3.26 and 3.27 that the wiggler nonlinearities have a significant impact on the dynamics in many of the reference lattices. However, looking at Figures 3.27 and 3.28, it appears that there are no significant new features associated with the modified CESR-c wiggler model, compared with the ideal nonlinear wiggler model. For the case of the ideal nonlinear wiggler, there is good agreement between the frequency map plots from MERLIN, and those from BMAD.

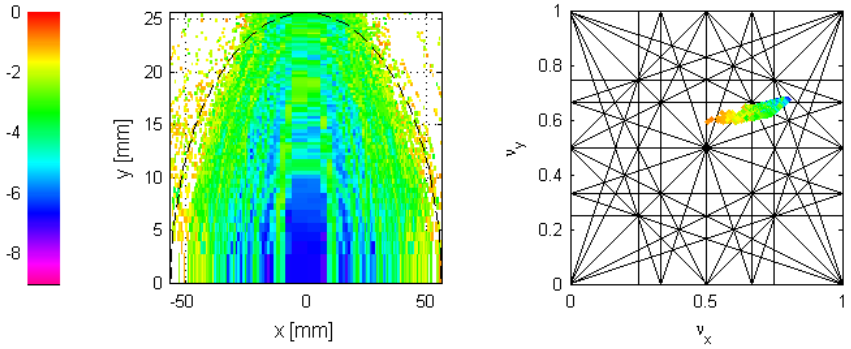

(a) Frequency map in $x - y$ space.

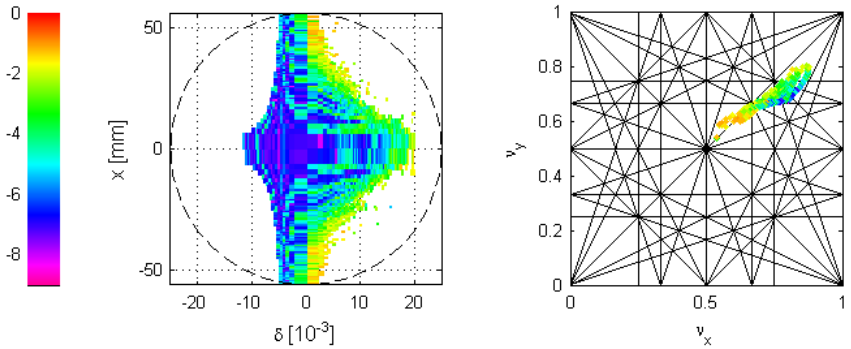

(b) Frequency map in $\delta - x$ space.

Figure 3.19: Frequency map analysis for PPA with ideal nonlinear wiggler model, computed with MERLIN. The upper plots show the frequency map in coordinate space; the broken line shows 12 times the rms injected beam size, assuming a normalized emittance of 0.01 nm·rad. The lower plots show the frequency map in $x-\delta$ space; the broken line shows an ellipse with limits 12 times the rms horizontal injected beam size, and an energy deviation of 2.5%.

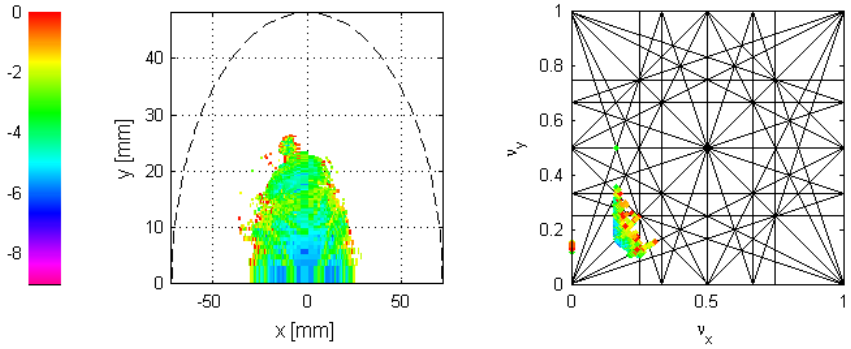

(a) Frequency map in $x - y$ space.

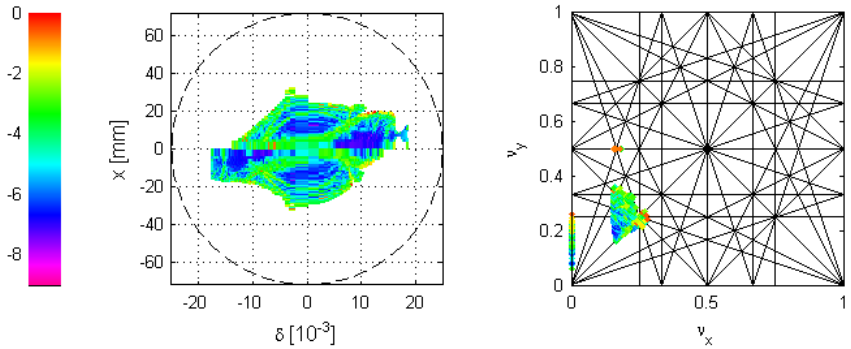

(b) Frequency map in $\delta - x$ space.

Figure 3.20: Frequency map analysis for OTW with ideal nonlinear wiggler model, computed with MERLIN. The upper plots show the frequency map in coordinate space; the broken line shows 12 times the rms injected beam size, assuming a normalized emittance of 0.01 nm·rad. The lower plots show the frequency map in $x-\delta$ space; the broken line shows an ellipse with limits 12 times the rms horizontal injected beam size, and an energy deviation of 2.5%.

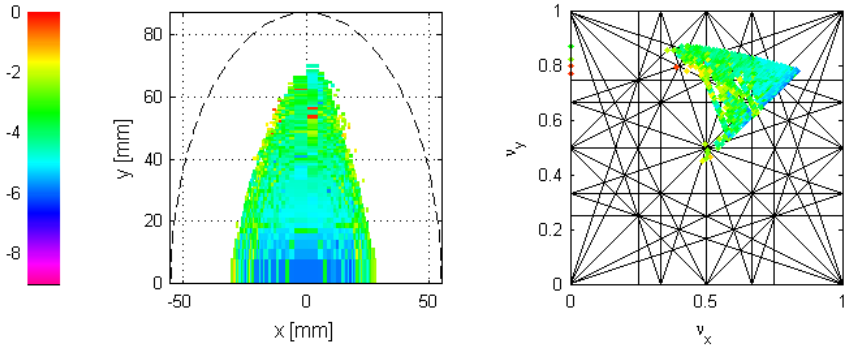

(a) Frequency map in $x - y$ space.

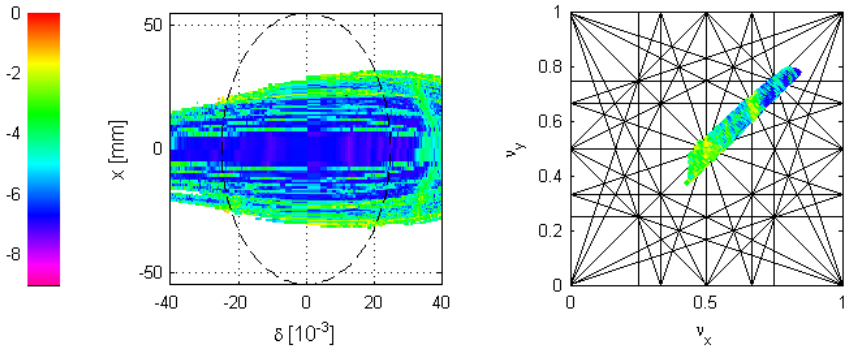

(b) Frequency map in $\delta - x$ space.

Figure 3.21: Frequency map analysis for OCS with ideal nonlinear wiggler model, computed with MERLIN. The upper plots show the frequency map in coordinate space; the broken line shows 12 times the rms injected beam size, assuming a normalized emittance of 0.01 nm·rad. The lower plots show the frequency map in $x-\delta$ space; the broken line shows an ellipse with limits 12 times the rms horizontal injected beam size, and an energy deviation of 2.5%.

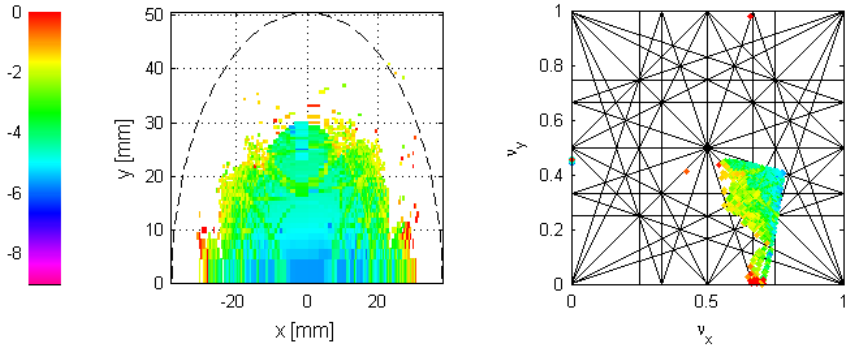

(a) Frequency map in $x - y$ space.

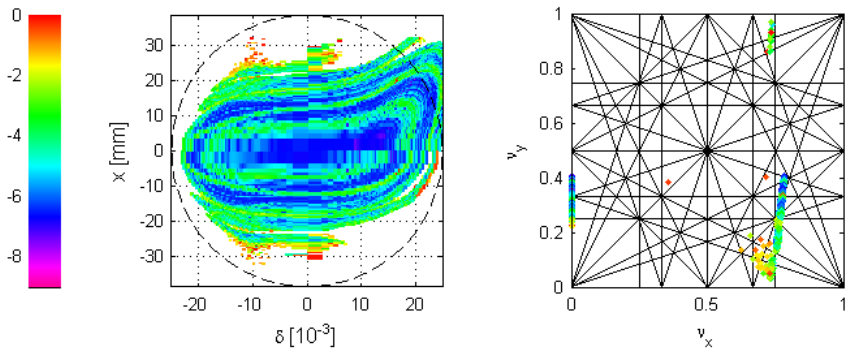

(b) Frequency map in $\delta - x$ space.

Figure 3.22: Frequency map analysis for BRU with ideal nonlinear wiggler model, computed with MERLIN. The upper plots show the frequency map in coordinate space; the broken line shows 12 times the rms injected beam size, assuming a normalized emittance of 0.01 nm·rad. The lower plots show the frequency map in $x-\delta$ space; the broken line shows an ellipse with limits 12 times the rms horizontal injected beam size, and an energy deviation of 2.5%.

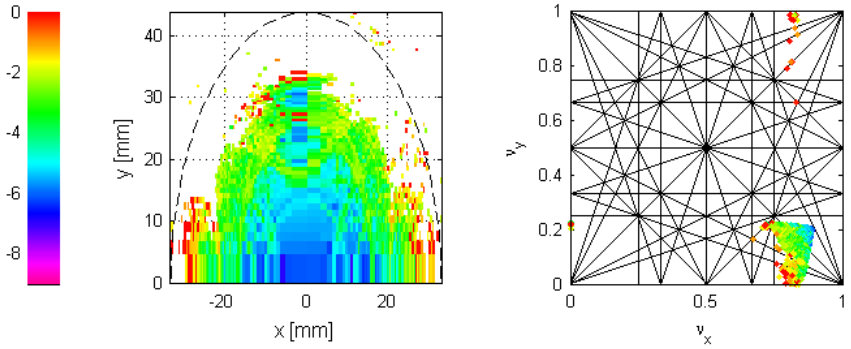

(a) Frequency map in $x - y$ space.

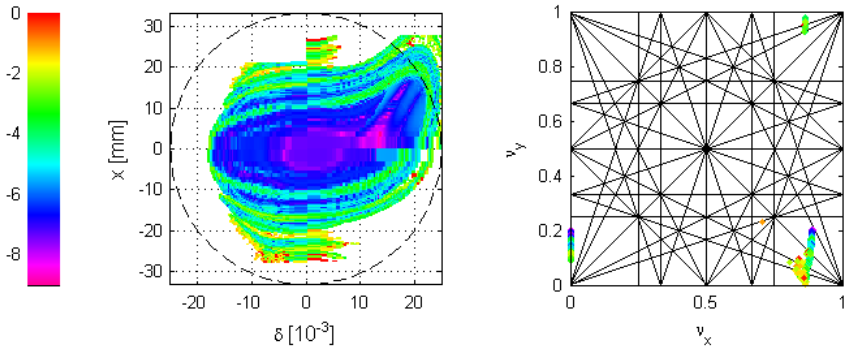

(b) Frequency map in $\delta - x$ space.

Figure 3.23: Frequency map analysis for MCH with ideal nonlinear wiggler model, computed with MERLIN. The upper plots show the frequency map in coordinate space; the broken line shows 12 times the rms injected beam size, assuming a normalized emittance of 0.01 nm·rad. The lower plots show the frequency map in $x-\delta$ space; the broken line shows an ellipse with limits 12 times the rms horizontal injected beam size, and an energy deviation of 2.5%.

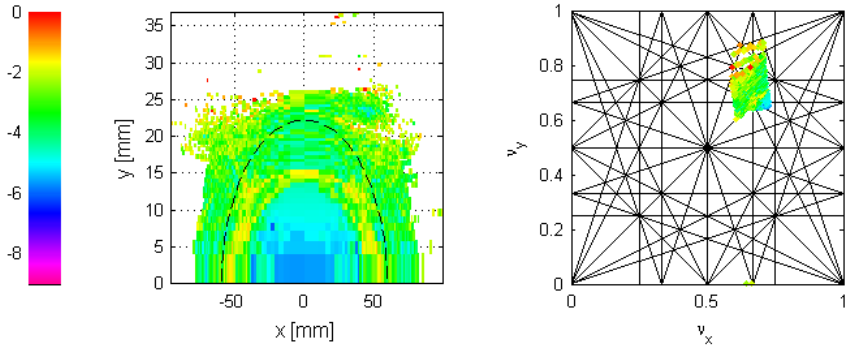

(a) Frequency map in $x - y$ space.

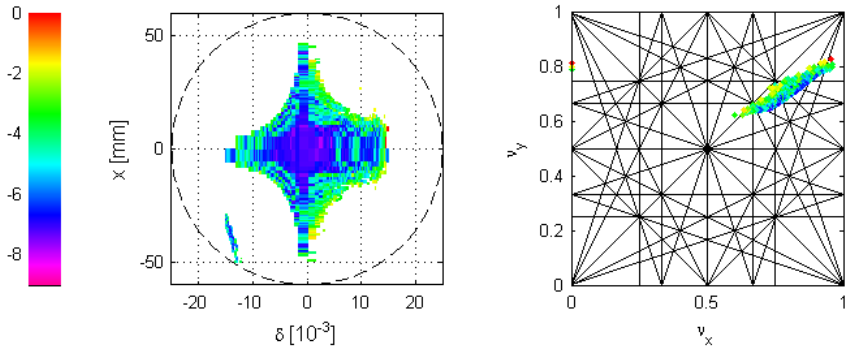

(b) Frequency map in $\delta - x$ space.

Figure 3.24: Frequency map analysis for DAS with ideal nonlinear wiggler model, computed with MERLIN. The upper plots show the frequency map in coordinate space; the broken line shows 12 times the rms injected beam size, assuming a normalized emittance of 0.01 nm·rad. The lower plots show the frequency map in $x-\delta$ space; the broken line shows an ellipse with limits 12 times the rms horizontal injected beam size, and an energy deviation of 2.5%.

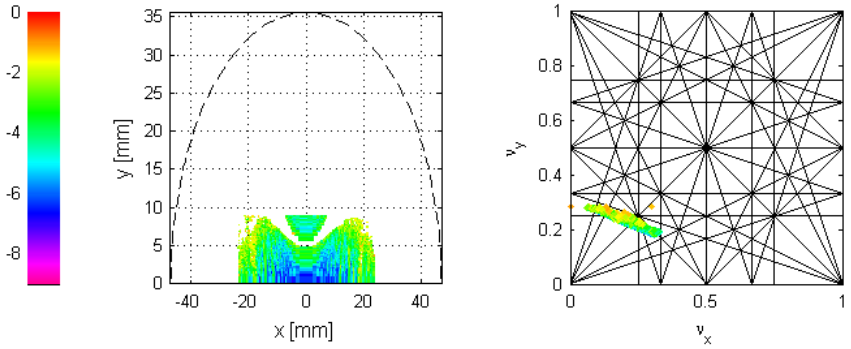

(a) Frequency map in $x - y$ space.

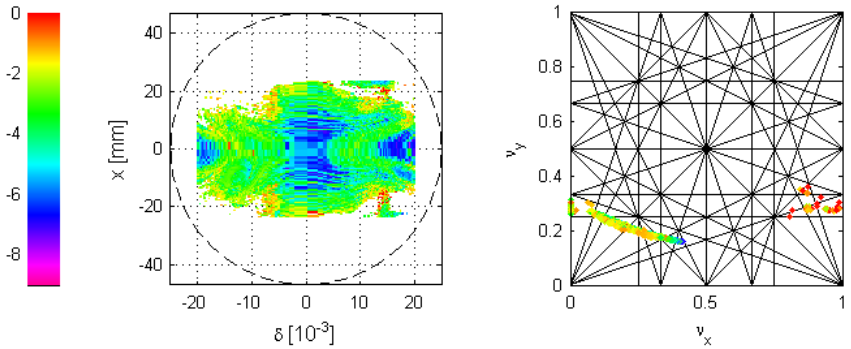

(b) Frequency map in $\delta - x$ space.

Figure 3.25: Frequency map analysis for TESLA with ideal nonlinear wiggler model, computed with MERLIN. The upper plots show the frequency map in coordinate space; the broken line shows 12 times the rms injected beam size, assuming a normalized emittance of 0.01 nm·rad. The lower plots show the frequency map in $x-\delta$ space; the broken line shows an ellipse with limits 12 times the rms horizontal injected beam size, and an energy deviation of 2.5%.

Comments

There is good agreement in the frequency maps calculated with MERLIN and with BMAD. The results are consistent with the dynamic aperture plots, but in many cases reveal large tune shifts with amplitude, and the effects of resonance lines in significant diffusion rates. Where the tune spread covers many resonance lines, the injection efficiency could easily be impaired by lattice errors driving those resonances. A detailed analysis of these effects has not been carried out.

3.1.5 Injected Positron Distribution

To allow studies with a "realistic" distribution of particles injected into the damping rings, simulations were performed of various versions of an undulator-based polarized positron source.

Figure 3.29 shows a positron distribution produced by Batygin [5]. We refer to this as the YB distribution. The original specification on the energy spread for this distribution was $|\delta| < 1\%$. 90% of the particles within this distribution satisfy the latest specifications:

$$A_x + A_y < 0.09 \text{ m} \cdot \text{rad} \quad (3.21)$$

$$|\delta| < 0.5\% \quad (3.22)$$

Figure 3.30 shows one positron distribution produced by Gai [25]. We refer to this as the WG1 distribution. As in the case of the YB distribution, the original specification on the energy spread for this distribution was $|\delta| < 1\%$. 96% of the particles within this distribution satisfy the latest specifications given by Equations (3.21) and (3.22).

Figure 3.31 shows a second positron distribution produced by Gai. We refer to this as the WG2 distribution; it was produced to meet the specification $|\delta| < 0.5\%$, with some relaxation on the transverse distribution. 98% of the particles within this distribution satisfy the latest specifications given by Equations (3.21) and (3.22).

3.1.6 Injection Efficiency

The injection efficiencies of the reference lattices, limited by dynamical effects, were estimated by tracking the realistic positron distributions described in Section 3.1.5 without physical apertures. The efficiency is defined as the ratio of particles surviving one damping time to the number of particles in the initial distribution. To estimate the margin for the acceptance

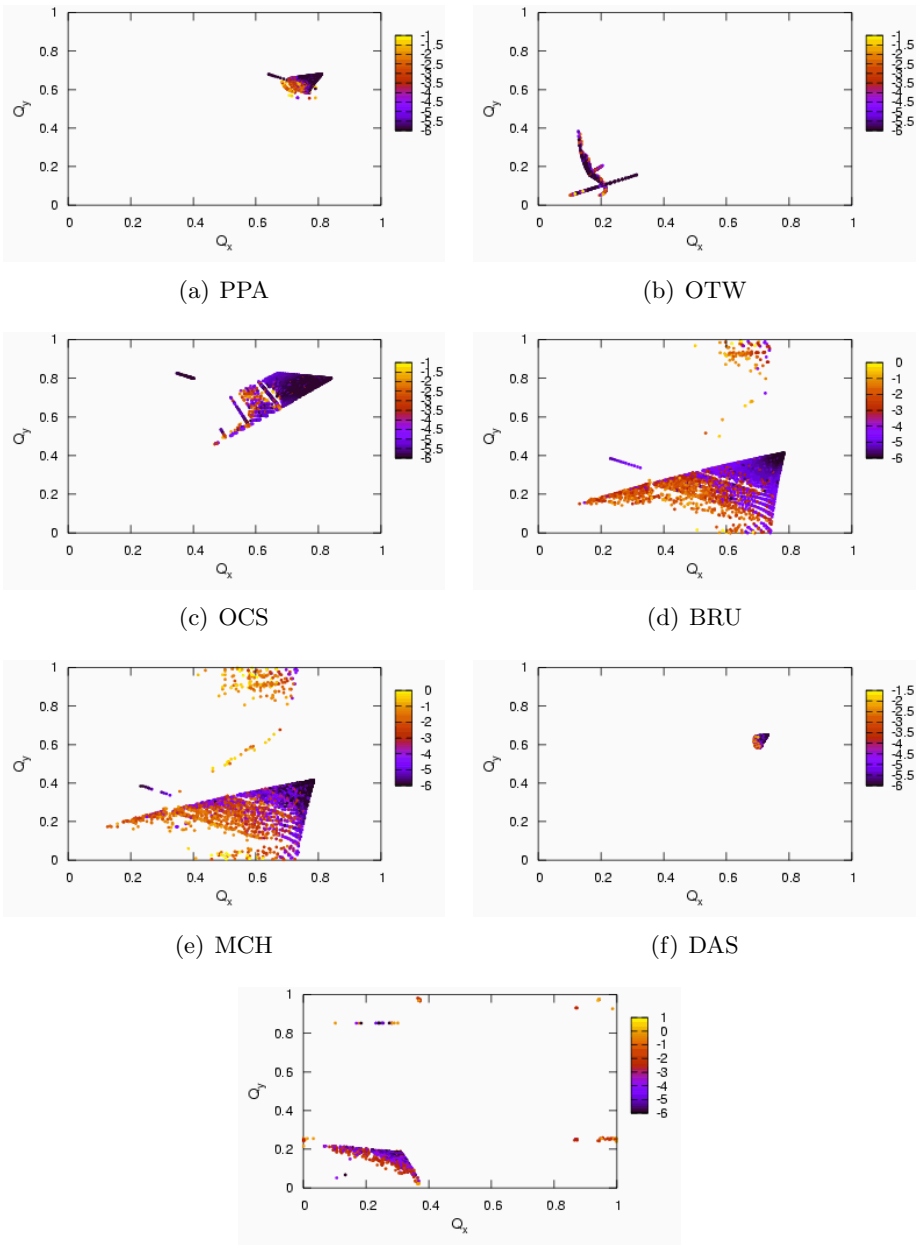

(a) PPA

(b) OTW

(c) OCS

(d) BRU

(e) MCH

(f) DAS

(g) TESLA

Figure 3.26: Frequency map analysis with linear wiggler model, computed with BMAD.

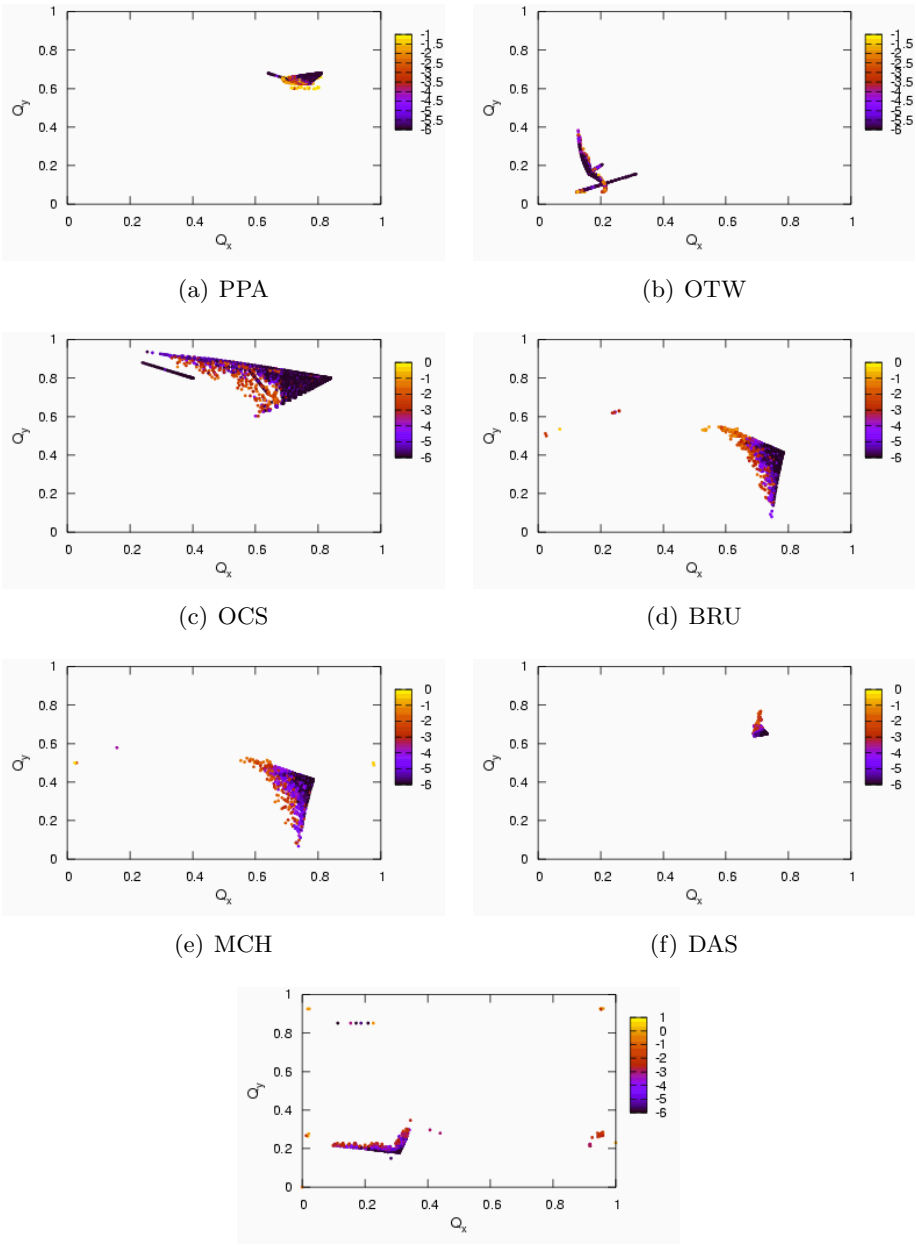

(a) PPA

(b) OTW

(c) OCS

(d) BRU

(e) MCH

(f) DAS

(g) TESLA

Figure 3.27: Frequency map analysis with ideal nonlinear wiggler model, computed with BMAD.

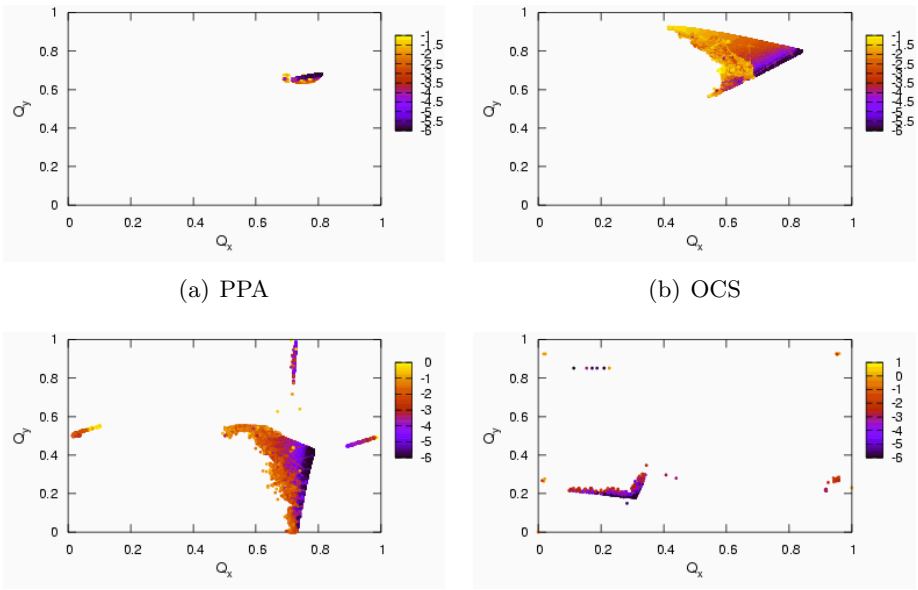

(a) PPA

(b) OCS

(c) MCH

(d) TESLA

Figure 3.28: Frequency map analysis with modified CESR-c wiggler model, computed with BMAD.

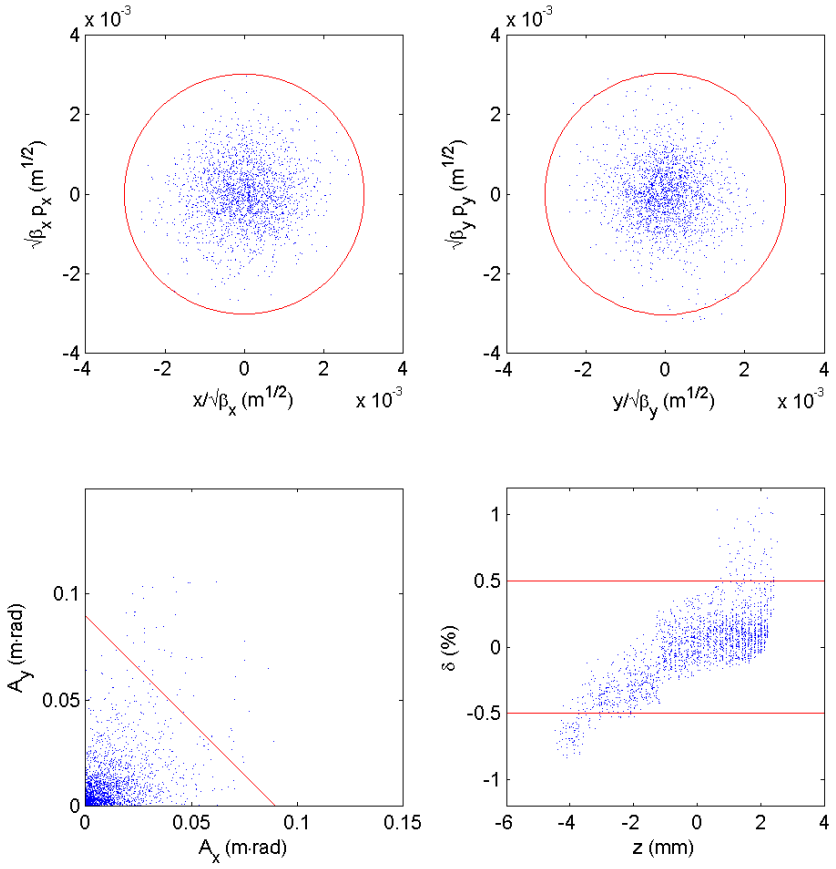

Figure 3.29: Distribution of injected positrons from Batygin (the YB distribution). Top: horizontal (left) and vertical (right) phase space in normalized coordinates; the red circles show the limits given by $A_{x,y} < 0.09$ m·rad. Bottom left: transverse distribution of betatron amplitudes; the red line shows the limit given by $A_x + A_y < 0.09$ m·rad. Bottom right: longitudinal phase space distribution; the red lines show the limits given by $|\delta| < 0.5\%$. 90% of the particles meet both the transverse and longitudinal specifications.

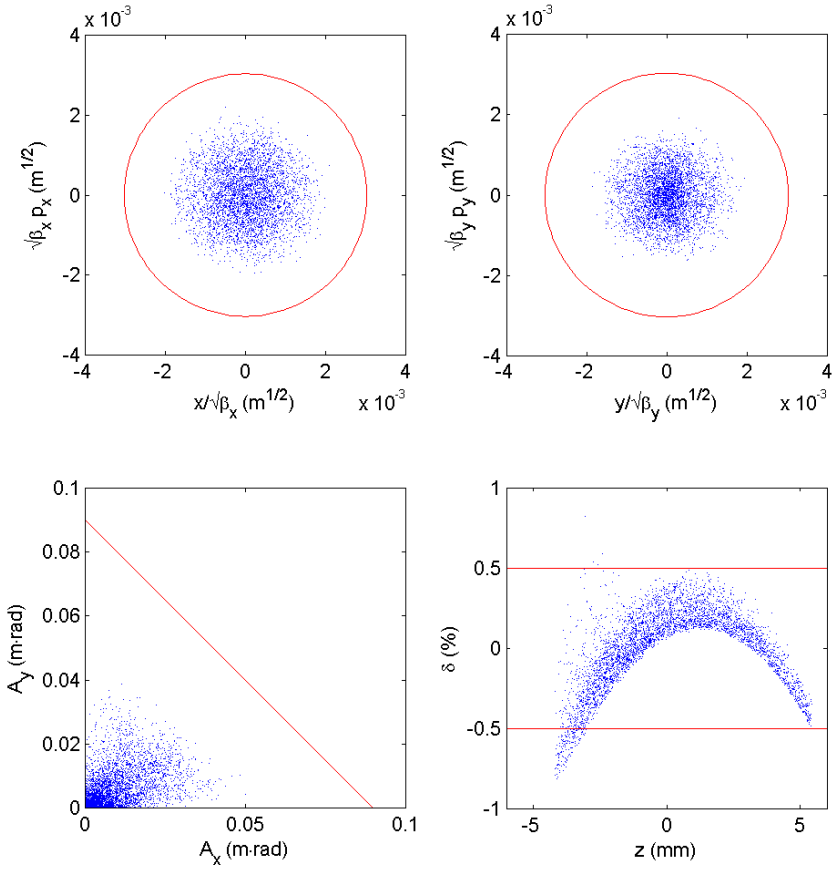

Figure 3.30: Distribution of injected positrons from Gai (the WG1 distribution). Top: horizontal (left) and vertical (right) phase space in normalized coordinates; the red circles show the limits given by $A_{x,y} < 0.09$ m·rad. Bottom left: transverse distribution of betatron amplitudes; the red line shows the limit given by $A_x + A_y < 0.09$ m·rad. Bottom right: longitudinal phase space distribution; the red lines show the limits given by $|\delta| < 0.5\%$. 96% of the particles meet both the transverse and longitudinal specifications.

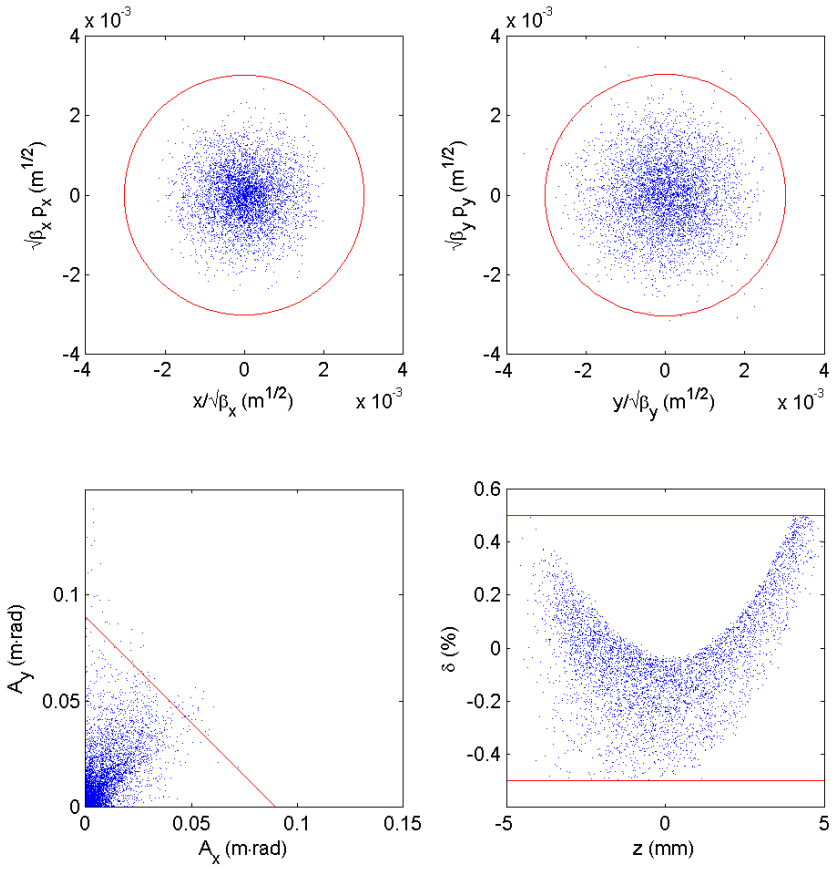

Figure 3.31: Second distribution of injected positrons from Gai (the WG2 distribution). Top: horizontal (left) and vertical (right) phase space in normalized coordinates; the red circles show the limits given by $A_{x,y} < 0.09$ m·rad. Bottom left: transverse distribution of betatron amplitudes; the red line shows the limit given by $A_x + A_y < 0.09$ m·rad. Bottom right: longitudinal phase space distribution; the red lines show the limits given by $|\delta| < 0.5\%$. 98% of the particles meet both the transverse and longitudinal specifications.

Table 3.9: Injection efficiencies with the YB injected positron distribution, without multipole errors, and with a linear wiggler model.

Scaling factors f_x, f_y, f_δ	PPA	OTW	OCS	BRU	MCH	DAS	TESLA
1,1,1	100	99	100	97	100	99	99
1,1,2	97	96	100	84	95	97	98
4,4,1	93	76	99	96	98	91	96
4,4,2	89	76	99	81	91	85	92

Table 3.10: Injection efficiencies with the YB injected positron distribution, in lattices with multipole errors and an ideal nonlinear model for the wiggler.

Scaling factors f_x, f_y, f_δ	OCS	MCH	DAS	TESLA
1,1,1	100	99.85	99.73	94.38
1,1,1/2	100	99.94	99.97	96.52

for each lattice, the distributions were modified by applying scaling factors to the horizontal and vertical actions and to the energy deviation for each particle in the distribution; the scaling factors are denoted f_x, f_y and f_δ respectively.

Injection efficiencies for the YB distribution (Figure 3.29) are given in Table 3.9. Tracking was performed with synchrotron oscillations, but without synchrotron radiation. No multipole errors were applied to the magnets, and a linear model was used for the wiggler. Most of the lattices achieve good injection efficiency with the nominal distribution, but only OCS shows any margin in the dynamic acceptance as the widths of the transverse or longitudinal distributions are increased.

Tracking of the YB distribution with multipole errors and the ideal nonlinear wiggler model was also performed for OCS, and for the three dogbone lattices (MCH, DAS and TESLA). The results are shown in Table 3.10. The multipole errors applied were those given in Tables 3.1–3.3; five different seeds of errors were used. For the dogbone lattices, the higher-order multipole errors and wiggler nonlinearities do have some impact, though it is small.

Injection efficiencies for the WG2 distribution (Figure 3.31) are given in Table 3.11. As in the case of the YB distribution, tracking was performed with synchrotron oscillations, but without synchrotron radiation. No multipole errors were applied to the magnets, and a linear model was used for

Table 3.11: Injection efficiencies with the WG2 injected positron distribution, without multipole errors, and with a linear wiggler model.

Scaling factors f_x, f_y, f_δ	PPA	OTW	OCS	BRU	MCH	DAS	TESLA
1,1,1	100	99.8	100	100	100	100	100
1,1,2		98.7	100	93.7	99.7	99.8	99.8
4,4,1	96.4	80.5	99.7	98.9	98.9	92.4	97.8
4,4,2	94.9	76.6	99.7	90.4	95.7	89.6	94.9

the wiggler. The injection efficiency is improved over the YB distribution in most cases; this is likely the result of the reduced energy spread.

It should be regarded as a cause for concern when there is little or no margin in the dynamic acceptance under the conditions used in these studies. An operating storage ring will be subject to a much wider range of errors and limitations (including focusing errors, alignment and coupling errors, and physical apertures) than were included in the tracking simulations, which means that the injection efficiency in practice is likely to be significantly worse than indicated by the simulation results. Only the OCS lattice shows a reasonable margin for the injection efficiency that would be required in a damping ring design.

3.1.7 Wiggler Physical Aperture

Injection efficiency will be limited by physical apertures in the vacuum chamber, as well as by dynamic effects. The limiting aperture is likely to be in the wiggler, where (for permanent magnet and conventional electromagnetic devices) the field strength that can be achieved falls rapidly as the vertical gap between the poles is increased. For peak fields of 1.6 T, a full vertical gap of the order of 20 mm between the poles may be expected in permanent magnet or conventional electromagnetic wigglers; for superconducting wigglers, much larger apertures can be achieved (see Section 4.2).

To estimate the physical aperture in the wigglers needed to achieve good injection efficiency, the WG1 and WG2 distributions were tracked through the reference lattices in MAD, with circular collimators of various apertures placed in the wigglers. Tracking included synchrotron oscillations and synchrotron radiation. No multipole errors were applied, and a linear model was used for the wiggler.

The results for the WG2 distribution are shown in Figures 3.33–3.39. Generally, the behavior is as expected, with more particles surviving as the

aperture is increased. With an 8 mm radius aperture, there are significant numbers of particles outside the physical aperture in most of the lattices. The situation could be improved by reducing the beta functions in the wiggler; however, the beam size decreases only as the square root of the beta function, and a smaller beta function will result in larger chromaticity, which will adversely impact the off-energy dynamics.

One interesting feature of the TESLA lattice, is that numbers of particles appear not to damp as expected, but remain at large betatron amplitudes even after one full damping time. This is likely the result of these particles being "trapped" on resonances in tune space.

Figure 3.32 summarizes the results for both WG1 and WG2 distributions. A better injection efficiency is generally achieved with the WG2 distribution, which has a larger transverse distribution but smaller energy spread than WG1. It is also clear that a physical aperture of at least 16 mm radius will be needed in the wiggler to achieve the necessary injection efficiency.

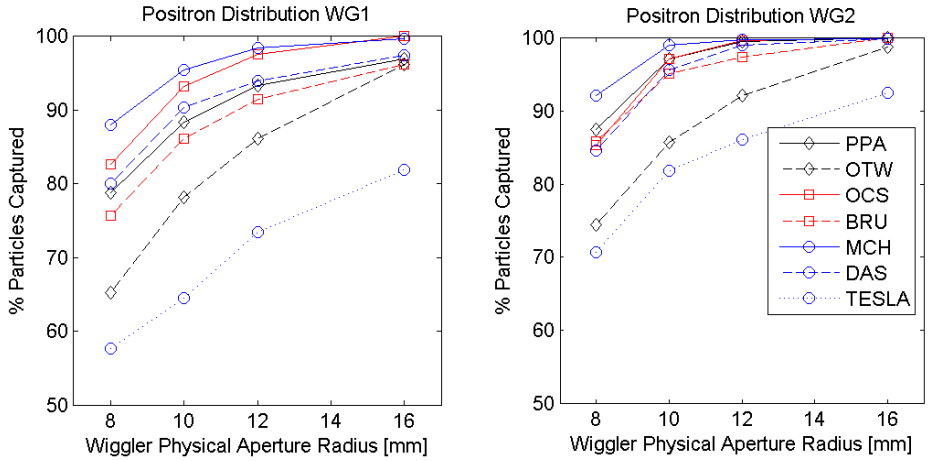

Figure 3.32: Injection efficiency with physical aperture in the wiggler. Left: results from tracking distribution WG1. Right: results from tracking distribution WG2.

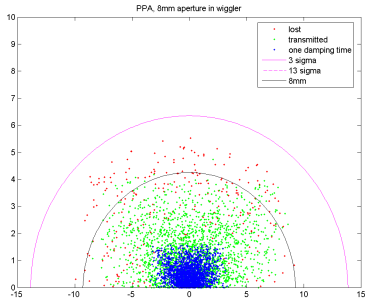

(a) 8 mm radius wiggler aperture.

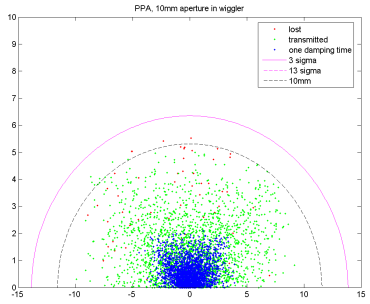

(b) 10 mm radius wiggler aperture.

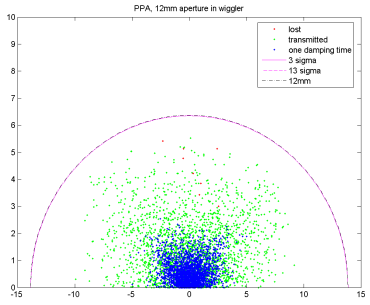

(c) 12 mm radius wiggler aperture.

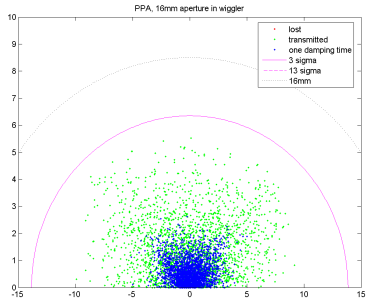

(d) 16 mm radius wiggler aperture.

Figure 3.33: Tracking the WG2 distribution in PPA, with a range of physical apertures in the wiggler. The green points show the starting coordinates of the surviving particles; the red points show the starting coordinates of the lost particles; the blue points show the coordinates of the surviving particles after one damping time. The black ellipse shows the physical aperture in the wiggler projected (by scaling with the square root of the beta functions) onto the injection point. Ellipses at 3σ and 13σ for $\gamma\epsilon$ =0.01 m·rad are also shown.

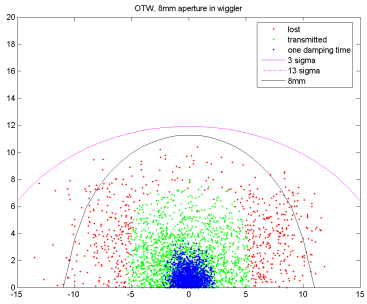

(a) 8 mm radius wiggler aperture.

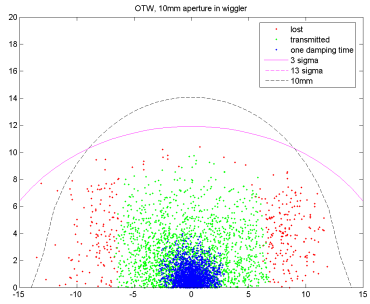

(b) 10 mm radius wiggler aperture.

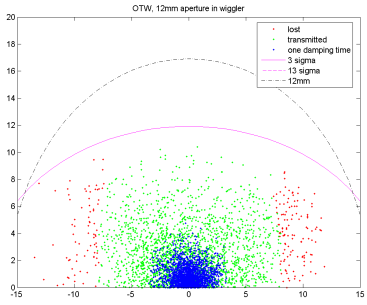

(c) 12 mm radius wiggler aperture.

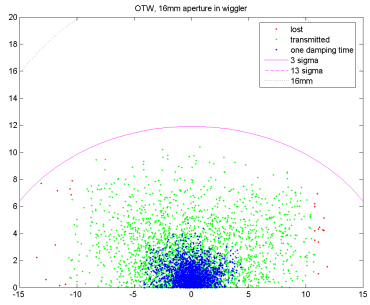

(d) 16 mm radius wiggler aperture.

Figure 3.34: Tracking the WG2 distribution in OTW, with a range of physical apertures in the wiggler. The green points show the starting coordinates of the surviving particles; the red points show the starting coordinates of the lost particles; the blue points show the coordinates of the surviving particles after one damping time. The black ellipse shows the physical aperture in the wiggler projected (by scaling with the square root of the beta functions) onto the injection point. Ellipses at 3σ and 13σ for $\gamma\epsilon$ =0.01 m·rad are also shown.

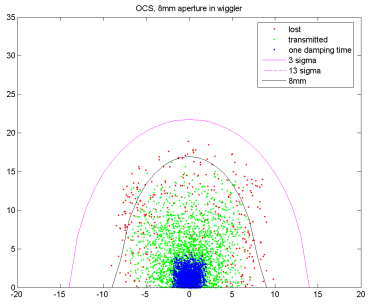

(a) 8 mm radius wiggler aperture.

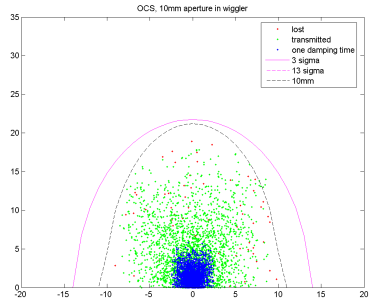

(b) 10 mm radius wiggler aperture.

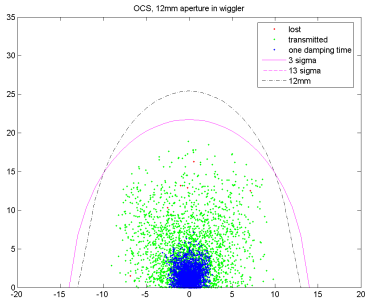

(c) 12 mm radius wiggler aperture.

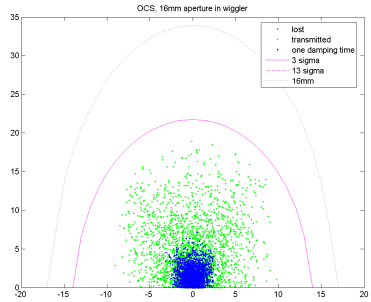

(d) 16 mm radius wiggler aperture.

Figure 3.35: Tracking the WG2 distribution in OCS, with a range of physical apertures in the wiggler. The green points show the starting coordinates of the surviving particles; the red points show the starting coordinates of the lost particles; the blue points show the coordinates of the surviving particles after one damping time. The black ellipse shows the physical aperture in the wiggler projected (by scaling with the square root of the beta functions) onto the injection point. Ellipses at 3σ and 13σ for $\gamma\epsilon$ =0.01 m·rad are also shown.

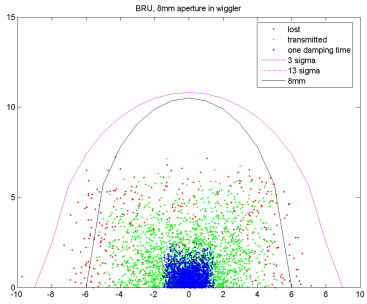

(a) 8 mm radius wiggler aperture.

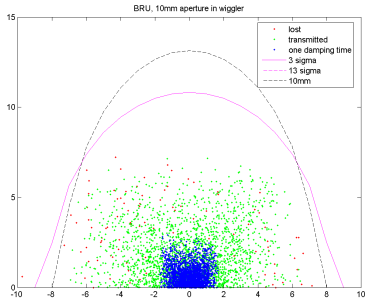

(b) 10 mm radius wiggler aperture.

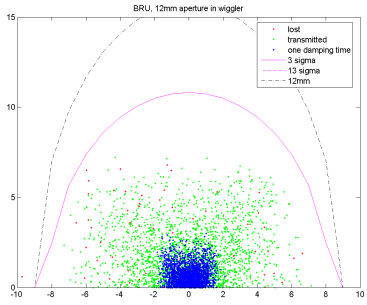

(c) 12 mm radius wiggler aperture.

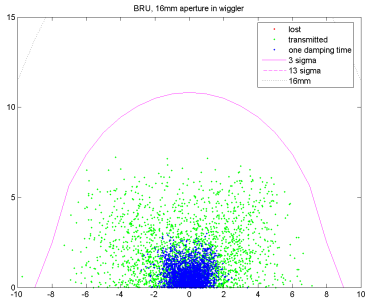

(d) 16 mm radius wiggler aperture.

Figure 3.36: Tracking the WG2 distribution in BRU, with a range of physical apertures in the wiggler. The green points show the starting coordinates of the surviving particles; the red points show the starting coordinates of the lost particles; the blue points show the coordinates of the surviving particles after one damping time. The black ellipse shows the physical aperture in the wiggler projected (by scaling with the square root of the beta functions) onto the injection point. Ellipses at 3σ and 13σ for $\gamma\epsilon$ =0.01 m·rad are also shown.

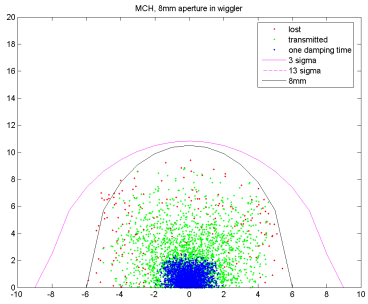

(a) 8 mm radius wiggler aperture.

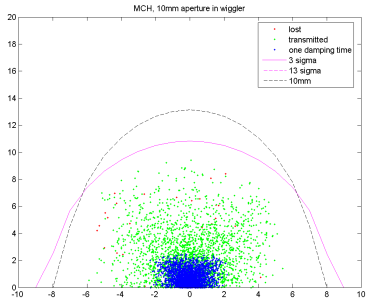

(b) 10 mm radius wiggler aperture.

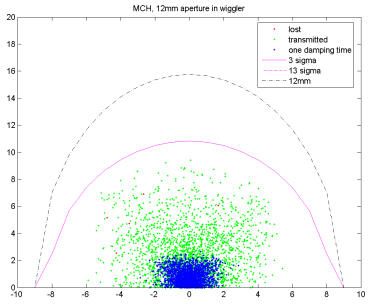

(c) 12 mm radius wiggler aperture.

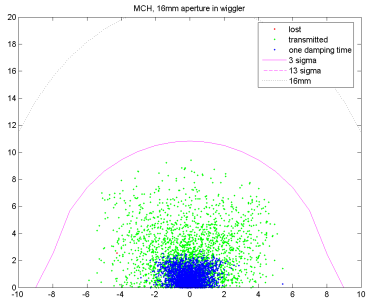

(d) 16 mm radius wiggler aperture.

Figure 3.37: Tracking the WG2 distribution in MCH, with a range of physical apertures in the wiggler. The green points show the starting coordinates of the surviving particles; the red points show the starting coordinates of the lost particles; the blue points show the coordinates of the surviving particles after one damping time. The black ellipse shows the physical aperture in the wiggler projected (by scaling with the square root of the beta functions) onto the injection point. Ellipses at 3σ and 13σ for $\gamma\epsilon$ =0.01 m·rad are also shown.

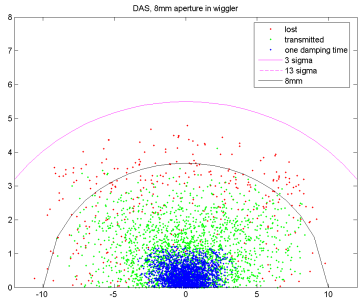

(a) 8 mm radius wiggler aperture.

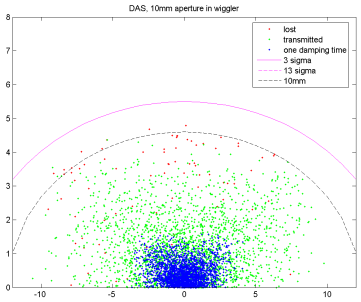

(b) 10 mm radius wiggler aperture.

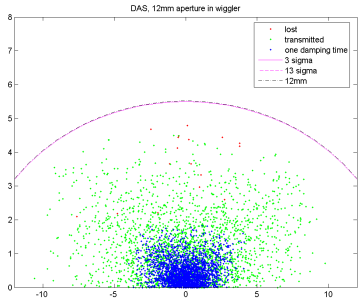

(c) 12 mm radius wiggler aperture.

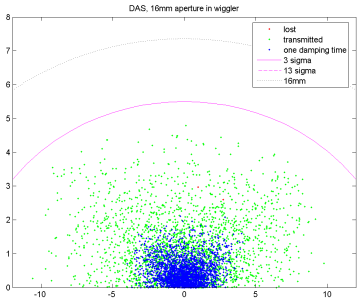

(d) 16 mm radius wiggler aperture.

Figure 3.38: Tracking the WG2 distribution in DAS, with a range of physical apertures in the wiggler. The green points show the starting coordinates of the surviving particles; the red points show the starting coordinates of the lost particles; the blue points show the coordinates of the surviving particles after one damping time. The black ellipse shows the physical aperture in the wiggler projected (by scaling with the square root of the beta functions) onto the injection point. Ellipses at 3σ and 13σ for $\gamma\epsilon$ =0.01 m·rad are also shown.

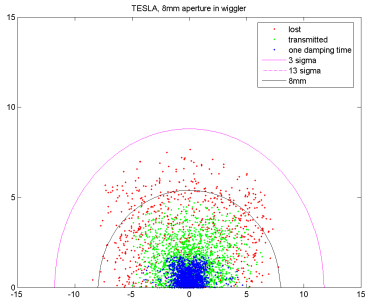

(a) 8 mm radius wiggler aperture.

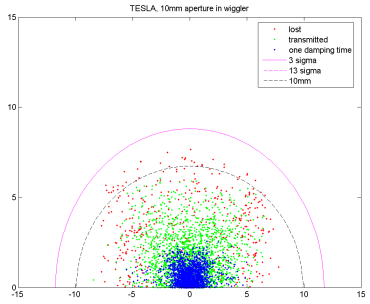

(b) 10 mm radius wiggler aperture.

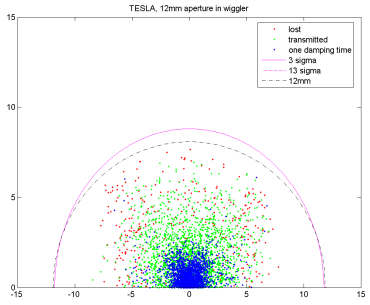

(c) 12 mm radius wiggler aperture.

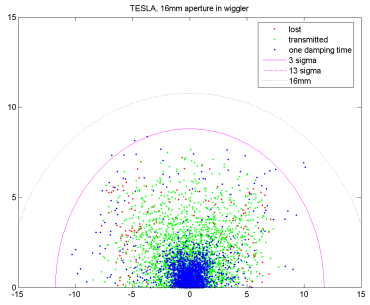

(d) 16 mm radius wiggler aperture.

Figure 3.39: Tracking the WG2 distribution in TESLA, with a range of physical apertures in the wiggler. The green points show the starting coordinates of the surviving particles; the red points show the starting coordinates of the lost particles; the blue points show the coordinates of the surviving particles after one damping time. The black ellipse shows the physical aperture in the wiggler projected (by scaling with the square root of the beta functions) onto the injection point. Ellipses at 3σ and 13σ for $\gamma\epsilon$ =0.01 m·rad are also shown.

3.1.8 Comments and Conclusions

Survival plots suggest that most of the reference lattices achieve the specified acceptance even with multipole errors and nonlinear wiggler model. These results are supported by frequency map analysis. However, there is only one lattice (OCS) that shows any real margin in the acceptance. This conclusion is confirmed by tracking studies using positron distributions from simulations of the positron source: scaling the transverse or longitudinal amplitudes of the injected particles by a small factor leads in most cases to significant particle loss.

Further concerns are raised by the tracking with physical aperture. Examination of the distribution of particles lost by physical "collimation" in the wiggler (Figures 3.33–3.39) shows that even particles close to the injected beam core can be lost; this is likely the result of resonance lines in tune space driving particles to large amplitudes. Under these conditions, minimizing particle loss in the ring by applying collimation in the injection line may be difficult.

Our studies do not include the full range of effects that may be expected to limit the dynamic aperture in an operating machine. Although good agreement between the measured and observed dynamic apertures is observed in many rings, the agreement is typically achieved only after significant work characterizing and minimizing errors. Particularly during commissioning, the dynamic aperture may be much worse than suggested by simulations. For the ILC, it will be important to achieve good injection efficiency into the damping rings as early as possible both for tuning the ring itself (which may be difficult with stored beam because of the short lifetime), and for providing beam for commissioning and tuning downstream systems. We may also expect that, at least in the early stages, the positron source may produce a beam somewhat larger than the baseline specifications.

It is therefore important that the damping ring have as much acceptance margin as possible. The only reference lattice that shows a sufficient margin is OCS. We believe that the high symmetry of the lattice plays an important role. This hypothesis is supported by studies of a modified BRU design: reshaping the lattice to improve the symmetry resulted in a lattice which had a significantly improved dynamic aperture (Figures 3.9 and 3.10). One reason why it is difficult to achieve a good acceptance margin in the dogbone lattices may be the chromaticity in the long straights. Although it is possible to "restore" symmetry to a dogbone lattice by tuning the phase advance over the straights to an integer, this only works for particles with zero energy error. Without dispersion in the straights it is not possible to apply local

chromatic correction, and the dynamic energy acceptance of the dogbone lattices is very limited as a result.

Given the risks of difficult and delayed commissioning and damage from radiation, and the potential difficulty of fixing any problems should they occur, the baseline damping ring design must have a significant margin for the acceptance. While a dogbone lattice may still turn out to be an acceptable solution, at present we believe that a circular lattice is much the safer option for the damping rings. Additionally, the physical apertures must be large enough not to limit the injection efficiency; in the wiggler, this means the aperture should be at least 16 mm radius.

3.2 Low-Emittance Tuning

The extracted normalized vertical emittance from the damping rings is specified at 0.02 μm. The KEK-ATF has achieved an equilibrium normalized vertical emittance of 0.01 μm [33]; however, the KEK-ATF operates at a much lower energy (1.28 GeV) than is likely for the ILC damping rings. For storage rings, it is more appropriate to compare the geometric emittance, in terms of which the lowest KEK-ATF emittance of 4 pm is a factor of two larger than the extracted emittance required from the damping rings.

The luminosity of the linear collider depends directly on the emittance at the interaction point. However, the luminosity is inversely proportional to the beam *size*, which is proportional to the square root of the emittance. Also, the emittance of the beam extracted from the damping rings will be diluted by various effects in all the systems between the damping rings and the interaction point. The emittance dilution is additive rather than multiplicative, and is expected to be of the order of 0.02 μm (normalized). Therefore, the luminosity of the linear collider is not highly sensitive to the vertical emittance from the damping rings. Nevertheless, since the best vertical emittance so far achieved in a storage ring (at the KEK-ATF) is still a factor of two away from that needed to achieve the design luminosity in the ILC, the tuning of the damping rings for low vertical emittance is an important issue.

In storage ring operation, the vertical emittance is typically dominated by magnet misalignments. In this section, we will consider the sensitivity of the reference lattices to those magnet misalignments that are expected to be most significant in terms of generating vertical emittance. The results will be put in context by comparison with the KEK-ATF. However, some vertical emittance is always generated by the vertical opening angle of the

synchrotron radiation. In most regimes, this is a very small effect that can generally be ignored; however, the specification of an extremely small vertical emittance for the damping rings makes it worthwhile to calculate the contribution from the vertical opening angle of the synchrotron radiation. This can be found from the lattice functions; the expression is [56][1]:

$$\epsilon_y = \frac{13}{55}\frac{C_q}{J_y I_2}\int \frac{\beta_y}{|\rho|^3} ds \tag{3.23}$$

where $C_q = 3.832 \times 10^{-13}$ m, J_y is the vertical damping partition number (equal to 1 in all the reference lattices), I_2 is the second synchrotron radiation integral, β_y is the vertical beta function, ρ is the local bending radius of the orbit resulting from dipole fields, and the integral is taken around the entire circumference of the lattice. The emittance of Equation (3.23) represents a fundamental lower limit on the vertical emittance in a given lattice. Applying this equation to the reference lattices, we find the results shown in Table 3.12. In most cases, the radiation limited normalized vertical emittance is less than 5% of the specified extracted vertical emittance of 20 nm; we therefore expect that this effect will not be a serious limitation on any of the damping ring configurations being considered.

Table 3.12: Lower limit on the normalized vertical emittance in the reference lattices, from the vertical opening angle of the synchrotron radiation.

Lattice	Radiation limited normalized vertical emittance [nm]
KEK-ATF	0.183
PPA	0.621
OTW	0.469
OCS	0.758
BRU	0.608
MCH	0.813
DAS	0.648
TESLA	1.09

As we mentioned above, effects resulting from magnet misalignments dominate the vertical emittance actually achieved in storage rings. The

[1]Note that Equation (3.23) includes the correlation between the photon energy and the angle of emission, and for this reason differs by roughly a factor of two from expressions found in some other references.

two fundamental effects that we need to consider are vertical dispersion and betatron coupling. Vertical dispersion generates vertical emittance in exactly the same way that horizontal dispersion from the dipoles in a storage ring generates horizontal emittance: when a particle emits a photon at a point with non-zero dispersion, there is a change in the closed orbit resulting from the change in the particle's energy, and the betatron amplitude of the particle changes as a result. Betatron coupling results in a direct transfer of horizontal emittance into the vertical plane. Both vertical dispersion and betatron coupling need to be considered when calculating the vertical emittance in a lattice; the relative contributions of each effect depend on the exact misalignments of elements in the lattice.

Vertical misalignment of the quadrupoles generates vertical steering, which is a direct source of vertical dispersion. Vertical closed orbit distortion from vertical steering, together with real vertical misalignments of the sextupoles, leads to a vertical beam offset in the sextupoles with respect to the magnetic center of the sextupole: this results in betatron coupling, and additional sources of vertical dispersion from the coupling of horizontal dispersion into the vertical plane. Finally, rotations of quadrupoles around the beam axis have a similar effect to vertical misalignments of the sextuoples.

Low emittance lattices are generally very sensitive to magnet misalignments. This means that a lattice relying solely on survey alignment for minimizing coupling effects will typically have a very large vertical orbit distortion, and a vertical emittance of roughly the same order as the horizontal emittance. Coupling correction, generally through the use of vertical orbit corrector magnets and skew quadrupoles, is required to achieve emittance ratios of 1% or less. In characterizing the performance of a particular lattice, it is important to include simulations of coupling correction. However, the sensitivity of the vertical emittance to magnet alignments is relevant: this indicates the likely difficulty of achieving the required vertical emittance from coupling correction, and also the frequency with which coupling correction needs to be performed as magnets move. We therefore begin our analysis by estimating the sensitivity of the vertical closed orbit to vertical quadrupole alignment, and the sensitivity of the vertical emittance to vertical sextupole motion and quadrupole tilt (rotation about the beam axis). In each case, it is possible to make a rough analytical estimate of the sensitivity, and compare this with the results of a simulation.

We define the sensitivity of the vertical emittance to a particular misalignment (e.g. sextupole vertical misalignment or quadrupole tilt) as the rms misalignment that, averaged over a large number of error sets or seeds,

will generate a specified vertical emittance. For the KEK-ATF, we take the specified vertical emittance as 4.5 pm, which is roughly the lowest value that has been achieved. For the damping ring reference lattices, the specified vertical emittance is the equilibrium emittance required to achieve an extracted normalized vertical emittance of 20 nm, assuming an injected normalized vertical emittance of 0.01 m, and a store time of 200 ms. There are variations in beam energy and damping time between the different reference lattices, and the specified equilibrium vertical emittance therefore also varies between the different lattices. The specified equilibrium emittance $\epsilon(\infty)$ can be found from the usual damping equation:

$$\epsilon(t) = \epsilon(0)\exp\left(-\frac{2t}{\tau}\right) + \epsilon(\infty)\left[1 - \exp\left(-\frac{2t}{\tau}\right)\right] \tag{3.24}$$

where $\epsilon(t)$ is the emittance at time t, and τ is the damping time. The specified equilibrium emittances for the reference lattices are shown in Table 3.13.

Table 3.13: Specified equilibrium vertical emittance in the reference lattices.

Lattice	Circumference [m]	Energy [GeV]	Damping time [ms]	Specified normalized vertical emittance [nm]
KEK-ATF	138	1.28	28.5	11.3
PPA	2824	5.0	20.0	20.0
OTW	3223	5.0	12.1	20.0
OCS	6114	5.066	22.2	19.9
BRU	6333	3.74	25.5	18.4
MCH	15935	5.0	26.9	16.6
DAS	17014	5.0	27.0	16.3
TESLA	17000	5.0	27.9	14.2

For the dogbone lattices, all calculations and simulations were performed with the coupling bumps turned off: the effects of the coupling bumps on sensitivity to misalignments has not been considered in detail.

3.2.1 Vertical Quadrupole Misalignments

Vertical quadrupole misalignments result in vertical closed orbit distortion, which can generate vertical emittance from vertical dispersion, and from betatron coupling as a result of vertical beam misalignment in the sextupoles.

The sensitivity of a lattice to vertical quadrupole misalignment can be characterized by an amplification factor A, which relates the rms closed orbit $\sqrt{\langle y_{co}^2 \rangle}$ to the rms quadrupole misalignment $\sqrt{\langle y_{quad}^2 \rangle}$:

$$\sqrt{\langle y_{co}^2 \rangle} = A \sqrt{\langle y_{quad}^2 \rangle} \tag{3.25}$$

The amplification factor can be estimated from the lattice functions:

$$A^2 \approx \frac{\langle \beta_y \rangle}{8 \sin^2 \pi \nu_y} \sum_{quads} \beta_y \left(k_1 L\right)^2 \tag{3.26}$$

where ν_y is the vertical tune, the summation extends over all quadrupoles, and $k_1 L$ is the integrated strength of each quadrupole. The brackets $\langle\rangle$ indicate an average around the lattice. It should be emphasized that for a given rms of quadrupole misalignments, the actual size of the closed orbit distortion depends on the particular set of machine errors, and can vary over a wide range; the amplification factor calculated from Equation (3.26) represents an average over a large set of machine errors. This is illustrated in Figures 3.40 and 3.41, which show the results of simulations in Merlin [78] of the effects of quadrupole misalignments in the PPA lattice.

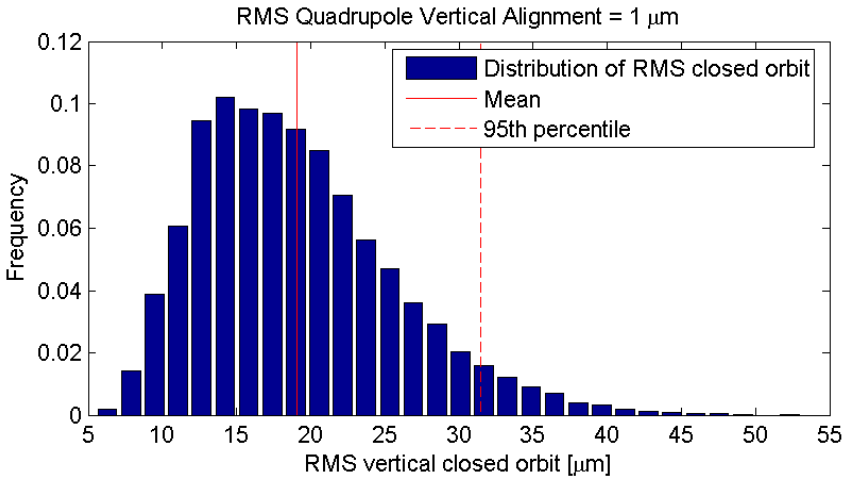

Figure 3.40: Distribution of rms closed orbit distortion in the PPA lattice, for 10,000 sets of quadrupole misalignments with 1 μm rms.

Figure 3.40 shows the distribution of the rms closed orbit distortion in the PPA lattice, for 10,000 sets of quadrupole misalignments; the rms

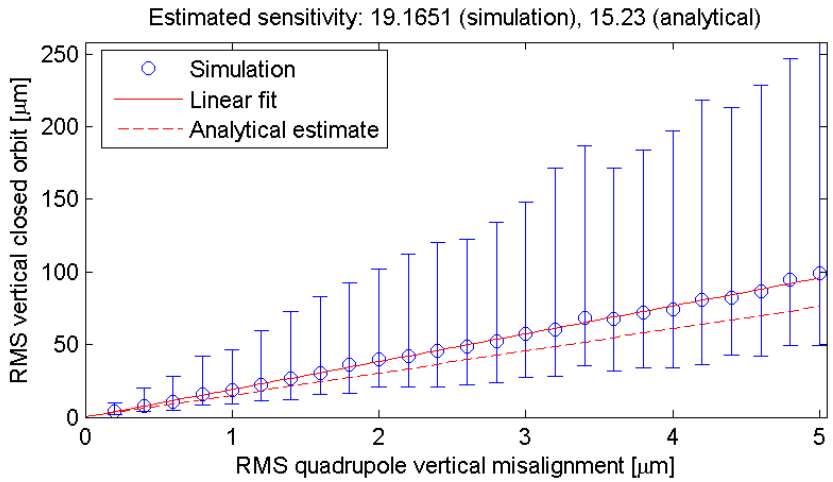

Figure 3.41: Closed orbit distortion rms in the PPA lattice, for rms quadrupole misalignments up to 5 μm. The circles show the average over 100 sets with a given rms; the error bars indicate the 5th and 95th percentiles. The solid red line shows a linear fit; the broken red line shows the prediction from Equation (3.26).

quadrupole misalignment in each case was 1 μm. The solid vertical line shows the mean of the distribution, and the broken vertical red line shows the 95th percentile. The distribution is wide, but the value of the mean agrees well with the prediction from Equation (3.26). Figure 3.41 shows the rms closed orbit for a range of rms quadrupole misalignments up to 5 μm in the PPA lattice. For each value of rms quadrupole misalignment, 100 different sets of errors were used; the plotted points show the mean, with the error bars showing the 5th and 95th percentiles. The solid red line shows a linear fit to the mean values, and the broken red line shows the prediction from Equation (3.26). Similar plots are obtained for all the reference lattices.

The results of the calculations and simulations of quadrupole misalignments for all the reference lattices are shown in Figure 3.42. Larger values indicate a greater sensitivity to quadrupole misalignments: smaller values are desirable. There is no clear relationship between the lattice circumference and the orbit amplification factor: other factors, such as the vertical betatron tune and the values of the beta functions are more important.

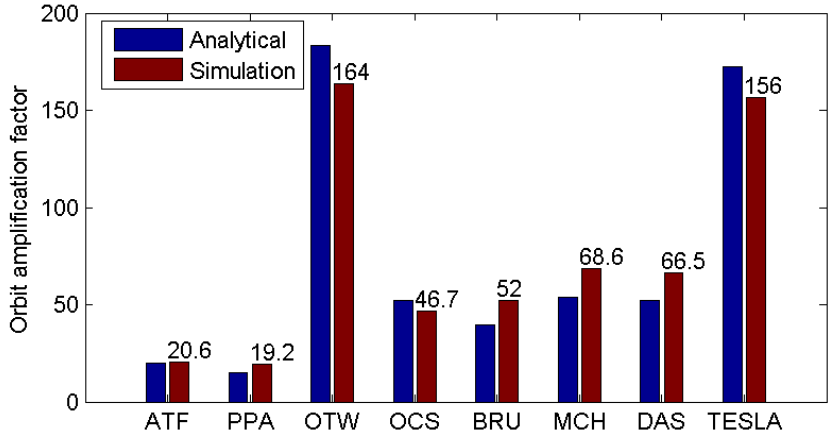

Figure 3.42: Orbit amplification factors in the damping ring reference lattices, compared with the KEK-ATF. The labelled bars show the result of simulations in Merlin; the unlabelled bars show the result of the analytical calculation using Equation (3.26).

3.2.2 Vertical Sextupole Misalignments

A vertical offset of the closed orbit with respect to the magnetic center of a quadrupole leads to the generation of vertical emittance in two ways. First, horizontal dispersion at the quadrupole location is coupled into the vertical plane, and emission of synchrotron radiation where the vertical dispersion is non-zero generates vertical emittance. Second, horizontal betatron oscillations are directly coupled into the vertical plane. If we consider the case where there is no closed orbit distortion, but the sextupoles have random vertical misalignments with respect to the vertical orbit, we can estimate the vertical emittance analytically:

$$\begin{aligned}\frac{\epsilon_y}{\langle y_{sext}^2\rangle} &\approx \frac{J_x\left[1-\cos 2\pi\nu_x\cos 2\pi\nu_y\right]}{4J_y\left[\cos 2\pi\nu_x-\cos 2\pi\nu_y\right]^2}\epsilon_x\sum_{sexts}\beta_x\beta_y\left(k_2L\right)^2 \\ &\quad+\frac{J_z\sigma_\delta^2}{4\sin^2\pi\nu_y}\sum_{sexts}\beta_y\eta_x^2\left(k_2L\right)^2 \end{aligned} \tag{3.27}$$

The first term in Equation (3.27) gives the contribution to the vertical emittance from betatron coupling; the second term gives the contribution from vertical dispersion. $\langle y_{sext}^2\rangle$ is the mean square sextupole vertical misalignment; J_x, J_y and J_z are the horizontal, vertical and longitudinal damping partition numbers; ν_x and ν_y are the horizontal and vertical betatron tunes; β_x and β_y are the horizontal and vertical beta functions; η_x is the horizontal dispersion; σ_δ^2 is the rms energy spread; k_2L is the integrated sextupole strength; the summations extend over all sextupoles in the lattice. As in the case of quadrupole misalignments, Equation (3.27) gives the results that might be expected from averaging over many different sets of machine errors; for a given set of misalignments, the actual vertical emittance is sensitive to the exact distribution of misalignments, so there will be a wide distribution of vertical emittances corresponding to a number of sets of misalignments.

Figure 3.43 shows the distribution of normalized vertical emittances in the PPA lattice, for 10,000 sets of sextupole misalignments with 45 μm rms. The simulations were again performed using Merlin. The solid vertical red line shows the mean of the distribution, which for this case coincides with the specified equilibrium vertical emittance. The broken red line shows the 95th percentile.

Figure 3.44 shows the normalized vertical emittance in the PPA lattice, for a range of rms sextupole misalignments up to 100 μm. The circles show the average over 100 sets with a given rms; the error bars indicate the 5th and 95th percentiles. The solid red line shows a quadratic fit to the mean, and the broken red line shows the prediction of Equation (3.27).

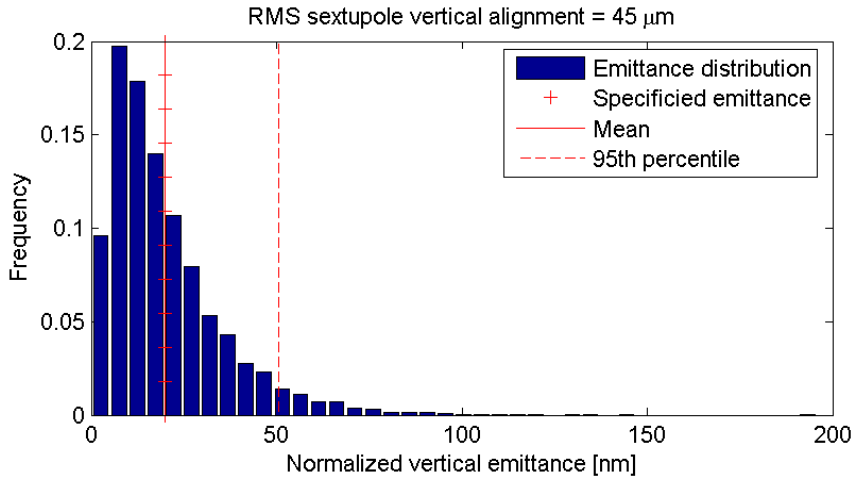

Figure 3.43: Distribution of vertical emittances in the PPA lattice, for 10,000 sets of sextupole misalignments with 45 μm rms.

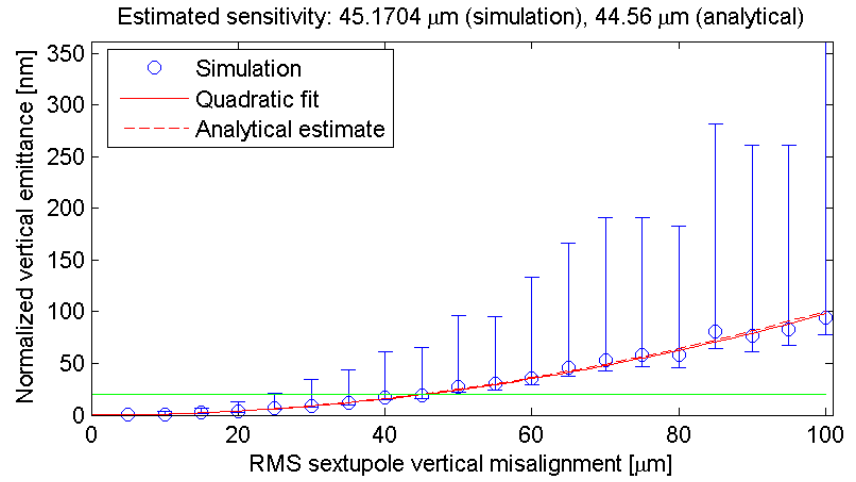

Figure 3.44: Vertical emittance in the PPA lattice, for rms sextupole misalignments up to 100 μm. The circles show the average over 100 sets with a given rms; the error bars indicate the 5th and 95th percentiles. The horizontal green line shows the specified normalized vertical emittance of 20 nm.

The results of calculations and simulations of vertical sextupole misalignments in all the reference lattices are shown in Figure 3.45. Recall that the sensitivity is defined as the rms sextupole misalignment that will generate the specified vertical emittance. Smaller values therefore indicate a *greater* sensitivity to sextupole misalignments, and larger values are more desirable.

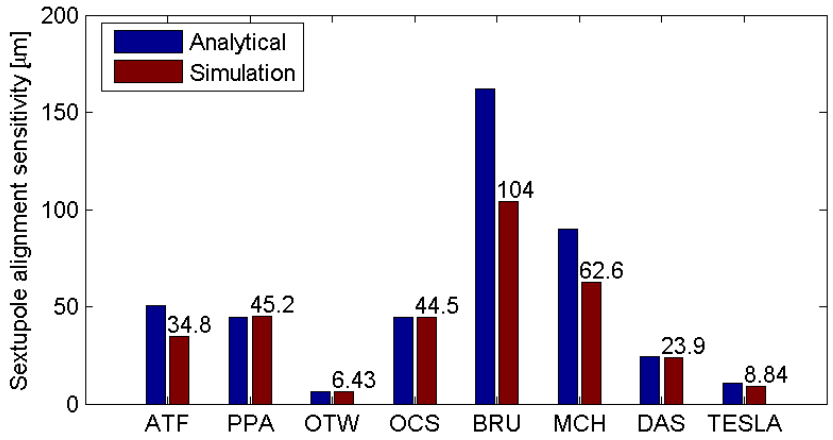

Figure 3.45: Sextupole alignment sensitivity in the damping ring reference lattices, compared with the KEK-ATF. Smaller values indicate a *greater* sensitivity to sextupole misalignments.

The effects of sextupole misalignments were also simulated in SAD [62]. For this study, 100 sets of random vertical misalignments with fixed rms 10 μm were applied to the sextupoles. A comparison between the SAD results and corresponding results obtained in Merlin is shown in Figure 3.46. There is good agreement between the results of the simulation codes.

As was the case for the quadrupole misalignments, there is no clear correlation between circumference and sensitivity. Other factors, such as the type of lattice and proximity of the working point in tune space to coupling resonances are more significant.

3.2.3 Quadrupole Tilts

Rotation of the quadrupoles around the beam axis generates vertical emittance by the same mechanisms as vertical displacement of the closed orbit with respect to the magnetic centers in sextupoles: both types of misalign-

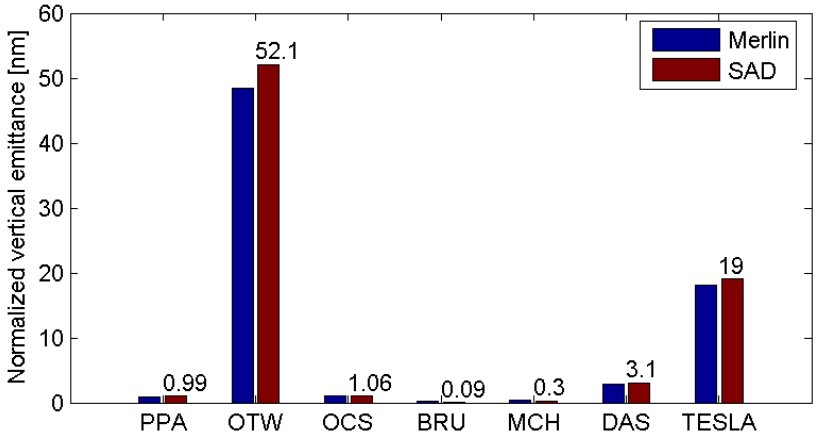

Figure 3.46: Comparison between vertical emittance in the reference lattices generated by 10 μm vertical sextupole misalignment, simulated by SAD and by Merlin. The average emittance over 100 different sets of alignment errors (different sets for each code) is plotted.

ment result in vertical dispersion and in betatron coupling. We can derive an expression for the vertical emittance generated by quadrupole tilts analogous to Equation (3.27) for vertical sextupole misalignments:

$$\frac{\epsilon_y}{\langle\theta^2_{quad}\rangle} \approx \frac{J_x\left[1-\cos 2\pi\nu_x\cos 2\pi\nu_y\right]}{4J_y\left[\cos 2\pi\nu_x-\cos 2\pi\nu_y\right]^2}\epsilon_x\sum_{quads}\beta_x\beta_y\left(k_1L\right)^2 + \frac{J_z\sigma_\delta^2}{4\sin^2\pi\nu_y}\sum_{quads}\beta_y\eta_x^2\left(k_1L\right)^2 \tag{3.28}$$

$\langle\theta^2_{quad}\rangle$ is the mean square quadrupole tilt; other symbols are as defined for Equation (3.27). The first term in Equation (3.28) gives the contribution to the vertical emittance from betatron coupling, and the second term gives the contribution from vertical dispersion. As is the case for other types of misalignment, the exact vertical emittance is sensitive to the distribution of quadrupole tilts around the lattice. Figure 3.47 shows the distribution of vertical emittances in the PPA lattices, for 10,000 sets of quadruople tilts with 200 μrad rms. The solid vertical red line shows the mean of the distribution, which in this case coincides with the specified vertical emittance in the PPA lattice. The broken vertical red line shows the 95th percentile.

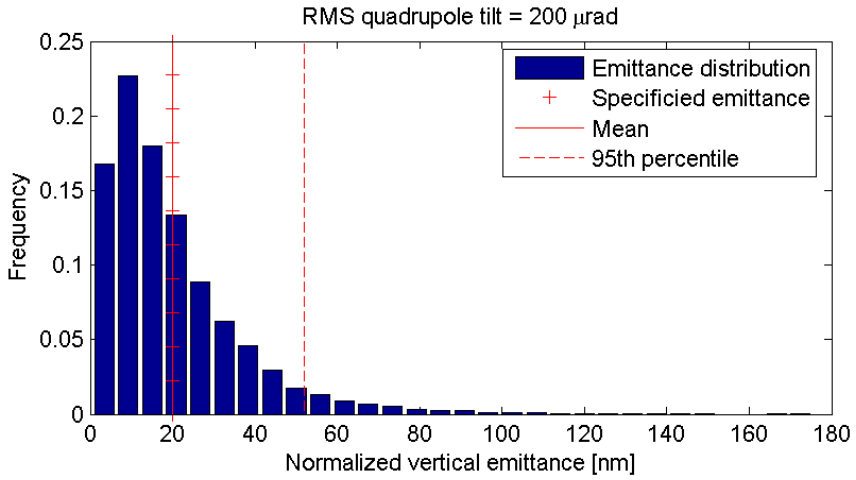

Figure 3.47: Distribution of vertical emittances in the PPA lattice, for 10,000 sets of quadrupole tilts with 200 μrad rms.

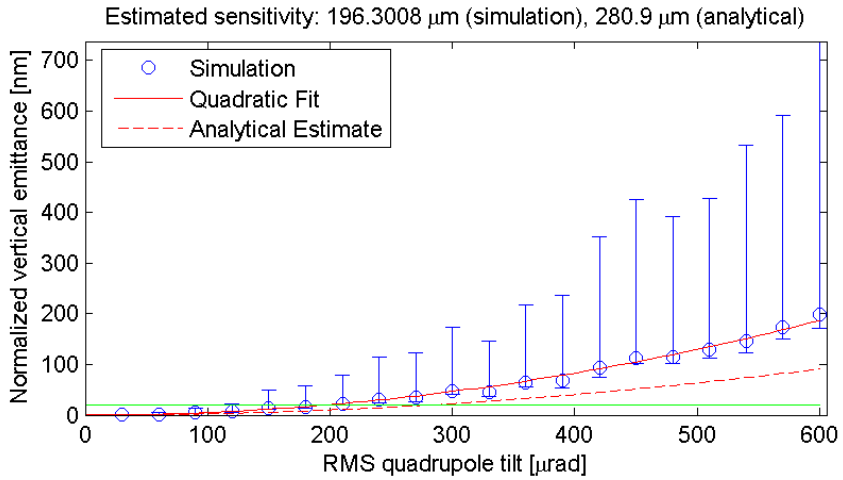

Figure 3.48: Vertical emittance in the PPA lattice, for rms quadrupole tilts up to 600 μrad. The circles show the average over 100 sets with a given rms; the error bars indicate the 5th and 95th percentiles. The horizontal green line shows the specified normalized emittance of 20 nm.

Figure 3.48 shows the normalized vertical emittance in the PPA lattice, for a range of rms quadrupole tilts up to 600 μrad. The circles show the average over 100 sets with a given rms; the error bars indicate the 5th and 95th percentiles. The solid red line shows a quadratic fit to the mean, and the broken red line shows the prediction of Equation (3.28).

The results of calculations and simulations of quadrupole tilts in all the reference lattices are shown in Figure 3.49. Recall that the sensitivity is defined as the rms quadrupole tilt that will generate the specified vertical emittance. Smaller values therefore indicate a *greater* sensitivity to quadrupole tilts, and larger values are more desirable.

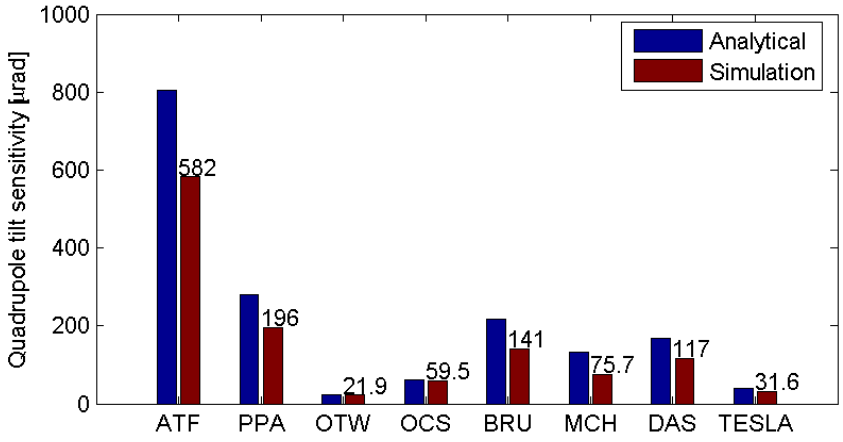

Figure 3.49: Quadrupole tilt sensitivity in the damping ring reference lattices, compared with the KEK-ATF. Smaller values indicate a *greater* sensitivity to quadrupole tilts.

The effects of quadrupole tilts were also simulated in SAD. For this study, 100 sets of random tilts with fixed rms 30 μrad were applied to the quadrupoles. A comparison between the SAD results and corresponding results obtained in Merlin is shown in Figure 3.50. There is good agreement between the results of the simulation codes.

Again, there is no clear correlation between the circumference and the sensitivity to magnet misalignments.

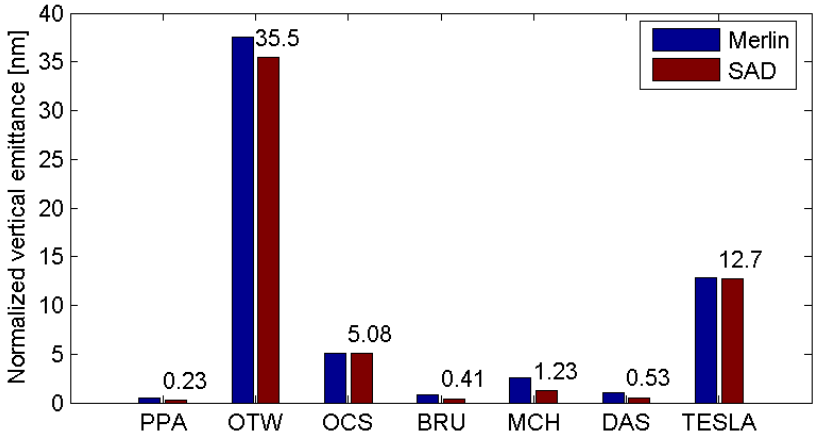

Figure 3.50: Comparison between vertical emittance in the reference lattices generated by 30 μrad quadrupole tilt, simulated by SAD and by Merlin. The average emittance over 100 different sets of alignment errors (different sets for each code) is plotted.

3.2.4 External Field Sensitivity

Stray magnetic fields around a storage ring can generate vertical emittance from vertical steering. The senstivities of the reference lattices to external fields was studied by simulation in SAD. A horizontal magnetic field was applied every 100 m around the circumference; the strength of the field was random, with rms 10^{-6} Tm (corresponding to an rms kick for a 5 GeV beam of 6×10^{-8} rad). No corrections were applied. The average vertical emittance in each of the reference lattices over 100 sets of random fields is shown in Table 3.14.

The 17 km dogbone lattices are significantly more sensitive to external magnetic fields than the other lattices: this is a consequence of the large beta functions in the long straight sections of these lattices, and could be an operational issue for a 17 km damping ring.

3.2.5 Coupling Correction Simulations

Simulations of tuning the reference lattices for low vertical emittance in the presence of alignment errors have been carried out in SAD. The procedure was the same as that used for earlier simulations of low emittance tuning

Table 3.14: External field senstivities in the reference lattices. The vertical emittance is generated by random horizontal fields with rms strength 10^{-6} Tm placed every 100 m around the ring. The average over 100 sets of random fields is shown.

Lattice	Normalized vertical emittance [nm]
PPA	0.014
OTW	0.16
OCS	0.006
BRU	0.28
MCH	3.70
DAS	4.85
TESLA	9.85

for the KEK-ATF damping ring [42], and has been successfully applied to this ring to achieve a vertical emittance of around 4.5 pm [33]. Briefly, the procedure is as follows. First, the closed orbit distortion is corrected using steering magnets to minimize the quantities:

$$\sum_{BPMs} x^2$$

and

$$\sum_{BPMs} y^2$$

where the sums extend over all BPMs, and $x(y)$ is the horizontal (vertical) reading at each BPM. Second, a combined correction is applied to the vertical closed orbit and vertical dispersion. The corrector magnets are again used, this time to minimize the quantity:

$$\sum_{BPMs} y^2 + r^2 \sum_{BPMs} \eta_y^2$$

η_y is the measured vertical dispersion. r is a weight which is generally optimized by simulation. In the present case, a value of 0.05 was used for all lattices. Finally, a coupling correction was applied using skew quadrupoles superposed on the sextupoles. The coupling correction attempted to minimize the quantity:

$$\sum_{H-steers} \left(\frac{\sum_{BPMs} \Delta y^2}{\sum_{BPMs} \Delta x^2} \right)$$

where $\Delta x(\Delta y)$ is the horizontal (vertical) change in beam position at a BPM, due to a change in strength of a steering magnet. In the simulations, two horizontal steering magnets were used to characterize the coupling in this way.

The errors applied to the lattices before the coupling correction simulation are shown in Table 3.15. The errors included BPM offsets and rotations, as well as magnet offsets and rotations. The numbers of BPMs and corrector elements used in the simulations are shown in Table 3.16. The lattice decks for OTW and TESLA include BPMs, and all these were used in the simulations; for all other lattices, BPMs were positioned at each quadrupole. Similarly, for OTW and TESLA, the decks include orbit correctors: for the coupling correction simulations, subsets of the correctors were chosen. For the other lattices, correctors were distributed around the lattices, located at quadrupoles. For the skew quadrupoles, the OTW and TESLA lattices include these elements in the decks, and subsets were chosen to use in the correction simulations. In the other lattices, skew quadrupoles were distributed around the lattices, located at the sextupoles.

Table 3.15: Alignment errors applied to magnets and BPMs in the coupling correction simulations.

Magnet offset	30 μm
Magnet tilt	0.3 mrad
BPM offset	100 μm
BPM tilt	20 mrad

Table 3.16: Numbers of corrector elements used in the coupling correction simulations.

Lattice	Number of x/y orbit correctors	Number of skew quadrupoles	Number of BPMs
PPA	128/128	56	768
OTW	120/120	92	240
OCS	127/127	96	760
BRU	131/131	101	850
MCH	99/99	101	1038
DAS	135/135	56	808
TESLA	135/135	101	946

For each lattice, 200 sets of random errors were applied to the magnets and to the BPMs, and the coupling correction procedure (as described

above) was applied to each set. The vertical emittances for each lattice after each stage of the correction, averaged over the 200 sets, are shown in Table 3.17.

Table 3.17: Vertical emittance achieved in coupling correction simulations. The values are normalized vertical emittances in nm, averaged over 200 sets of errors. Note that 'COD' is closed orbit distortion correction.

Lattice	No correction	COD only	COD and dispersion only	COD, dispersion and coupling
PPA	879	67.4	4.12	1.74
OTW	101,000	60,400	2680	1820
OCS	667	526	106	22.7
BRU	1,630	80.4	2.09	5.05
MCH	4,700	189	6.88	9.27
DAS	10,000	266	22.5	6.12
TESLA	88,100	1,670	29.6	12.6

There is a wide variation of performance of the reference lattices in terms of vertical emittance achieved by the coupling correction procedure. We should note that the arrangement of correction elements has not been optimized for each lattice. However, the results do appear to be consistent with the senstivities of the lattices to various misalignments. For example, the OTW lattice has the largest orbit ampification factor, and is the most sensitive lattice to sextuple alignment errors and quadrupole tilt errors. Apart from OCS (which comes close) all the other lattices achieve on average the specified vertical emittance after coupling correction. BRU and MCH actually achieve lower vertical emittances *before* coupling correction: for these lattices, it appears that good results can be achieved simply from correction of the closed orbit distortion and the vertical dispersion.

3.3 Beam Jitter

Minimizing the transverse jitter of the extracted beam is important for two reasons. First, preservation of the emittance in the downstream systems depends on the beam following closely the design trajectory. Second, the luminosity is sensitive to the relative transverse displacements of the bunches at the interaction point: a relative vertical offset of $1\sigma_y$ can result in a luminosity loss of as much as 40% [38]. The vertical beam size from the damping

rings is much smaller than the horizontal, so more attention is generally given to the vertical jitter. Two of the principal sources of vertical jitter will be vertical magnet motion and power supply ripple, and the effects of long-range wake fields and the bunch-by-bunch feedback system. The timescales of these sources are very different. Magnet motion and power supply ripple will occur on timescales of the order of 10 ms and longer: all bunches will be affected equally, and the effects can (in principle) be corrected in the extraction line by a feedback system reacting to the first bunches in the train. The effects of wake fields will operate on the timescale of a few nanoseconds, and can lead to transverse offsets that are different from one bunch to the next. These effects are much more difficult, or impossible, to correct. Horizontal jitter is also important; however, the sources in the horizontal plane will generally be easier to control than the corresponding sources in the vertical plane, because the horizontal beam size is much larger than the vertical. One significant source in the horizontal plane that will be less significant than for the vertical plane, is the bunch-to-bunch amplitude variation of the extraction kicker.

Longitudinal jitter is also an important consideration. Depending on the bunch compressor configuration, the tightest specifications may be on either the energy jitter, or on the phase (longitudinal position or timing) jitter. At the entrance to the main linac, phase jitter is the main concern, since this will be amplified to a large energy jitter at the end of the linac. Energy jitter, on the other hand, will be reduced by adiabatic damping as the beam is accelerated. The bunch compressors may convert phase jitter from the damping rings into energy jitter at the entrance to the main linac and vice-versa (90° rotation in longitudinal phase space), or they may simply transfer phase jitter to phase jitter, and energy jitter to energy jitter (180° rotation in longitudinal phase space). A systematic phase variation along the bunch train will result from beam loading effects in the RF cavities if there are gaps in the fill; these effects may be compensated by systems downstream of the damping rings. Random bunch-to-bunch phase and energy jitter can result from noise in the RF system, and from longitudinal long-range wake fields.

3.3.1 Transverse Jitter

Slow Jitter

While transverse jitter on timescales of the order of 10 ms will lead to systematic effects along the bunch train that may be corrected by feedback

systems in the extraction line, it is still desirable to minimize the effects as much as possible. Here, we consider just the effects of quadrupole motion in the vertical plane.

The "orbit amplification factors" for each of the reference lattices have been calculated in Section 3.2.1. The amplification factor gives the ratio between the rms closed orbit distortion, and the rms quadrupole misalignment that causes the closed orbit distortion. Let us define the quadrupole vibration tolerance, QVT, as the rms vertical quadrupole misalignment that will generate an rms closed orbit distortion equal to $1\sigma_y$, where σ_y is the vertical beam size. This is roughly the level of beam stability that is specified, so the QVT indicates the tolerable amplitude of vibration of the quadrupoles. From Equations (3.25) and (3.26), we find:

$$\mathrm{QVT} = 2|\sin\pi\nu_y|\sqrt{\frac{2\epsilon_y}{\sum_{quads}\beta_y(k_1L)^2}} \tag{3.29}$$

where ν_y is the vertical tune, ϵ_y is the vertical emittance, k_1L is the integrated normalized quadrupole strength, β_y is the vertical beta function, and the sum extends over all quadrupoles.

The values of the QVT for the KEK-ATF and the ILC damping ring reference lattices are shown in Figure 3.51. There is no clear correlation with circumference: other factors, such as the lattice tune and the beta functions, are more significant. Note that typical values are of the order 200 nm: it should be possible to keep quadrupole vibrations below this level, but careful attention must be paid to the suppression of noise sources (such as flow of cooling water) and to the design of the magnet supports.

Fast Jitter

Bunch-to-bunch or fast jitter is potentially more dangerous than slow jitter, since it will be more difficult to correct with a feedback system. In the case that the extraction line from the damping ring includes a "turn-around" before the main linac, it will be possible in principle to operate a feedback system acting across the turn-around; nonetheless it is desirable to keep the bunch-to-bunch jitter as small as possible.

The long-range wake fields are potentially a principal source of bunch-to-bunch jitter in the damping rings: the wake field effects are discussed in Section 3.4.3. A bunch-by-bunch feedback system will be needed to suppress coupled-bunch instabilities; growth times may be as short as a few tens of turns. In this regime, it is possible that noise in the feedback system could

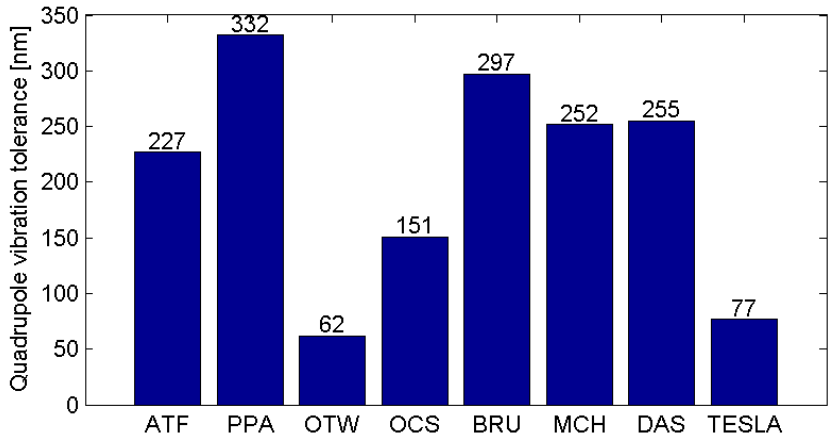

Figure 3.51: Vertical quadrupole vibration tolerance in the reference lattices, compared with the KEK-ATF. The quadrupole vibration tolerance is defined as the rms quadrupole misalignment that will generate a closed orbit distortion equal to the beam size.

itself drive bunch-to-bunch jitter. The jitter amplitude from feedback system noise is given by [84]:

$$J_{equ} = \frac{T_0}{\tau}\frac{\sigma_{\Delta y}^2}{\beta_y} \tag{3.30}$$

where J_{equ} is the jitter amplitude expressed as the coherent betatron action of a bunch; τ is the growth time of the instability; T_0 is the revolution period of the ring; β_y is the vertical beta function at the feedback pickup location; $\sigma_{\Delta y}$ is the resolution of the feedback pickup. If we assume a specification on the bunch-to-bunch jitter $J_{equ} \leq 0.1\epsilon_y$ and a vertical emittance ϵ_y =2 pm, a growth time of ten turns ($\tau/T_0 = 10$), a beta function at the pickup β_y =10 m, then the required pickup resolution is approximately 5 μm. This is challenging, but within the capability of modern technology.

3.3.2 Longitudinal Jitter

Potential sources of longitudinal beam jitter include transient beam loading from gaps in the fill (which will result in systematic phase variations along the bunch train), noise on the RF system and long-range wake fields (which will each result in random bunch-to-bunch phase and energy variations).

Quantitative studies for the ILC damping rings have not been performed at this time.

3.4 Collective Effects

There are many collective effects that may affect beam quality in the damping rings. These include impedance-driven instabilities, intrabeam scattering, space-charge effects, electron-cloud effects in the positron ring and ion effects in the electron ring. We must also consider Touschek lifetime; although the lifetime is likely to be very much longer than the nominal 200 ms store time of the beam during normal operation, achieving a reasonable lifetime for commissioning and tuning will be important.

In this section, we consider all the effects listed above. Calculations and simulations have been performed in most cases for all the reference lattices. We begin by describing the impedance models used to estimate the impedance-driven instabilities, and present the results of calculations of instability thresholds and growth rates. We then proceed to estimate the emittance growth from intrabeam scattering, the Touschek lifetime, and the potential impact of space-charge effect. We finally consider the possible effects associated with electron cloud in the positron damping rings, and ions in the electron damping rings.

3.4.1 Impedance Models

The impedance of the RF cavities and vacuum chamber can drive single-bunch and coupled-bunch instabilities. Without engineering designs of the cavities and the chamber, it is not possible to make accurate assessments of the thresholds and growth rates associated with the instabilities. However, it is possible to use information from operating machines and appropriate scaling arguments to estimate the characteristics of the impedance-driven instabilities in the damping rings. In this section, we describe the impedance models that we use to evaluate the damping ring configuration options. We consider the total impedance as the sum of the higher-order modes (HOMs) in the RF cavities, the resistive wall (RW) impedance, and the impedance of the vacuum chamber components.

Higher-Order Modes in RF Cavities

Some of the reference lattices specify the number of cavities in the ring. For this study, to allow a fair comparison, we assume the same type of RF

cavities for all rings, with a voltage of 2 MV per cavity. This is comparable to the cavity voltage achieved in CESR (1.8 MV), KEK-B (1.6 $\sim$ 2.0 MV) and planned for LHC (2.0 MV). This may be conservative: accelerating gradients up to 20–25 MV/m in superconducting cavities at 4.5 K may give 4–5 MV for a gap of 20 cm. The TESLA damping ring specifies a gradient of 15 MV/m and an active length of 30 cm, which gives 4.5 MV per cavity and a total of 12 cavities in the ring. For the present studies, we assume 2 MV per cavity, so we use 25 cavities in the TESLA damping ring, rather than 12 as specified in the original design. The total number of cavities assumed for each ring is given in Table 3.18.

Table 3.18: Numbers of RF cavities assumed in the reference lattices.

Lattice	Number of cavities, N_{cav}
PPA	8
OTW	10
OCS	9
BRU	11
MCH	26
DAS	24
TESLA	25

We assume that the superconducting RF cavities are one-cell cavities with one cavity per cryomodule; in reality, the cavities can be arranged in pairs with one pair per cryomodule. The impedance relevant for beam stability is the sum of the HOMs of the cavity (excluding the fundamental mode), and the impedance from the ferrite loading and the tapers connecting the cavity with the beam pipe. We do not consider here problems associated with beam loading. Parameters of the HOMs are taken from the KEK-B Design Report: the longitudinal HOMs are given in Table 3.19 and the transverse HOMs are given in Table 3.20. Note that R/Q is defined as $R/Q = V^2/P$, therefore the loss factor of a mode is $\kappa = (\omega/4)(R/Q)$.

The narrow-band impedance is the sum of the contributions from all modes:

$$Z_\parallel(\omega) = N_{cav} \sum \frac{(R/Q)_\parallel Q_\parallel}{1 - iQ_\parallel \left(\omega/\omega_\parallel - \omega_\parallel/\omega\right)} \tag{3.31}$$

$$Z_\perp(\omega) = N_{cav} \sum \frac{(\omega_\perp/\omega)(R/Q)_\perp Q_\perp}{1 - iQ_\perp \left(\omega/\omega_\perp - \omega_\perp/\omega\right)} \tag{3.32}$$

where N_{cav} is the total number of cavities in the ring. The total loss factor of the fundamental mode is 0.15 V/pC and of the HOMs is only 0.065 V/pC.

Table 3.19: Longitudinal HOMs in the KEK-B superconducting RF cavities.

$f_\parallel$ [MHz]	$(R/Q)_\parallel$ [Ω]	Loaded $Q_\parallel$
783	0.12	132
834	0.34	72
1018	6.6	106
1027	6.4	95
1065	1.6	76
1076	3.2	65
1134	1.7	54

Table 3.20: Transverse HOMs in the KEK-B superconducting RF cavities.

$f_\perp$ [MHz]	$(R/Q)_\perp$ [Ω]	$Q_\perp$
609	1.9	92
648	40.2	120
688	170.4	145
705	227.3	94
825	6.16	60
888	3.52	97

The total loss factor of the KEK-B cryomodule $\kappa = 2.3$ V/pC is dominated by the contribution of the tapers and loads and is taken into account below, together with the rest of the vacuum components.

Resistive-Wall Wake Field

The transverse resistive-wall wake field for a beam pipe with circular cross-section of radius b and length l is given by:

$$W_\perp(z) = \frac{A_\perp}{\sqrt{z}} \tag{3.33}$$

where (in mks units)

$$A_\perp = \frac{2}{\pi}\sqrt{\frac{Z_0 c}{4\pi}\frac{c}{\sigma_c}}\frac{l}{b^3} \tag{3.34}$$

σ_c is the conductivity of the vacuum chamber. For comparing the reference lattices, we assume the same chamber radius in corresponding sections of the rings, shown in Table 3.21.

The growth rates of the coupled-bunch modes driven by the resistive-wall wake field depend on the beta functions. For the dogbone lattices, the beta

Table 3.21: Assumed vacuum chamber radius in different sections of the damping rings.

Section	Radius, b [mm]
Arc	22
Wiggler	8
High-β long straight	49

functions vary by an order of magnitude and are correlated with the radius of the vacuum chamber, taking large values in the straight sections where the aperture is large, and smaller values in the wiggler where the aperture is narrow. It is therefore convenient to calculate the quantity $\langle \beta_\perp A_\perp \rangle$ defined by:

$$\langle \beta_\perp A_\perp \rangle = \frac{2}{\pi}\sqrt{\frac{Z_0 c}{4\pi}\frac{c}{\sigma_c}}\frac{1}{C}\int \frac{\beta_\perp}{b^3} ds \tag{3.35}$$

where $\beta_\perp$ is the (horizontal or vertical) beta function, and the integral is taken around the entire circumference of the ring (but note that since we divide by the circumference, this expression gives the wake per unit length, not the total wake of the ring).

The resistive-wall loss factor for a gaussian bunch of rms length σ_z is given (in mks units) by:

$$\kappa_\parallel = \frac{\Gamma\left(\frac{3}{4}\right)}{(2\pi\sigma_z)^{3/2}}\sqrt{\frac{Z_0 c}{4\pi}\frac{c}{\sigma_c}}\int \frac{1}{b} ds \tag{3.36}$$

Section lengths and the corresponding vertical beta functions are shown in Table 3.22. Note that the wiggler length includes the drifts and quadrupoles adjacent to each wiggler unit: the length of the wiggler section is then somewhat longer than the magnetic length of the wiggler. The (weighted) resistive-wall wake fields and loss factors for the reference lattices are shown in Table 3.23. Note that we assume the bunch lengths given in Table 2.1, and an aluminum vacuum chamber with conductivity $\sigma_c = 3.8 \times 10^7 \quad \Omega^{-1}\mathrm{m}^{-1}$.

Broadband Impedance

The impedance of the numerous vacuum chamber components is mostly inductive. The total impedance can be defined by two parameters: the inductance L of the ring, and the total loss factor $\kappa_\parallel$. The total impedance is written (in mks units):

$$Z_\parallel(\omega) = -i\frac{\omega L}{(1 - i\omega a/c)^{3/2}} \tag{3.37}$$

Table 3.22: Section lengths, vertical beta functions and quadrupole quantities in the reference lattices.

Lattice	Arc section			Wiggler section			Long straight section		
	Length [m]	$\langle\beta_y\rangle$ [m]	# quads	Length [m]	$\langle\beta_y\rangle$ [m]	# quads	Length [m]	$\langle\beta_y\rangle$ [m]	# quads
PPA	2709	12.6	395	115	8.20	23	0	-	0
OTW	1002	24.8	402	202	4.94	72	2019	90.9	64
OCS	5846	39.0	604	268	9.21	80	0	-	0
BRU	3634	14.4	662	540	9.96	170	2159	142.9	46
MCH	3634	14.4	648	540	9.96	170	11761	142.9	248
DAS	3240	13.1	458	560	8.20	112	13214	133.6	266
TESLA	2229	24.8	572	529	13.4	104	14242	142.1	270

Table 3.23: Resistive-wall wake fields and loss factors in the reference lattices.

Lattice	$\langle\beta_y/b^3\rangle$ [mm^{-2}]	Weighted RW wake field $C\langle\beta_\perp A_\perp\rangle$ [V/pC/m$^{1/2}$]	RW loss factor $\kappa_\parallel$ [V/pC]
PPA	1.80	864	6.11
OTW	1.81	994	4.97
OCS	4.29	4465	13.3
BRU	2.84	3071	6.69
MCH	1.86	5055	11.4
DAS	1.64	4759	21.6
TESLA	2.13	6168	20.3

where the parameter a has to be chosen to give the loss factor $\kappa_\parallel$ for a gaussian bunch with rms length σ_z:

$$\kappa_\parallel(\sigma_z) = \int Z_\parallel(\omega) e^{-(\omega\sigma_z/c)^2} \frac{d\omega}{2\pi} \tag{3.38}$$

$Z_\parallel(\omega)$ is the pure inductive impedance at low frequencies, but rolls off as $1/\sqrt{\omega}$ at high frequencies (according to the diffraction model). The wake field corresponding to the impedance of Equation (3.37) is:

$$W_\parallel(z) = \frac{1}{2\pi} \int_{-\infty}^{\infty} e^{i\omega z/c} Z_\parallel(\omega) d\omega \tag{3.39}$$

$$= \begin{cases} \frac{c^2 L}{\sqrt{\pi a^3 z}} \left(1 + \frac{2z}{a}\right) e^{z/a} & \text{if } z \le 0 \\ 0 & \text{if } z > 0 \end{cases} \tag{3.40}$$

In terms of the wake field, the loss factor (3.38) is:

$$\kappa_\parallel(\sigma_z) = \frac{1}{2\sqrt{\pi}\sigma_z} \int_{-\infty}^{\infty} W_\parallel(z) e^{-(z/2\sigma_z)^2} dz \tag{3.41}$$

To estimate the broadband impedance of the damping rings, we scale from the PEP-II LER:

$$L = L_{\rm PEP} \sum_i \left(\frac{N_{quads,i}}{N_{\rm PEP}}\right) \left(\frac{b_{\rm PEP}}{b_i}\right)^2 + N_{cav} L_{SC} \tag{3.42}$$

where the sum is over different sections of the damping ring (arc, wiggler and long straights), $L_{\rm PEP} = 100$ nH is the estimated inductance, $N_{\rm PEP} = 292$ is the number of quadrupoles, and $b_{\rm PEP} = 31.5$ mm is the beam-pipe radius in PEP-II LER. The last term in Equation (3.42) takes into account the inductance of the tapers in the cryomodules. The inductance of a taper $L_{SC} = 0.45$ nH is estimated using Yokoya's formula $L = (Z_0/4\pi c) l \alpha^2$, where $l = 0.15$ m is the taper length and $\alpha = 175$ mrad is the taper angle.

The loss factor $\kappa_\parallel$ is taken as the sum of the PEP-II LER loss factor $\kappa_{\rm PEP}$ and the loss factors of the KEK-B cryomodules κ_{SC}:

$$\kappa_\parallel = \kappa_{\rm PEP} \left(\frac{N_{quads}}{N_{\rm PEP}}\right) \left(\frac{\sigma_{\rm PEP}}{\sigma_z}\right)^2 + N_{cav} \kappa_{SC} \frac{\sigma_{\rm PEP}}{\sigma_z} \tag{3.43}$$

The PEP-II LER loss factor (without IR) has been estimated at $\kappa_{\rm PEP} = 2.5$ V/pC at a bunch length $\sigma_{\rm PEP} = 10$ mm. It is scaled here with the number of quads and with the inverse square of the bunch length. The dependence

on the bunch length corresponds to observations in PEP-II. The loss factor of a cryomodule is obtained from $\kappa_{SC} = 0.5$ V/pC at $\sigma_z = 10$ mm by scaling proportional to $1/\sigma_z$: such a dependence approximately reproduces the experimental bunch-length dependence of the loss factor in the KEK-B cryomodules.

The inductance and loss factors can be calculated for the damping rings from Equations (3.42) and (3.43), using the vacuum chamber radius and numbers of quadrupoles given in Tables 3.21 and 3.22. From the loss factor, we can calculate the roll-off parameter a by solving Equation (3.41) with the wake field of Equation (3.4.1). The results are shown in Table 3.24.

The magnitude of the overall (longitudinal) impedance of a machine can be characterized by the parameter Z/n, defined as:

$$\frac{Z}{n} = \frac{\sigma_z}{R} \sum_{n=-\infty}^{\infty} \left| \frac{Z_\parallel(n\omega_0)}{n} \right| e^{-(n\sigma_z\omega_0/c)^2} \tag{3.44}$$

In the parameter regime of the damping rings,

$$\frac{Z}{n} \approx \sqrt{\pi}\omega_0 L \tag{3.45}$$

Values for the broadband impedance characteristics are given in Table 3.24. Note that our estimates are based on the assumption that the number of vacuum components scales in proportion to the number of quadrupoles (which, in turn, is assumed to be proportional to the number of optical cells). Without a detailed design of the vacuum chamber, this is probably the best assumption to make at the present time; however, it may not be correct. For example, the very long straight sections in the dogbone lattices have relatively few quadrupole magnets, but the number of pumps could be large to achieve the necessary vacuum pressure.

The energy change of particles in a bunch resulting from the broadband wake field over one turn is given by:

$$\Delta E(z) = -\int_z^\infty \lambda(z') W_\parallel(z - z') dz' \tag{3.46}$$

The energy change for a bunch in PPA, with the nominal bunch charge and bunch length, is shown in Figure 3.52.

The transverse impedance is calculated from the sum of the HOMs of the superconducting RF cavities, the transverse resistive-wall impedance, and the transverse impedance $Z_\perp(\omega)$ of the vacuum chamber components.

Table 3.24: Longitudinal broadband impedance characteristics of the damping rings.

Lattice	Inductance L [nH]	Loss factor $\kappa_{\parallel}$ [V/pC]	Roll-off parameter a [mm]	Estimated impedance Z/n [mΩ]
PPA	403	16.6	0.474	475
OTW	678	21.1	0.357	701
OCS	852	23.8	0.319	465
BRU	1379	15.4	0.430	726
MCH	1404	25.7	0.711	294
DAS	965	39.9	0.476	189
TESLA	1003	43.3	0.498	196
PEP-II LER	100	2.5	1.37	151

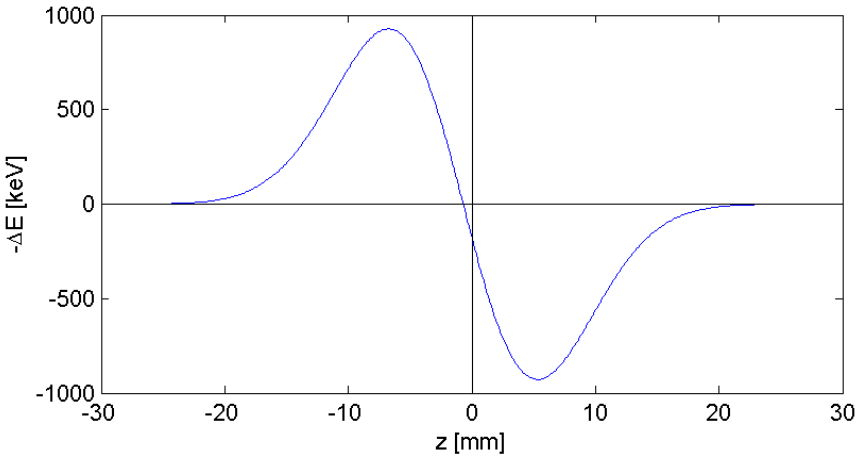

Figure 3.52: Energy change of particles in a bunch from the broadband impedance in PPA. The bunch length is 6 mm rms, and the number of particles is 2.4×10^{10}.

$Z_\perp(\omega)$ is found by scaling from the longitudinal broadband impedance:

$$Z_\perp(\omega) = \frac{C}{\pi b^2}\frac{Z_\parallel(\omega)}{n} \tag{3.47}$$

where $n = \omega/\omega_0$. For transverse instabilities, the beta function at the location of the impedance is significant, so we use the quantity $Z_\perp\beta_\perp$ defined by:

$$Z_\perp\beta_\perp = \frac{1}{\pi}\frac{Z}{n}\int \frac{\beta_\perp}{b^2}ds \tag{3.48}$$

In this expression, we assume that the sources of the longitudinal impedance are uniformly distributed around the ring, but that the corresponding transverse impedance varies locally with the inverse square of the vacuum chamber radius. Using the chamber radius in different sections from Table 3.21, the lengths and beta functions in different sections from Table 3.22, and the longitudinal impedances from Table 3.24, we estimate the transverse impedances shown in Table 3.25.

Table 3.25: Transverse broadband impedance of the damping rings.

Lattice	$\int \frac{\beta_y}{b^2}ds$ $[10^8]$	Estimated transverse impedance $Z_\perp\beta_\perp$ [MΩ]
PPA	0.858	13.0
OTW	1.43	31.9
OCS	5.10	75.5
BRU	3.21	74.2
MCH	8.92	83.5
DAS	8.95	53.8
TESLA	10.7	66.8

3.4.2 Single-Bunch Impedance-Driven Instabilities

Longitudinal Instability

The broadband impedance can drive a longitudinal microwave instability. Applying the Keil-Schnell-Boussard criterion, we find an estimate for the impedance above which beam instability may occur:

$$\frac{Z}{n} = Z_0\sqrt{\frac{\pi}{2}}\frac{\gamma\alpha_p\sigma_\delta^2\sigma_z}{N_0 r_e} \tag{3.49}$$

Table 3.26 shows the threshold impedance for the damping rings, compared with the estimated impedance (scaled from PEP-II LER) given in Table 3.24. Also shown, for comparison, is the estimated instability threshold for PEP-II LER, calculated using the parameters in Table 3.27.

Table 3.26: Microwave instability threshold for the damping rings estimated from the Keil-Schnell-Boussard criterion.

Lattice	Estimated impedance Z/n [mΩ]	Estimated instability threshold Z/n [mΩ]
PPA	475	187
OTW	701	299
OCS	465	134
BRU	726	622
MCH	294	510
DAS	189	95
TESLA	196	100
PEP-II LER	151	92

Table 3.27: Parameters for PEP-II LER used for estimating the microwave instability threshold.

Beam energy	3.1 GeV
Number of particles per bunch, N_0	7.0×10^{10}
Momentum compaction factor, α_p	1.25×10^{-3}
Energy spread, σ_δ	7.1×10^{-4}
RMS bunch length, σ_z	10 mm

We should note that although it appears that most of the rings are significantly above the instability threshold in these estimates, the exact threshold can be very sensitive to details of the wake field. The scaling arguments that we have used here are not sufficiently reliable to predict the instability behavior with real confidence, but for a more rigorous analysis, a detailed design of the vacuum components would be required. Such a design is not yet available. Nonetheless, our results may be indicative of the regime in which the damping rings are likely to operate, and it would seem prudent to take measures in the design of the lattice that would raise the threshold, for example by designing for a large momentum compaction factor. A longer bunch length would also help, by reducing the peak current.

Transverse Instability

The transverse impedance of the vacuum chamber can drive a transverse instability in the beam. We can write the threshold of the instability in a form similar to that for the threshold of the longitudinal instability:

$$Z_\perp \beta_\perp = Z_0 \frac{4\sqrt{2}}{3} \frac{\gamma \alpha_p \sigma_\delta C}{N_0 r_e} \tag{3.50}$$

Table 3.28 compares the estimated threshold with the estimated impedance (based on the scaling from PEP-II LER) given in Table 3.25. In all cases, the instability threshold looks safely above the estimated impedance.

Table 3.28: Transverse single-bunch instability thresholds for the damping rings.

Lattice	Estimated transverse impedance $Z_\perp \beta_\perp$ [MΩ]	Estimated instability threshold $Z_\perp \beta_\perp$ [MΩ]
PPA	13.0	104
OTW	31.9	178
OCS	75.5	160
BRU	74.2	676
MCH	83.5	1045
DAS	53.8	311
TESLA	66.8	330

We also studied the transverse mode-coupling instability (TMCI) in more detail, using the Satoh-Chin formalism [64], in which the frequencies of the coherent modes are found by solving an eigenvalue problem. The instability threshold is defined by coupling between two modes, usually modes $m = 0$ and $m = -1$. The results of calculations are shown in Figure 3.53; threshold bunch currents are compared with the nominal bunch currents in Table 3.29. The threshold currents are significantly larger than the nominal currents, so TMCI should not be a performance limitation in any of the reference lattices.

3.4.3 Coupled-Bunch Impedance-Driven Instabilities

Transverse Instabilities

The main impedance contribution to the growth rate of the coupled-bunch instability is from the resistive-wall impedance. In the vertical plane, the

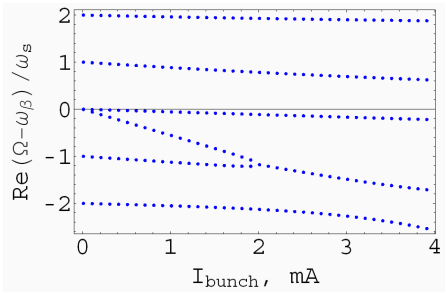

(a) PPA

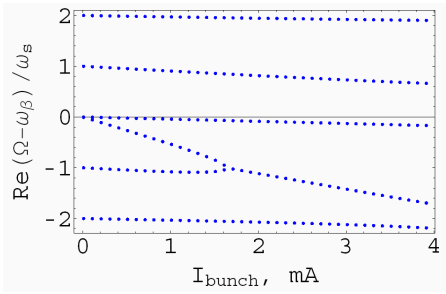

(b) OTW

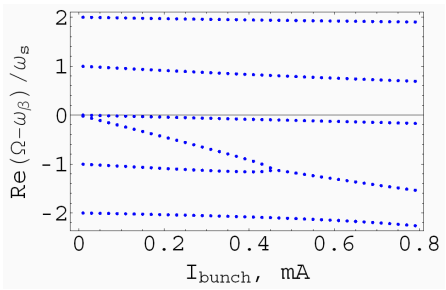

(c) OCS

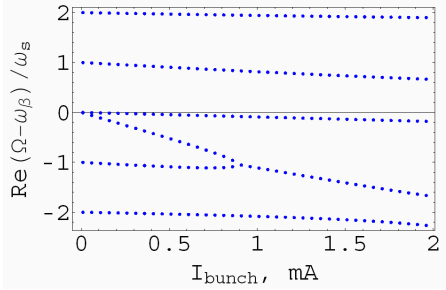

(d) BRU

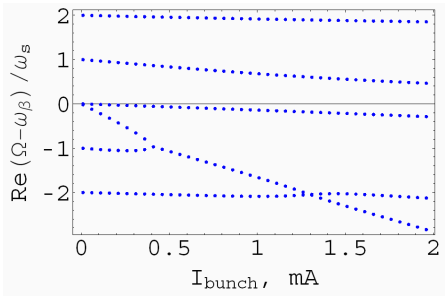

(e) MCH

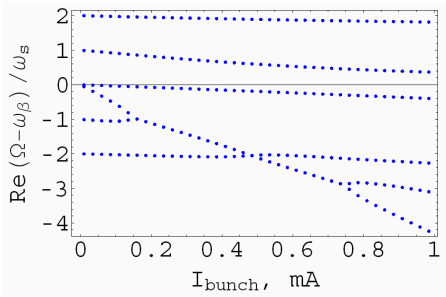

(f) DAS

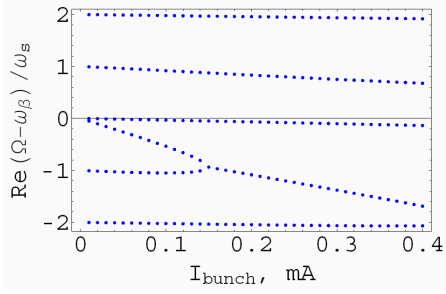

(g) TESLA

Figure 3.53: Transverse mode-coupling instability thresholds.

Table 3.29: Transverse mode-coupling instability thresholds.

Lattice	Nominal bunch current [mA]	TMCI threshold bunch current [mA]
PPA	0.340	2.0
OTW	0.298	1.6
OCS	0.157	0.45
BRU	0.152	0.90
MCH	0.060	0.40
DAS	0.057	0.15
TESLA	0.057	0.15

growth rate of the fastest growing mode is given by:

$$\Gamma = \frac{4\pi}{Z_0 c}\frac{c}{4\gamma}\frac{\langle I\rangle}{I_A}\sqrt{\frac{C}{1-[\nu_y]}}\langle\beta_y A_y\rangle \tag{3.51}$$

where γ is the relativistic factor, $\langle I\rangle$ is the average current, $I_A \approx 17$ kA is the Alfvén current, C is the circumference, $[\nu_y]$ is the fractional part of the tune, and $\langle\beta_y A_y\rangle$ is the weighted resistive-wall wake field, given by Equation (3.35). We assume a circular vacuum chamber, and a uniformly filled ring with the bunch spacing and bunch charge given in Table 2.1; in some cases, this results in a higher average current than given in the table, because the gaps between bunch trains have been filled. Using values for the weighted resistive-wall wake field from Table 3.23, and other parameters from Table 2.1, we find the growth rates given in Table 3.30. Note that modern bunch-by-bunch feedback systems are capable of damping modes with growth times longer than approximately 15 turns.

Table 3.30: Growth rates of resistive-wall instability, with vacuum chamber apertures given in Table 3.21.

Lattice	Growth rate, Γ [ms^{-1}]	Growth time, f_0/Γ [turns]
PPA	1.38	77.0
OTW	0.800	116
OCS	3.28	14.9
BRU	1.75	27.0
MCH	0.544	34.6
DAS	0.494	35.7
TESLA	0.416	42.4

The growth rates are strongly dependent on the vacuum chamber aperture. An increase in the aperture, even in the relatively short wiggler section, can significantly ease the requirements on the feedback system. As an example, we consider the case with the radius in the wiggler increased to 16 mm (and the same radius in the arcs and straight sections); the results are shown in Table 3.31.

Table 3.31: Growth rates of resistive-wall instability, with 16 mm radius vacuum chamber in the wiggler.

Lattice	Growth rate, Γ [ms^{-1}]	Growth time, f_0/Γ [turns]
PPA	0.940	113
OTW	0.567	164
OCS	2.75	17.8
BRU	0.860	55.1
MCH	0.376	50.0
DAS	0.355	49.6
TESLA	0.277	63.6

The tune shift $\Delta\nu_y \approx \Gamma/\omega_0$ caused by the resistive-wall impedance is equal to the growth rate divided by the angular revolution frequency. Generally speaking, it can vary along the bunch train and distort the optics for bunches in the tail of the train. However, for the damping rings the effect is small, see Table 3.32.

Table 3.32: Tune shifts from resistive-wall impedance.

Lattice	RW Tune shift [10^{-3}]
PPA	2.07
OTW	1.36
OCS	10.6
BRU	5.89
MCH	4.61
DAS	4.46
TESLA	3.76

The growth rates calculated with the total transverse impedance (including cavity HOMs) differ very little from the results obtained using just the resistive-wall impedance.

Longitudinal Instabilities

The frequency $\Omega^{(\mu)}$ of coupled-bunch mode number μ driven by a longitudinal impedance $Z_{\parallel}(\omega)$ is given by [14]:

$$\Omega^{(\mu)} - \omega_s = i\frac{4\pi}{Z_0 c}\frac{MNr_e\alpha_p f_0}{4\pi\gamma\nu_s}\sum_{p=-\infty}^{\infty} p_{eff}\omega_0 e^{-(p_{eff}\omega_0\sigma_z/c)^2} Z_{\parallel}(p_{eff}\omega_0) \quad (3.52)$$

where

$$p_{eff} = pM + \mu + \nu_s \quad (3.53)$$

M is the number of bunches in the ring, N is the number of particles per bunch, α_p is the momentum compaction, ν_s is the synchrotron tune, and $f_0 = \omega_0/2\pi$ is the revolution frequency. The instability of the μ-th mode corresponds to the positive values of the growth rate:

$$\Gamma = \mathrm{Im}\,\Omega^{(\mu)} \quad (3.54)$$

An example of the growth rate for a full range of modes in PPA is shown in Figure 3.54. The maximum growth rates for all the reference lattices are shown in Table 3.33. The growth rates are slower than the synchrotron radiation damping rates by an order of magnitude.

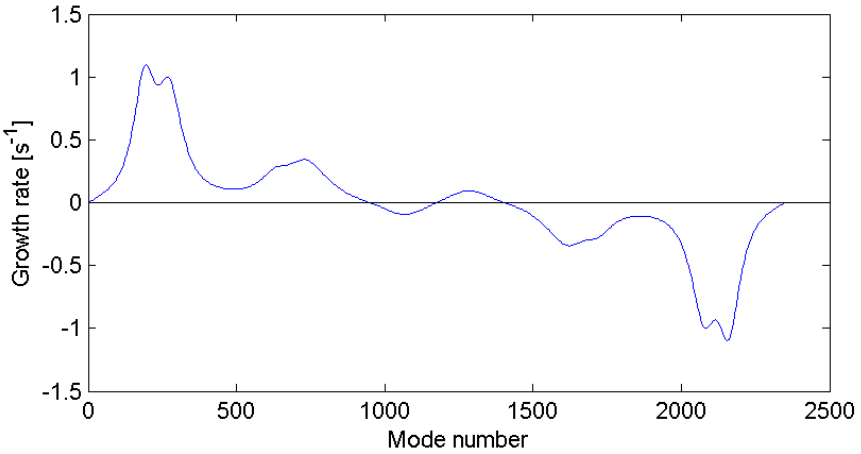

Figure 3.54: Growth rates of longitudinal coupled-bunch modes in PPA, driven by cavity HOMs.

Table 3.33: Peak growth rates of longitudinal coupled-bunch modes driven by cavity HOMs.

Lattice	Growth rate [s^{-1}]
PPA	1.12
OTW	0.962
OCS	0.294
BRU	1.01
MCH	0.182
DAS	0.042
TESLA	0.067

It is worth noting that the typical Q factor for the higher-order modes in superconducting RF cavities using ferrite HOM absorbers is of the order 100. For the frequencies of the HOMs in the range from 1 to 3 GHz, this means that the width of the resonance of each mode Δf_{res} is of the order of 10 to 30 MHz. In Equation (3.52), the summation over the frequency goes in steps equal to $M\omega_0$. The typical number of bunches in the ILC damping ring is $M \sim 3000$, and the revolution frequencies range from $2\pi \times 100$ kHz for a 3 km ring, to $2\pi \times 18$ kHz for a 17 km ring; so for the damping rings, we find that $\Delta f_{res} \gtrsim M\omega_0/2\pi$, which means that for each oscillation mode μ, the dominant contribution comes from only a single term in the summation.

The transient beam loading in the RF cavities resulting from gaps in the bunch train is known to cause RF phase variation of the individual bunches. The effect, however, should be small because of the high Q factor of superconducting cavities.

3.4.4 Intrabeam Scattering

Intrabeam scattering (IBS) can lead to growth in the transverse and longitudinal emittances. Experimental studies of IBS in electron storage rings have been performed in the KEK-ATF [33], and in the LBNL-ALS [68]. The effect is strongly dependent on the vertical emittance; good quantitative data have only been obtained at the KEK-ATF, which has achieved the lowest vertical emittance of any operating storage ring. There are a number of different formalisms that can be used to calculate IBS growth rates. The basic theory has been developed by Piwinski [54] and extended by Bjorken and Mtingwa [9]. Several approximations have been developed that allow rapid calculation of the growth rates, and are convenient for determining the equilibrium beam sizes in a storage ring [2, 43]. We have performed calculations

of the equilibrium emittances in the ILC positron damping ring reference lattices using the formulas of Kubo *et al* [43]; results from this method are in good agreement with the experimental results from the KEK-ATF. We should note that during operation of the ILC damping rings, the beams will be extracted before they come to full equilibrium; however, we are not capable at present of calculating the precise behavior of a bunch of particles approaching equilibrium in the presence of radiation damping and IBS. Since the extracted bunches are reasonably close to equilibrium, we calculate the effect of IBS on the equilibrium beam sizes, and use these results as an indication of the impact of IBS on operation of the damping rings.

We should emphasize that the results presented here are for the positron damping rings. In the case that the electron damping ring has a longer radiation damping time (that may be allowed by the fact that the injected electron beam will be much smaller than the injected positron beam), IBS will have a larger effect. For this reason, it may be necessary to design the electron damping ring with a shorter damping time than would be required in the absence of IBS.

The IBS growth rates are essentially functions of the charge density; allowing a longer bunch therefore has the benefit of reducing the IBS growth rates. Two of the reference lattices, BRU and MCH, were designed for a natural (zero-charge) bunch length of 9 mm, while the others were designed for a natural bunch length of 6 mm. To provide a meaningful comparison of IBS growth rates between the different reference lattices, the bunch length in the BRU and MCH lattices was reduced to 6 mm. Although this is possible in principle by increasing the RF voltage, it would not be reasonable in practice because of the very high RF voltages required.

Figure 3.55 shows the growth in horizontal emittance from IBS as a function of bunch charge in the seven reference lattices. The horizontal green line shows the nominal 8 μm normalized horizontal emittance of the extracted beam. The nominal number of particles per bunch is 2.4×10^{10} for PPA, 2.2×10^{10} for OTW, and 2×10^{10} for the other lattices. The natural (zero-charge) emittances of the different lattices range between 3 μm and 6.6 μm. The growth from IBS is a function of the optics in the lattice, and is also strongly dependent on the energy. Lattices with lower energy are more sensitive to IBS, and in Figure 3.55 it is clear that the most rapid growth in horizontal emittance is in the BRU lattice, which is at a significantly lower energy than the others (3.74 GeV compared to 5 GeV). All the reference lattices meet the specification on the horizontal emittance at the nominal bunch charge, though it does seem prudent to design the damping ring lattice with a natural emittance somewhat below 8 μm to allow for IBS emittance

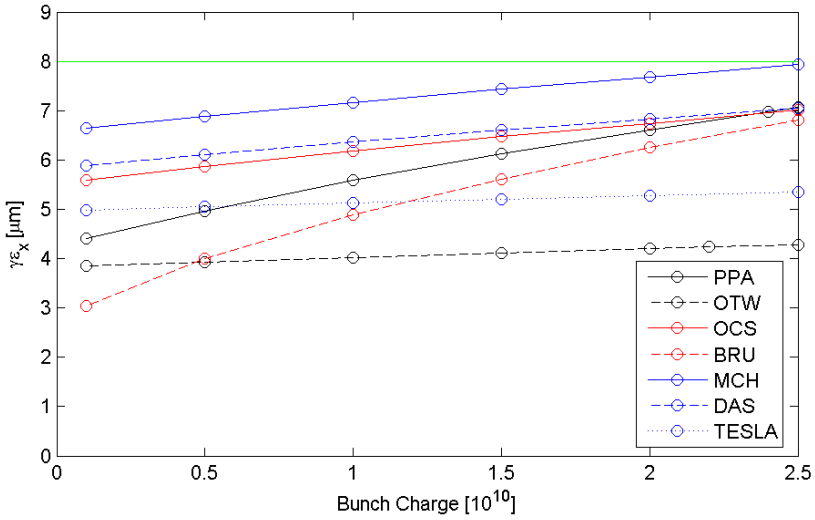

Figure 3.55: Horizontal emittance growth from IBS.

growth.

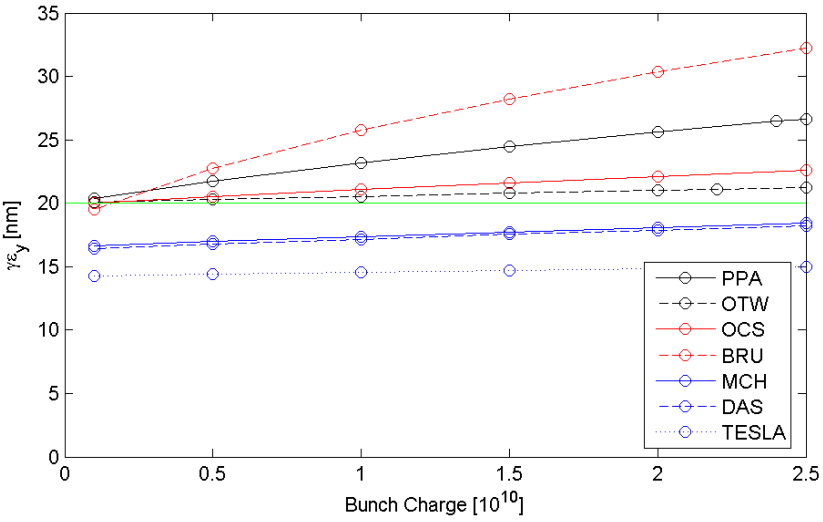

Figure 3.56: Vertical emittance growth from IBS.

Figure 3.56 shows the growth in vertical emittance from IBS as a function of bunch charge in the seven reference lattices. The vertical emittance growth from IBS is dependent to a large extent on the way in which the vertical emittance is generated, i.e. whether it comes from vertical dispersion, or from betatron coupling. If the vertical emittance is generated from vertical dispersion, then the IBS emittance growth is a function of the vertical optical functions; however, if the vertical emittance is generated by betatron coupling, then the relative vertical IBS emittance growth is equal to the relative horizontal IBS emittance growth. Since the vertical emittance in an operating storage ring is generally a combination of vertical dispersion and betatron coupling and depends on random alignment errors, the precise situation in any ring cannot be well known in advance. However, it is possible to make reasonable assumptions, and for the present studies we assume that the vertical dispersion and the betatron coupling contribute equally to the vertical emittance in any given lattice. This situation is achieved when the rms residual vertical dispersion is between 1.4 mm and 4.3 mm, depending on the lattice. Note that the nominal value of the equilibrium vertical emittance depends on the damping time, which varies between the reference lattices; a lattice with a longer damping time needs to achieve a lower equilibrium vertical emittance, since the beam is further from equilibrium at the time it is extracted.

The differences between the reference lattices are perhaps more obvious in the case of vertical IBS emittance growth, than in the case of horizontal IBS emittance growth. The dogbone lattices have relatively little vertical emittance growth: this is because of the large beam size in the long straight sections (even in the absence of coupling bumps) where the beta function is large. In both the horizontal and vertical planes, the BRU lattice has the largest relative emittance growth, because of its lower energy compared to the other lattices. Of the 5 GeV lattices, PPA has the lowest beta functions and largest relative emittance growth.

The vertical IBS emittance growth can in principle be compensated by tuning the lattice for a lower zero-charge equilibrium vertical emittance. However, the ultralow vertical emittances required in the damping rings will not be easy to achieve; and reducing the vertical emittance further will enhance the IBS growth rates, leading to diminishing returns. From these results, it seems inadvisable to reduce the beam energy in the damping rings below 5 GeV, and attention should be given to designing optics that have sufficiently large beta functions, that the vertical IBS growth rates are reasonably low.

Figures 3.57 and 3.58 show the growth in bunch length and energy spread

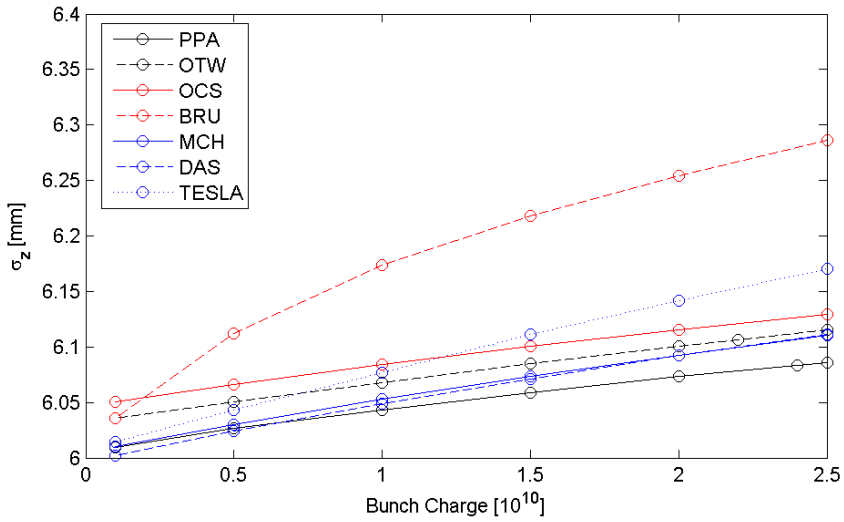

Figure 3.57: Growth in bunch length from IBS.

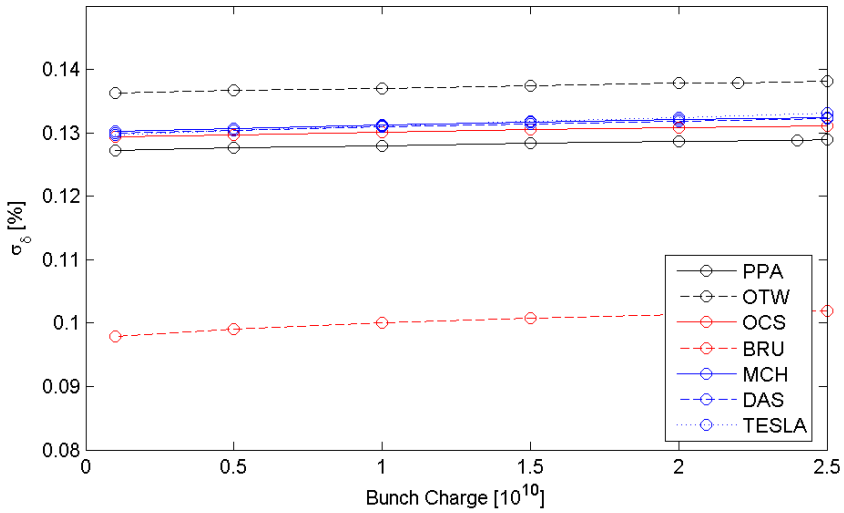

Figure 3.58: Growth in energy spread from IBS.

from IBS. As we mentioned above, to allow a meaningful comparison between the lattices, they were all tuned for the present studies to a natural bunch length of (close to) 6 mm. The relative emittance growth from IBS is rather smaller in the longitudinal plane than in either the horizontal or vertical. This is because a small change in longitudinal momentum from a scattering event can lead to a large change in transverse oscillation amplitude, if the scattering occurs where there is large dispersion. In the case of the bunch length, we see again that the lattice with largest increase from IBS is BRU, which is at a significantly lower energy. For the other lattices, the increase in bunch length from IBS is less than 2% at the nominal bunch charge. In the case of the energy spread, the BRU lattice, because of the lower energy, has a significantly lower natural energy spread than the other lattices and the effects of IBS are small in comparison to this difference.

Finally, we note that increasing the bunch length can be expected to reduce the IBS growth rates proportionately. Although this may be helpful in some cases, the IBS emittance growth does not appear to be sufficiently strong to motivate an increase in the nominal bunch length from 6 mm to (say) 9 mm, except in the case of a damping ring operating at an energy significantly below 5 GeV. In terms of other configuration options (for example the ring circumference) IBS is not a strong factor in making a decision. The effect of IBS in the electron damping ring, where the radiation damping time may be longer than in the positron damping ring, remains to be studied.

3.4.5 Touschek Lifetime

While the beams are stored for only a few milliseconds in regular operation, and Touschek lifetimes are measured in minutes or hours, a very short lifetime could cause problems during commissioning and tuning. It is therefore appropriate to make an estimate of the Touschek lifetime that might be expected in the different damping ring reference lattices. A detailed calculation requires a model of the energy acceptance of the lattice, including dynamical and physical apertures. While there are clearly differences between the lattices in the dynamic energy acceptance, insufficient information is available at present for more than a rough estimate of the Touschek lifetime. For the present, therefore, we assume a fixed energy acceptance of 1% in each case. Since the Touschek lifetime is proportional to the square of the energy acceptance (in the regime in which the damping rings will operate), it is straightforward from this assumption to estimate the lifetime if a different value of the energy acceptance is thought to be more appropriate.

Formulae for calculating the Touschek lifetime are well known [55]. A

calculation has been implemented in BMAD [63]. An approximation valid for flat beams and non-relativistic energies in the rest frame of the beam is given by [79]:

$$\frac{1}{\tau} = \frac{r_e^2 c N_0}{8\pi\gamma^2\delta_{max}^3\sigma_x\sigma_y\sigma_z} D(\epsilon) \tag{3.55}$$

where r_e is the electron radius, c is the speed of light, N_0 the number of particles per bunch, δ_{max} is the energy acceptance, γ is the relativistic factor, and σ_x, σ_y and σ_z are the horizontal, vertical and longitudinal rms bunch sizes. The function $D(\epsilon)$ is given by:

$$\frac{2D(\epsilon)}{\sqrt{\epsilon}} = -3e^{-\epsilon} + \epsilon\int_\epsilon^\infty \frac{\ln u}{u} e^{-u} du + (3\epsilon - \epsilon\ln\epsilon + 2)\int_\epsilon^\infty \frac{e^{-u}}{u} du \tag{3.56}$$

and the parameter ϵ is given by:

$$\epsilon = \left(\frac{\beta_x \delta_{max}}{\gamma\sigma_x}\right)^2 \tag{3.57}$$

where β_x is the horizontal beta function.

Table 3.34: Touschek lifetime in the reference lattices, assuming 1% energy acceptance.

Lattice	Beam energy [GeV]	Particles per bunch [10^{10}]	Bunch length [mm]	Touschek lifetime from BMAD [min]	Touschek lifetime from Equation (3.55) [min]
PPA	5.0	2.4	6	17	16
OTW	5.0	2.2	6	18	17
OCS	5.066	2.0	6	34	33
BRU	3.74	2.0	9	14	18
MCH	5.0	2.0	9	93	68
DAS	5.0	2.0	6	52	44
TESLA	5.0	2.0	6	62	50

The results of the calculation (averaging around the lattice) are given in Table 3.34; there is good agreement between the calculation in BMAD, and the approximate calculation using Equation (3.55). We assumed 1% energy acceptance, and the equilibrium beam sizes given in Table 2.1. The dogbone lattices have the longest lifetimes, because the large beta functions in the long straight sections (the calculations were performed without coupling insertions) reduce the charge density over a substantial part of the lattice.

The lifetime in MCH is particularly long because of the longer bunch length (9 mm compared to 6 mm in DAS and TESLA). Although BRU also has a 9 mm bunch length, the beam lifetime in this lattice is relatively short, because of the lower energy (3.74 GeV compared to 5 GeV in the other lattices).

Although a beam lifetime less than 30 minutes could possibly have some impact on commissioning, the Touschek lifetime of all the reference lattices is likely to be reasonable, particularly if an energy acceptance greater than 1% can be achieved. The Touschek lifetime should not be a significant factor in making configuration choices for the damping rings.

3.4.6 Space-Charge Effects

Direct space-charge effects have the potential to impact the performance of the ILC damping rings because of the combination of long circumference and small emittance together with the energy range where the damping rings are expected to operate. A signature of the importance of space charge is the vertical tuneshift, which could be significantly above 0.20 for the longest proposed lattices.

Space charge is not expected to be of any consequence on injection efficiency or dynamic aperture since it becomes relevant only toward the end of the damping cycle, when the vertical beam size is small. However, it could cause an unacceptable degradation of the 20 nm (normalized) vertical emittance specified at extraction. There are two basic ways by which space charge could have an adverse effect: by enlarging the width of existing lattice resonances, and by driving new resonances. In the course of studies of the damping rings reference lattices, we found evidence for both effects. Since the vertical emittance is much smaller than the horizontal emittance, vertical motion is particularly vulnerable to mechanisms that may provide coupling with the other degrees of freedom.

Studies were performed by numerical tracking using the codes SAD and MaryLie/Impact (MLI). Both these codes use a weak-strong approximation in which the space-charge force is calculated as if produced by a 6-D (in phase space) gaussian bunch; this is a reasonable approximation for the bunch distribution in the damping rings toward the end of the damping cycle. During tracking, the space-charge force was applied in the kick approximation, and radiation effects were not included. The nature of the weak-strong approximation means that emittance growth is likely to be overestimated, compared to a self-consistent calculation. However, the main objective in the studies was not to quantify the emittance degradation exactly (which would require

more advanced modeling) but to establish whether there would exist conditions for no growth at all that could be indicated for safe operation of the damping rings.

In presenting the results, we place emphasis on exploration of the tune space and the identification of dangerous resonances. Some calculations were repeated with both codes for reciprocal validation; the agreement in the outcome between the two codes was generally good. Most of the proposed lattices were studied, including some of their variants. For example: in addition to the original "C-shaped" TESLA lattice we also considered an "S-shaped" design with better symmetry properties; for the MCH lattice we took into consideration multiple choices of RF voltage; and for both the MCH and TESLA lattices we also studied the option of using coupling bumps. Not included in the studies were PPA and OTW (on the assumption that space charge should have negligible effects in these relatively small lattices), and DAS (on the basis of its similarities with the other dogbone lattices).

Linear Space-Charge Tune Shifts

Space-charge effects in a storage ring are commonly characterized by the linear tune shift induced by space-charge forces. For a gaussian bunch in an uncoupled lattice, the tune shifts may be written:

$$\Delta\nu_x = -\frac{1}{4\pi}\frac{2r_e}{\beta^2\gamma^3}\int_0^C \frac{\lambda\beta_x}{\sigma_x(\sigma_x+\sigma_y)}ds \tag{3.58}$$

$$\Delta\nu_y = -\frac{1}{4\pi}\frac{2r_e}{\beta^2\gamma^3}\int_0^C \frac{\lambda\beta_y}{\sigma_y(\sigma_x+\sigma_y)}ds \tag{3.59}$$

where β_x, β_y are the horizontal and vertical beta functions, and σ_x, σ_y are the horizontal and vertical beam sizes. The longitudinal peak density $\lambda(s) = N/\sqrt{2\pi}\sigma_z(s)$ is kept under the integral because, for some of the reference lattices, the rms bunch length varies appreciably from one position in the lattice to another. The case where the lattice is linearly coupled is relevant for the dogbone lattices with coupling bumps. The coupling bumps are designed to mitigate the effects of space charge in the vertical plane by enlarging the vertical beam in the long straight sections. A first-order

calculation for the tune shifts in the coupled case yields:

$$\Delta\nu_{\rm I} = -\frac{1}{4\pi}\frac{2r_e}{\beta^2\gamma^3}\int_0^C \lambda\left(\beta_{11}^{\rm I}F_{11} + 2\beta_{13}^{\rm I}F_{12} + \beta_{33}^{\rm I}F_{22}\right)ds \quad (3.60)$$

$$\Delta\nu_{\rm II} = -\frac{1}{4\pi}\frac{2r_e}{\beta^2\gamma^3}\int_0^C \lambda\left(\beta_{11}^{\rm II}F_{11} + 2\beta_{13}^{\rm II}F_{12} + \beta_{33}^{\rm II}F_{22}\right)ds \quad (3.61)$$

where the coupled lattice functions β_{ij}^k are defined by the relationship between the matched rms beam sizes and the normal-mode emittances ϵ_k, $k = {\rm I, II, III}$ [83]:

$$\langle x^2\rangle = \beta_{11}^{\rm I}\epsilon_{\rm I} + \beta_{11}^{\rm II}\epsilon_{\rm II} + \beta_{11}^{\rm III}\epsilon_{\rm III} \quad (3.62)$$

$$\langle xy\rangle = \beta_{12}^{\rm I}\epsilon_{\rm I} + \beta_{12}^{\rm II}\epsilon_{\rm II} + \beta_{12}^{\rm III}\epsilon_{\rm III} \quad (3.63)$$

$$\langle y^2\rangle = \beta_{33}^{\rm I}\epsilon_{\rm I} + \beta_{33}^{\rm II}\epsilon_{\rm II} + \beta_{33}^{\rm III}\epsilon_{\rm III} \quad (3.64)$$

The quantities F_{ij} are the components of the matrix:

$$\mathbf{F} = \frac{1}{(\sigma_\xi + \sigma_\eta)}\mathbf{R}^{-1}(\theta)\begin{pmatrix} 1/\sigma_\xi & 0 \\ 0 & 1/\sigma_\eta \end{pmatrix}\mathbf{R}(\theta) \quad (3.65)$$

where

$$\mathbf{R}(\theta) = \begin{pmatrix} \cos\theta & \sin\theta \\ -\sin\theta & \cos\theta \end{pmatrix} \quad (3.66)$$

σ_ξ and σ_η are the rms bunch sizes along the major and minor semi-axes of the transverse bunch distribution in coordinate space, as shown in Figure 3.59. θ is the tilt angle of the transverse bunch distribution with respect to the horizontal and vertical coordinates of the accelerator.

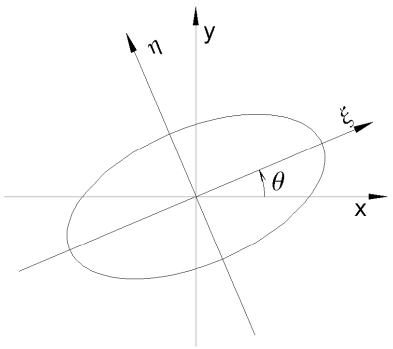

Figure 3.59: Beam transverse isodensity and coordinate frames.

The linear space-charge tune shifts for selected reference lattices are shown in Table 3.35. The space-charge force is highly nonlinear, and we emphasize that the values given in Table 3.35 describe the actual tune shift only for particles with very small amplitude of betatron and synchrotron motion. Most particles in the bunch see significantly smaller tune shifts.

Table 3.35: Linear space-charge tune shifts in selected damping ring reference lattices. In each case, the number of particles per bunch is 2×10^{10} and the vertical emittance is 2 pm. "w/b" indicates "with coupling bumps."

Lattice	circumference [km]	σ_z [mm]	ϵ_x [μm]	$\Delta\nu_x$	$\Delta\nu_y$
PPA	2.8	6.0	0.43	-0.001	-0.021
OCS	6.1	5.8	0.56	-0.002	-0.083
MCH (65 MV)	15.9	7.8	0.68	-0.009	-0.176
MCH (65 MV) w/b	15.9	7.8	0.68	-0.009	-0.038
MCH (115 MV)	15.9	6.9	0.68	-0.010	-0.199
MCH (115 MV) w/b	15.9	6.9	0.68	-0.011	-0.041
TESLA	17.0	6.0	0.50	-0.019	-0.313

Space-Charge Study with SAD

Estimation of space-charge forces requires calculation of the beam envelope at different points along the beamline. As the beam envelope is affected by space charge, SAD performs iterative calculations until convergence. The equilibrium beam envelope $\langle x_i x_j \rangle$, a 6×6 matrix, is the matrix of second-order moments around the beam center. At the entrance of the ring it must satisfy the equilibrium condition:

$$\langle x_i x_j \rangle = M \langle x_i x_j \rangle M^{\mathrm{T}} + r_{ij} \tag{3.67}$$

where M is the 6-D linear transfer matrix around the ring, and r_{ij} is a matrix representing excitation by synchrotron radiation. The matrix M consists of a symplectic part representing the lattice (with space-charge defocusing)and a non-symplectic part representing radiation damping. It is easy to transfer the envelope at the entrance to any location around the ring using the transfer matrix from the entrance to the desired point. As only a linear matrix appears in Equation (3.67), the linear part of the space charge force is taken into account. All nonlinearities are included in the particle tracking performed later, but for the envelope calculation, only the linear part evaluated at the center of the beam is used. The space-charge force is applied at

the entrance of each element as a thin lens. For drift elements, which can be much longer than magnetic elements, accuracy is improved by additionally applying the space-charge force at the center of the drift. The equilibrium emittances are obtained as the eigenvalues of the beam envelope; in the case that the coupling is small, these emittances correspond to horizontal, vertical and longitudinal planes, respectively.

For planar machines such as the ILC damping rings, the mode II (vertical) emittance becomes very small. To obtain a realistic value of the vertical emittance, one method is to add machine errors to selected components in the ring; for example, one can add vertical offsets to the sextupoles. The envelope method can then be used to calculate the effect of space charge on the equilibrium vertical emittance. Figure 3.60 shows the vertical emittance resulting from random vertical misalignments of the sextupoles in the TESLA damping ring, with and without space charge. In this case, space charge increases the equilibrium vertical emittance by approximately 50%.

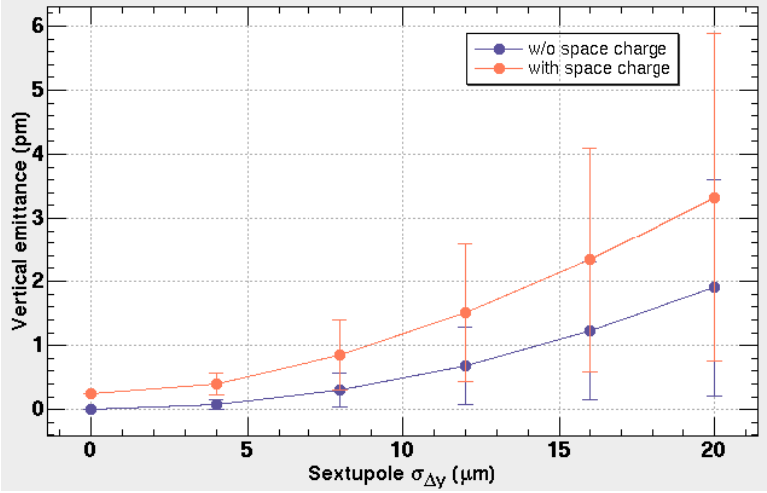

Figure 3.60: Equilibrium vertical emittances with (orange) and without (blue) space charge, as functions of the random vertical misalignments of the sextupoles in the TESLA damping ring, including the coupling bumps in the long straights. Twelve seeds for the random misalignments are used for each value of rms misalignment. Space-charge forces increase the vertical emittance by approximately 50%. With space charge, the emittance with zero sextupole misalignment is non-zero because the coupling bumps are no longer closed. The number of particles per bunch is 2×10^{10}.

As an alternative to misaligning the sextupoles, one can generate vertical emittance by giving an artificial value to the envelope at the entrance of the ring. This is equivalent to an artificial radiation excitation r_{ij}. The resulting beam envelope still matches the beam optics around the ring, except for the radiation in mode II, but the mismatch in this case is small unless the radiation damping is very large. Using random sextupole misalignments to generate vertical emittance has the drawback that the vertical emittance depends on the seed of the random errors, so for the studies described here, the vertical emittance was generated by using an artificially-excited beam envelope.

With an ultra-relativistic beam, the space-charge forces can be treated as lying in a plane perpendicular to the beam axis. For a gaussian beam, the space-charge potential may be written:

$$U(x,y,z) = f(\xi,\eta)\exp\left(-\frac{z^2}{2\sigma_z^2}\right) \tag{3.68}$$

where f is the 2-D electrostatic potential in the transverse plane. f is a function of ξ/σ_ξ, η/σ_η and the aspect ratio $R = \sigma_\eta/\sigma_\xi$, where ξ and η are respectively the major and minor axes of the transverse beam ellipse (see Figure 3.59). To reduce calculation time, SAD first calculates $f(\xi,\eta)$ at $60 \times 60 \times 20$ mesh points within the range $0 \le \xi/\sigma_\xi \le 15$, $0 \le \eta/\sigma_\eta \le 15$, $10^{-5} \le R \le 1$ using semi-analytical numerical integration. The mesh points are linearly separated in the (ξ,η) plane, and logarithmically separated in the R direction. During tracking, the force is obtained from values on the mesh using cubic spline interpolation. For particles outside of the mesh region, the original semi-analytical formula is applied.

A phenomenon typically observed in the tracking simulations is a diffusion-like emittance growth. Figure 3.61 shows an example of this effect for the mode I (horizontal) and mode II (vertical) emittances. Note that no emittance growth was observed with space charge turned off. The simulations used 100 particles in the tracking; it was confirmed that no significant change in the results was obtained if the number of tracked particles was increased to 400. It should also be noted that in the tracking, the strong beam was kept unchanged. This will likely give an overestimate of the emittance growth from space charge.

Where an effect causes the emittance to grow linearly with time in the absence of radiation damping, the equilibrium emittance that can be expected when radiation damping is present may be estimated from:

$$\epsilon = \epsilon_0 + \frac{n_d}{2}\frac{\Delta\epsilon}{\Delta n} \tag{3.69}$$

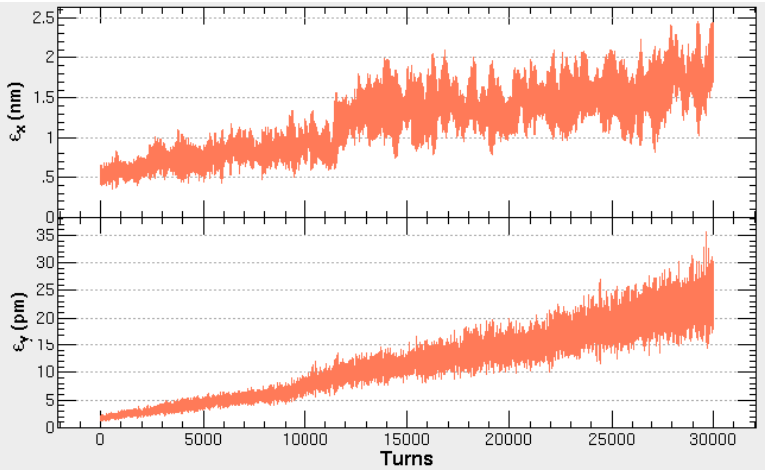

Figure 3.61: Emittance growth observed in a tracking simulation with space charge for the TESLA damping ring with coupling bumps. Both the horizontal (top) and vertical (bottom) emittances grow approximately linearly with time. 100 particles were tracked in the simulation. Synchrotron radiation was turned off. The number of particles per bunch was $2{\times}10^{10}$.

where ϵ_0 is the equilibrium without space charge and n_d is the radiation damping time (in turns) respectively. Since tracking with radiation is time-consuming, we use Equation (3.69) to estimate the equilibrium emittance while performing tune scans to study the dependence of space-charge emittance growth on the working point in tune space.

Tune scans were performed for various damping rings reference lattices. In each case, changes in tune were achieved by inserting quadrupoles into the lattices and varying their strengths, while matching the appropriate optical functions. The equilibrium emittances were obtained from Equation (3.69), with the linear growth rate $\Delta\epsilon/\Delta n$ obtained by tracking up to 400 turns without radiation. Figures 3.62 and 3.63 show the results for the TESLA "S-shaped" damping ring lattice. Note that the coupling bumps were adjusted to produce a properly round beam in the straights. The MCH lattice was studied with two different RF voltages, 54 MV and 115 MV, corresponding to bunch lengths of (approximately) 10 mm and 7 mm; the results are shown in Figures 3.64–3.67. In each simulation, 100 particles were tracked, with radiation turned off. The total number of particles per bunch was 2×10^{10}.

In general, although there are areas associated with resonance lines where significant emittance growths are observed, there are also substantial areas of tune space where there is minimal emittance growth. The coupling bumps do not necessarily improve the situation, and can themselves drive resonances. This may be more serious for the MCH lattice with 115 MV RF, which has a larger synchrotron tune than the other lattices, reducing the "safe" areas. Also, the MCH lattice shows stronger horizontal resonances than the "S-shaped" TESLA lattice, with or without the coupling bumps.

Results for the 6 km lattices are shown in Figures 3.68 (OCS) and 3.69 (BRU). The OCS looks the safest of all the reference lattices from point of view of space charge; however the BRU lattice looks worse even than the dogbone lattices. Note that the energy of the BRU lattice, 3.74 GeV, is somewhat lower than the other lattices, which are all around 5 GeV.

Space-Charge Study with MaryLie/Impact

MaryLie/Impact (MLI) is a hybrid code combining MaryLie routines for lattice design, map calculation and tracking, with routines from Impact for space-charge calculations. MLI is capable of fully self-consistent space-charge simulations; however, such simulations are too lengthy for studies of a range of conditions in the large damping ring lattices, and, we believe, are not necessary. Instead, additional routines have been developed for modeling space charge in the weak-strong approximation, where the space-

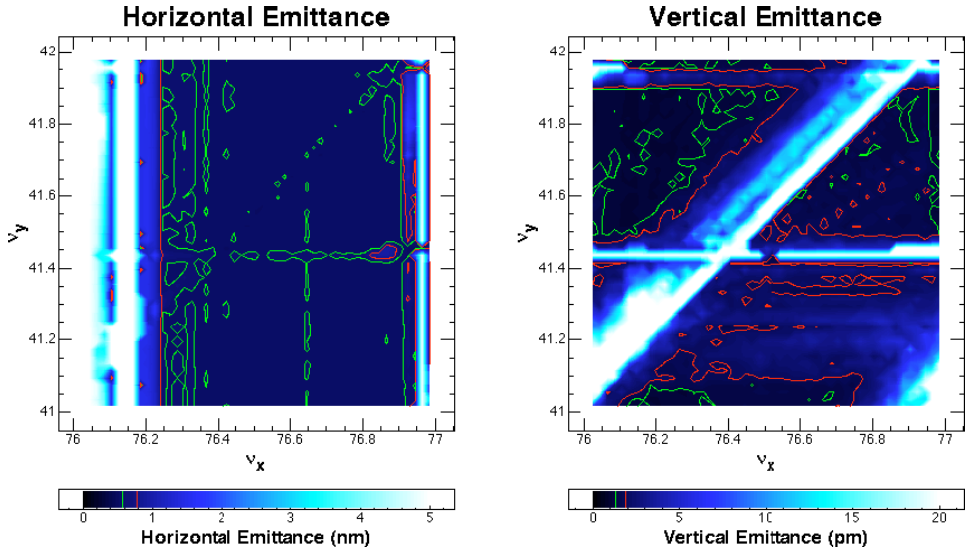

Figure 3.62: Tune scan of emittance growth from space charge in the TESLA damping ring lattice without coupling bumps.

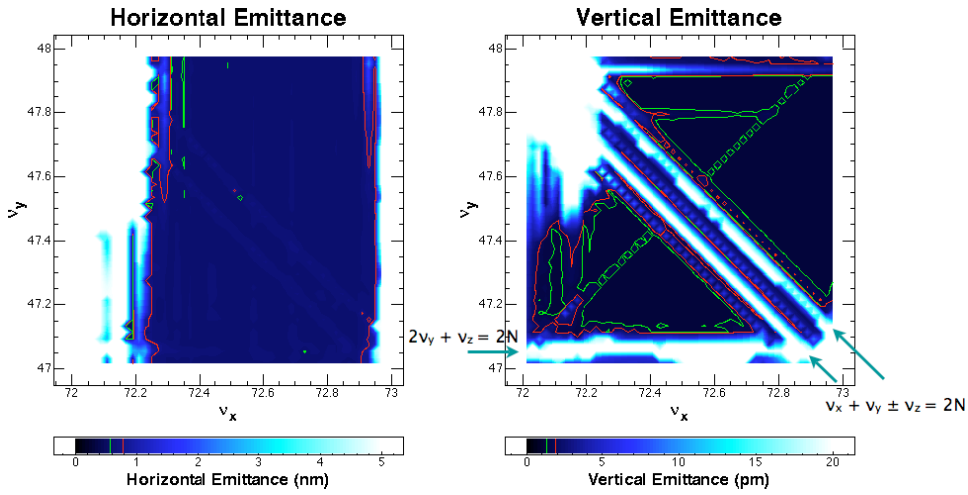

Figure 3.63: Tune scan of emittance growth from space charge in the TESLA damping ring lattice with coupling bumps.

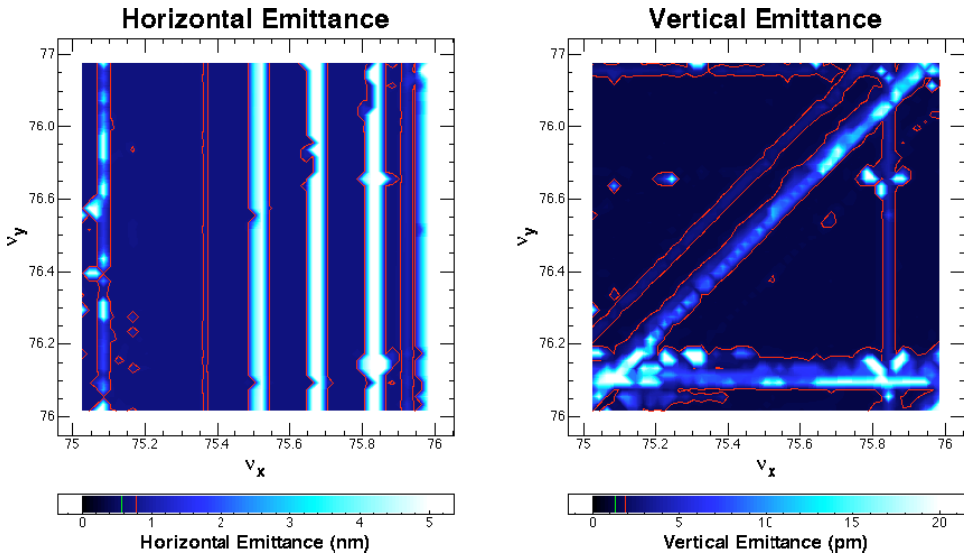

Figure 3.64: Tune scan of emittance growth from space charge in the MCH damping ring lattice (54 MV RF) without coupling bumps.

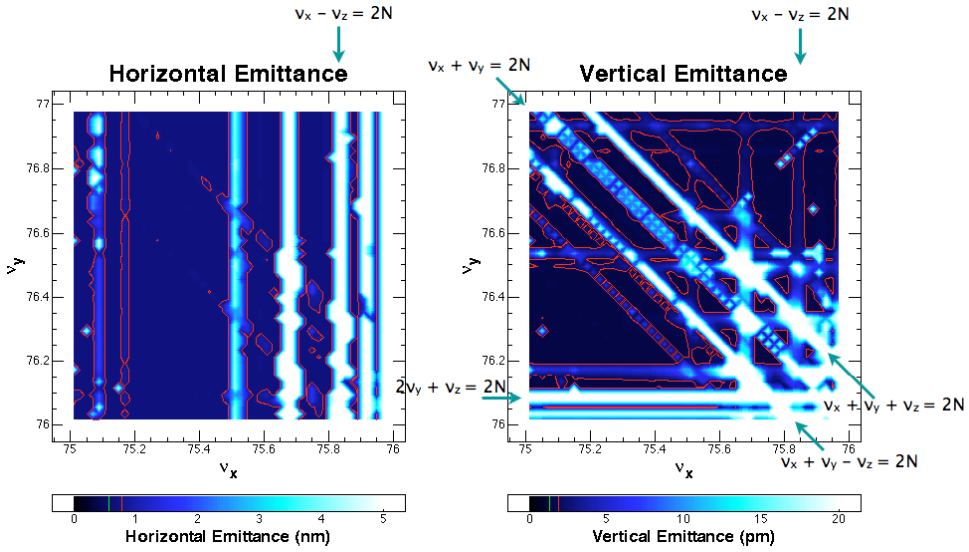

Figure 3.65: Tune scan of emittance growth from space charge in the MCH damping ring lattice (54 MV RF) with coupling bumps.

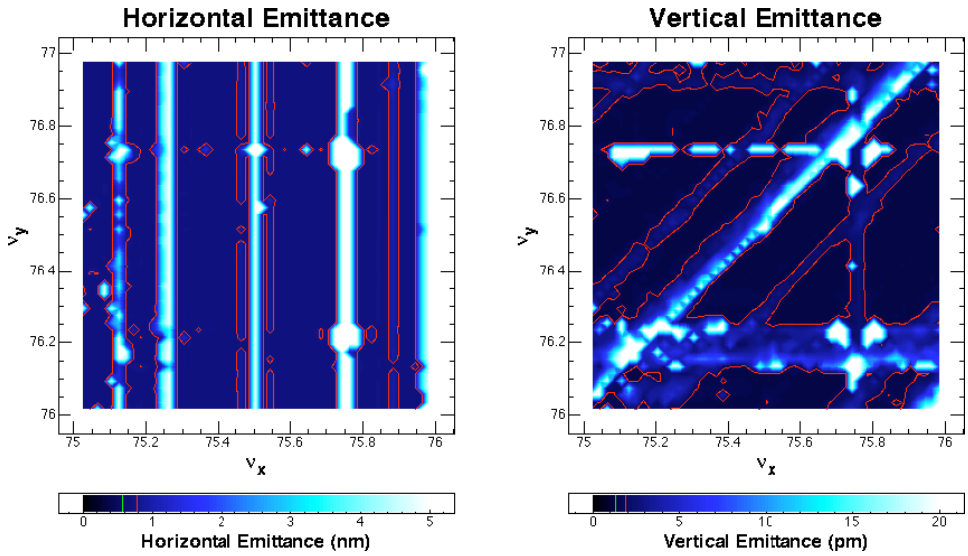

Figure 3.66: Tune scan of emittance growth from space charge in the MCH damping ring lattice (115 MV RF) without coupling bumps.

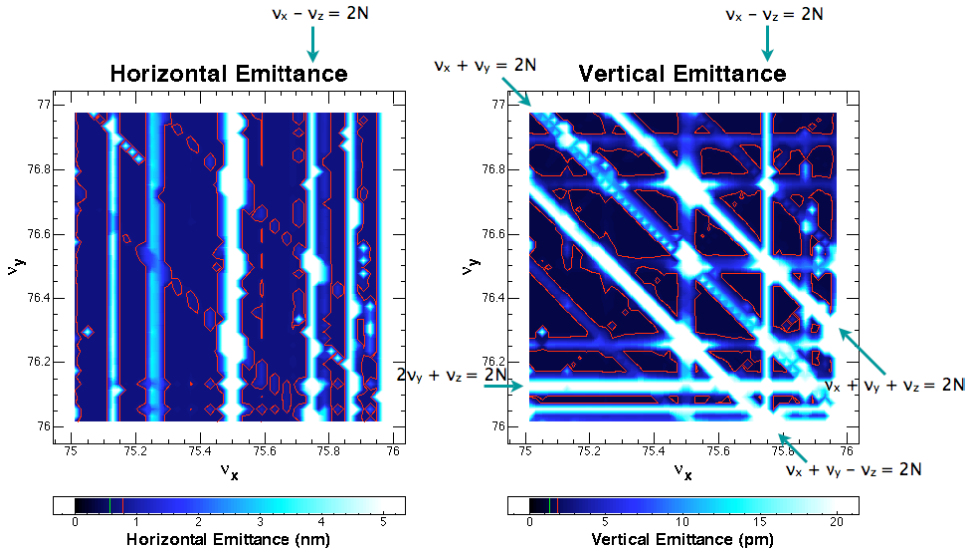

Figure 3.67: Tune scan of emittance growth from space charge in the MCH damping ring lattice (115 MV RF) with coupling bumps.

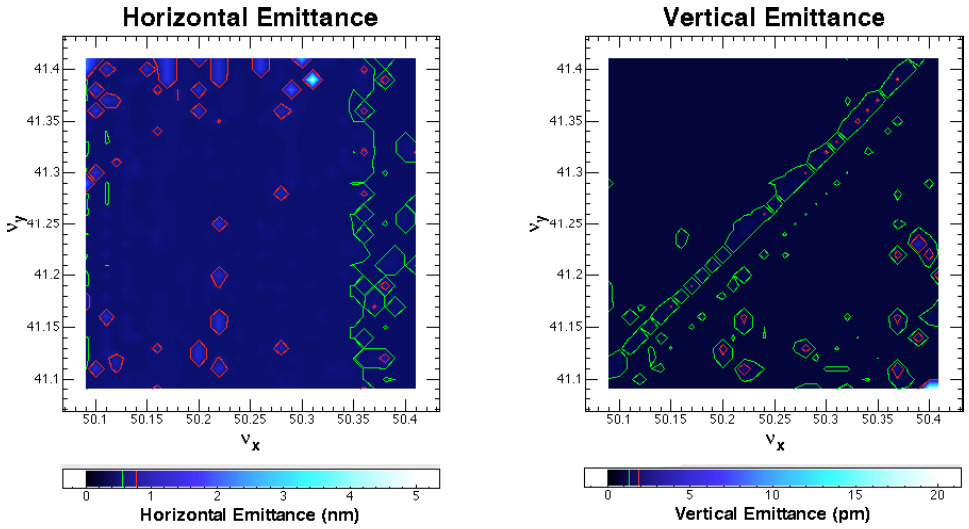

Figure 3.68: Tune scan of emittance growth from space charge in the OCS damping ring lattice.

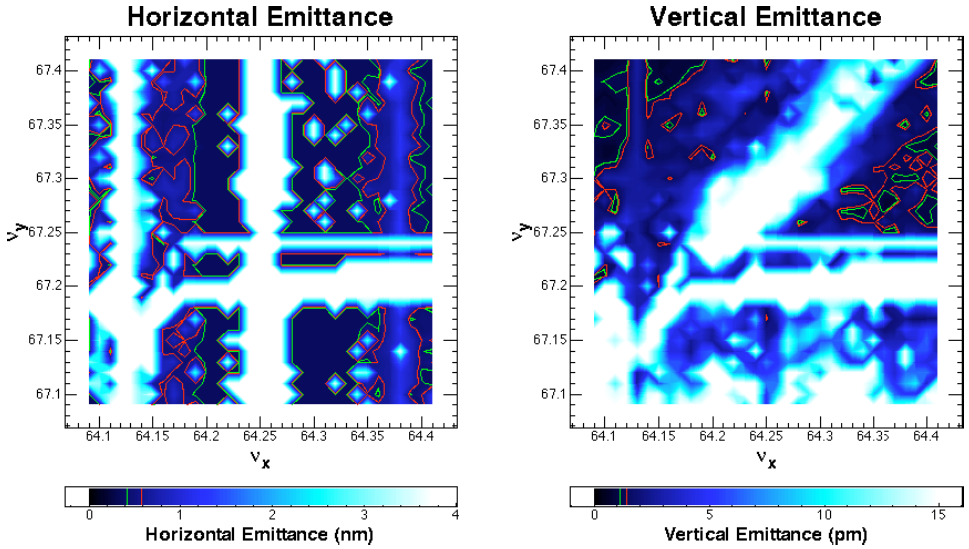

Figure 3.69: Tune scan of emittance growth from space charge in the BRU damping ring lattice.

charge forces are calculated as if produced by an unperturbed 6-D gaussian bunch matched to the linear lattice.

For tracking in MLI, the lattice elements (including drifts) are split into a number of slices, and space-charge forces are applied at the center, in a kick approximation. Particle propagation between space-charge kicks is carried out using symplectic tracking. In these studies, radiation effects were not included, and simulations were limited to the end of the damping cycle where beam sizes are the smallest and space-charge forces are at their largest. The approximation (valid for ultra-relativistic beams) was also made that the space-charge forces are perpendicular to the beam trajectory.

We develop the model of space charge used in MLI for the present studies as follows. First, we allow the ellipses representing isodensities of the transverse charge distribution to be tilted with respect to the accelerator x and y axes (see Figure 3.59). We use ξ and η to denote the coordinates along the principal axes of the isodensity ellipses, and π_ξ and π_η the canonically conjugate momenta to those coordinates. In the complex number notation $\pi = \pi_\xi + i\pi_\eta$, the evolution of the momenta of a particle in the sole presence of space-charge forces can be written:

$$\frac{d\pi}{ds} = F \tag{3.70}$$

The force F is given by:

$$F = 2\sqrt{\pi}\frac{r_e}{\gamma^3}\frac{n(z)}{S}\left[w\left(\frac{\xi+i\eta}{S}\right)e^{-\frac{\xi^2}{2\sigma_\xi^2}-\frac{\eta^2}{2\sigma_\eta^2}} + w\left(\frac{\xi\frac{\sigma_\eta}{\sigma_\xi}+i\eta\frac{\sigma_\xi}{\sigma_\eta}}{S}\right)\right] \tag{3.71}$$

where $S = \sqrt{2(\sigma_\xi^2 - \sigma_\eta^2)}$, σ_ξ and σ_η are the rms bunch sizes in the ξ and η directions, r_e is the classical radius of the electron, γ is the relativistic factor, $w(z)$ is the error function of complex argument, and $n(z)$ is the longitudinal bunch density. For a gaussian bunch, $n(z) = \exp(-z^2/2\sigma_z^2)/\sqrt{2\pi}\sigma_z$. Numerical evaluation of Equation (3.71) in MLI uses a Padé approximant representation of the error function of complex argument $w(z)$ implemented in a routine based on work by Talman [39]. Numerical tests were carried out to check the accuracy of this approximation against evaluation using *Mathematica* [80] built-in functions, which are believed to be accurate through machine precision. Relative deviations of order 10^{-6} or better were found at points in the beam core, and 10^{-3} outside the core (where the strength of the kick is considerably smaller).

Having found the space-charge force in the $\xi - \eta$ plane, it is just a matter of carrying out a rotation to recover the equations of motion in the $x - y$

plane. We have:

$$\begin{pmatrix} f_x(x,y) \\ f_y(x,y) \end{pmatrix} = \mathbf{R}^{-1}(\theta) \begin{pmatrix} \mathrm{Re}\, F(\xi,\eta) \\ \mathrm{Im}\, F(\xi,\eta) \end{pmatrix} \tag{3.72}$$

with $\xi = x\cos\theta + y\sin\theta$ and $\eta = -x\sin\theta + y\cos\theta$, and

$$\mathbf{R}(\theta) = \begin{pmatrix} \cos\theta & \sin\theta \\ -\sin\theta & \cos\theta \end{pmatrix} \tag{3.73}$$

In the kick approximation, the space-charge force is applied as an impulse, leaving the transverse coordinates of a particle unchanged while inducing momentum changes $\Delta p_x = Lf_x$ and $\Delta p_y = Lf_y$, where L is the length of the lattice element slice over which the space-charge force applies. At each location where the space-charge kick is applied, we need to know the longitudinal position z of a particle with respect to the bunch center, the rms transverse bunch sizes σ_ξ and σ_η, the rms bunch length σ_z and the tilt angle θ. Note that σ_ξ, σ_η and σ_z are obtained from the eigenvalues of the "reduced" sigma matrix, $\mathbf{\Sigma}_{red}$, where

$$\mathbf{\Sigma}_{red} = \begin{pmatrix} \langle x^2\rangle & \langle xy\rangle & \langle xz\rangle \\ \langle xy\rangle & \langle y^2\rangle & \langle yz\rangle \\ \langle xz\rangle & \langle yz\rangle & \langle z^2\rangle \end{pmatrix} \tag{3.74}$$

The tilt angle θ is obtained from the eigenvectors of $\mathbf{\Sigma}_{red}$.

The space-charge routines in MLI were tested by calculating the space-charge tune shift for particles with very small betatron and synchrotron amplitudes, and comparing with the predictions of the linear theory given in Table 3.35. Excellent agreement was found.

To estimate the impact of space-charge effects in the damping ring reference lattices, we performed tune scans, calculating the horizontal and vertical emittance growths over a range of working points in tune space. Tune adjustments for each lattice were performed by inserting pure phase rotations, with proper matching so as not to perturb the lattice functions. For each working point, a distribution of 200 particles was tracked for 150 turns (400 in the case of OCS), and the normal-mode emittances ϵ_{I} and ϵ_{II} were calculated after each turn. The color-density plots in Figures 3.70–3.76 show the maximum values of the normal-mode emittances achieved during the course of the tracking for various lattices under different conditions. The tunes specifying each working point correspond to the unperturbed (i.e. zero space charge) case; the black dots indicate the design working points.

Figure 3.70 shows the results of tune scans for the MCH lattice with 65 MV RF voltage, corresponding to a synchrotron tune $\nu_s = 0.19$. The horizontal emittance is not affected by space-charge forces, and we show only the result for the zero-charge case. In the region explored, there was no horizontal emittance growth outside two well-defined synchro-betatron resonances at $\nu_x + 2\nu_s = n$ and $\nu_x + \nu_s = n$. Vertically, there is no apparent growth in the absence of space charge, whereas some growth is apparent at $N = 2\times10^{10}$ and $N = 4\times10^{10}$ along difference coupling resonances and their synchrotron-tune satellites. The form of the main resonance[2], $2\nu_y - 2\nu_x = 2n$, suggests that this is a fourth-order resonance induced by the space-charge nonlinearities, i.e. a term x^2y in the equation of motion for vertical oscillations, arising from a Taylor expansion of Equation (3.71). Indeed, one can construct a simple, first-order dynamical model and verify that the strength of this term integrated over the lattice would be sufficient to cause a significant growth within a few turns [76]. Notice that, as expected, the width of the resonance lies above the $\nu_y = \nu_x + n$ line because the tune depression causes particles to meet the resonance condition when the bare tune $\nu_y > \nu_x + n$. The width of the resonance is a measure of the tune shift and is clearly larger for higher bunch charge (compare the two bottom pictures in Figure 3.70). The satellite resonances $2\nu_y - 2\nu_x \pm 2m\nu_s = 2n$, observed at $2\nu_s$ above and below the coupling resonance are caused by the modulation of the space-charge force resulting from synchrotron oscillations. This modulation occurs with a frequency $2\nu_s$ as the longitudinal charge density depends quadratically on the londitudinal displacement z.

In the presence of lattice errors, one may expect further degradation of the vertical emittance. In particular, lowest-order errors that drive coupling with the horizontal motion have the potential to cause significant increase in the vertical emittance. In this study, we considered the impact of randomly-distributed skew-quadrupole like errors that may result, for example, from vertical offsets of the chromatic sextupoles. Specifically, we considered a zero-average gaussian distribution of the offsets with a standard deviation σ_{sxt} comparable to that which would be required to generate an equilibrium vertical emittance of 2 pm if radiation effects were included. For the MCH lattice, the appropriate value is $\sigma_{sxt} = 60$ μm. Even without space charge, these errors excite harmful resonances. In addition to the strengthening of the difference resonances, some synchro-betatron resonances also appear. Presence of space charge makes things worse in two ways: space-charge detuning causes the resonance widths to increase, and the space-charge forces

[2]Note that this lattice has periodicity two, and so only even harmonics are allowed.

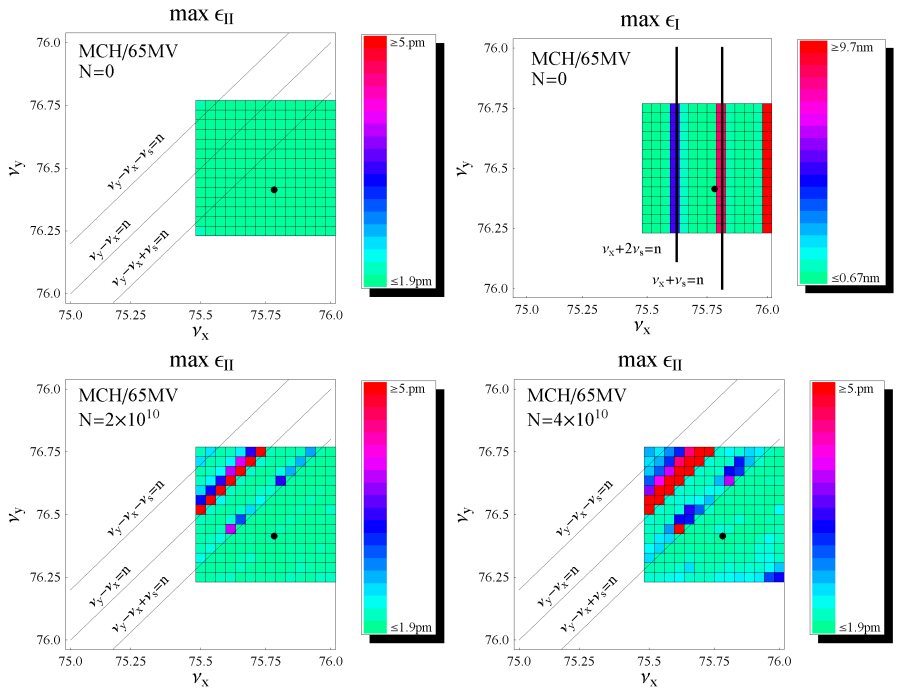

Figure 3.70: Tune scan of emittance growth in the MCH damping ring lattice (65 MV RF) with space charge, but without coupling bumps.

cause decoherence of the large-amplitude betatron oscillations that arise from the lattice resonances. The net effect can be observed in Figure 3.71 where, in addition to the difference resonance lines already encountered in Figure 3.70, we observe sizeable vertical emittance growth at $\nu_y = \nu_s + n$ and $\nu_y = 2\nu_s + n$.

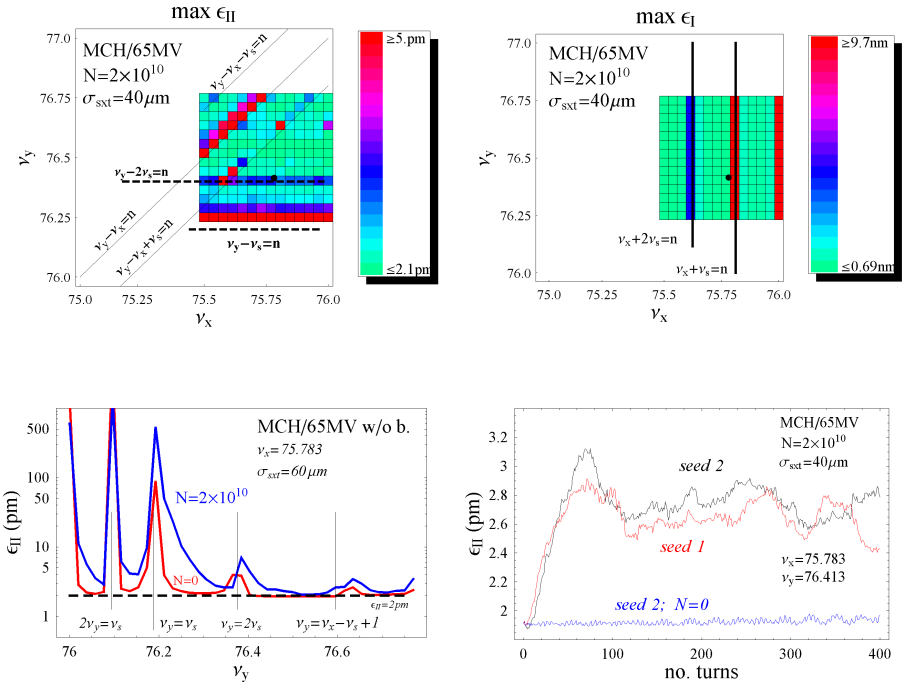

Figure 3.71: Space-charge emittance growth in the MCH damping ring lattice (65 MV RF) without coupling bumps, with 40 μm rms sextupole vertical misalignments. The top plots show the results of the 2-D tune scan. The bottom left-hand plot shows the results of a 1-D (vertical) tune scan: the maximum vertical emittance over 400 turns is plotted without space charge (red line) and with space charge (blue line). The bottom right-hand plot shows the time evolution of the vertical emittance at the design working point for two different seeds of random skew-quadrupole errors with space charge (red and black lines) and for one seed without space charge (blue line).

Also in Figure 3.71, the presence of resonances is highlighted by a 1-D

scan of the tune plane in which we vary the vertical tune while keeping the horizontal tune fixed at its design value ($\nu_x = 75.783$). In the left-hand plot, the two curves represent the maximum emittance achieved within 150 turns without space charge (red curve) and with $N = 2 \times 10^{10}$ particles per bunch (blue curve). We should remark that the strong integer resonance at $\nu_y = 76$ and the second-order resonance $2\nu_y = \nu_s + 76$ are already present in an error-free lattice without space charge. The picture at the bottom-right of Figure 3.71 shows the time evolution of the emittance for two seeds used in the random generation of the lattice errors. For comparison, the result for a run with no space charge (but with random lattice errors) is also shown (blue curve). The working point $\nu_y = 76.413$ is $\nu_y - 2\nu_s - 76 = 0.037$ away from the $2\nu_s$ resonance. In the absence of space charge this is sufficiently far that there is no impact on the emittance, but when space charge is included, the resonance width is increased and vertical emittance growth is observed.

The use of coupling bumps at each end of the long straight sections in the dogbone lattices has been proposed as a way to mitigate the effects of space charge [18]. The coupling bumps consist of a pair of skew-quadrupole triplets, and reduce the tune shifts by enlarging the vertical beam size between the pair. If the bump is properly closed, it does not contribute to any global coupling in the ring. The linear theory (see Table 3.35) suggests that coupling bumps may be quite effective at reducing space-charge tune shifts. Unfortunately, coupling bumps also appear to excite a number of resonances that reduce the usable regions of tune space; see Figure 3.72.

One effect of the coupling bumps is to cause vertical emittance growth at resonances that, without the coupling bumps, are visible only in the horizontal plane. There are also some additional (sum) resonances that are absent without the bumps. All these resonances are manifest even before adding space charge. In fact, from these tracking simulations, the only visible effect of space charge is the additional excitation of the sum resonance $\nu_x + \nu_y = n$ (left picture in the middle row of Figure 3.72). There do remain patches of tune space unaffected by resonances and which, presumably, could accommodate bunches with a number of particles larger than $N = 2 \times 10^{10}$. However, these patches are further reduced when a distribution of random skew-quadrupole errors is superposed onto the ideal lattices (bottom left picture in Figure 3.72); and they do not enclose the currently proposed working point.

Not surprisingly, a larger RF voltage (see Figure 3.73) shows the same patterns of vertical emittance growth as for the MCH lattice with 65 MV RF voltage. The synchro-betatron resonances are shifted in accordance with a larger synchrotron tune ($\nu_s = 0.25$ versus $\nu_s = 0.19$ in the 65 MV case)

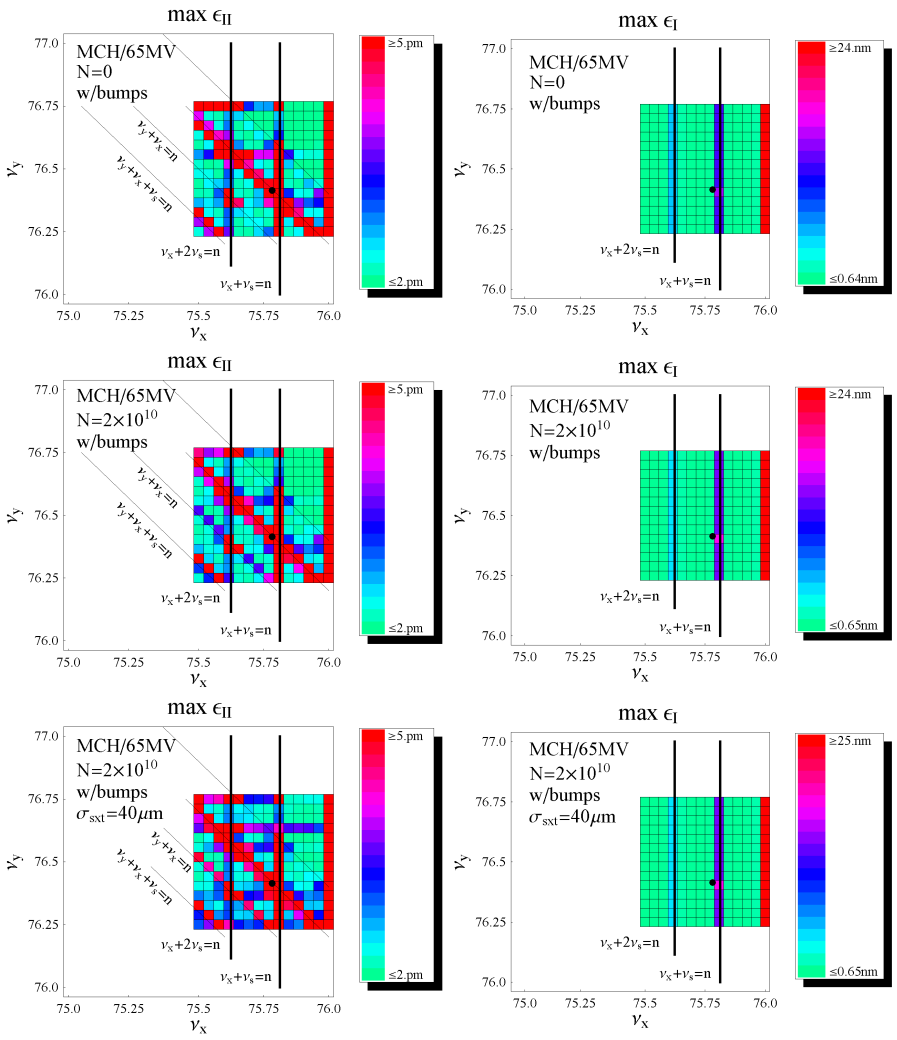

Figure 3.72: Tune scan of emittance growth in the MCH damping ring lattice (65 MV RF) with space charge and coupling bumps. Top: zero bunch charge. Middle: 2×10^{10} particles per bunch. Bottom: 2×10^{10} particles per bunch, and 40 μm rms sextupole vertical misalignments.

and their effect is slightly enhanced because of the large longitudinal beam density resulting from a shorter bunch length.

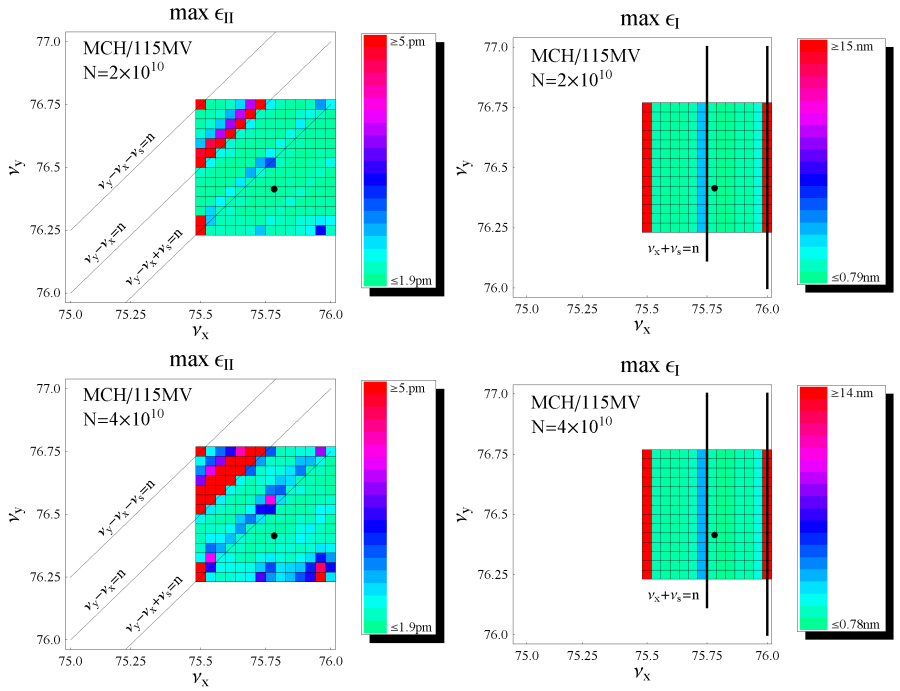

Figure 3.73: Tune scan of emittance growth in the MCH damping ring lattice (115 MV RF) with space charge, but without coupling bumps. Top: 2×10^{10} particles per bunch. Bottom: 4×10^{10} particles per bunch.

The results of tune scans for the TESLA damping ring lattice are shown in Figure 3.74. Again, without space charge (not shown) there is no noticeable emittance growth, whereas some growth is apparent when space charge is present. In the absence of lattice errors (top left picture) the growth takes place along difference resonances. Compared with the MCH case, these resonances appear wider, partly because of the proximity of the satellite resonances $\nu_y - \nu_x \pm \nu_s = n/2$ –note that the synchrotron tune is smaller in this case ($\nu_s = 0.075$). Also, the difference resonances are more closely spaced since the TESLA lattice does not share the super-periodicity two of the MCH lattice. (Note that the results shown in Figure 3.74 are for the "C-shaped" lattice contained in the original TESLA TDR proposal. An

"S-shaped" variant of this lattice exhibiting a higher degree of symmetry was studied in simulations with SAD, and displays better dynamical properties.) The tune scan in the presence of lattice errors is dominated by the strong $\nu_y = \nu_s + n$ resonance. The random vertical displacement of the sextupoles here had a standard deviation of $\sigma_{sxt} = 6$ μm, close to the 8 μm value that would be expected to generate a vertical emittance of 2 pm in the presence of radiation.

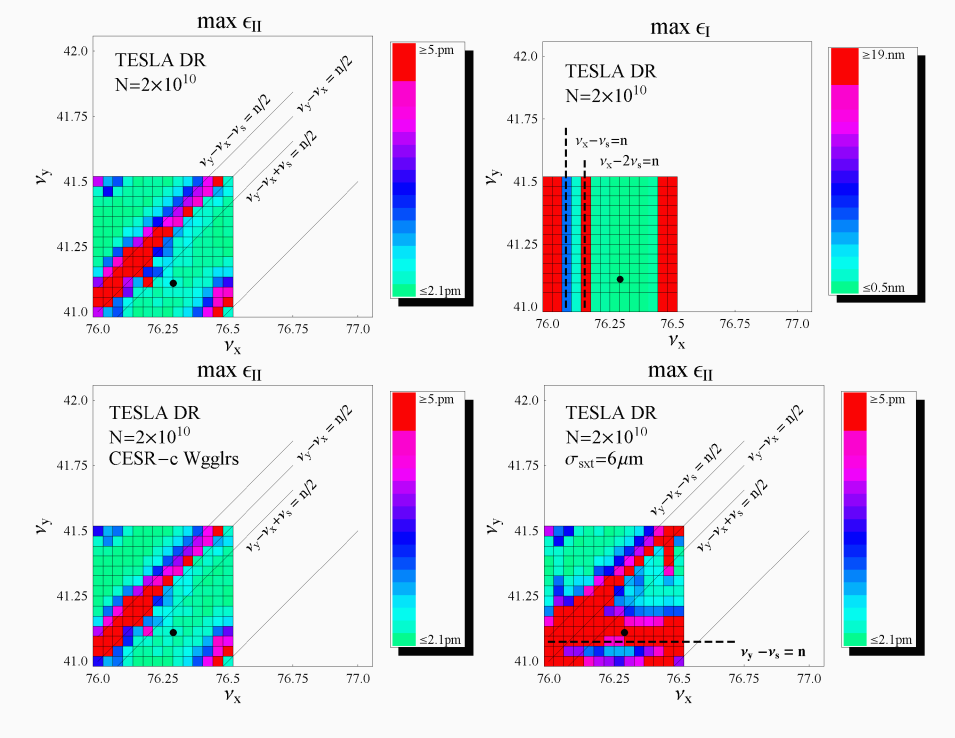

Figure 3.74: Tune scan of emittance growth in the TESLA "C-shaped" damping ring lattice with space charge, without coupling bumps. Top: linear wiggler model, no sextupole misalignments. Bottom left: CESR-c nonlinear wiggler model, no sextupole misalignments. Bottom right: CESR-c nonlinear wiggler model, 6 μm rms sextupole vertical misalignments.

In the bottom left picture of Figure 3.74 we show the results from a simulation performed using a realistic nonlinear model for the wiggler, based on a scaled-down version of the CESR-c wigglers. By contrast, in all the other space-charge simulations in this report, the wigglers were modeled

as a sequence of "linear" elements (dipoles and drift spaces). Comparison between the two cases shows virtually no difference, and would seem to indicate that there will be little impact on vertical emittance growth from the wiggler nonlinearities.

Finally, we report results of tune scans for the smaller circumference (6 km) OCS lattice. The tune shift calculated from the linear theory is small in this case, so we expect that space charge will have a smaller impact than in the 17 km lattices: indeed, Figure 3.75 shows no apparent effects from space charge. The tune shift, however, is not completely negligible; for instance, it is larger than in the dogbones with coupling bumps, where some effects from space charge were still noticeable. It is likely that the good behavior of the OCS lattice is due, in part, to its high degree of symmetry. Inclusion of lattice errors shows some impact on emittance growth (Figure 3.76) but most of the region explored in tune space remains clear.

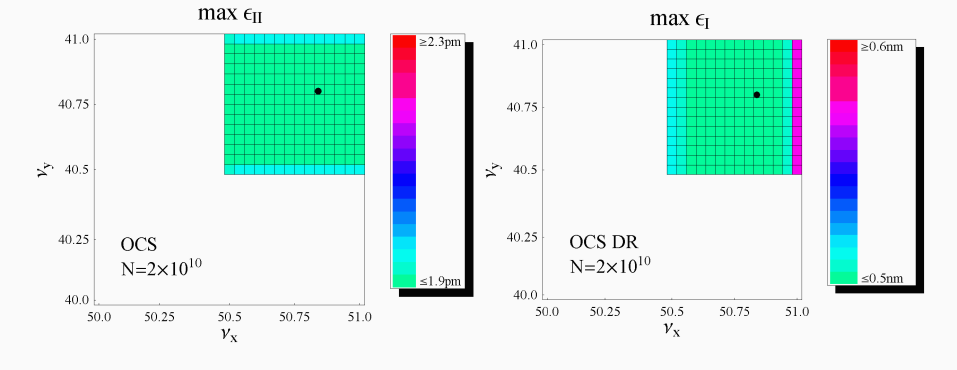

Figure 3.75: Tune scan of emittance growth in the OCS damping ring lattice with space charge.

Conclusions

Our studies show that space-charge effects are noticeable in the 16 - 17 km reference lattices, and may also be seen in one of the 6 km lattices.

- The 6 km OCS lattice stands out as the safest choice among the lattice considered. The shorter circumference is a factor accounting for the mild impact of space charge compared to the dogbone lattices, but apparently not the only one. The BRU lattice has similar circumference (and somewhat lower energy) but behaves poorly. The high degree

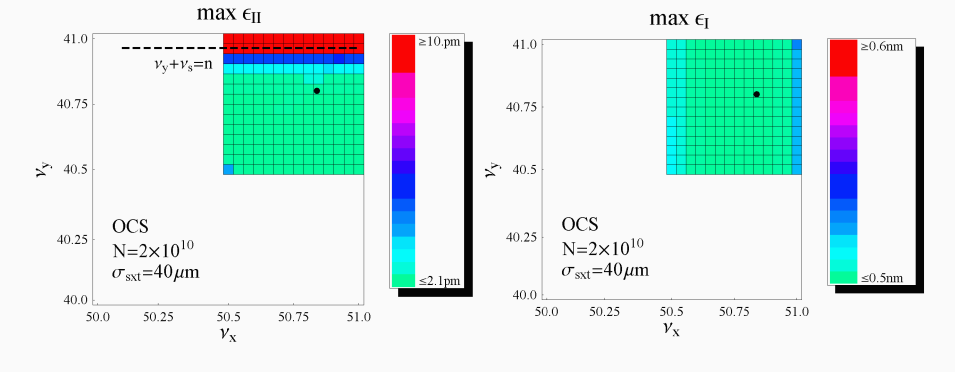

Figure 3.76: Tune scan of emittance growth in the OCS damping ring lattice with space charge and 40 μm rms sextupole vertical misalignments.

of symmetry of the OCS lattice does seem to play a decisive role in mitigating harmful resonances.

- The 16–17 km dogbone lattices are clearly more vulnerable to space charge and are at higher risk; but, on paper, they may not be impossible to operate. There are areas of tune space far enough from dangerous resonances whether or not errors are included. The presence of these resonances, however, limits the flexibility in the choice of working point and there may be conflicts with other requirements. We should add that some dogbone lattices are preferable to others: for example, the "S-shaped" TESLA lattice is superior to the "C-shaped" lattice because of the higher symmetry.

- The MCH lattice has a large synchrotron tune that causes resonance lines to be more dispersed in tune space. This may be more limiting to the choice of the working point.

- In general, it appears that the coupling bumps do not offer a decisive advantage, because of the resonances they can excite. Their effectiveness depends on the lattice. For the "S-shaped" TESLA lattice, the coupling bumps can restore some flexibility in the choice of working point, as the locations of harmful resonances with and without the bumps are quite different. It may be argued that in this case, the coupling bumps overall make a larger area of tune space accessible. However, for MCH it is not obvious that the coupling bumps are help-

ful, since the resonances excited by the bumps are more widely spread than the resonances without the bumps.

- We have not carried out a detailed study of the smaller (3 km) lattices, though we expect that space charge should not be an issue for these configurations.

3.4.7 Electron-Cloud Effects

Under certain conditions, electrons can accumulate to high density in the vacuum chamber of a positron storage ring, where they cause a variety of beam instabilities including single-bunch and coupled-bunch instabilities. Electron-cloud effects have been a limitation on the performance of the B-Factories, requiring installation of solenoids to suppress the build-up of the cloud [23, 44], and are expected to be a significant issue in the ILC positron damping ring. The build-up of electron cloud is dependent on the bunch charge and bunch spacing, and on the vacuum chamber geometry and surface properties. Primary electrons are generated by photoemission or gas ionization, and are accelerated in the beam potential, eventually striking the wall to release secondaries. An electron cloud develops if the beam conditions and chamber properties are such as to generate secondaries at a high rate. The larger bunch spacing in the longer damping rings may help to mitigate the build-up of the cloud by reducing the production rate; similarly, coating the chamber with a material (such as titanium nitride) that has a low secondary electron yield may also reduce the cloud density. For a complete evaluation, both the build-up of the electron cloud and the effects of the cloud on the beam must be evaluated. Here, we report the results of simulations of cloud build-up in the positron damping ring reference lattices, and give estimates of the cloud density at which instabilities are expected to occur.

Electron Cloud Build-Up

We first consider the build-up of electron cloud in different sections of the damping ring. We consider separately the field-free (long straight and arc drift) regions, and the dipoles, quadrupoles, sextupoles and wigglers. Figure 3.77 shows an example of simulations using the code POSINST [24]: the cloud density in an OCS dipole (averaged over a region within 1 mm of the beam) is shown as a function of bunch number, for peak secondary electron yield (SEY) of the chamber surface of 1.2 and 1.4. We see that reducing

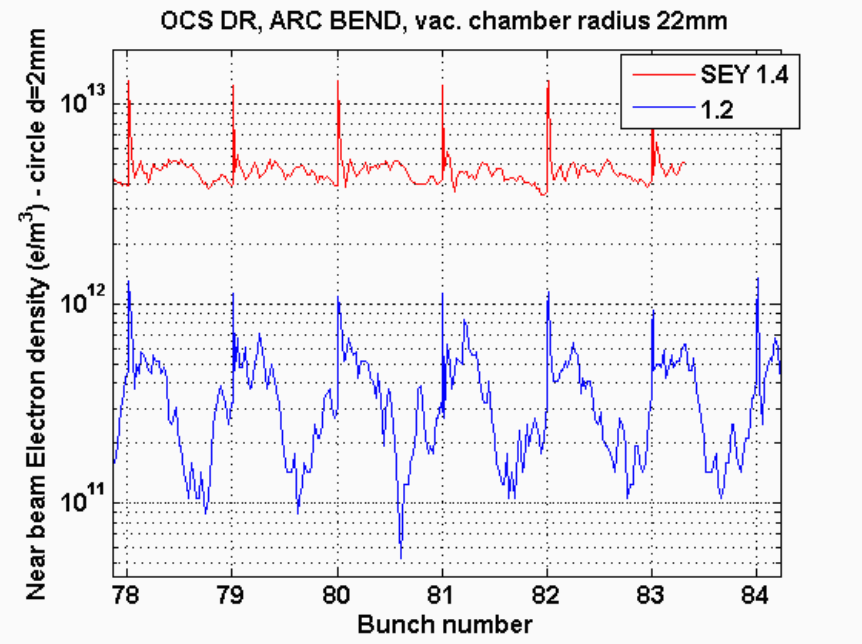

Figure 3.77: Electron-cloud density in a dipole in OCS, with circular vacuum chamber of radius 22 mm, and SEY 1.4 (upper curve) and 1.2 (lower curve). The density is averaged over a circular cross-section of radius 1 mm, centered on the beam. The density is shown during the passage of bunches numbered 78 to 84 in a train.

the peak SEY from 1.4 to 1.2 can reduce the electron-cloud density near the beam by more than an order of magnitude.

Further examples, this time of the cloud density in the OCS wiggler, are shown in Figures 3.78 and 3.79. In Figure 3.78, the cloud density is shown averaged over the full cross-section of the vacuum chamber; the density near the beam, shown for SEY 1.2 in Figure 3.79, peaks at a value that is larger by an order of magnitude.

Table 3.36 shows the results of simulations of electron cloud build-up in the positron damping rings, assuming a peak SEY of the chamber surface of 1.2. The value shown for the density is the value reached after a number of bunch passages, averaged across a circular region of radius 1 mm centered on the beam. The chamber is assumed to have a circular cross-section, with diameter depending on the region of the machine, as shown in Table 3.37. The bunch spacing used in the simulations is the nominal spacing for each

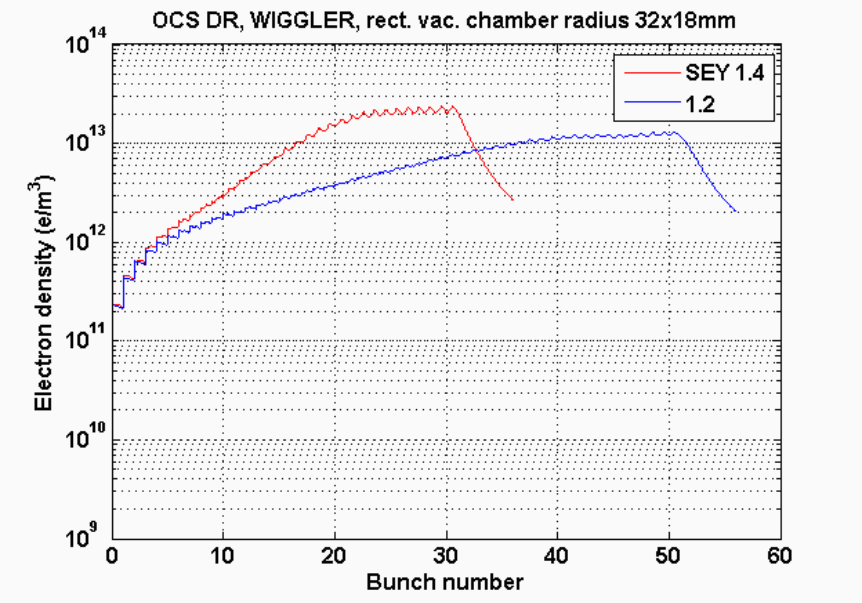

Figure 3.78: Electron-cloud density in a wiggler in OCS, with rectangular cross section, width 32 mm and height 18 mm. Results are shown for SEY 1.4 (upper curve) and 1.2 (lower curve). The density is averaged over the full cross-section of the chamber.

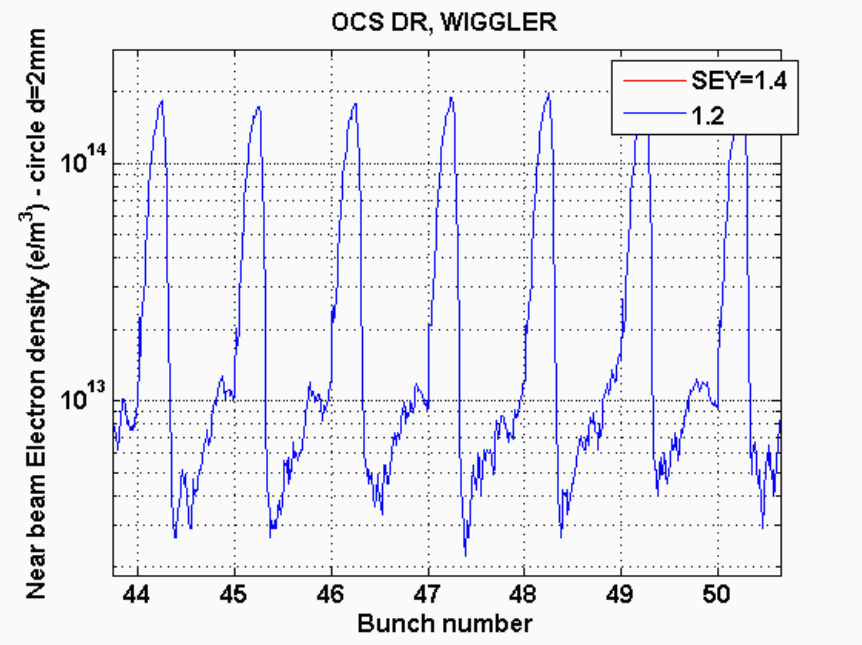

Figure 3.79: Electron-cloud density in a wiggler in OCS, with rectangular cross section, width 32 mm and height 18 mm. Results are shown for SEY 1.2. The density is averaged over a circular cross-section of radius 1 mm, centered on the beam.

lattice (given in Table 2.1) except for MCH, where the maximum possible bunch spacing of 18.8 ns was used instead of the nominal 15.4 ns. The lattice 2×OCS represents a damping ring consisting of a pair of rings with 6 km circumference, possible stacked one on top of the other, so that the bunch separation and average current are effectively halved, compared to a single 6 km ring.

Table 3.36: Electron cloud density in different sections of the positron damping rings. The chamber peak SEY is 1.2, and there is no solenoid in the drift sections.

		OCS	BRU	2×OCS	MCH	DAS	TESLA
Long straight	length [m]	0	0	0	11761	13214	14242
	ρ_e [mm^{-3}]	0	0	0	2	2	2
Arc drift	length [m]	5211	4092	5211	1876	2368	1345
	ρ_e [mm^{-3}]	300	194	79	40	40	40
Dipole	length [m]	434	1445	434	1445	654	695
	ρ_e [mm^{-3}]	400	400	39	28	28	28
Quadrupole	length [m]	178	254	178	311	323	200
	ρ_e [mm^{-3}]	300	300	21	8	8	8
Sextupole	length [m]	96	101	96	101	22	100
	ρ_e [mm^{-3}]	300	300	21	8	8	8
Wiggler	length [m]	196	441	196	441	433	417
	ρ_e [mm^{-3}]	9200	9200	1200	650	650	650
Total	C [m]	6114	6334	6114	15935	17014	17000
	$\langle\rho_e\rangle$ [mm^{-3}]	592	943	110	27	25	22

Table 3.37: Vacuum chamber diameter in different regions of the damping rings, used in simulations of electron cloud build-up.

Region	Chamber diameter [mm]
Long straight	100
Arc drift	50
Dipole	50
Quadrupole	50
Sextupole	50
Wiggler	32

The average cloud density around the ring is defined as:

$$\langle\rho_e\rangle = \frac{1}{C}\int \rho_e(s)ds \tag{3.75}$$

where the integral extends over the full circumference C. We note that

the average cloud density tends to be dominated by the cloud density in the dipoles and the wiggler. Solenoids, which were used successfully in the B-Factories to suppress electron-cloud effects, would not be effective in these regions: solenoids work to suppress the cloud by providing longitudinal magnetic field that traps low-energy secondary electrons near the wall, but in dipoles and wigglers the dominant field component will be perpendicular to the chamber wall, allowing electrons to be drawn into the beam.

The cloud density reached in the wiggler is sensitive to the wiggler aperture. Figure 3.80 shows the results of simulations of the cloud build-up in the OCS and BRU lattices, with apertures in the wiggler of 18 mm, 32 mm, and 46 mm. We note that an aperture of 46 mm may be achieved in a superconducting wiggler, but would be difficult to achieve in a hybrid or normal-conducting wiggler (see Section 4.2). We see that with an aperture in the wiggler of 46 mm, a reduction in the cloud density by a factor of two may be achieved, compared to an aperture of 18 mm. A further reduction in cloud density (to a value below the instability threshold) may be expected by using two 6 km damping rings for the positrons, instead of a single 6 km ring.

Laboratory studies of low-SEY coatings have demonstrated that achieving a peak SEY of 1.2 should be possible, for example using titanium nitride, with appropriate conditioning [53]. Conditioning can be by electron bombardment, and may occur during start-up operations; under these conditions, it may be expected that a properly coated chamber may achieve a peak SEY below about 1.3. Other possible approaches include the cutting of grooves in the vacuum chamber, and the use of clearing electrodes: further studies of these techniques are needed. The impedance effects of all measures that may be taken to suppress the electron cloud need to be carefully considered.

Analytical Estimates of Instability Thresholds

The limiting instability mode for the electron cloud in the positron damping ring is expected to be a single-bunch, head-tail instability. The instability may be modeled as the effect of a short-range wake field resulting from an interaction between the beam and the electron cloud. Since the vertical beam size is much smaller than the horizontal, the beam is more sensitive to vertical effects, so here we focus on the vertical dynamics. We use a resonator model for the wake field, where the integrated wake function $W_1(z)$

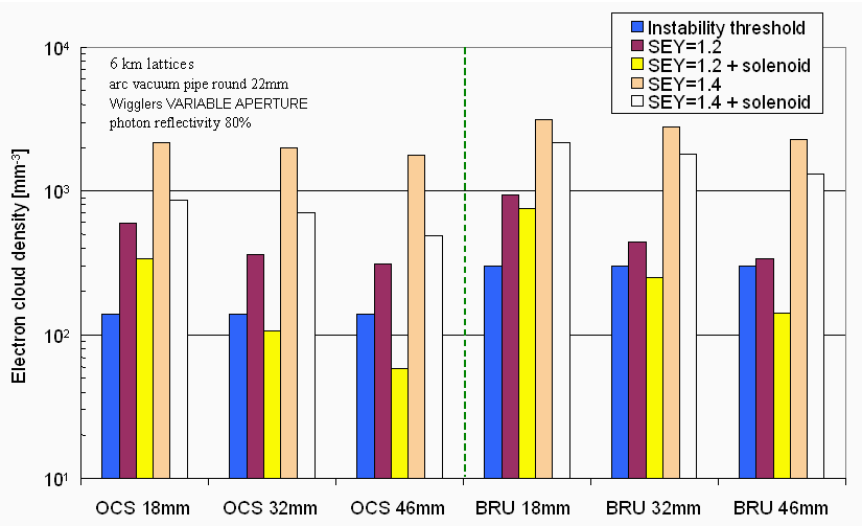

Figure 3.80: Effect of wiggler aperture on electron cloud density in the 6 km lattices. The cloud density averaged around the ring is shown for chamber SEY of 1.2 and 1.4, with and without solenoids in the field-free regions. The cloud density at which single-bunch instability is expected to occur is shown for comparison.

is written:

$$W_1(z) = c\frac{R_s}{Q}\exp\left(\frac{\omega_e z}{2Qc}\right)\sin\left(\frac{\omega_e}{c}z\right) \tag{3.76}$$

The wake function defines the deflecting force on a particle at longitudinal position z in a bunch (increasing z is towards the head of the bunch):

$$\Delta p_y(z) = \frac{r_e}{\gamma}\int_z^\infty W_1(z'-z)\lambda_+(z')y(z')dz' \tag{3.77}$$

where λ_+ is the beam line density within a bunch, r_e is the classical electron radius, and γ is the relativistic factor of the beam. The resonator frequency ω_e is given by the oscillation frequency of electrons in the field of the beam:

$$\omega_e = \sqrt{\frac{\lambda_+ r_e c^2}{\sigma_y(\sigma_x+\sigma_y)}} \tag{3.78}$$

where $\sigma_{x(y)}$ are the transverse beam sizes. The amplitude of the wake field is given by

$$c\frac{R_s}{Q} = K\frac{\lambda_e}{\lambda_+}\frac{L}{\sigma_y(\sigma_x+\sigma_y)}\frac{\omega_e}{c} \tag{3.79}$$

where L is the beamline length over which the wake field acts. The electron cloud density λ_e is the local line density near the beam, and is related to the electron volume density ρ_e by:

$$\lambda_e = 2\pi\rho_e\sigma_x\sigma_y \tag{3.80}$$

K is an enhancement factor due to the cloud size. The wake force can be calculated by a numerical method [50], and we find that K is roughly between two and three, for a sufficiently large cloud compared to the beam size. Q characterizes the damping of the electron coherent motion, which results from the nonlinear interaction with the beam. Q can be estimated by a numerical method, and for a coasting beam is roughly between five and ten. Q is reduced by other sources which induce a frequency spread of the electrons, namely variations of beam charge density along z and of beam size along the beamline; therefore, it is not easy to know the value of Q with any great accuracy.

The electron phase advance in the bunch, $\omega_e\sigma_z/c$, is an important parameter for the instability characteristics. A large phase advance helps Landau damping; however, it also induces a strong cloud concentration and pinching close to the beam, with the result that K increases. The wake force with a range characterized by Q is efficient only for a bunch with length

$\omega_e \sigma_z / c > Q$; that is, the effective Q value is the minimum of the "true" Q value and $\omega_e \sigma_z / c$.

The threshold for the fast head-tail instability can be found by applying the Keil-Schnell-Boussard criterion, which is based on a coating beam model. This model is appropriate where the electron phase advance in a bunch is much larger than one (as is the case for all the reference lattices). The threshold cloud density for a given bunch intensity is given by [48]:

$$\rho_{e,th} = \frac{2}{\sqrt{3}} \frac{1}{KQ} \frac{\gamma \nu_s}{r_e \beta C} \frac{\omega_e \sigma_z}{c} \tag{3.81}$$

where β and ν_s are the average vertical beta function and the synchrotron tune, respectively. For finite chromaticity ξ, ω_e is replaced by $\omega_e + \omega_0 \xi / \alpha_p$, where α_p is the momentum compaction factor of the lattice.

To apply Equation (3.81) we use an approximate value of the beta function in the dipoles, where there is the dominant contribution of the electron cloud to the average density. The estimated threshold values for the different damping ring lattices are shown in Table 3.38. Values for the B-Factories (positron or low-energy rings) are also shown, for comparison. For the damping rings, we assume $K \times Q = 3 \times 5$, $\beta = 30$ m (except for TESLA, where $\beta = 15$ m), and zero chromaticity.

Table 3.38: Threshold electron cloud density in different damping ring lattices, compared with the B-Factories.

	PPA	OTW	OCS	BRU	MCH	DAS	TESLA	PEP-II	KEK-B
γ	9785	9785	9914	7319	9785	9785	9785	6067	6849
ν_s	0.027	0.042	0.034	0.12	0.15	0.067	0.071	0.030	0.015
$\omega_e \sigma_z / c$	15	15	15	15	15	15	15	3	3
KQ	15	15	15	15	15	15	15	9	9
β [m]	30	30	30	30	30	30	15	18	11
C	2824	3223	6114	6333	15935	17014	17000	2200	3000
$\rho_{e,th}$ [mm^{-3}]	1278	1742	753	1894	1258	526	1116	628	425

We note that the threshold cloud densities for instability in the damping rings are generally comparable with those in the B-Factories. At the same time, it could be more difficult to suppress the electron cloud in the damping rings because of the ineffectiveness of solenoids in the regions of the damping ring where the cloud density is expected to be greatest.

Simulations of Electron-Cloud Single-Bunch Instabilities

We now consider in more detail the instabilities driven by electron cloud, and attempt to determine with greater accuracy the instability thresholds,

by using simulation codes. We discuss single-bunch instabilities, incoherent emittance growth, and coupled-bunch instabilities caused by the electron cloud.

Though the wake field represented by the resonator model permits us to study the instability with a simple analytic formula, the estimation of the threshold includes factors that are not well determined, in particular the enhancement K and the quality factor Q. Since K is related to pinching, one may choose $K \sim \omega_e \sigma_z / c$. A value of Q which is larger than $\omega_e \sigma_z / c$ is not meaningful. To avoid the need for approximations for these factors, we can perform tracking simulations [49, 61, 46]. Here, we show simulation results obtained from a strong-strong code, PEHTS [46]. In this code, a bunch of positrons and the electron cloud are each represented by macro-particles, and the interactions between them are calculated by solving the two-dimensional Poisson equation using the particle-in-cell method.

The interactions between the beam and the cloud are applied at several, or several tens, positions in the ring, where the beta function is assumed to be uniform. Since the interaction points are discrete, an artificial incoherent emittance growth sometimes appears, from which the head-tail instability has to be distinguished. The head-tail instability appears with a sufficient number of interactions in a synchrotron period, and, since the synchrotron period is much longer than a revolution time, the instability threshold does not depend on the number of interactions in a revolution. To determine whether an observed emittance growth is the result of the fast head-tail instability, tests are carried out to see whether the emittance growth is independent of the number of interactions; if this is the case, then the emittance growth is indeed the result of the fast head-tail instability. The profiles of the bunch and the cloud are also monitored; if the fast head-tail instability occurs in the simulation, then the centroids of the bunch and the cloud vary coherently along the bunch length.

Note that some incoherent emittance growth can in fact occur in a real machine; however, in the simulations, increasing the number of interactions (with uniform beta function) does not give the true incoherent emittance growth. This is discussed in more detail below.

Figure 3.81 shows the emittance growth resulting from the fast head-tail instability caused by electron cloud for the damping ring lattices. Each plot shows the emittance growth for various cloud densities. The threshold density is determined by the density at which the emittance growth first appears.

Figure 3.82 shows a snapshot of the vertical centroid positions of the bunch and the cloud, and the vertical beam size, as functions of the longi-

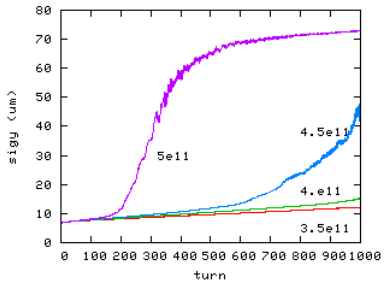

(a) OTW

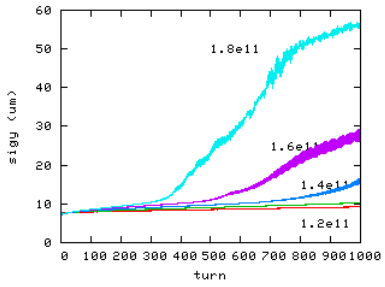

(b) OCS

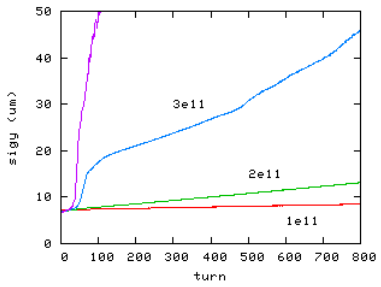

(c) BRU

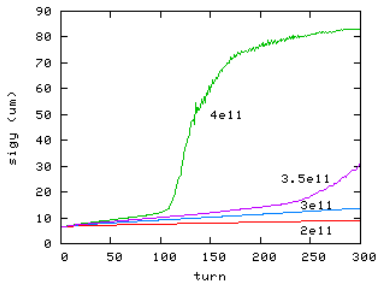

(d) MCH

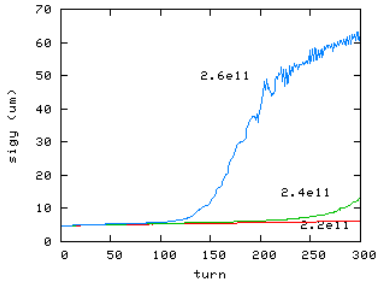

(e) DAS, $\beta = 15$ m

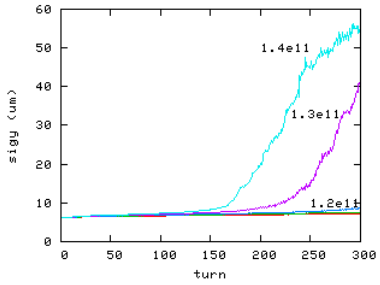

(f) TESLA

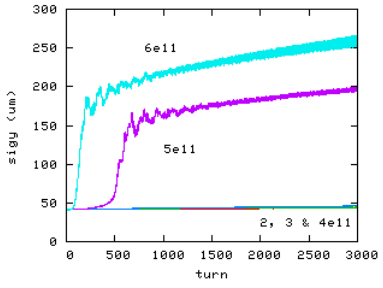

(g) KEK-B

Figure 3.81: Emittance growth from fast head-tail instability caused by electron cloud.

tudinal position in the bunch. The cloud density is above threshold. The amplitudes of the coherent motion of the bunch and the cloud increase with the beam size, so in this case we can say that the fast head-tail instability is the dominant cause of the emittance growth.

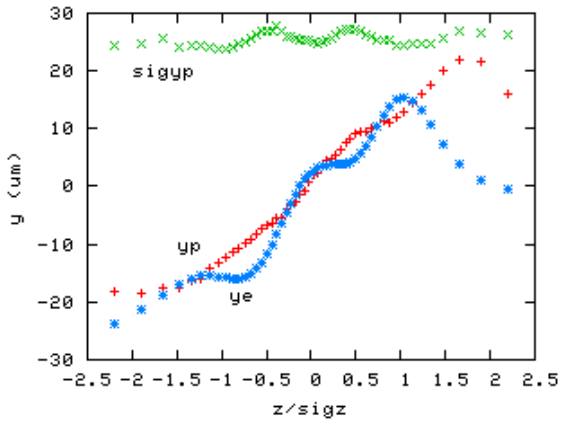

Figure 3.82: Beam and electron cloud profiles along a bunch in OCS after 1000 turns, with $\rho_e = 1.6 \times 10^{11}$ m^{-3}. The bunch size and the centroids of the bunch and electron cloud are plotted.

The instability threshold values are summarized in Table 3.39. The analytical estimates are compared with those given by simulation. The thresholds from simulation are systematically lower than the thresholds found from the analytical estimate. We suppose that the lower threshold density in the simulations are the result of the concentration and pinching of electrons from the attractive force of beam. The force from the beam may be characterized by the electron phase advance during a bunch passage, $\omega_e \sigma_z / c$; a higher phase advance leads to a lower threshold density. In the B-factories, the phase advances are much smaller than in the damping rings, therefore the analytical estimates are in better agreement with the simulations. The instability threshold values found from the simulations are likely to be more reliable than those from the analytical estimates.

We see in Table 3.39 that the tune shift near the instability threshold density is not very large. However, electrons are concentrated and pinched by the beam force, with the result that the density near the beam increases towards the tail of the bunch, and the tune shift also increases as a consequence. The cloud density distribution before a bunch passage and at the

Table 3.39: Threshold densities for fast head-tail instability driven by electron cloud.

	PPA	OTW	OCS	BRU	MCH	DAS	TESLA	KEK-B
$\rho_{e,th}$ [mm^{-3}]	1278	1742	753	1894	1258	526	1116	425
$\rho_{e,sim}$ [mm^{-3}]	-	400	140	300	300	120	240	400
$\Delta\nu_y(\rho_{e,sim})$	-	0.011	0.0074	0.021	0.041	0.018	0.018	0.005

center of the bunch are shown in Figure 3.83. The density increases by a factor of 30 and as a result, the tune shift increases to more than 0.5 at the instability threshold cloud density.

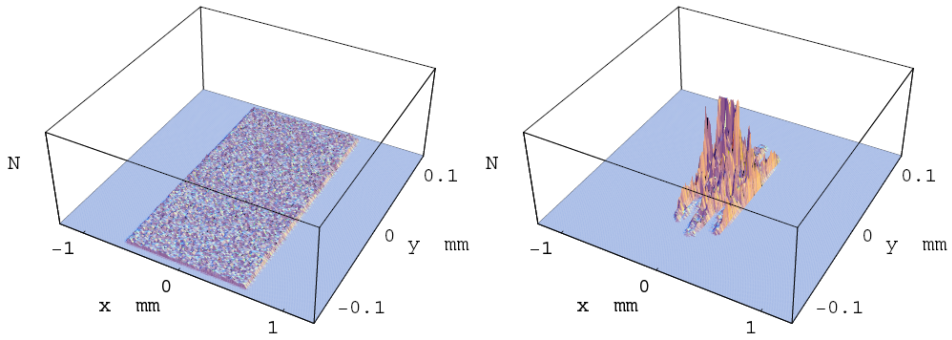

Figure 3.83: Electron-cloud density (a) before interacting with a bunch, and (b) at the interaction with the center of a bunch.

Associated with the tune shifts is an incoherent emittance growth, which may be understood in terms of symplectic diffusion resulting from a nonlinear force [47, 7]. To study this effect, we develop a model as follows. In a periodic system like a circular accelerator, the nonlinearity of the whole ring may be characterized by a one-turn map. The one-turn map in the presence of electron cloud is written as:

$$M = e^{-:F_{1,n}:} e^{-:\phi_n:} \cdots e^{-:F_{3,2}:} e^{-:\phi_2:} e^{-:F_{2,1}} e^{-:\phi_1:} \tag{3.82}$$

where $e^{-:F_{i,i-1}:}$ is the linear transfer map from s_{i-1} to s_i, and ϕ is the electric

potential of the electron cloud. M can be rewritten in the form:

$$M = e^{-:F_1:} \prod_{i=1}^{n} e^{:F_{i,1}:} e^{-:\phi_i:} e^{-:F_{i,1}:} \tag{3.83}$$

$$= e^{-:F_1:} T \exp\left\{ - \int : \phi(e^{-:F_{i,1}:}\mathbf{x}) : ds_i \right\} \tag{3.84}$$

where $e^{-:F_{i,1}:}$ is the transfer map from s_1 to s_i, $e^{-:F_1:}$ is the linear part of the one-turn map (i.e. the one-turn map in the absence of electron cloud), and T is the "s-ordered" product (analogous to a time-ordered product). The integral is performed with the appropriate beta function and betatron phase at the cloud position s_i.

The effects of the nonlinear forces can be found by integrating the motion of particles in the beam through the lattice, element by element. Since the integration is very time consuming, we use a simplified model. Let us suppose that the electron cloud in one section of the lattice dominates; for example, the electron cloud in the damping rings may exist predominantly in the wiggler section. We now consider the wiggler as constructed from periodic units, with each unit having a phase advance of $2m\pi$. For example, if each wiggler cell has a phase advance of 60°, then each unit would consist of six cells, and we would have $m = 1$. The map for a single unit is:

$$M(2m\pi) = T \exp\left\{ - : \int_{\text{unit}} \phi(e^{-:F_{i,1}:}\mathbf{x}) : ds_i \right\} \tag{3.85}$$

and the map for the full section, assumed to consist of N units is:

$$M(2Nm\pi) = T \exp\left\{ -N : \int_{\text{unit}} \phi(e^{-:F_{i,1}:}\mathbf{x}) : ds_i \right\} \tag{3.86}$$

Finally, since the rest of the lattice can be represented by a linear map $e^{-:F_{\text{frac}}:}$ with fractional tune, the one-turn map now becomes:

$$M = e^{-:F_{\text{frac}}:} T \exp\left\{ -N : \int_{\text{unit}} \phi(e^{-:F_{i,1}:}\mathbf{x}) : ds_i \right\} \tag{3.87}$$

Furthermore, if ϕ is symmetric under $x \to -x$ and/or $y \to -y$, a set of cells with phase advance $m\pi$ can be taken as the basic unit, rather than a set of cells with phase advance $2m\pi$. Using this model of a realistic lattice, the computation time for tracking can be reduced drastically.

We can apply the above model to the dogbone damping rings, where the wiggler sections may be treated as consisting of 60° FODO cells. For

units of three and six cells, the phase advance is π and 2π, respectively. We compare the emittance growths for the three-cell and six-cell models, with the same integrated electron cloud density in each case. Figure 3.84 shows the lattice functions in the wiggler section. Figure 3.85 shows the emittance growth for the three-cell (π phase advance) and six-cell (2π phase advance) models, for three different cloud densities. The results for the two versions of the "realistic lattice" model are in good agreement.

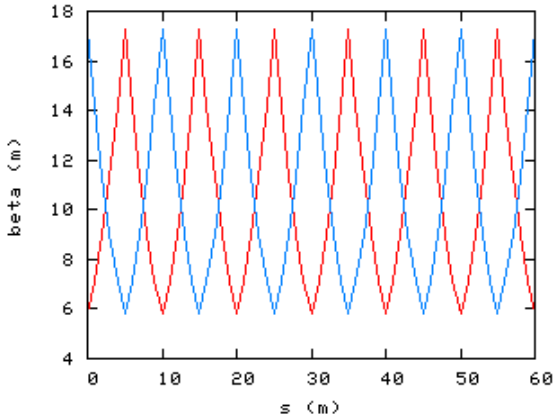

Figure 3.84: Lattice functions in a six-cell wiggler unit.

Figure 3.86 shows the emittance growth for various cloud densities in the wiggler sections of the MCH and TESLA lattices. In MCH we observe a threshold for emittance growth at $\rho_e = 4 \times 10^{11}$ m^{-3}, which is consistent with the uniform beta model. For TESLA, we observe emittance growth at a cloud density of $\rho_e = 10^{12}$ m^{-3}. The threshold is higher than that given by the uniform beta model; but note that the tracking time is limited to 300 turns, which may be too short to observe a head-tail instability. Figure 3.87 shows the bunch and cloud profiles for MCH and TESLA. In neither case can clear coherent motion be seen, though emittance growth certainly occurs. Any coherent motion may be smeared by the strong nonlinear force. It is probably safer to use the threshold value given by the uniform beta model, rather than that obtained from the realistic lattice model.

We next discuss the OCS lattice, whose Twiss parameters are shown in Figure 3.88. The phase advances in units constructed from four arc cells are 3π and 2π for the horizontal and vertical planes, respectively. Figure 3.89 shows the emittance growth in the OCS lattice for the case where

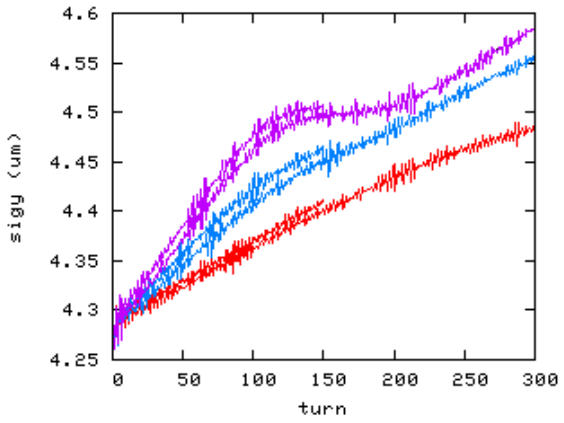

Figure 3.85: Incoherent emittance growth from electron cloud in wiggler section of dogbone damping rings. Results for three different cloud densities are shown; the two lines for each density show the results from models based on three-cell units and six-cell units.

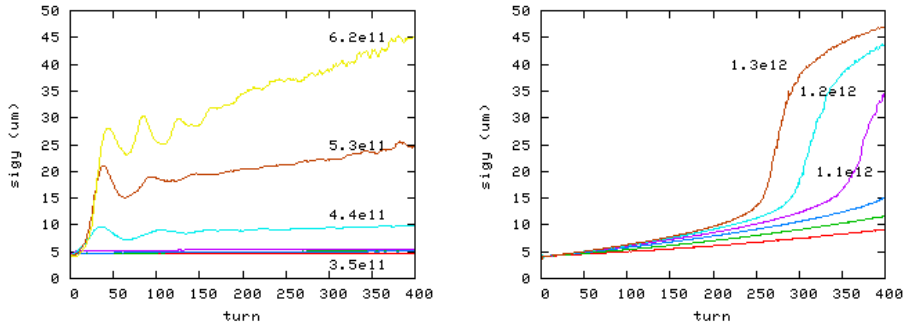

(a) MCH (b) TESLA

Figure 3.86: Incoherent emittance growth from electron cloud in MCH and TESLA. Only electron cloud in the wiggler section is included.

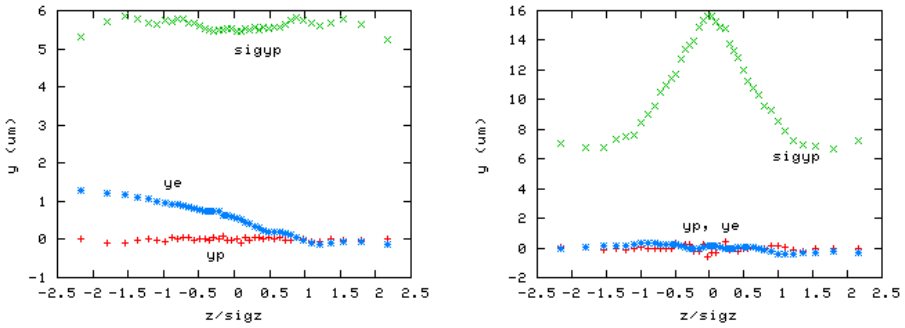

(a) MCH, $\rho_e = 4.8 \times 10^{11}$ m^{-3} (b) TESLA, $\rho_e = 4.4 \times 10^{11}$ m^{-3}

Figure 3.87: Beam and electron cloud profiles above emittance-growth threshold for MCH and TESLA.

electron cloud occurs throughout the lattice, and also for the case where electron cloud occurs only in the dipoles. The threshold is found to be $\rho_e = 7.7 \times 10^{11}$ m^{-3}, which is half that of the uniform beta model, see Figure 3.90 and Table 3.39. Also shown in Figure 3.89 is a slower emittance growth at cloud densities below the threshold. We believe that this growth is due to an incoherent effect. The growth rate, which is $0.5 \times 10^{-3}\sigma_y$/turn, is less than the radiation damping rate of 2×10^{-3}, and the growth saturates at 40% increase in emittance; therefore, it does not seem to be serious. The coherent fast head-tail instability dominates over the incoherent growth in OCS.

For the OCS lattice, we should try to understand why the realistic lattice model gives a lower threshold for the instability than the uniform beta model. Since the dispersion is not taken into account in the uniform beta model, the horizontal beam size is smaller than in the realistic lattice model. The contributions of the dispersion to the horizontal beam size dominates over the contribution of the emittance: $\varepsilon_x\beta_x = 5.3 \times 10^{-9}$ m^2, while $(\eta\sigma_\delta)^2 = 6.7 \times 10^{-8}$ m^2. To confirm the effect of the dispersion, we compare the results with two cases without dispersion: in the first case, the nominal emittance of 0.56 nm is used, but the beam size is artificially reduced by a factor of 3.3; in the second case, the nominal beam size is used, but the emittance is increased a factor of ten. Figure 3.91 shows the emittance growth for these two cases. In both cases, the threshold, which is 1.2–1.4$\times 10^{11}$ m^{-3}, is consistent with that given by the uniform beta model. We conclude that the dispersion in the arc section lowers the instability threshold.

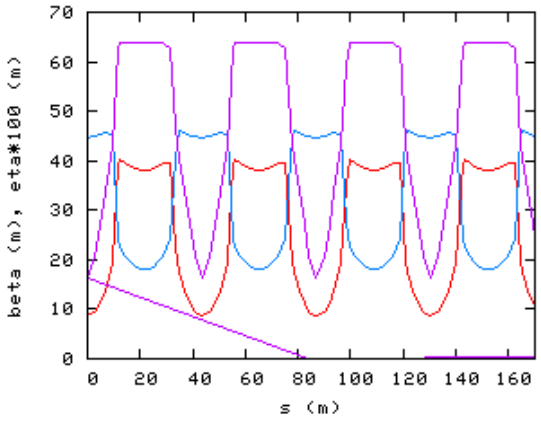

Figure 3.88: Lattice functions in arc unit of OCS. The phase advances in this unit are 3π and 2π in the horizontal and vertical planes respectively.

Coupled-Bunch Instability

The electron cloud can have a long-range effect that can drive coupled-bunch instabilities. As for the single-bunch instabilities, the coupled-bunch effects of the electron cloud can be modeled in terms of a wake field; the characteristics of the wake field depend strongly on the motion of the electrons in the cloud. The wake field in a drift space has a low quality factor ($Q \sim 1$), while that in magnetic field tends to have a higher quality factor. The wake field amplitude R_s/Q is determined by the number of electrons that contribute to the instability. Here, we discuss the coupled-bunch instability resulting from electrons in a drift space. The actual instability characteristics are determined by a summation of the wake fields in every section, including drifts, bending magnets, quadrupoles and wigglers.

Figure 3.92 shows the long-range wake fields for the OTW and OCS lattices. The cloud line densities are $\lambda_e = 7 \times 10^7$ m^{-1} and 5×10^7 m^{-1}, respectively. The growth rate of the coupled-bunch instability is estimated from the formula [13]

$$(\Omega_m - \omega_\beta)L/c = \frac{N_+ r_e c}{2\gamma\omega_\beta} \sum_{k=1}^{n} W_1(-kL_{sp}) e^{2\pi i k(m+\nu_\beta)/M} \tag{3.88}$$

Figure 3.93 shows the growth rates of the coupled-bunch modes driven by the electron cloud. The growth times were found to be 7.5 ms (700 turn) and

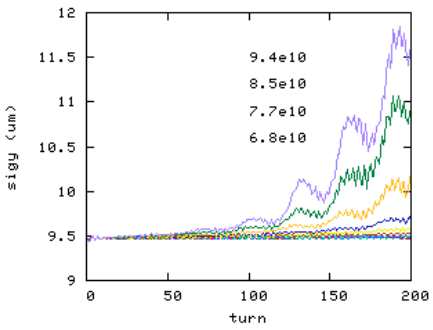

(a) Electron cloud throughout lattice.

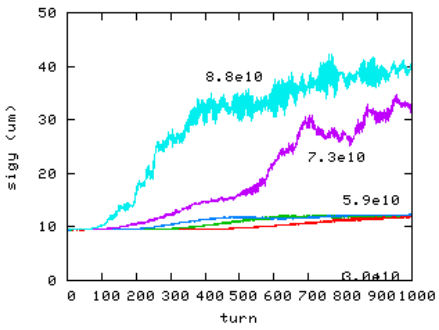

(b) Electron cloud only in bends.

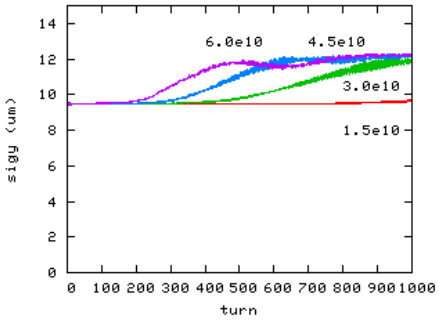

(c) Slow emittance growth below threshold.

Figure 3.89: Emittance growth caused by electron cloud in OCS. (a) Electron cloud occurs throughout the lattice. (b) Electron cloud occurs only in the bending magnets. (c) Slow emittance growth below instability threshold.

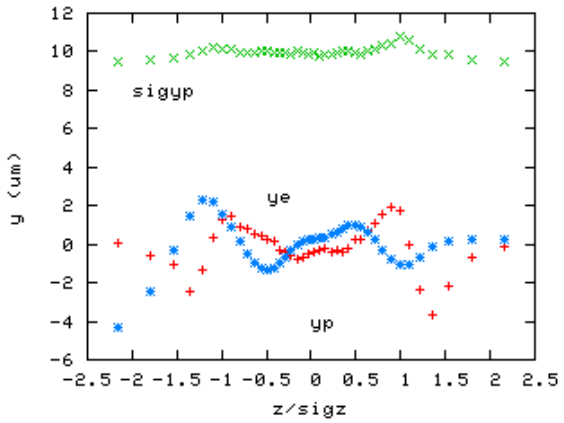

Figure 3.90: Beam and electron cloud profiles above instability threshold for OCS after 200 turns, $\rho_e = 7.7 \times 10^{10}$ m^{-3}.

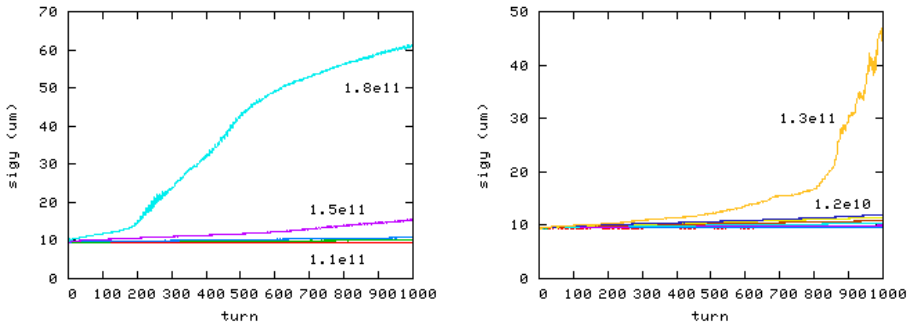

(a) ϵ_x = nominal; $\sigma_x = 0.3\times$nominal. (b) $\epsilon_x = 10\times$nominal; σ_x = nominal.

Figure 3.91: Emittance growth from electron cloud in OCS with zero dispersion.

10 ms (500 turn) for the OTW and OCS lattices, respectively. The growth times are long enough that it will be possible to suppress the instabilities by using a bunch-by-bunch feedback system.

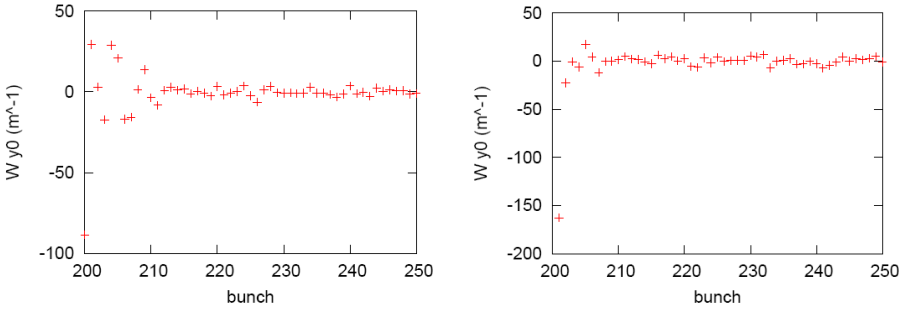

(a) OTW, $\lambda_e = 7 \times 10^7$ m^{-1}. (b) OCS, $\lambda_e = 5 \times 10^7$ m^{-1}.

Figure 3.92: Long-range wake fields from electron cloud in OTW and OCS.

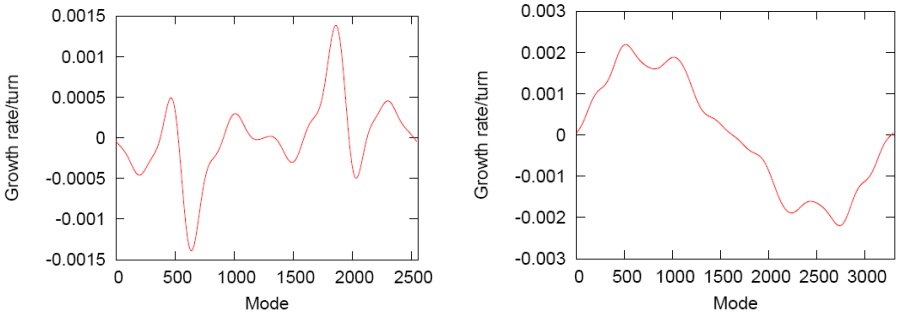

(a) OTW (b) OCS

Figure 3.93: Growth rates for coupled-bunch instabilities driven by electron cloud in OTW and OCS.

Comments and Conclusions

The build-up of electron cloud in the reference lattices has been studied with a simulation code. The cloud density thresholds for single-bunch instabilities have been estimated analytically and in simulations. Electron-cloud induced tune shifts and incoherent emittance growth have also been considered. Coupled-bunch instability growth rates have been estimated

analytically. The most serious effect of the electron cloud is likely to be a fast head-tail single-bunch instability, which would prevent the desired beam quality being achieved. Incoherent emittance growth is a potential concern which needs further study; the growth rates of coupled-bunch instabilities are low enough that these instabilities may be suppressed with feedback systems.

Figure 3.94 shows the simulated mean electron cloud density in the reference lattices, compared with the estimated instability thresholds, again from simulations. Assuming the same SEY in each case, the instability limit is more likely to be exceeded in the smaller rings.

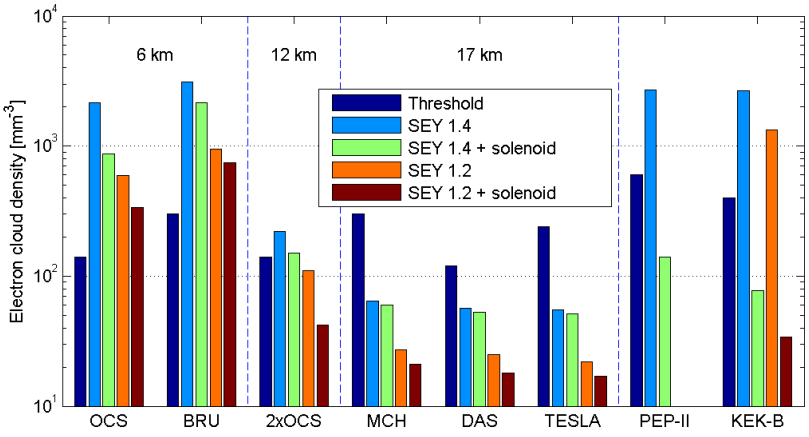

Figure 3.94: Electron cloud densities in the reference lattices and the B-Factories, compared with the estimated instability thresholds.

With a chamber having a secondary electron yield in the range 1.2–1.4, the dogbone rings are expected to be close to or just below the single-bunch instability threshold, while the 3 km and 6 km rings will likely be above threshold. Solenoids would provide little benefit, since the electron cloud in the dipoles and wigglers dominate, and solenoid windings would not be effective inside strong fields. This is in contrast to the B-Factories, where suppressing the electron cloud in the long field-free regions was sufficient to bring the machines below threshold.

A damping ring with a large circumference (17 km, and perhaps 12 km) would be preferred from point of view of electron-cloud effects, since the longer bunch separation reduces the build-up of electron cloud to more

manageable levels. If the peak SEY in the dipoles and wigglers can be brought down close to 1, then a 6 km ring may be feasible. The 3 km rings are likely to be extremely difficult. A high synchrotron tune can be helpful in raising the instability threshold, but this needs to be balanced with other effects, such as problems associated with synchrobetatron coupling.

3.4.8 Ion Effects

There are various ion effects in electron storage rings and synchrotrons. Most of these are "conventional" effects that occur when ions are trapped by a circulating electron beam for multiple revolutions. To avoid conventional ion trapping, a gap is introduced in the electron beam; clearing electrodes can also be used. However, even with gaps, the beam can still be affected by the fast ion instability (FII) [57, 10, 34]. In the fast ion instability, individual ions remain close to the beam only for a single passage of the beam, and are not trapped for multiple turns. The effects of the ions depend on the beam size, and so can vary with position in the ring (as the beta functions change from one point to another) and, in the damping rings, with time (as the emittances decrease during the damping cycle). Here, we consider the ion effects as functions of time in the arcs, wigglers, and long straights of the reference lattices. We assume that the vacuum pressure, as well as the beta function, varies between the different sections. The pressure depends on the amount of synchrotron radiation and pumping; for the studies reported here, we assume a pressure of 0.1 ntorr in the long straights (where there is a wide aperture and negligible synchrotron radiation), a pressure of 0.5 ntorr in the arcs, and a pressure of 2 ntorr in the wiggler (where there is intense synchrotron radiation, and there may also be aperture restrictions that restrict pumping).

Without gaps in the fill pattern, ions with a relative molecular mass greater than $A_{x(y)}$ will be trapped, where

$$A_{x(y)} = \frac{N_0 r_p s_b}{2\left(\sigma_x + \sigma_y\right)\sigma_{x(y)}} \tag{3.89}$$

where N_0 is the number of electrons per bunch, r_p is the classical radius of the proton, s_b is the bunch spacing in units of distance, $\sigma_{x(y)}$ is the horizontal (vertical) rms beam size. The beam sizes are large at injection, and, as a result, all ions can be trapped. As the emittance damps, ion oscillations in the stronger focusing sections, where the beam sizes are smallest, become unstable before the oscillations in the weaker focusing sections.

Growth Times of Fast Ion Instability

In the linear theory, the exponential FII growth rate for coherent transverse oscillations of an electron bunch is given by [57, 70, 85]:

$$\frac{1}{\tau_e} \approx \frac{1}{3}\sqrt{\frac{2}{3}}\frac{c}{\Delta\omega_i/\omega_i}\beta_y k_y \tag{3.90}$$

where $\Delta\omega_i/\omega_i$ is the relative spread of ion frequencies in the potential of the electron beam, β_y is the beta function, and k_y is the focusing force on the beam from the ions. k_y is given by:

$$k_y = \frac{\lambda_i r_e}{\gamma\sigma_y\left(\sigma_x + \sigma_y\right)} \tag{3.91}$$

where γ is the relativistic factor of the electron beam, r_e is the classical electron radius, and λ_i is the average line density of ions. After the passage of n_b bunches with N_0 particles per bunch, the ion line charge density, λ_i, is given by:

$$\lambda_i = \sigma_i \frac{p}{kT} N_0 n_b \tag{3.92}$$

where σ_i is the ionization cross-section, and p is the partial pressure of the gas species involved in the instability. In these studies, we assumed that the dominant ion species is CO^+, that the ionization cross section is 2 Mb, and that the ion tune spread $\Delta\omega_i/\omega_i$ is 0.3. The build-up of ions during the passage of a bunch train given by Equation (3.92) means that bunches towards the end of a bunch train will experience the fastest instability growth rates.

There have been some experimental studies of FII at the ALS [10] and the PLS [34], with results that are qualitatively in agreement with the above theory. Observations have also been made at the TRISTAN-AR [22], and in the high-energy rings of the KEK-B and PEP-II B-factories.

In the damping ring reference lattices, the FII growth time is obtained by averaging over the different sections, taking into account variations in beam size and gas pressure between different sections. To compare the reference lattices, a long bunch train is initially assumed, with n_b the total number of bunches in the ring. As the beam size damps after injection, the growth rate tends to increase; see Equations (3.90)–(3.91). However, depending on the optics, the beam can become small enough that the oscillations of ions above a certain mass become unstable and are no longer trapped. Ions in sections of the ring where this occurs no longer contribute to the instability, and the growth rates can decrease as a result. For CO^+, this generally happens

in the wigglers, and may or may not happen in the arcs depending on the damping ring lattice design. CO^+ ions will be trapped in the long straights of the dogbone rings throughout the damping process.

Figures 3.95–3.101 show the masses of trapped ions, the growth rates averaged over the lattice and the incoherent growth rates in each of the seven reference lattices during the damping process. The initial normalized emittance is 45 μm. Coupling bumps are not applied in the straight sections of the dogbone lattices. In each of Figures 3.95–3.101, the left-hand plot shows the masses of trapped ions in different sections of the lattice as a function of time during the damping process; the two curves for each section indicate the range of minimum trapped masses resulting from variations in the lattice functions. The horizontal broken line indicates a mass of 28, for CO^+. The central plot shows the growth rates from CO^+ averaged over the lattice, taking into account different vacuum pressures and whether or not the ions are trapped in particular locations. The right-hand plot shows the incoherent tune shifts from the ions.

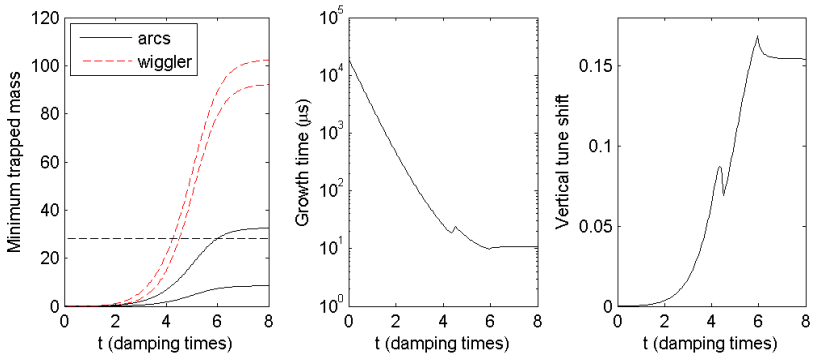

Figure 3.95: Ion trapping, effective growth time and incoherent tune shifts from CO^+ ions during the damping process in PPA. See the text for further explanation.

The growth times for the circular (3 km and 6 km) lattices are shown again in Figure 3.102. The growth times for the dogbone lattices, with and without coupling bumps in the long straights, are shown in Figure 3.103. The minimum growth times at any point during the damping process for all the reference lattices are summarized in Figure 3.104.

Other gases present in the vacuum chamber are expected to include H_2 and H_2O. The estimated FII growth times from H^+ ions (with the same

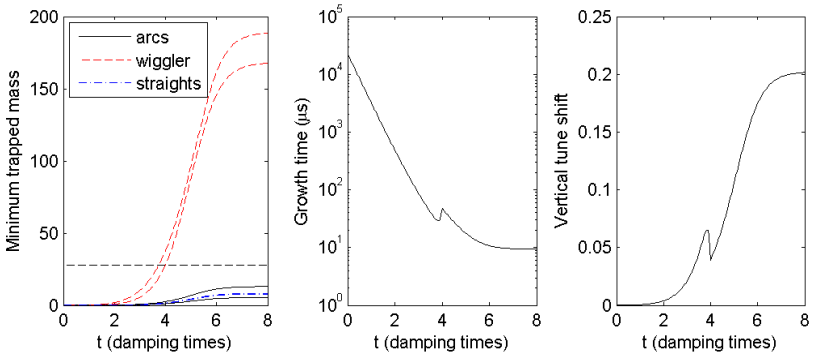

Figure 3.96: Ion trapping, effective growth time and incoherent tune shifts from CO^+ ions during the damping process in OTW. See the text for further explanation.

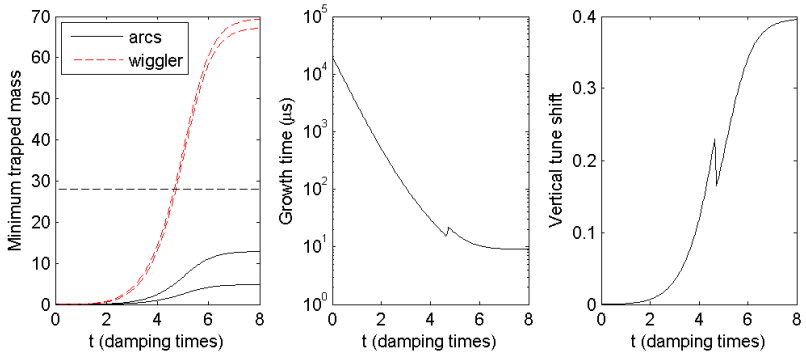

Figure 3.97: Ion trapping, effective growth time and incoherent tune shifts from CO^+ ions during the damping process in OCS. See the text for further explanation.

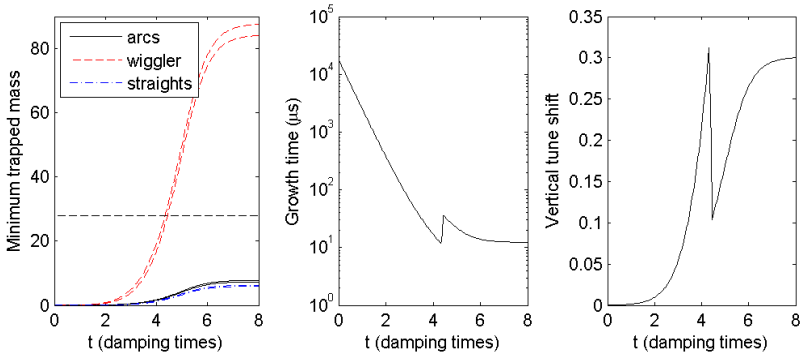

Figure 3.98: Ion trapping, effective growth time and incoherent tune shifts from CO^+ ions during the damping process in BRU. See the text for further explanation.

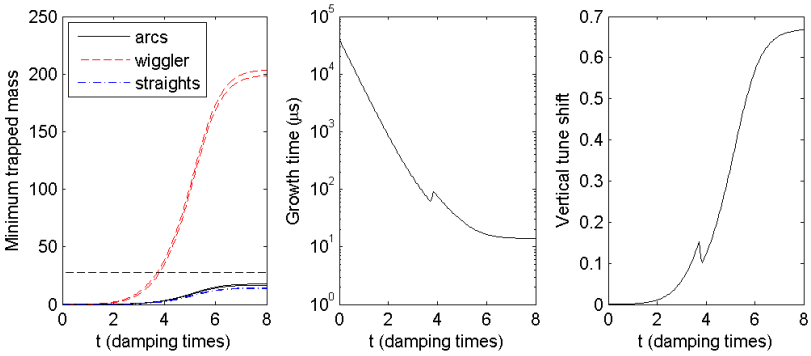

Figure 3.99: Ion trapping, effective growth time and incoherent tune shifts from CO^+ ions during the damping process in MCH. See the text for further explanation.

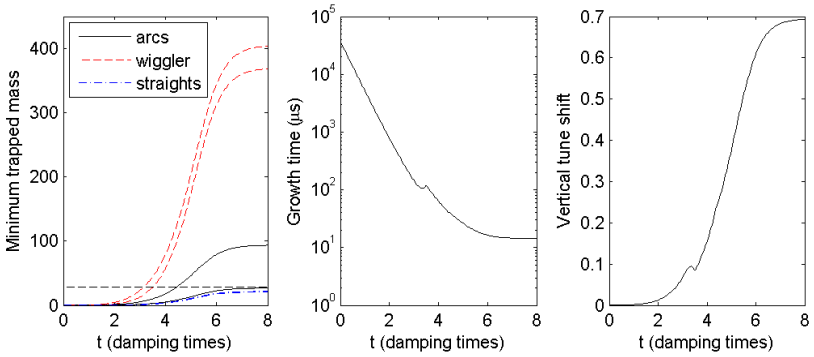

Figure 3.100: Ion trapping, effective growth time and incoherent tune shifts from CO^+ ions during the damping process in DAS. See the text for further explanation.

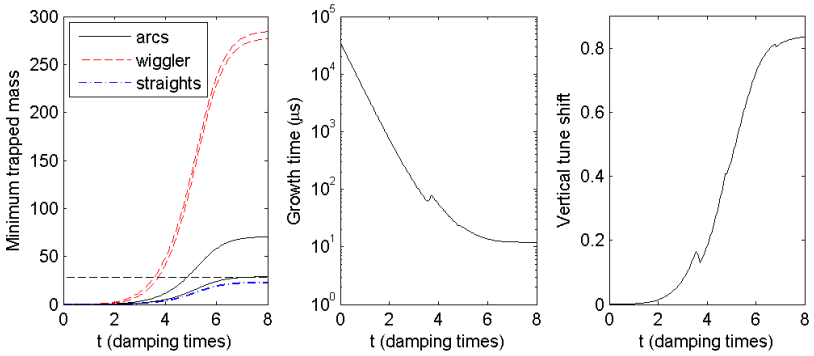

Figure 3.101: Ion trapping, effective growth time and incoherent tune shifts from CO^+ ions during the damping process in TESLA. See the text for further explanation.

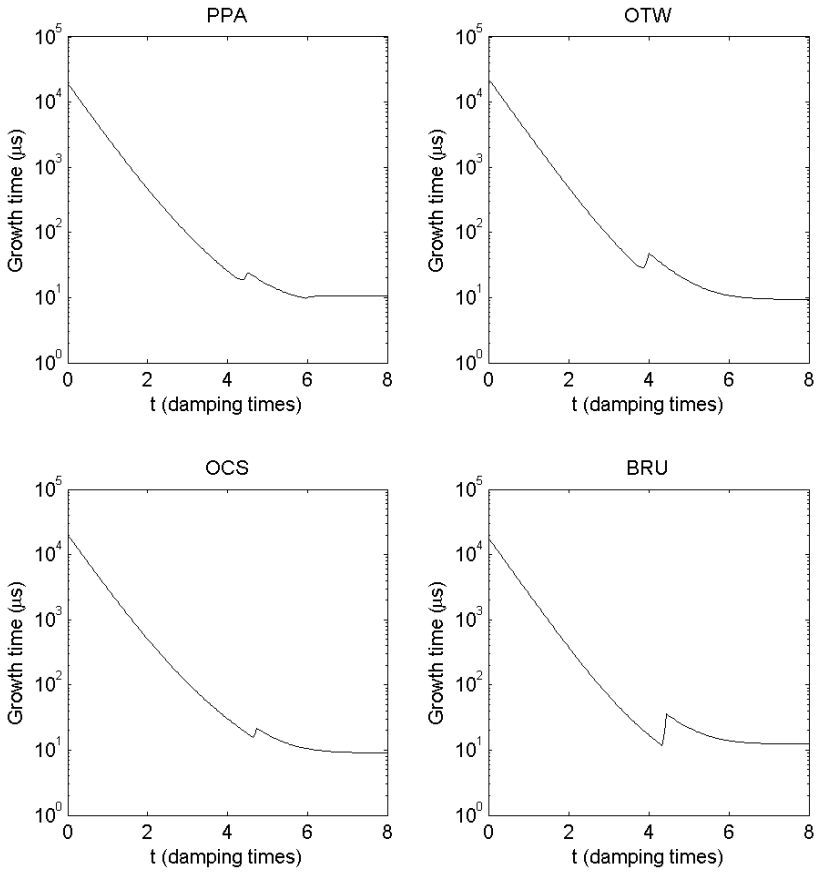

Figure 3.102: Effective FII growth times in the circular (3 km and 6 km) lattices as a function of time during the damping process.

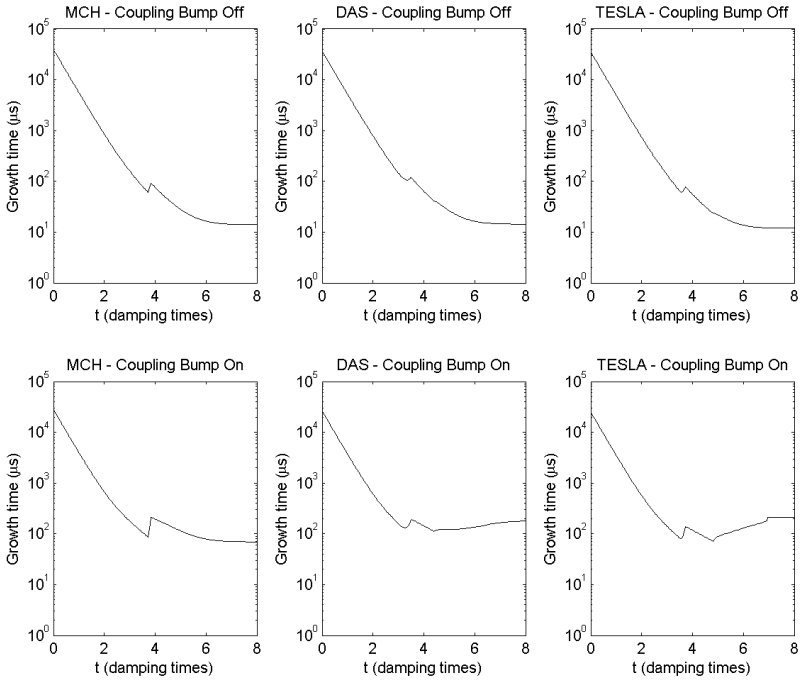

Figure 3.103: Effective FII growth times in the dogbone lattices as a function of time during the damping process. The upper plots show the growth times without coupling bumps in the long straights; the lower plots show the growth times with the coupling bumps turned on.

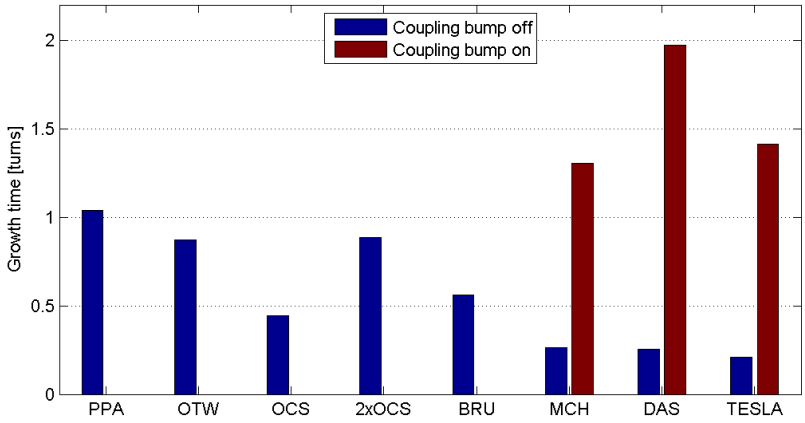

Figure 3.104: Shortest growth times from CO^+ ions in the reference lattices.

conditions used for calculations with CO^+) are roughly two orders of magnitude longer than for CO^+, because the smaller mass of H^+ means that the oscillations of the ions in the beam become unstable much sooner. Additionally, the ionization cross section is much smaller for H^+ (assumed to be 0.35 Mb) than for CO^+ (assumed to be 2 Mb). Therefore, the effects of H^+ ions are negligible, although hydrogen can be one of the major components of the residual gas in the vacuum chamber. A typical analysis in the Photon Factory [40] indicated a composition of 48% CO and 41% H_2.

The growth rates predicted from the linear theory of the fast ion instability are extremely fast, and beyond the reach of a feedback system. Some other form of mitigation is needed; this may be provided by introducing gaps in the fill, the effects of which are discussed below.

Incoherent Tune Shifts

Assuming that the trapped ions have a gaussian distribution, the tune shift from the ions can be written:

$$\Delta\nu_y = \frac{1}{4\pi}\frac{r_e}{\gamma}\int \frac{\lambda_i \beta_y}{\sigma_y^{\text{ion}}\left(\sigma_x^{\text{ion}} + \sigma_y^{\text{ion}}\right)} ds \tag{3.93}$$

where $\sigma_{x(y)}^{\text{ion}}$ is the rms horizontal (vertical) ion distribution. In our studies we assumed that $\sigma_{x(y)}^{\text{ion}} = \sigma_{x(y)}/\sqrt{2}$, where $\sigma_{x(y)}$ is the rms horizontal

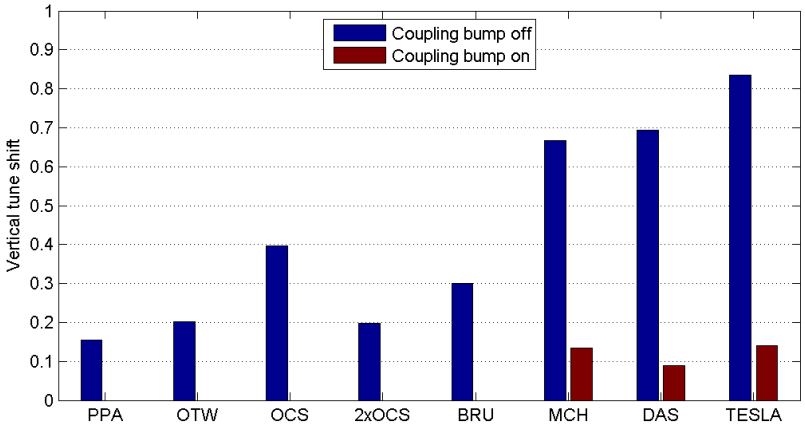

Figure 3.105: Maximum tune shifts from CO^+ ions in the reference lattices.

(vertical) electron beam size. The vertical tune shifts from CO^+ during the damping process in each of the reference lattices are shown in Figures 3.95–3.101; the maximum tune shifts at any point during the damping process are summarized in Figure 3.105. Again, H^+ ions have a significantly weaker effect than CO^+ ions, and the tune shifts resulting from H^+ ions are two orders of magnitude smaller than from CO^+ ions.

The tune shift is sensitive to the optics; in particular, a large beta function results in a large tune shift. The tune shifts in OCS are larger than in the other circular lattices for that reason. The large beta functions in the straights of the dogbone lattices result in large tune shifts when the beam is not coupled; however, with the coupling bumps turned on, the beam size is increased without any real increase in the beta functions, and the tune shifts are reduced as a result.

The tune shifts from CO^+ are large, and could limit operational performance of the damping rings, particularly in the case of the 6 km rings. Using ion-clearing gaps, as discussed next, could reduce the tune shifts to tolerable levels.

Gaps Between Bunch Trains

Arranging the bunches in the ring in short trains separated by gaps can suppress ion effects if the gaps are sufficiently long to clear ions between the

trains. The shorter the train, the lower the ion density, and the slower the instability growth rates.

We must also consider the length of the gap necessary for clearing ions accumulated during the passage of a bunch train. Let $t_{\rm gap}$ be the length (in seconds) of the gap and T be the total length (in seconds) of the bunch train plus the gap. The stability condition for ions trapped over the passage of several trains can be expressed in terms of the ion oscillation frequency ω_i:

$$n\pi < \theta < n\pi + 2\tan^{-1}\frac{2}{\omega_i t_{\rm gap}} \tag{3.94}$$

where $\theta = \omega_i(T - t_{\rm gap})$. $\theta/2\pi$ is the number of oscillations an ion makes during the passage of a bunch train. Figure 3.106 shows the stable ranges of θ as a function of the gap length normalized to the ion oscillation frequency. During the damping process, the beam size shrinks and the ion frequency changes; oscillations that were stable can become unstable, and vice versa. As a result, ions are unlikely to be trapped for many bunch passages, even if the gap is relatively short.

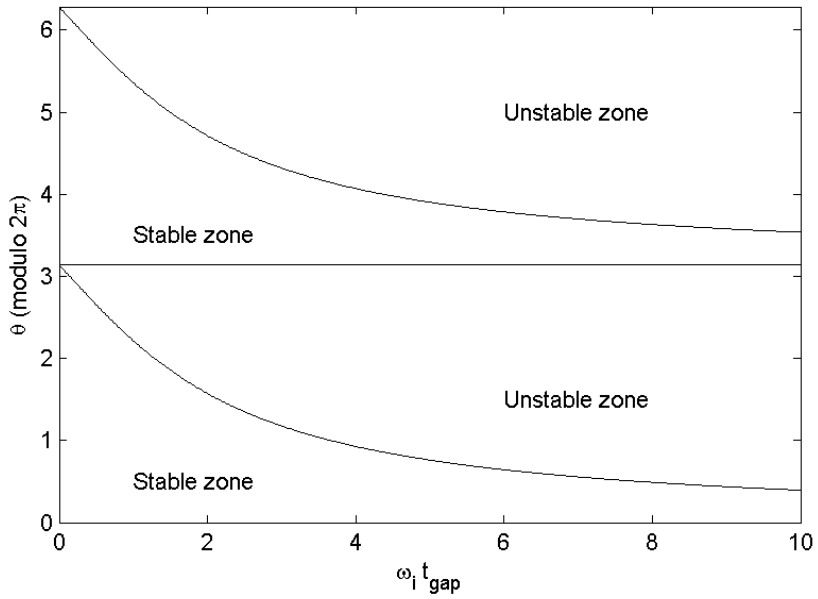

Figure 3.106: Stability of ion oscillations as a function of the length of gap between bunch trains.

Simulations suggest that the exponential decay time or "diffusion time", $\tau_{\rm ions}$, of the ion density close to the beam (within $\sqrt{3}\sigma$ of the beam center) is of the order of ion oscillation period while the beam is present. When the ion oscillation period is short, the ions are moving quickly and disperse rapidly when the gap arrives.

From the above considerations, it is clear that the density of ions depends on the length of the bunch trains, and on the length of the gap between bunch trains. Let $\lambda_i(t_{\rm gap})$ be the ion density at the end of a bunch train, when the ring is filled with a certain number of bunches arranged in trains, with gaps of length $t_{\rm gap}$ between bunch trains. Let $\lambda_{i,1}$ be the ion density in the case that the ring has a single long bunch train, with a gap sufficiently long to clear the ions completely. We can define an "ion-density reduction factor" (IRF) as the ratio of the ion density in the two cases (multiple "short" gaps, and a single "long" gap):

$$\mathrm{IRF} = \frac{\lambda_i(t_{\rm gap})}{\lambda_{i,1}} \approx \frac{1}{N_{\rm train}} \frac{1}{1-\exp(-\frac{t_{\rm gap}}{\tau_{\rm ions}})} \tag{3.95}$$

Note that in the case $t_{\rm gap} \to 0$, the ring is completely filled and ions can accumulate indefinitely: the ion density increases without limit. With a fixed gap, having a larger number of (shorter) bunch trains helps to keep the ion density low; however, for a fixed circumference and total number of bunches, the length of the gap shrinks as the number of bunch trains increases. The optimum beam fill pattern depends on the diffusion time, the circumference, and the number of bunches.

In the case of the TESLA lattice, gaps of 40 ns between trains of 20 bunches can reduce the ion density in the arcs by a factor of 7 (see Figure 3.107). In the case of OCS, the nominal fill pattern (which includes gaps of 50 ns between trains of 47 bunches) gives an IRF of 0.05; studies show that this fill pattern is close to optimal.

The ion-density reduction factor varies with time during the damping process, and depends on the optics. It is possible to optimize the fill pattern in a given lattice, and it seems likely that an IRF of 0.1 can be achieved in all the reference lattices. Even with an IRF of 0.1, the fast ion instability growth rates are fast; present technology for bunch-by-bunch feedback systems are not capable of suppressing instabilities with growth times shorter than 15 or 20 turns. With any of the reference lattices, further mitigation of the ion instabilities, beyond the use of gaps in the fill will be necessary. Possibilities include the reduction of the residual gas pressure below the values assumed in these studies (0.1 ntorr in the long straights; 0.5 ntorr in the arcs, and 2

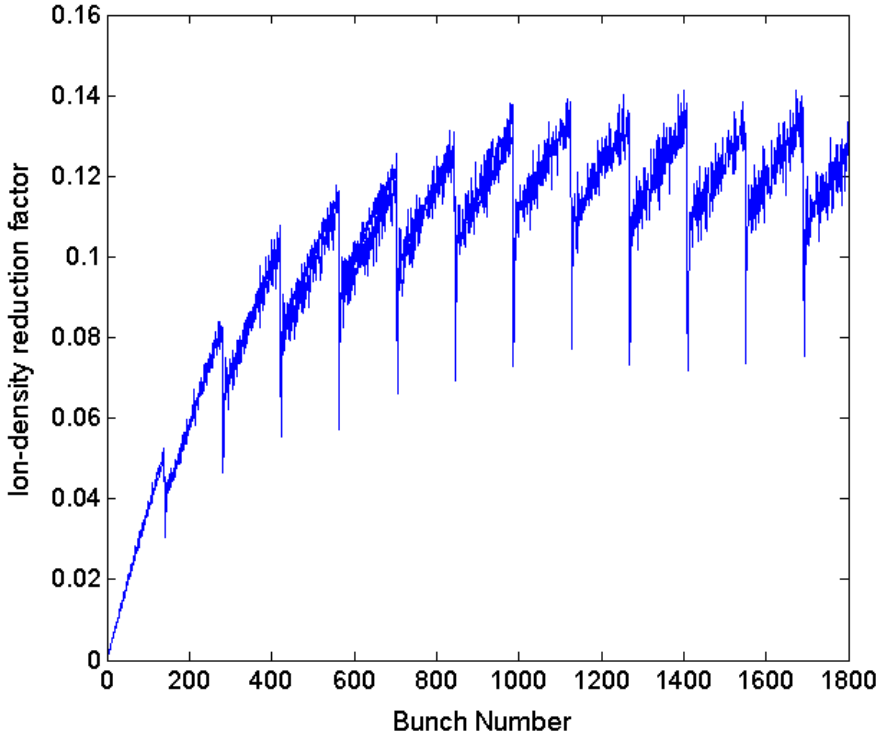

Figure 3.107: Build-up of ion density in the arcs of the TESLA lattice, with gaps between trains. Each train consists of 20 bunches with a 4 ns bunch separation; each gap between trains is 40 ns. The ion density at the end of each train, normalized to the expected density at the end of a single train of 2780 bunches, is plotted.

ntorr in the wigglers), or the use of clearing electrodes to increase the rate of dissipation of the ion cloud during the gaps.

The gaps in the KEK-B and PEP-II high-energy rings are 230 ns and 130 ns respectively [67]. In the case of the PEP-II HER, the gaps are about 1.2 times the calculated period of CO^+ oscillations in the beam, and are expected to be effective at clearing ions. Under these conditions, the growth rates of the fast ion instability are much faster than the synchrotron radiation damping rates, but are within the reach of the bunch-by-bunch feedback systems.

Simulations

The exponential growth times in the long straights of two of the 17 km reference lattices (DAS and TESLA) were estimated using a tracking code. A weak-strong model was used, in which a "weak" ion beam was represented by macroparticles, and only coherent motion of each electron bunch was allowed. The interaction between the ions and the electron beam was calculated using the Bassetti-Erskine formula. CO^+ ions were generated at a single "interaction point" in the ring. Variation in the beta function around the ring was represented by a variation in the beta function at the interaction point. All electron bunches were initially set to zero displacement. To speed up the simulations, we used a reduced bunch train of 282 bunches (instead of the nominal 2820) bunches, with the bunch charge and bunch separation increased by a factor of 10. We considered beam sizes representing both an injected beam (with normalized horizontal and vertical emittances equal to 10 μm) and an equilibrium beam (with normalized horizontal and vertical emittances 5 μm and 0.02 μm respectively). For the nominal beta functions, we used the average beta functions in the straight sections in each lattice (106 m for DAS, and 120 m for TESLA).

The simulation gives the betatron action of the last bunch in the train as a function of the number of turns. The results for 0.1 ntorr with the injected emittance in TESLA are shown in Figure 3.108. Coherent oscillations of the electron bunch grow from initial noise in the ion distribution. The oscillations grow rapidly, but saturate at an amplitude corresponding to an action of around 100 pm (the nominal vertical emittance is 2 pm). A larger spread in beta functions helps to reduce the growth rate. Figure 3.109 shows how the growth in coherent amplitude depends on the residual gas pressure; as expected, a lower pressure reduces the growth rate.

Figure 3.110 shows the simulated growth in vertical action from fast ion instability in the TESLA straights, with the beam emittances at their

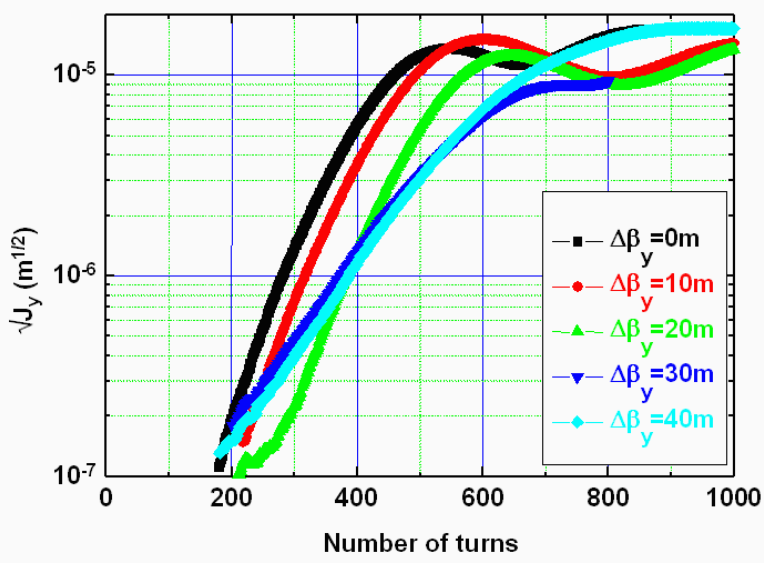

Figure 3.108: Simulation of fast ion instability in the straight section of TESLA. The square root of the coherent vertical betatron action of the last bunch in a long train is plotted as a function of turn number. The assumed residual gas pressure is 0.1 ntorr. The different colored lines represent different assumptions for the spread in beta functions.

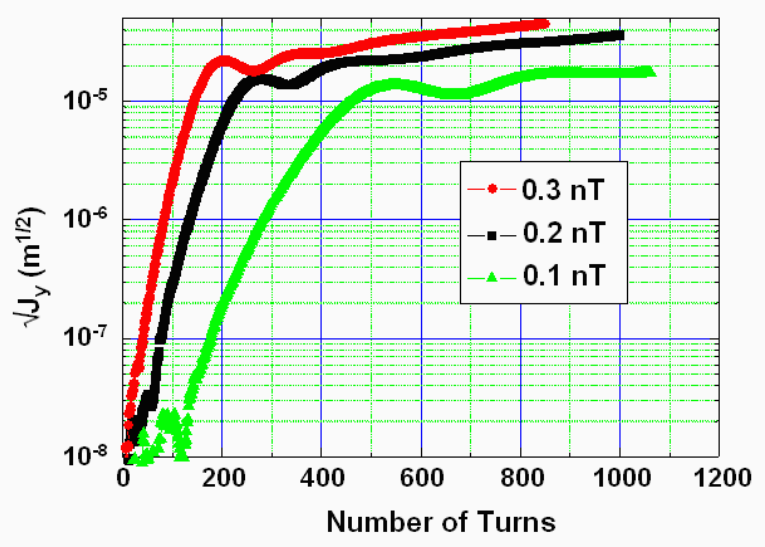

Figure 3.109: Simulated growth of coherent betatron motion of the last bunch in a bunch train in the TESLA straights for different vacuum pressures.

nominal equilibrium values. The initial growth is somewhat faster than with larger emittances, but the amplitude at which the oscillations saturate seems rather lower (but still large compared to the emittance).

Exponential growth times were estimated from the tracking results for a variety of residual gas pressures and beta spreads in the straight sections of TESLA. The results are shown in Figure 3.111. The shortest growth times, for 0.1 nT and equilibrium beam emittance, are around 1 ms. Using Equations (3.90)–(3.92), we find exponential growth times of the order of 10 μs under these conditions (assuming a relative tune spread of 0.3). For the injected beam (1 nm geometric emittance in each plane), the simulations indicate a growth time of around 4 ms; the analytical estimate gives a growth time of approximately 680 μs.

Comparable results have been obtained for another 17 km reference lattice (DAS).

Conclusions

Ion effects have been estimated analytically for the reference lattices, using theories that are in qualitative agreement with observations at existing fa-

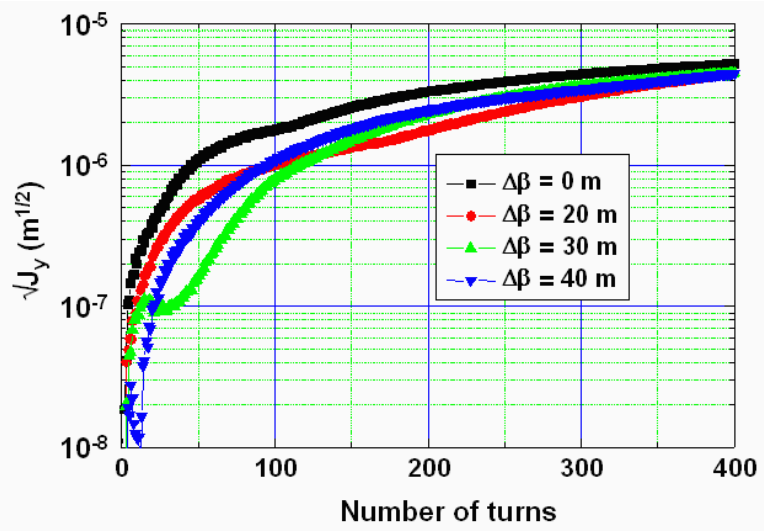

Figure 3.110: Simulated growth of coherent betatron motion of the last bunch in a bunch train in the TESLA straights with the beam emittances at their equilibrium values.

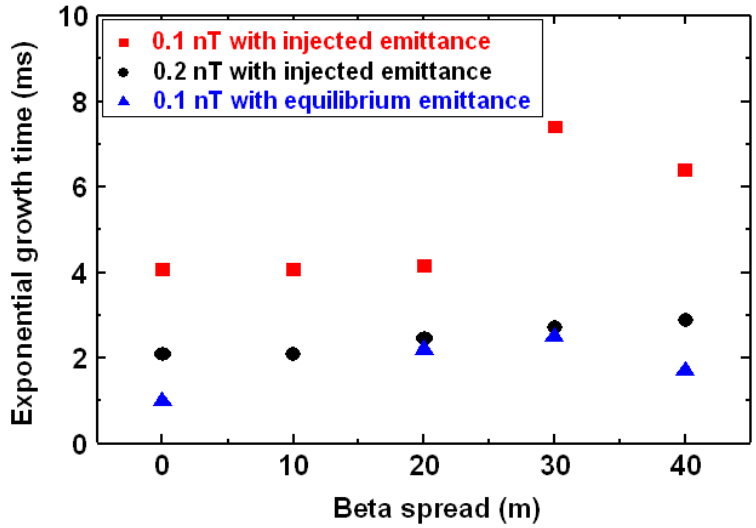

Figure 3.111: FII growth rates in the TESLA straights, from simulations with different beam emittances and vacuum pressures.

cilities. The ion effects vary with time during the damping process (because of the reduction in beam size), and also depend on the residual gas pressure and composition, the optics of the particular lattice, the bunch spacing, lengths of the bunch trains and lengths of the gaps between bunch trains. For our calculations, we assumed partial pressures of CO of 0.1 ntorr in the long straights, 0.5 ntorr in the arcs and 2 ntorr in the wigglers. The effects of CO^+ dominate over H^+. With a uniform fill, the growth time of the fast ion instability in each of the reference lattices will be less than a single turn. By introducing gaps in the fill, the growth rates can be reduced by an order of magnitude; however, this is still not sufficient to ensure beam stability even with a bunch-by-bunch feedback system. With gaps, the tune shifts expected from the ions are within tolerable limits.

The 17 km rings (MCH, DAS and TESLA) have growth rates from analytical estimates that are roughly a factor of three slower than the other rings; this is likely a combination of the optics, fill pattern and lower average residual gas pressure. Larger circumferences can help by allowing large gaps between short bunch trains.

Growth rates of coherent beam motion from the fast ion instability in the straights of two of the 17 km lattices have also been estimated by simulation, using a weak-strong approximation. The growth rates in the simulation are between one and two orders of magnitude slower than expected from the analytical theory. There are effects not included in the analytical estimates that may appear in the simulations and lead to to reduction in the growth rates, for example decoherence of the ion motion in the nonlinear potential of the beam [69]. However, such effects are not likely fully to resolve the large difference between the analytical results and the simulations. Given that the fast ion instability is a potential limiting effect in the operation of the damping rings, efforts should be made to resolve the discrepancy between the theory and simulation, and to make confident predictions of the effects to be expected in the damping rings.

Although there are still considerable uncertainties in the results, it does appear prudent to start to explore ways to reduce the impact of ion effects as much as possible. Possibilities include the reduction of the residual gas pressure to values significantly below those assumed for these studies, and the use of clearing electrodes to enhance the rate of dissipation of the ions in the gaps.

3.5 Polarization

If highly spin-polarized electron and positron beams are to be available at the interaction point(s) of the ILC, it is essential that the damping rings cause no significant depolarization. However, at first sight the enhancement of synchrotron radiation by the wigglers in damping rings has the potential to cause spin depolarization. Thus a special investigation of depolarization in the ILC damping rings has been made. In fact, there are in principle a total of three effects, associated with the damping rings, which can either reduce the value of the polarization at the interactions point(s) or add uncertainty to the direction of the polarization at the interaction point(s). These are respectively the effect of synchrotron radiation just mentioned, and two effects related to a possible mismatch of the incoming spin distribution with the "natural" spin motion in the ring.

We begin with the effect of synchrotron radiation. Spins precess in the magnetic fields (dipole, quadrupoles...) according to the Thomas-BMT equation [4]. But synchrotron radiation consists of individual photons that are emitted stochastically and therefore put some random motion (noise) into the particle orbits. The quadrupole fields are inhomogeneous. It is then easy to see that in this case, the noise is transmitted to the spin motion and that a set of initially mutually parallel spins can start to spread out, i.e. become depolarized. In principle, synchrotron radiation can also lead to a build-up of polarization via the Sokolov-Ternov effect [4].

The natural "reference direction" for describing spin motion in a storage ring or a damping ring is the unit vector $\hat{n}_0$, the periodic solution (of unit length) of the Thomas-BMT equation on the closed orbit [4]. In storage mode $\hat{n}_0$ gives the direction of the equilibrium polarization of the beam.

A damping ring for the ILC must be well enough equipped and aligned to ensure that the closed orbit distortion is so small that the design vertical emittance is attained. Then, radiative depolarization from vertical betatron motion will be suppressed. Moreover, the tilt of $\hat{n}_0$ will be small and then radiative depolarization associated with horizontal betatron motion and synchrotron motion will be suppressed [4]. Thus, on closer inspection, we expect that the depolarization of a spin polarized beam should be negligible over the few damping times that the beam is in the ring. In particular, if one stays away from first order spin-orbit resonances [4], the depolarization time will be at least many minutes. The Sokolov-Ternov effect is irrelevant on this time scale. In any case, the alternating signs of the strong and dominating wiggler fields ensure that the maximum Sokolov-Ternov polarization would be below 1%.

In storage rings with beams at equilibrium, the rate of depolarization can often be estimated by analytical means [4, 37]. However, in damping rings the beams come to equilibrium only after several damping times. Then the depolarization is estimated using Monte-Carlo tracking algorithms which simulate the stochastic emission of radiation. Two such codes come into question, namely Merlin [78], and SLICKTRACK [4] which is used at DESY for simulating depolarization in HERA. SLICKTRACK is an extension, by inclusion of a Monte-Carlo simulation of 3-D spin motion, of the code SLICK (= thick lens and faster version of the code SLIM, for linearized spin motion).

For the damping rings of the ILC, radiative depolarization has been estimated using SLICKTRACK. Two of the seven damping ring designs, namely the 17 km TESLA ring and the 6 km OCS ring, have been considered. Realistic misalignments were included and the closed orbit was corrected. The emittances of the injected beam were twice as large as those planned for the real setup. Two energies were chosen: the design energy of 5.066 GeV, an energy far from first order spin-orbit resonances, and 4.8 GeV, an energy close to a first order synchrotron resonance.

In spite of these non-optimal choices of initial conditions, SLICKTRACK showed that for both energies, and over the time when a beam is in a damping ring, the loss of polarization was negligible, thus confirming the expectations. Example results are illustrated for the OCS ring in Figures 3.112 (4.8 GeV) and 3.113 (5.066 GeV) which show the typical time evolutions of the spin distribution, at a fixed point in the ring.

For these calculations, it is assumed that the direction and value of the injected polarization is the same at all points in phase space and, in particular, that the polarization is initially parallel to $\hat{n}_0$. Then we set all spins parallel to $\hat{n}_0$, corresponding to 100% initial polarization[3]. The curves in Figures 3.112 and 3.113 show the mean squares of the angles of tilt of spins away from $\hat{n}_0$ as the particle distributions come to equilibrium. After about 15 longitudinal damping times (8000 turns), the mean squared angle is at most a few 10^{-6} (radians)^2, implying a relative loss of polarization of the order of about 1 part in a million. The tilt of $\hat{n}_0$ from the vertical is around 1.5 milliradians in these examples. The very different levels of spin diffusion exhibited in Figures 3.112 and 3.113 reflect the distances from the first order

[3]Note that the behaviors of different ensembles of spins are indistinguishable if they have the same spin density matrix. For fermions this means that the ensembles have the same polarization vector. We can then choose the simplest spin distribution compatible with a given polarization. Thus, to simulate polarizations less than 100% we would set some spins parallel to $\hat{n}_0$ and some antiparallel to $\hat{n}_0$.

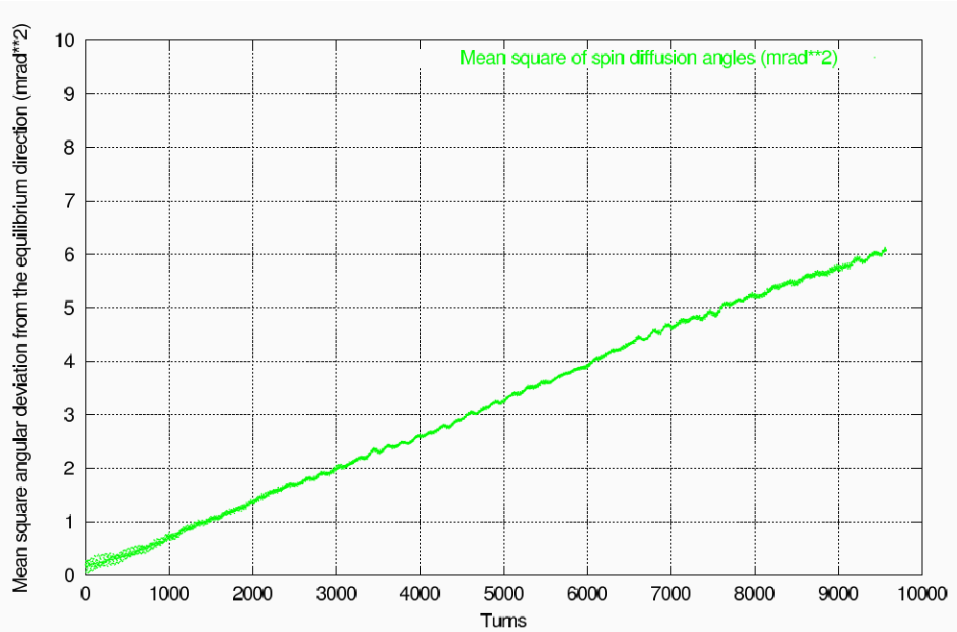

Figure 3.112: Spin diffusion in the OCS lattice at 4.8 GeV. The plot shows the mean square angle (mrad^2) of tilt of the spin away from $\hat{n}_0$ *vs* turn number.

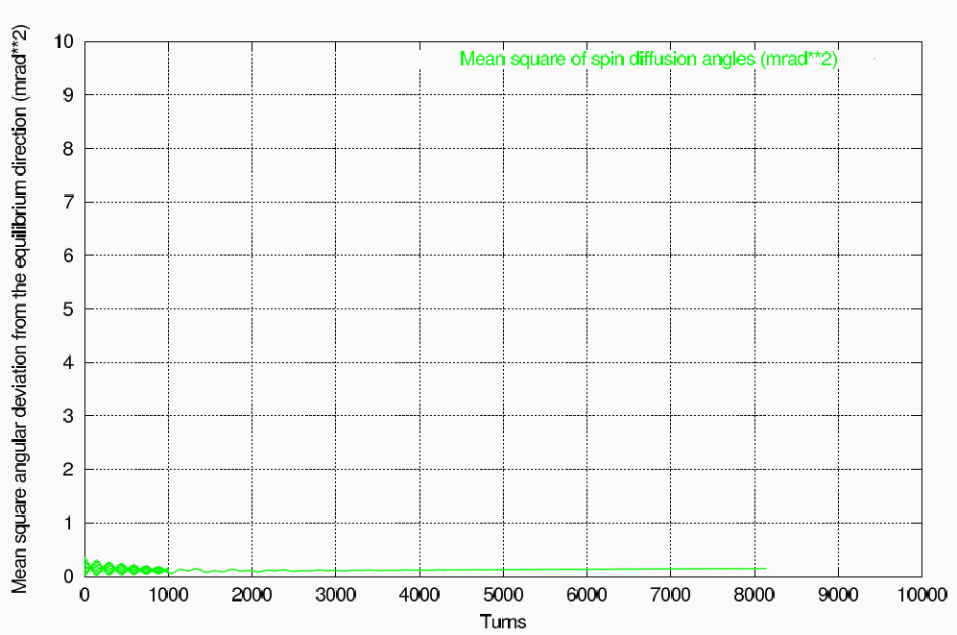

Figure 3.113: Spin diffusion in the OCS lattice at 5.066 GeV. The plot shows the mean square angle (mrad^2) of tilt of the spin away from $\hat{n}_0$ *vs* turn number.

spin-orbit resonances. Note that the approximate linearity (with respect to the number of turns) of the mean square angles, reflects the fact that the stochasticity of the photon emission causes the tips of the spin vectors to execute a random walk in the plane perpendicular to $\hat{n}_0$. If cosines of spin diffusion angles had been observed instead, such details would have been suppressed. This illustrates nicely the potential for diagnostics contained in the Monte-Carlo formalism of SLICKTRACK.

For the TESLA ring, one obtains mean squared angles of a up to few hundred 10^{-6} (radians)^2. One reason for this is that even for perfect alignment, $\hat{n}_0$ can be tilted by several milliradians from the vertical by the presence of the vertical bends needed for following the terrain.

We now come to the other two effects alluded to earlier. Whereas radiative depolarization is irreversible, the other two effects are not associated with radiation and are then governed by reversible equations of spin motion. Both can be understood by starting from the concepts of "equilibrium spin-orbit motion" and the so-called "invariant spin field" [3, 31]. Briefly, if the beam is in equilibrium with non-zero emittances and spins are set initially parallel to $\hat{n}_0$, the spin distribution will then fluctuate; see, for example, Figure 9 in [31]. We see evidence of this effect, overlaid with the effects of radiation, during the first 1000 turns in Figures 3.112 and 3.113. After the first 1000 turns, the particle amplitudes have damped down, and with them the fluctuations of the spin distribution. However, at 5.066 GeV the initial fluctuations determine the final mean square spin angles. Nevertheless, in the case of the damping rings, the effects of such fluctuations are negligible. Note that earlier work with Merlin for 1.98 GeV in the NLC damping rings [81] which confirmed the positions of spin-orbit resonances, did not include synchrotron radiation and was therefore concerned with just these kinds of fluctuations.

A second and much more important effect (but which is of basically the same nature) is illustrated in Figure 3.114. Here, all spins are set initially at 100 mrad from $\hat{n}_0$, and in the same direction. It is seen (first curve) that the mean square spin angle is so large that it is not significantly influenced by synchro-betatron motion and synchrotron radiation. The second and third curves indicate that the projections of the polarization on the radial and longitudinal directions oscillate almost sinusoidally in antiphase, as the polarization vector basically just precesses around $\hat{n}_0$. In other words, in contrast to other situations [30], there is essentially no decoherence of the spins so that they remain almost parallel to each other.

Thus, if the injected polarization is tilted sufficiently from $\hat{n}_0$, the direction of the polarization at ejection will depend on the time at which the

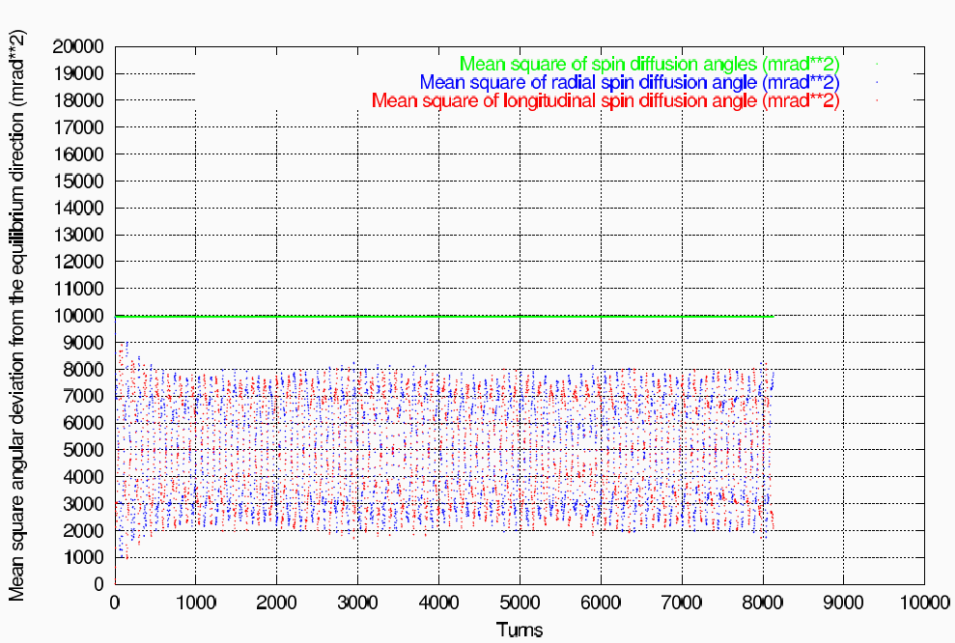

Figure 3.114: Spin diffusion in the OCS lattice at 5.066 GeV, for spins initially at 100 mrad from $\hat{n}_0$. The plot shows the mean square angles (mrad^2) of tilt of the spin away from $\hat{n}_0$ *vs* turn number.

kickers are fired. That, in turn, will determine the direction of the polarization vector at the interaction point(s). It is therefore necessary to ensure that the injected polarization is sufficiently parallel to the vertical, or for these damping rings, to $\hat{n}_0$. Note that even for 100 milliradians the vertical component of the polarization is still 99.5% of the ideal.

The radiative depolarization is negligible also with injected transverse emittances ten times as large as those planned for the real setup. This, and the other results presented here, therefore suggest that it is unlikely that the degree of radiative depolarization is a factor in the choice of the damping ring design. Instead, it is likely to be more important to ensure that the injected polarization vector is close enough to the vertical to satisfy the requirements of the experiments mounted at the interaction point(s). These results for the ILC damping rings will be checked in the future using Merlin with radiation included.

Chapter 4

Technical Subsystems

There are a number of technical subsystems in the damping rings, for which choices need to be made between various options. For example, the injection and extraction kickers may be based on Fourier series pulse compression systems, or on relatively conventional strip-lines driven by fast pulsers. For the damping wigglers, the choices of technology are permanent magnet, normal-conducting electromagnetic, or superconducting devices. In this chapter, we consider the various subsystems, and evaluate the principal technology options.

4.1 Injection and Extraction Kickers

The kickers must be capable of injecting and extracting individual bunches, while leaving other stored bunches undisturbed. The general specifications for the injection/extraction kickers are given in Table 4.1. During injection and extraction, the kickers fire at a repetition rate set by the bunch spacing in the linacs (between 3 MHz and 7 MHz), for a time given by the linac pulse length (1 ms). Each time the kicker fires, it produces a pulse with rise/fall times less than the bunch spacing in the damping ring, so that individual bunches are injected or extracted, while other bunches in the ring are undisturbed. Some schemes are possible that allow slower fall times than rise times. The kicker parameters are challenging. As well as fast rise and fall times, there are demanding requirements on the pulse-to-pulse stability, to keep the bunch-to-bunch jitter of extracted bunches as small as possible. The stability requirements may be eased by using a feedback system in the extraction line (acting across a "turn-around") to correct any jitter.

Table 4.1: Assumed optics and general specifications for the injection/extraction kickers.

Kick angle	0.6 mrad
β_x at kicker and septum	50 m
Kicker-septum R_{12}	50 m
Beam offset at septum	30 mm
Kicker repetition rate (minimum)	3 MHz
Kicker repetition rate (maximum)	6 MHz
Kicker macro-pulse length	1 ms
Kicker rise/fall time	$<$ bunch spacing
Pulse-to-pulse stability	0.07%
Residual kick on preceding or following bunch	0.42 μrad

Two principal options for the kicker technology have been considered. The first uses RF deflecting structures, with RF frequencies and amplitudes combined in such a way as to give the desired pulse timing ("Fourier series kicker"). The second uses conventional strip-lines, fed by a fast pulser ("strip-line kicker").

4.1.1 Fourier Series Pulse Compression Kicker

It is interesting to consider a design in which a pulsed kicker is replaced by a low-Q RF device filled with a broadband signal whose amplitudes, frequencies, and phases correspond to the Fourier components of a periodic, narrow pulse. Instead of energizing the system only when a bunch was about to be injected (or extracted) to the damping ring, the device would run continuously. This might allow the frequencies, phases, and relative amplitudes of the impulse to be determined with great precision. With a properly chosen set of parameters, the system would kick every M^{th} bunch in a train, leaving undisturbed the train's other $(M-1)$ bunches. Injection (or extraction) of an entire bunch train would be completed by the end of the M^{th} orbit through the system. Here, we consider a kicker with M =60, admitting the construction of a 6 km circumference damping ring. A detailed description of the studies has been prepared [28].

The kicker system would be installed in a bypass section of the ring. During injection, a deflector system would route the beam through the bypass. Once injection was completed, a gap between bunch trains would allow time for the deflectors to be turned off. The beam would then orbit in the damping ring, bypassing the kicker. The deflectors would be energized again

at extraction, routing the beam through the kicker.

We are focusing on a particular implementation in which an RF amplifier sends a broadband signal down a waveguide to a $Q \approx 25$ RF structure. Dispersion in the waveguide shifts the relative phases of the Fourier components of the signal so that it is compressed: RF power arrives at the RF structure in short, periodic bursts, filling it in order to eject the target bunch without disturbing adjacent bunches. The RF structure is able to store energy, so its maximum field strength is approximately 20 times greater than the maximum field strength in the downstream end of the waveguide.

A schematic representation of the kicker is shown in Figure 4.1. Our studies assume the values for the kicker's parameters shown in Table 4.2.

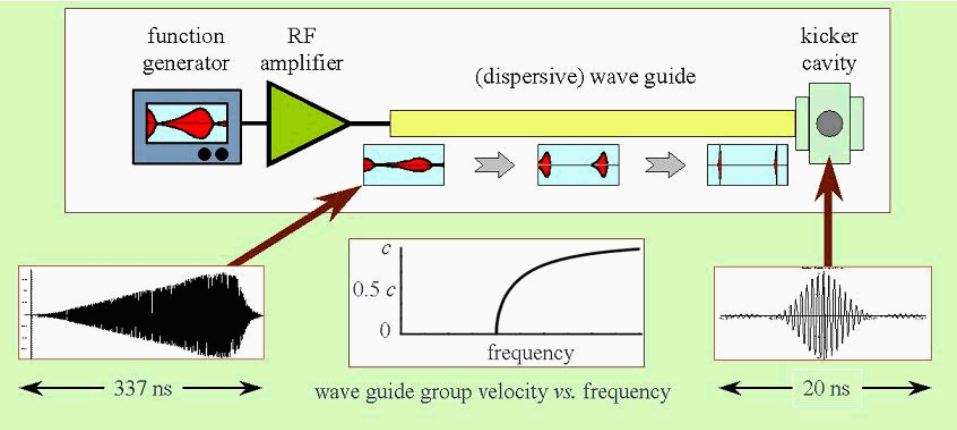

Figure 4.1: Schematic representation of a Fourier series pulse compression kicker.

The kicker's field integral is a function of time. We use the term "major zero" to refer to the kicker's (zero-valued) field integral when an unkicked bunch passes through the device. Since the bunch spacing in a train is uniform, the time interval between major zeroes is the same as the interval between the kicking impulse and the first major zero.

We have been studying an impulse function of the following form:

$$A(t) = \frac{1}{N^2} \frac{\sin^2\left(\frac{1}{2}\omega_{DR}t\right)}{\sin^2\left(\frac{1}{2}\omega_L t\right)} \cos\left(\omega_{RF}t\right) = \frac{1}{N^2} \frac{\sin^2\left(\frac{1}{2}N\omega_L t\right)}{\sin^2\left(\frac{1}{2}\omega_L t\right)} \cos\left(\Gamma N\omega_L t\right) \quad (4.1)$$

The initial term is a normalized ratio of squares of sine functions: this envelope function sets the spacing between kicking peaks and major zeroes.

Table 4.2: Fourier series pulse compression kicker parameters.

Parameter	Symbol	Value
Main linac bunch frequency	$f_L(\omega_L \equiv 2\pi f_L)$	3 MHz
Damping ring bunch frequency	$f_{DR}(\omega_{DR} \equiv 2\pi f_{DR})$	180 MHz
RF structure center frequency	$f_{RF}(\omega_{RF} \equiv 2\pi f_{RF})$	1845 MHz
RF structure Q	Q	25
Waveguide cutoff frequency	f_{cutoff}	1300 MHz
"On" field integral	$A(0)$	(100 ± 0.07) gauss-meters
"Off" field integral	$A(t)$	(0 ± 0.07) gauss-meters
f_{DR}/f_L	N	60
f_{RF}/f_{DR}	Γ	10.25
f_{RF}/f_L	ΓN	615
Bunch length (rms)	σ_z	6 mm
Bunch length (rms)	σ_z/c	~ 20 ps

The parameter N is the ratio of the bunch spacing in the main linac to the bunch spacing in the damping ring. Besides controlling the locations of the major zeroes, the envelope function also flattens the kicker's field integral $A(t)$ in the vicinity of the zeroes, since the ratio of the squares of sine functions also has zero slope at major zeroes in $A(t)$. As a result, the variation in field integral between the center and ends of an individual (unkicked) bunch is insignificant.

A graph of the Fourier amplitudes of $A(t)$ is shown in Figure 4.2. These amplitudes will yield a unit strength kicking pulse.

Figure 4.3 shows the kicking peak in the time interval from -50 ps to +50 ps. The shape is dominated by the high frequency modulation term $\cos(\Gamma N \omega_L t)$. The kick drops rapidly away from its maximum at $t = 0$. This raises two separate issues: first, whether the kicker's injection efficiency is adequate; and second, whether the extracted bunches are sufficiently free of kicker-induced distortion, so that head-center-tail effects do not degrade the ILC's luminosity. Recall that the rms length of a damping ring bunch is 20 ps. To address these issues, one promising strategy would be to install a corrector in the injection and extraction lines to compensate for the time dependence of the impulse delivered to a bunch. A single-frequency RF system running at f_{RF} could deliver an impulse of the opposite sign to bunches shortly before(after) injection(extraction). The residual error in kick after a corrector is about one third as large as the required kicker precision of 0.07%. Modifications to the kicker RF system intended to flatten

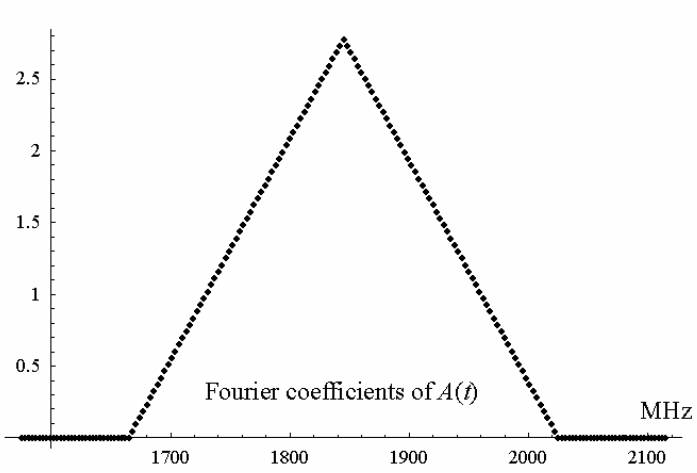

Figure 4.2: Fourier amplitudes of the field integral impulse $A(t)$. The peak is at frequency $f_{RF} = 1845$ MHz; the amplitudes become identically zero at $f_{RF} \pm 180$ MHz. These amplitudes will yield a unit strength kicking pulse.

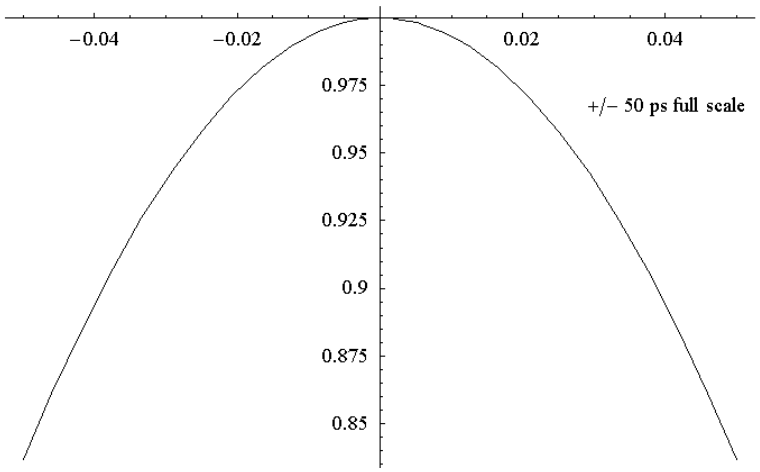

Figure 4.3: Kicking peak in a time interval 50 ps around $t = 0$. The rms bunch length is 20 ps.

the kicking peak will generally increase the required amplifier bandwidth, through introduction of a low frequency tail, higher frequency bands in the vicinity of harmonics of the cavity center frequency, or both.

The Fourier series kicker needs to apply a 10% bandwidth impulse to kicked bunches. It is an interesting technical challenge to devise a method to sum the effects of the various frequency components. An early (naïve!) conception of the kicker used one cavity for each frequency component, letting the beam sum the effects of the individual Fourier components. Another idea [27], originally described by Joe Rogers, uses a low-Q cavity that can support the range of frequencies comprising the kicking pulse.

It is possible that the kicker system's sensitivity to errors might be reduced (at the expense of greater input power) if the cavity center frequency were chosen to be above or below the kicking pulse's frequency band. This is worth investigating in detail at a later time.

The pulse is delivered to the cavity through a waveguide. We consider a rectangular waveguide with cutoff frequency $f_{cutoff} = 1300$ MHz driven in its dominant mode [15]. The cutoff frequency depends on the waveguide's geometry, shown schematically in Figure 4.4. When $b > a$, we have $f_{cutoff} = c/(2b)$, where c is the speed of light in vacuum. Our 1300 MHz waveguide has $b \approx 11.5$ cm.

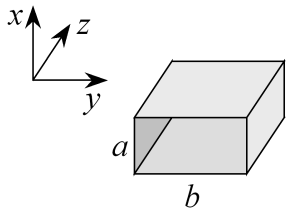

Figure 4.4: Waveguide geometry. Power propagates in the $+z$ direction. For this waveguide, $f_{cutoff} = c/(2b)$.

Besides providing a path between the amplifier and the RF structure, the waveguide serves as the dispersive transport that compresses the amplifier signal. The waveguide's group velocity as a function of frequency is:

$$\frac{v_g}{c} = \sqrt{1 - \left(\frac{f_{cutoff}}{f}\right)^2} \tag{4.2}$$

Figure 4.5 shows $v_g(f)$ in the frequency range 0 to 4000 MHz. Energy pumped into the upstream end of the waveguide will propagate down the

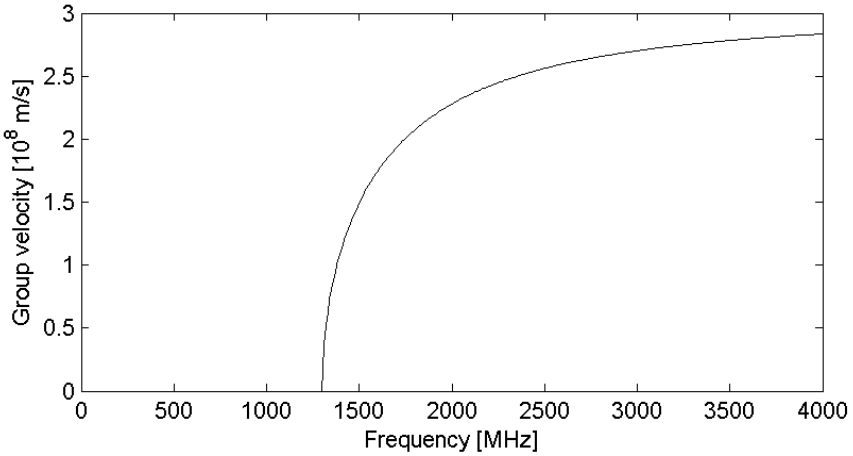

Figure 4.5: Waveguide group velocity as a function of frequency in the range 0 to 4000 MHz. The cutoff frequency f_{cutoff} in this case is 1300 MHz.

guide with speed equal to the group velocity, filling the waveguide. The phase velocity $v_p(f) = c^2/v_g(f)$ determines the change in phase along the length of the waveguide for individual frequency components. Since the relative phases of various Fourier components will vary with position along the length of the waveguide, it is possible to deliver a compressed pulse to the cavity through careful injection of a signal whose peak power is not very different from its average power. This is shown in Figure 4.6, where we plot the field in the waveguide as a function of time, at different distances from the downstream end of the waveguide. The field amplitude at the entrance to the waveguide is roughly 1% of the maximum field inside the RF kicking structure.

We have not yet optimized the length or cutoff frequency of the waveguide. Operating with a cutoff frequency closer to the cavity's center frequency would provide more dispersion per meter, allowing use of a shorter waveguide at the expense of greater sensitivity to inaccuracies in waveguide geometry.

To estimate the required amplifier power, we assume that a 100 Gauss-meter impulse (3 MeV/c) is adequate. The kicking impulse under consideration requires an amplifier capable of generating signals in the frequency range (1800 ± 180) MHz. Recall that the electric and magnetic fields in a resonant structure are 90° apart in phase. As a result, we can estimate the energy stored in the RF structure if we know its volume and the maximum

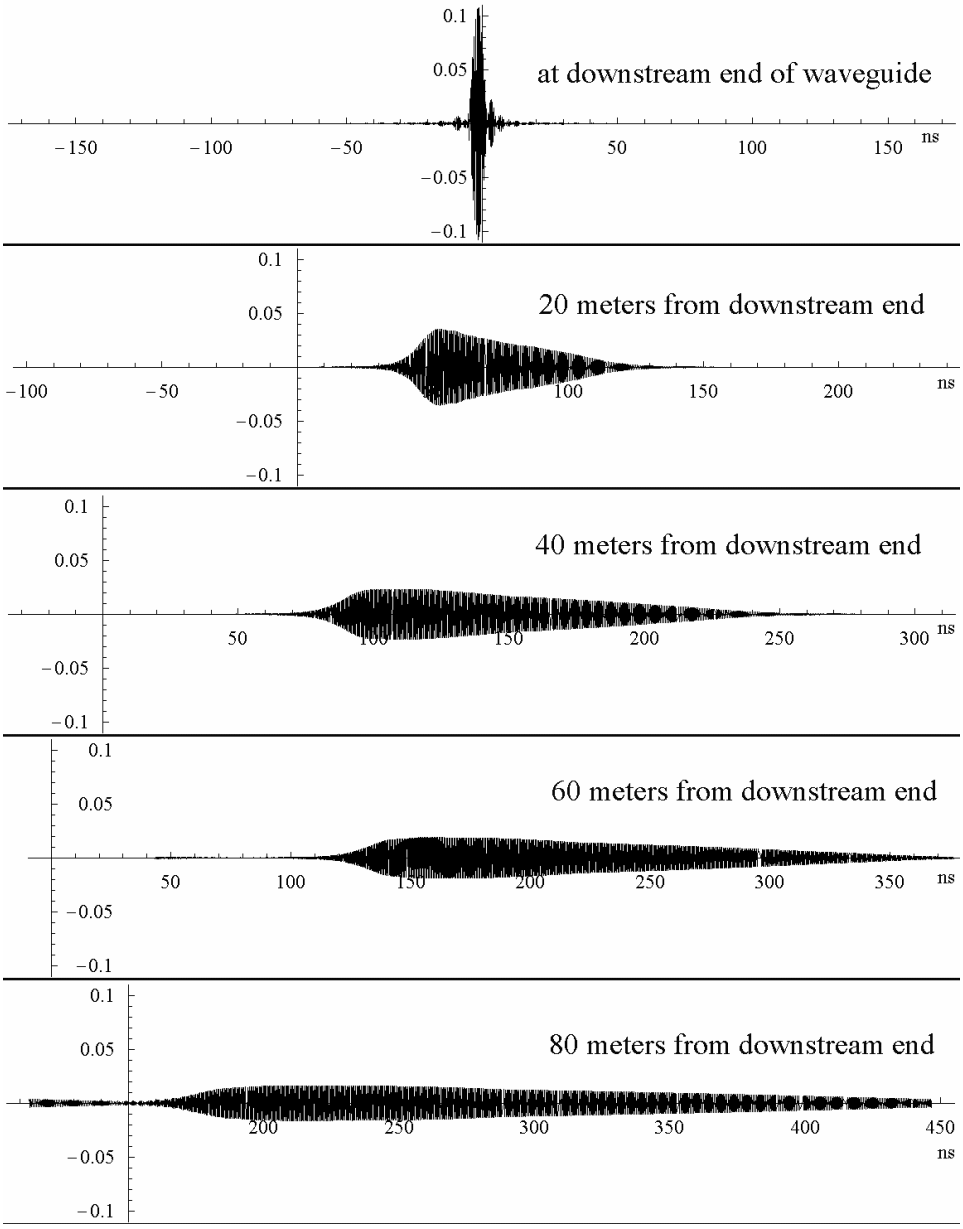

Figure 4.6: Fields as functions of time at different distances from the downstream end of the waveguide.

electric or magnetic field it contains. Consider a generic RF device, shown schematically in Figure 4.7. The energy densities (in mks units) associated with electric field E and magnetic field B are $\epsilon_0 E^2$ and B^2/μ_0. To inject or extract a bunch, the field strength in the kicker must satisfy:

$$\langle E \rangle L \geq 3 \text{ MeV} \tag{4.3}$$

or

$$\langle B \rangle L \geq 0.01 \text{ T} \cdot \text{m} \tag{4.4}$$

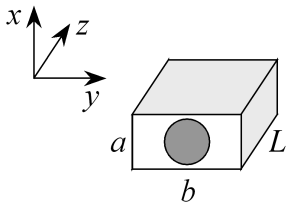

Figure 4.7: Generic RF kicking structure. The beam travels in the $+z$ direction.

The average values of $\sin z$ and $\sin^2 z$ over the interval $(0, \pi)$ are $2/\pi$ and $\frac{1}{2}$ respectively. If we assume the fields in the RF structure vary sinusoidally with z for a half wavelength along the structure's length, we have:

$$\frac{\langle E^2 \rangle}{\langle E \rangle^2} = \frac{\langle B^2 \rangle}{\langle B \rangle^2} = \frac{\pi}{4} \tag{4.5}$$

so that:

$$\langle E^2 \rangle = \frac{\pi}{4} \left(\frac{3 \text{ MeV}}{L} \right)^2 \tag{4.6}$$

and

$$\langle B^2 \rangle = \frac{\pi}{4} \left(\frac{0.01 \text{ T} \cdot \text{m}}{L} \right)^2 \tag{4.7}$$

As a result, the energy stored in the RF device will be:

$$U = abL\epsilon_0 \langle E^2 \rangle = abL \frac{\langle B^2 \rangle}{\mu_0} = \frac{ab}{L} 62.5 [\text{Jm}^{-1}] \tag{4.8}$$

A device with $a = b = 5$ cm and $L = 10$ m will hold energy $U = 0.015625$ joules. Since the kicker is filled at 3 MHz, it requires 47 kW of RF power, neglecting losses and coupling efficiencies. Note that the transverse electric

field inside an RF structure of these dimensions is approximately 300 kV/m. It appears that this power range, frequency and bandwidth suggest the use of a traveling wave tube amplifier (TWTA) rather than a klystron [51]. We have not yet made more than a cursory investigation of technical issues associated with the choice of amplifier.

We imagine driving the RF amplifier input with a programmable function generator. The device could be reprogrammed to compensate for drifts in the behavior of the amplifier, waveguide, and RF structure. We have not yet selected a commercial device with suitable properties.

We have not modeled the coupling efficiencies between amplifier and waveguide or waveguide and RF structure. It is possible that reflections at the coupler between the waveguide and the cavity will require a circulator to be installed in the waveguide. We have not studied the effects of losses in the waveguide, or of nonlinear behavior anywhere in the system besides the amplifier. We have not yet simulated in detail the kicker's effect on bunches that pass through it a number of times before being extracted.

The TESLA Technical Design Report [72] describes the maximum allowable kicker error as 0.07 Gauss-meters, both for bunches that are to pass through the kicker undisturbed (when its field integral is zero) and bunches that are to be extracted. Imperfections or drifts in amplifier performance, waveguide geometry, RF structure parameters, and bunch timing will all contribute to kicker performance errors, which can be corrected through adjustment of the signal produced by the programmable function generator. Small corrections can be made through adjustment in overall amplitude and timing of the function generator signal; larger adjustments will require changing the mix of Fourier amplitudes and phases in the signal sent to the RF amplifier.

We generally find that errors that are recognized can be corrected through reprogramming of the function generator that drives the amplifier. Not all problems can be remedied through clever use of a low-level RF system to recognize impulse inaccuracies: noise, mixed with amplifier nonlinearities can introduce errors that cannot be removed through reprogramming [28].

Groups from UIUC and FNAL are collaborating on the engineering studies necessary to see if the concept of a Fourier series pulse compression kicker is workable. These groups have plans to use the A0 16 MeV electron beam at FNAL for initial kicker tests and they have begun studies of a fast stripline kicker at A0 in order to establish the infrastructure necessary for more sophisticated RF kicker tests there [29].

4.1.2 Fast Strip-Line Kicker

The damping ring injection/extraction kickers may be constructed from strip-lines driven by fast high-power pulsers. The strip-lines consist of two long, "parallel plate" electrodes within the vacuum chamber on opposite sides of the beam; a voltage pulse traveling down the electrodes produces electric and magnetic fields that deflect the beam. For relativistic bunches traveling in the same direction as the voltage pulse, the deflections from the electric and magnetic fields cancel: to achieve a net deflection, the voltage pulse must be traveling in the opposite direction to the bunches, in which case the electric and magnetic fields produce equal deflections acting in the same direction.

The voltage required for a given deflection can be estimated from a very simple model, as follows. If the strip-lines consist of parallel plates of length L and separated by a gap d, then a voltage between the plates V will produce a deflection:

$$\Delta p_x = 2g\frac{eV}{E}\frac{L}{d} \tag{4.9}$$

where E is the beam energy, the factor of two accounts for the combined effect of the electric and magnetic fields, and g is a geometry factor (< 1) that accounts for the finite width of the electrodes. For a kicker with rise/fall times of a few ns, the strip-line length L must not be longer than about 300 mm. Let us assume a length of 300 mm, a gap of 30 mm, and a beam energy of 5 GeV; then to give a deflection of 0.6 mrad, a voltage pulse of 150 kV is needed. This is not practical from a single pulser. However, we can use a sequence of strip-lines, each driven by its own pulser, to provide a combined deflection; with 15 strip-lines, the required voltage pulse from each pulser is reduced to 10 kV. Using multiple pulser/strip-line units does have some advantage in reducing random jitter on the kick amplitude, which can be expected to vary as $1/\sqrt{N}$, where N is the number of units.

We should also note that with this system, there is a lower limit on the bunch separation set by the length of the strip-lines, even where the voltage pulse has perfectly "hard" edges (i.e. zero rise and fall times). The reason is that by the time the target bunch reaches the entrance of the strip-lines, the voltage pulse must already have traveled their full length (starting from the far end). Any bunch that is ahead of the target bunch by less than twice the length of the strip-lines will see some deflection from the voltage pulse. Similar considerations apply to bunches following the target bunch. For strip-lines of length 30 cm, therefore, the minimum bunch separation is 2 ns: to this must be added the true rise/fall time of the voltage pulse.

Pulsers are available commercially with specifications for the rise/fall time, peak voltage and repetition rate approaching those required for the ILC damping ring injection/extraction kickers, e.g. from FID GmbH [21] and Behlke Electronic GmbH [6]. Strip-lines have been installed to test pulsers with beam in the KEK-ATF; the strip-lines are 327 mm long, and are designed to produce deflections of 0.1 mrad with voltage pulses of 7 kV and a beam energy 1.28 GeV. This small deflection is not large enough to extract the beam, but is sufficient to cause trajectory oscillations with amplitudes of up to 300 μm, which can be observed with the BPMs. The kickers are installed so as to produce a vertical deflection in the beam; in the ILC daming rings, injection and extraction are expected to be horizontal.

Figure 4.8 shows the kicker chamber in KEK-ATF, with the strip-lines (consisting of four long curved plates; the horizontal deflecting plates are not connected) and feed-throughs. Different pulsers can be connected to the strip-lines for testing. Studies can be performed with a single bunch stored in the ring: typically, BPM readings are recorded while the bunch performs a single orbit of the ring; the kicker is located part-way round the ring, so that upstream BPMs read (close to) zero, while downstream BPMs record the trajectory resulting from the deflection applied by the kicker. The kick amplitude can be determined by fitting the trajectory in a lattice model to the recorded BPM values. A typical example is shown in Figure 4.9.

The pulser can be synchronized to the ring RF frequency. By adjusting the timing of the pulse with respect to the arrival time of the bunch at the strip-lines, and plotting the kick amplitude as a function of the pulse timing, one obtains the effective profile of the voltage pulse at the strip-lines. An example is shown in Figure 4.10. In this case, the total width of the main pulse is around 5 ns. We observe a small pulse ahead of the main pulse, and a tail of more than 5 ns following the main pulse; these effects are systematic, and if they cannot be addressed by other means, may be corrected by using compensating kickers in the damping rings.

Studies at the KEK-ATF are continuing. Although results so far indicate the feasibility of kickers with rise/fall times sufficient to allow damping ring circumferences of 6 km (with bunch separations as short as 4 ns), the full specifications have not yet been achieved. Pulse repetition rates of 3 MHz have been demonstrated, but the specifications for the pulse amplitude stability look still to be very challenging.

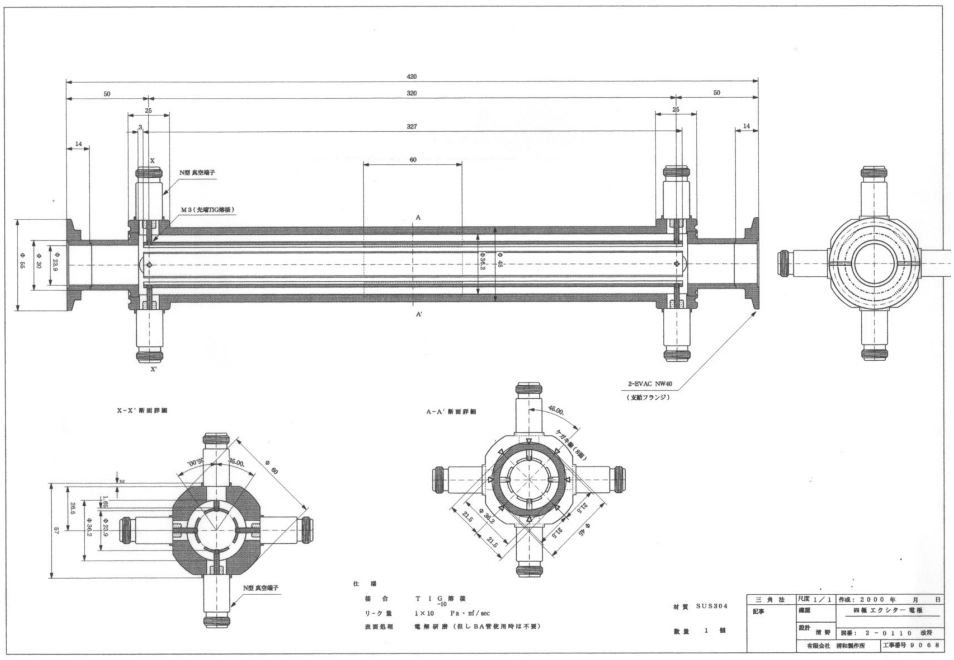

Figure 4.8: Vacuum chamber for kicker tests in KEK-ATF. The chamber contains four strip-line electrodes of length 327 mm.

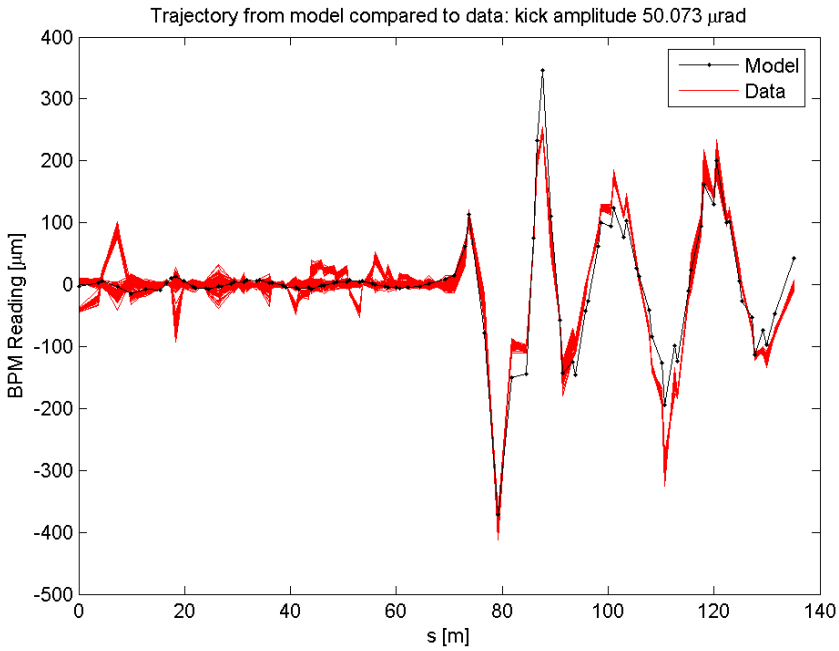

Figure 4.9: Kicked beam trajectory in the KEK-ATF. The red lines show a set of 100 different trajectories, starting with a "flat" trajectory each time. The strip-lines shown in Figure 4.8 are at the 70 m point: upstream BPMs record the unkicked trajectory, while downstream BPMs record the kicked trajectory. The black line shows a fit from a lattice model.

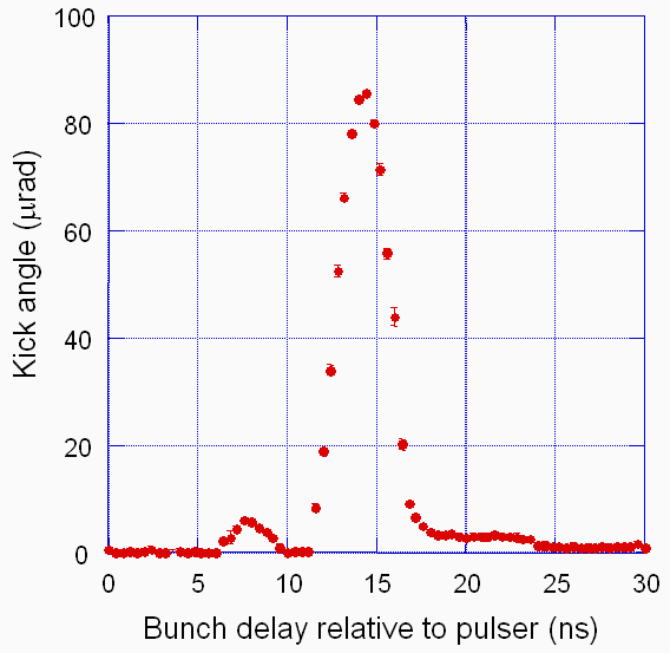

Figure 4.10: Example of kicker pulse shape in KEK-ATF kicker tests. The pulse shape is found by measuring the kick amplitude as the pulser timing is varied relative to the arrival time of the bunch at the entrance to the strip-lines. The head of the pulse is to the left of the plot. The pulser used in this case was produced by FID GmbH (FPG5-3000M).

4.2 Wiggler

In most operating electron storage rings (for example, in third-generation synchrotron light sources) most of the sychrotron radiation energy loss comes from the dipoles; the insertion devices make a relatively small contribution. In the damping rings, however, the situation is reversed: because of the need to achieve rapid damping rates, the damping rings must include relatively long, high-field wigglers. In a 17 km damping ring, the total length of wiggler (at 1.6 T peak field) must be between 400 m and 500 m. The necessary wiggler length scales with the circumference, so even a 6 km ring needs over 100 m of wiggler. The scale of the wiggler system is such that the wiggler technology is an important choice for the damping rings. The key issues are field quality, physical aperture, resistance to radiation damage, construction and operating costs, and availability. There are three principal choices for the wiggler technology that have been considered for the ILC damping rings, all of which use steel poles:

- Hybrid technology uses permanent magnet material between the poles to provide the magnetic flux.
- Normal-conducting electromagnet technology uses current passing through conventional conducting coils wound round the poles to provide the flux.
- Superferric technology uses current passing through superconducting coils wound round the poles to provide the flux.

Globally, there is a significant amount of experience with all three technologies, and the specific advantages and disadvantages are generally understood. Representative designs, appropriate for the ILC damping rings, have been produced for each type of technology, and although detailed studies of all designs have not been completed, the results obtained so far give a good indication of the merits of each.

A hybrid wiggler design was produced for the TESLA TDR [72, 74], and was later revised by widening the poles, to reduce the transverse field roll-off. A more recent design was produced by Babayan, Melkumyan, and Nikoghosyan [1]; this includes shimming of the poles to flatten the transverse field profile. Field maps are available for all these designs to allow tracking studies to determine the impact on dynamic aperture.

The power consumption of normal-conducting electromagnetic wigglers was early recognized as a significant disadvantage of this technolgy, which

has therefore received less detailed study than the other options. However, there are potential advantages which make normal-conducting electromagnetic wigglers worth considering, and an outline design has been produced for the damping rings [65], principally to allow evaluation of the fabrication and operating costs.

Superferric wigglers have been installed in CESR-c, to increase the damping rates (see for example [71] and references therein). The experience has generally been positive. A modified version of the CESR-c design was produced for the damping ring reference lattices, and has been used in tracking studies to determine the impact on dynamic aperture; the results are reported in Section 3.1.3.

In the following sections, we consider for each of the three principal technology options, the field quality, physical aperture, power consumption, radiation resistance, fabrication costs and availability.

4.2.1 Field Quality

The magnetic field in a wiggler can be highly nonlinear, and this can have an adverse effect on the dynamic aperture. The nonlinearities may be characterized in a variety of ways: for example, one may simply look at the variation in vertical field with horizontal offset, on the midplane at the center of one set of poles. The larger the field roll-off (specifically, the larger the quadratic and higher order terms in the roll-off), the larger the dynamic nonlinearities are likely to be. The variation of the vertical field with horizontal position is a function of the gap between the poles, the pole width, and the shape of the pole faces. For a given gap, increasing the pole width reduces the vertical field roll-off; for a given pole width, reducing the gap reduces the vertical field roll-off. The minimum gap in the wiggler is set by the requirements for acceptance of the large injected positron beam. The maximum pole width is essentially set by cost considerations: for a normal-conducting electromagnetic wiggler, increasing the pole width increases the power consumption; while in the case of a hybrid wiggler, increasing the pole width increases the volume of permanent magnet material needed to supply the field. A superconducting wiggler has the advantage that a large gap and a relatively large pole width can be achieved without any real cost impact. This makes it much easier to achieve a good field quality in a practical design.

Figure 4.11 shows such a variation for four designs of wiggler: two hybrid wigglers (with and without pole shims), a normal-conducting wiggler, and a superconducting wiggler. In each case, the change in the field is normalized

Table 4.3: Full vertical gap, available gap, full pole width, peak field and transverse field roll-off in four wiggler designs. Note that the hybrid-II wiggler has shimmed pole faces; the pole faces of the other designs are flat. "NC" means "normal-conducting."

Technology	Full gap [mm]	Available gap [mm]	Full pole width [mm]	Peak field [T]	$\Delta B_y/B_y(0)$ at $x = 10$ mm [%]
Hybrid-I	25	25	60	1.67	0.57
Hybrid-II	25	25	60	1.65	0.056
Superferric	76	50	238	1.67	0.009
NC EM	30	30	60	1.60	0.13

to the peak field. The advantages inherent in a superconducting technology in terms of achieving good field quality, are apparent in the fact that the field roll-off is much smaller in the superconducting wiggler design than for the other designs. However, we note that a good field quality is also achieved in the shimmed hybrid wiggler design. Shims may also be applied to the normal-conducting design, and a significant improvement in field quality would then be expected. Table 4.3 gives the gap, pole width, peak field and transverse field roll-off in each of the four designs. The "available gap" is the vertical aperture available for the vacuum chamber, and is smaller than the full gap for the superferric wiggler, because of the cryostat; for the other technologies, the available gap is the same as the full gap. A specification on the transverse field roll-off has not been set; however, it is known that the field of the superferric design has relatively little impact on the dynamic aperture (this is the "modified CESR-c" field model discussed in Section 3.1.2), whereas the hybrid-I field has a significant impact [36].

A more detailed analysis of the nonlinear components of the wiggler fields is provided by the generalized gradients [77]. These indicate the multipole components of the field as a function of the longitudinal position, and may be obtained as the coefficients of an analytical fit to the numerical field data. In the present case, a fit is obtained to the normal component of the field on the surface of a cylinder centered on the magnetic axis; by maximizing the radius of the cylinder within the region of the field data, the residuals of the fit may be kept small; in particular, the residuals decrease exponentially from the cylindrical surface towards the magnetic axis. Dragt and Mitchell [20] have recently extended this fitting technique to an elliptical surface, which increases the volume enclosed by the fit and potentially improves the accuracy of the fit. Applied to the field data from the model of the

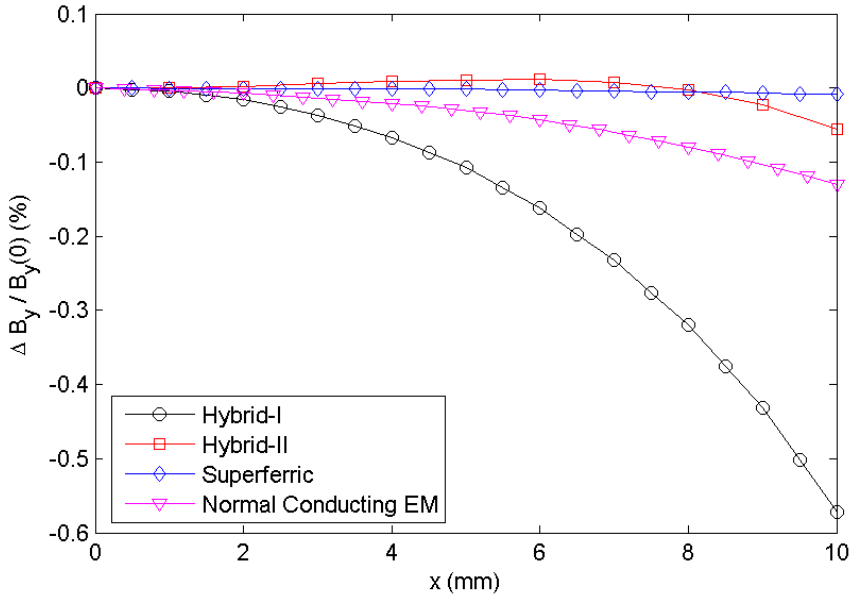

Figure 4.11: Transverse field profile of four wiggler designs. The plot shows the change in vertical field strength as a function of horizontal distance from the magnetic axis, on the mid-plane of the wiggler at the center of one set of poles. The change in field strength is normalized to the peak field. The hybrid-I design has flat pole faces; the hybrid-II design has shims on the pole faces to improve the field quality.

superferric (modified CESR-c) design, the results of the elliptical surface fit validate the results obtained from a cylindrical surface fit; though we note in this case the cylindrical surface fit benefits from the relatively large vertical aperture.

Briefly, the generalized gradients are defined as the coefficients of an analytical series expansion of the magnetic scalar potential, ψ. The magnetic field $\mathbf{B}$ is given by:

$$\mathbf{B} = \nabla\psi \tag{4.10}$$

and the scalar potential is expanded:

$$\psi = \sum_{m=1}^{\infty} \psi_{m,s}(\rho, z) \sin m\phi + \psi_{m,c}(\rho, z) \cos m\phi \tag{4.11}$$

where ρ, ϕ, z are cylindrical coordinates. Finally, the generalized gradients $c_{m,\alpha}$ are introduced as the coefficients in series expansions of the functions $\psi_{m,\alpha}(\rho, z)$ $(\alpha = s, c)$:

$$\psi_{m,\alpha}(\rho, z) = \sum_{l=0}^{\infty} (-1)^l \frac{m!}{2^{2l} l!(l+m)!} c_{m,\alpha}^{[2l]}(z) \rho^{2l+m} \tag{4.12}$$

Note that $c_{m,\alpha}^{[n]}(z)$ indicates the n-th derivative of $c_{m,\alpha}(z)$. For any functions $c_{m,\alpha}(z)$, the magnetic field defined by Equations (4.10) – (4.12) satisfies Maxwell's equations; also, any field satisfying Maxwell's equations may be expressed in the above form for suitable smooth functions $c_{m,\alpha}(z)$. It is clear that the gradient $c_1(z)$ is associated with the dipole component of the field, $c_3(z)$ is associated with the sextupole component of the field, $c_5(z)$ is associated with the decapole component of the field, and so on.

Three of the generalized gradients for single periods of the hybrid-I wiggler and the superferric (modified CESR-c) wiggler are shown in Figures 4.12 – 4.14. The gradient $c_1(z)$ (Figure 4.12) may be interpreted as the dipole component. Combined with the wiggling trajectory of a particle moving through the field, the "sextupole" gradient $c_3(z)$ (Figure 4.13) feeds down to linear focusing terms in the dynamical map, and the "decapole" gradient $c_5(z)$ (Figure 4.14) feeds down to third-order, or octupole-like, terms in the dynamical map. The significant observation here is that the gradient $c_5(z)$ is much larger for the hybrid-I design, than for the superferric design by more than an order of magnitude. This is consistent with the larger transverse roll-off seen in Figure 4.11, and it is to be expected that the hybrid-I wiggler field would have a larger impact on the dynamics in the damping rings than the superferric wiggler field.

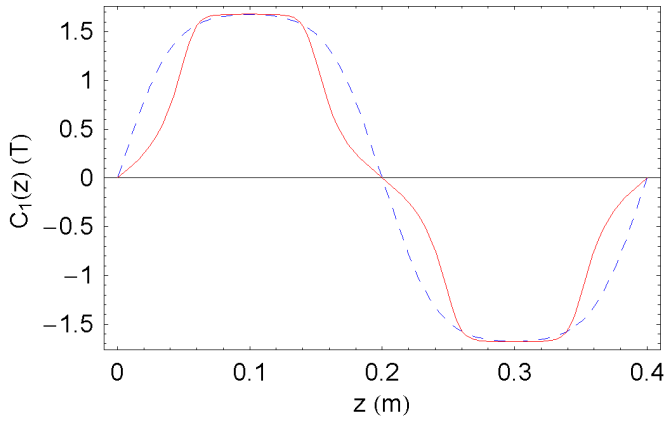

Figure 4.12: Generalized gradient $c_1(z)$ (dipole component) in two wiggler designs. The solid curve shows $c_1(z)$ in one period of the hybrid-I wiggler, while the broken curve shows $c_1(z)$ in one period of the superferric wiggler.

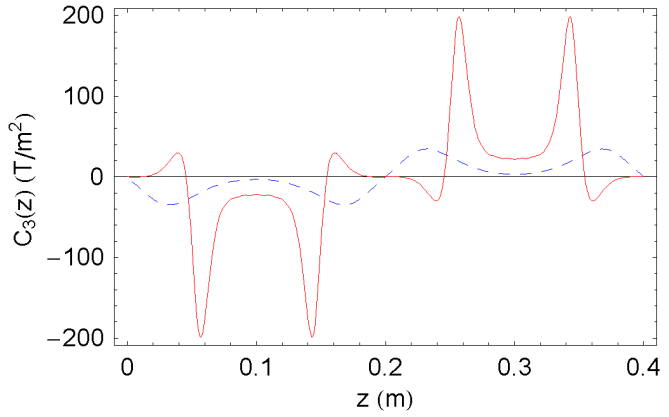

Figure 4.13: Generalized gradient $c_3(z)$ (sextupole component) in two wiggler designs. The solid curve shows $c_3(z)$ in one period of the hybrid-I wiggler, while the broken curve shows $c_3(z)$ in one period of the superferric wiggler.

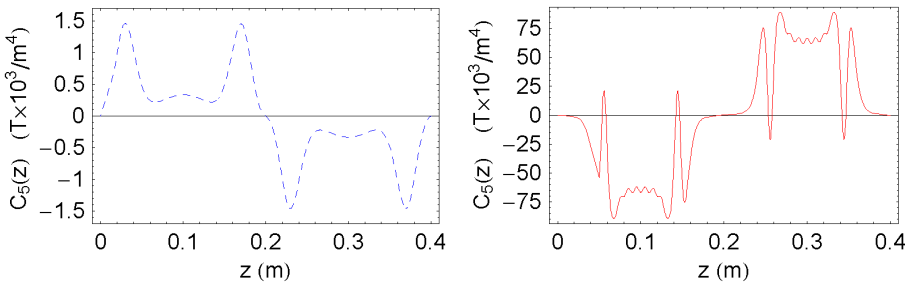

Figure 4.14: Generalized gradient $c_5(z)$ (decapole component) in two wiggler designs. The left-hand plot shows $c_5(z)$ in one period of the superferric wiggler, while the right-hand plot shows $c_5(z)$ in one period of the hybrid-I wiggler.

4.2.2 Physical Aperture

The physical aperture of the wiggler is a key consideration for the acceptance of the damping rings. Tracking with physical apertures (see Section 3.1.7) indicates that a vertical aperture of at least 32 mm will be necessary in the wiggler. The only design that achieves that goal at present is the one based on superferric technology, although the normal-conducting electromagnetic wiggler comes close. A large physical aperture is also desirable from point of view of resistive-wall wakefields (Section 3.4.3), and vacuum issues (Section 4.3).

4.2.3 Power Consumption

Normal-conducting electromagnetic and superferric wigglers require electrical power to provide the magnetic field. The power consumption of superferric wigglers is small; the total power required is of the order of 1 kW per meter. A normal-conducting electromagnetic wiggler, to provide a peak field of 1.6 T with a gap of 30 mm and a pole width of 60 mm, the power dissipated in the coils is of the order of 15 kW per meter [73, 65].

4.2.4 Radiation Resistance

The average injected power into the damping rings (at 5 GeV) is 225 kW; 0.1% injection beam losses will lead to a radiation power load of over 200 W. If the losses are distributed around the ring this may not be a severe

problem, but we must also consider the case that, because of the narrow aperture in the wiggler compared to the rest of the ring, the losses are localized in the wiggler. For normal-conducting electromagnetic and superferric wigglers, there should be no significant effects from radiation resulting from small beam losses over a period of time during normal operation. However, permanent magnet material used in hybrid wigglers can be damaged by the radiation dose, with a consequent loss in field strength.

We can make a rough estimate of the radiation dose accumulated by the permanent magnet material in a hybrid wiggler as follows. Let us consider a length of 100 m of wiggler, with a uniformly distributed radiation power load of 200 W. Because the vertical aperture is likely to be much narrower than the horizontal, we assume that all particles are lost in the vertical plane. The permanent magnet material makes up roughly half the length of the wiggler (the remainder being steel poles); if the pole width is 60 mm, and the radiation is deposited within a depth of 10 mm below the surface, the volume of magnetic material receiving a radiation dose is 0.06 m^3; for NdFeB, this corresponds to a mass of around 450 kg. Over the course of one year, assuming 5000 hours operation, the energy deposited in this mass is a little under 2 GJ. The annual radiation dose of the permanent magnet material is therefore 400 Mrad. It may be that our assumptions are pessimistic; nevertheless, even if only 10% of the beam losses (which in turn are assumed to be 0.1% of the injected beam power) are deposited in the permanent magnet material, this still corresponds to some tens of Mrad per year, at which dose some loss of magnetization can be expected to occur [41].

An alternate approach to estimating radiation dose was used in preparing the TESLA Technical Design Report [72]. Expected radiation exposures of between 10 and 50 krad/A·hr were inferred from studies of electron storage ring insertion devices [74]. The lattices presently under consideration operate with currents between 0.16 and 0.96 A. Assuming mid-range values, 30 krad/A·hr and 0.5 A, gives a yearly dose (assuming 5000 hours of operation) of approximately 75 Mrad.

Permanent magnet materials are available (e.g. SmCo) which are more resistant to radiation damage than NdFeB; however, there is a concern that these materials become activated by radiation. Given the limiting aperture inherent in the hybrid wiggler design, a suitable collimation system will be necessary to minimize damage from beam losses.

In a normal-conducting electromagnetic wiggler, the material most sensitive to radiation damage is likely to be the fiberglass/epoxy coil insulation; this material is believed to be resistant to radiation doses of at least 1 Grad

[66]. The epoxy used in a superferric wiggler is resistant to radiation doses up to 100 Mrad [66]. However, the large bore in a superferric wiggler means that beam losses should be more evenly distributed around the ring, with a consequent reduction in the overall dose in the wiggler. Additionally, the coils will be at large radius and can be well shielded from the beam. Therefore, the radiation dose in the coils of a superferric wiggler are unlikely to exceed a few hundred krad per year, and this type of wiggler should be the most robust against long-term radiation effects in the ring.

4.2.5 Costs

The total fabrication costs (for a device ready for installation) for a normal-conducting electromagnetic wiggler are estimated to be in the region of $100k per meter [45]. Additionally, power supplies will be needed, at a cost of roughly $20k per meter. Assuming 5000 hours operation per year, and a power cost of $0.10 per kW·hr, the cost of electrical power for a normal-conducting electromagnetic wiggler will be around $7.5k per meter per year.

For a hybrid wiggler with a fixed vertical gap of 25 mm and peak field of 1.6 T, the total fabrication costs are estimated at roughly $150k per meter [45]. The cost increases rapidly with increasing gap, because of the larger quantity of permanent magnet material required.

Fabrication costs for a superferric wiggler may be based on those for the CESR-c wigglers [59]; including power supplies and cryogenics, the estimated total fabrication cost is of the order of $160k per meter. Assuming that a superferric wiggler will be maintained in the cold state for the majority of each operating year, the estimated yearly cryogenics and power costs, at a rate of $0.10 per kW·hr, will be around $1k per meter per year.

4.2.6 Availability

For hybrid wigglers, the main availability issue is likely to be that of long-term radiation damage, as discussed above. Since there are no power supplies or mechanical moving parts associated with the wiggler, there are no realistic mechanisms by which individual sections of the wiggler might fail.

Normal-conducting electromagnetic wigglers may be affected by power supply or cooling system failures, or failures associated with the controls system, or the magnet itself (e.g. short circuits in the coils). However, since such failures will most likely affect individual sections of roughly 2 m, out of a total wiggler length of some hundreds of meters, the impact of the failure of individual sections will be small. For example, the vertical focusing of the

field of a single wiggler section contributes a vertical tune shift of the order of 0.01, which may easily be compensated by tuning the adjacent quadrupoles. There will be a degradation of damping time of the order of 1%, and an increase in emittance of less than 1%. Under these circumstances, failure of an individual wiggler section could be tolerated until the next shutdown; or, spare sections could be included in the damping ring to compensate failures.

Similar considerations apply to the superferric wigglers as to the normal-conducting electromagnetic wigglers. Failures may result from power supply or cryogenic system failures, or failures associated with the controls system, or the magnet itself. However, the impact of the failure of an individual section of wiggler will be limited.

CESR-c provides some experience of operating superferric wigglers in a storage ring. One significant difference between CESR-c and the damping rings, is that in the case of CESR-c, individual wigglers (out of a total complement of 12, compared to several hundred for the damping rings) have a much larger impact on the overall operation of the ring, and any wiggler fault will halt operations, and must be repaired before operations can be resumed. In a recent operating period of 300 days, combining operation with 6 wigglers and with 12 wigglers, there were a total of 11 wiggler faults [60], corresponding to roughly one fault per 250 wiggler-days of operation (mean time between failure of 6000 hours per wiggler). Of the 11 faults, 7 were related to the cryogenics, 2 to the power supplies, 1 to the controls system, and there was 1 quench. The average time to complete a full repair after a failure, was 2 hours 14 minutes. In the case of the damping rings, repairs can likely be deferred until a scheduled maintenance period.

4.2.7 Conclusions

With the exception of the aperture, all wiggler technologies appear feasible for the damping rings. A superferric wiggler design is already available with sufficient field quality; however, it may be expected that with pole-face shimming and design optimization, hybrid and normal-conducting electromagnetic wiggler designs could be produced that also meet the field quality requirements. The total fabrication costs of the three technology options are comparable; however, the operating cost (for electrical power) of a normal-conducting electromagnetic wiggler is a disadvantage for that option. Radiation damage is a concern for a hybrid wiggler. Availability is unlikely to be an issue for any of the options.

Given the benefits of a large physical aperture, particularly for the injection efficiency, a superferric wiggler is preferred for the baseline damping

rings configuration. However, if designs with sufficient aperture and field quality for hybrid and normal-conducting electromagnetic wigglers can be produced, and a suitable collimation system to minimize radiation damage in the hybrid wiggler can be demonstrated, then these will be viable alternatives. In particular, a hybrid wiggler may offer some advantages in terms of not requiring any auxiliary systems (power supplies, cooling, or cryogenics).

4.3 Vacuum System

In a conventional storage ring, the specification on the vacuum pressure is generally set by lifetime requirements. In standard operation of the damping rings, the beam is stored for 200 ms, so lifetime is not likely to be a significant issue (although good lifetime will be needed for commissioning and tuning). However, beam stability is a major concern; ion effects in the electron ring and electron-cloud effects in the positron ring will be major considerations in determining both the required vacuum pressure, and the overall design of the vacuum system. Studies of ion effects (Section 3.4.8) suggest that the vacuum pressure needed in the electron damping rings to ensure beam stability will be of order 1 ntorr, or better. For the initial overview of the requirements of the vacuum system presented here, it was assumed that the required vacuum level would be of order 10 ntorr.

4.3.1 Gas Sources

The main sources of gas in an accelerator vacuum system are:

- thermal desorption (or thermal outgassing);
- photon stimulated desorption from synchrotron radiation;
- in the positron ring: electron stimulated desorption resulting mainly from beam-induced electron multipacting;
- in the positron ring: ion stimulated desorption resulting from ionization of the residual gas molecules, and their acceleration in the field of the beam towards the chamber walls.

Thermal Desorption

There are two processes leading to thermal desorption. In the first, gas molecules diffuse through the bulk material of the vacuum chamber (from

depths of a few millimeters to layers just below the surface) and desorb from the surface. In the second process, molecules adsorbed on the surface (either when the surface is initially prepared, or following a vent) desorb when the chamber is pumped. The outgassing rate depends on many factors, including: the type of material, the cleaning procedure applied to the surface, the time for which the surface has been under vacuum etc.

Photon Stimulated Desorption

Photon stimulated desorption (PSD) is one of the most important sources of gas in the presence of synchrotron radiation. Gas molecules may desorb from a surface when and where photoelectrons leave from or arrive at the surface. As in the case of thermal desorption, the rate of PSD depends on: the type of material, the cleaning procedure applied to the surface, the history of the material, the time for which the surface has been under vacuum etc. Additionally, the rate of PSD depends on the energy of the incident photons, the photon flux, the integrated photon dose and the chamber temperature.

Photodesorption yields as functions of the accumulated photon dose for different materials are known. The data may be extrapolated for use in the design of new machines. Generally, the photodesorption yield η as a function of the accumulated photon dose D may be written as:

$$\eta = \eta_0 \left(\frac{D_0}{D} \right)^{\alpha} \tag{4.13}$$

where η_0, D_0 and α are constants for the material (generally, $0.65 < \alpha < 1$).

Electron Stimulated Desorption

Electron stimulated desorption (ESD) can be a significant gas source in a vacuum system when large numbers of electrons bombard the surface. As in the case of thermal desorption, the rate of PSD depends on: the type of material, the cleaning procedure applied to the surface, the history of the material, the time for which the surface has been under vacuum etc. Additionally, the rate of ESD depends on: the energy of electrons impacting the surface, electron flux, the integrated electron dose and the vacuum chamber temperature.

Beam-induced electron multipacting (BIEM) can be a significant problem in a vacuum chamber with a positively charged beam. In this process, electrons are accelerated by the field of the beam to energies of hundreds of electron-volts; when these electrons hit the chamber surface, they release

gas by ESD, and also release secondary electrons which are themselves accelerated by the beam, repeating the process. Under certain conditions, the number of electrons, and the number of gas molecules, can rise very rapidly.

Ion Stimulated Desorption

Ion stimulated desorption (ISD) can be a significant gas source in situations where large numbers of ions bombard the chamber surface. There are few experimental data; most of the research has been performed at CERN. As in the case of other desorption processes, the rate of ISD depends on: the type of material, the cleaning procedure applied to the surface, the history of the material, the time for which the surface has been under vacuum etc. The rate of ISD also depends on: the mass of the ions involved, the charge and energy of ions impacting the surface, the ion flux, the integrated ion dose, and the chamber temperature.

In the case of a positively-charged beam, ions generated by collisions of beam particles with residual gas molecules are accelerated by the beam potential towards the chamber wall. On striking the wall, more gas molecules are desorbed, raising the pressure, and increasing the rate of ion production which feeds the process. In the presence of ISD, the gas density in a vacuum chamber is given by:

$$n = \frac{Q}{S_{\text{eff}} - \chi\frac{\sigma I}{e}} = \frac{Q}{\chi\frac{\sigma}{e}\left(I_c - I\right)} \tag{4.14}$$

where: Q is the gas flow from thermal desorption, PSD and ESD; S_{eff} is the effective pumping speed; χ is the ion-induced desorption yield; σ is the ionization cross-section; and I is the beam current. When the beam current reaches the value of the critical current I_c, or when $S_{\text{eff}} < \chi\sigma I/e$, then the gas density increases dramatically. We note that the ion-induced desorption yield χ increases with the ion energy, which in turn increases with the beam current I. The anticipated ion energy, for beam currents in the damping ring ranging from 159 mA (DAS or TESLA, 17 km rings) to 959 mA (PPA, 3 km ring) are shown in Table 4.4.

The analysis of ion-induced pressure instability in the damping rings requires further study; however, it is to be expected that the larger the current, the higher the probability of an instability occurring.

4.3.2 Pressure Distribution

A preliminary estimate of the pressure distribution around the ring was made for the TESLA damping ring, considering only thermal and photon

Table 4.4: Energy of ionized gas molecules impacting the vacuum chamber.

Beam current [mA]	Ion energy in arcs [eV]		Ion energy in wigglers [eV]	
	H_2^+	CO^+	H_2^+	CO^+
159	35	35	50–220	50– 65
443	97	96	140–260	140–170
839	200	182	270–460	270–300
959	209	208	300–530	300–350

Table 4.5: Photon flux in the TESLA damping ring.

	Dipoles	Wiggler
Beam energy [GeV]	5.0	
Average current [mA]	159	
Magnetic field [T]	0.2	1.6
Effective length [m]	1044	234
Photon flux, Γ [photons/m/s]	1.2×10^{18}	9.8×10^{18}
Critical energy, ε_c [keV]	3.33	26.6
Power per unit length [kW/m]	0.20	12
Total power [kW]	210	3010

stimulated desorption. Parameters for the photon flux are given in Table 4.5.

Note that the photon flux Γ produced by a beam of average current I in a magnetic field of strength B is given by:

$$\Gamma = \frac{5}{2\sqrt{3}}\frac{\alpha}{m_e c} IB \tag{4.15}$$

where α is the fine structure constant, and m_e is the electronic mass. The critical photon energy ε_c in a bend of radius ρ is given by:

$$\varepsilon_c = \frac{3\gamma^3 c}{2\hbar\rho} \tag{4.16}$$

and the mean photon energy $\langle\varepsilon\rangle$ is given by:

$$\langle\varepsilon\rangle = \frac{8}{15\sqrt{3}}\varepsilon_c \tag{4.17}$$

The photon stimulated desorption q is calculated from:

$$q = \eta(\varepsilon_c, D)\Gamma(I, B) \tag{4.18}$$

Table 4.6: Photon stimulated desorption yields for various gas species and chamber materials. The values given are for chambers baked *in situ*, and after a photon dose of approximately 10^{21} photons/m, with critical photon energy $\varepsilon_c = 3$ keV.

Species	Aluminum	Stainless steel	Copper	NEG-coated stainless steel
H_2	0.05	6×10^{-4}	8×10^{-4}	1.5×10^{-5}
CO	0.025	7×10^{-5}	2×10^{-4}	1×10^{-5}
CO_2	0.012	4×10^{-5}	3×10^{-4}	2×10^{-6}
CH_4	0.003	1×10^{-5}	4×10^{-5}	2×10^{-7}

where η is the photon stimulated desorption yield (which is a function of the critical photon energy ε_c and the photon dose D) and Γ is the photon flux (which is a function of the beam current and magnetic field strength).

The photon stimulated desorption yields for various gas species and chamber materials are shown in Table 4.6.

We also include the thermal desorption rate in our calculations. Since the photon induced desorption yield decreases with conditioning, the thermal desorption rate gives the lower limit of the pressure after a large accumulated photon dose. After baking and long pumping, the thermal desorption rate can be of the order 10^{-3} ntorr·l/(s·cm^2).

Arcs

The gas pressure in the arcs is shown in Figures 4.15 – 4.17 for three different cases:

1. Figure 4.15, for a stainless steel vacuum chamber baked *in situ* at 300°C for 24 hours, but not conditioned – the accumulated photon dose is approximately 10^{21} photons/m;

2. Figure 4.16, for the same vacuum chamber as in case (1), but after 100 A·hrs beam conditioning;

3. Figure 4.17, for a TiZrV NEG-coated vacuum chamber activated at 180°C for 24 hours.

In each case, a chamber consisting of a straight tube with internal diameter 50 mm was assumed. The pressure is plotted as a function of the distance

between the pumps at fixed pumping speed (left-hand plots) and as a function of pumping speed at fixed distance between the pumps (right-hand plots).

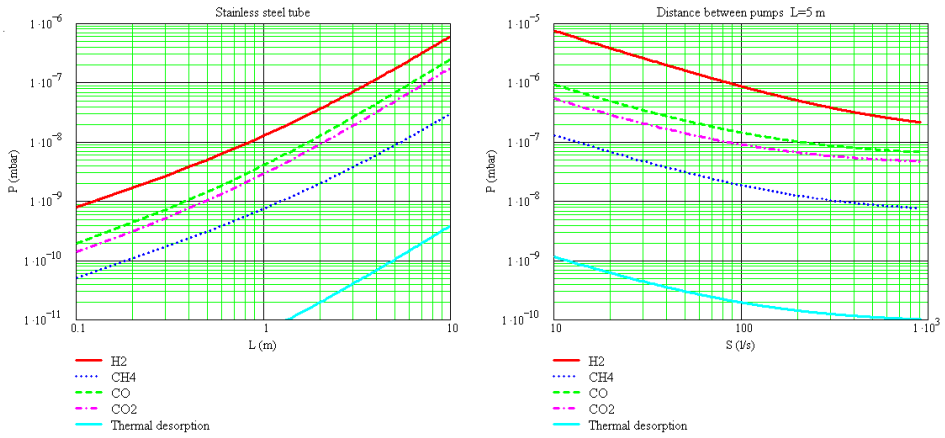

Figure 4.15: Vacuum pressure in the arcs with a stainless steel vacuum chamber baked at 300°C for 24 hours, but not conditioned – the accumulated photon dose is approximately 10^{21} photons/m. Left: pressure as a function of distance between pumps at fixed pumping speed. Right: pressure as a function of pumping speed, for fixed distance between pumps.

We make the following observations for the case of the stainless steel chamber.

- The photon stimulated desorption is much larger than the thermal desorption.
- Without conditioning, a pressure of 10 ntorr is achieved using pumps with pumping speeds of 1000 l/s every meter.
- After 100 A·hrs conditioning, a pressure of 10 ntorr is achieved using pumps with pumping speeds of 20 l/s every 20 meters.

For the NEG-coated chamber, we observe that the initial desorption rate is reduced, and there is some benefit from distributed pumping. An initial pressure of 10 ntorr (mainly CH_4) is achieved using pumps with pumping speeds of 10 l/s every 20 meters (to pump hydrocarbons and noble gases). Conditioning is also expected to improve the vacuum in this case; more

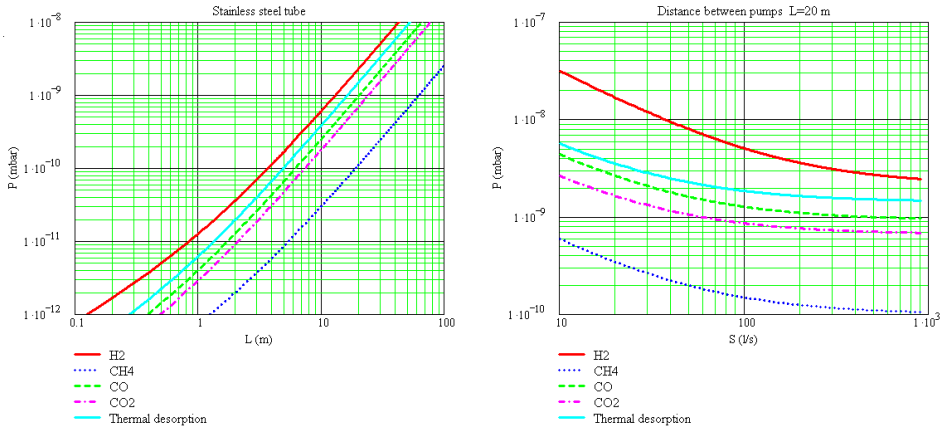

Figure 4.16: Vacuum pressure in the arcs with a stainless steel vacuum chamber baked at 300°C for 24 hours, after 100 A·hrs beam conditioning. Left: pressure as a function of distance between pumps at fixed pumping speed. Right: pressure as a function of pumping speed, for fixed distance between pumps.

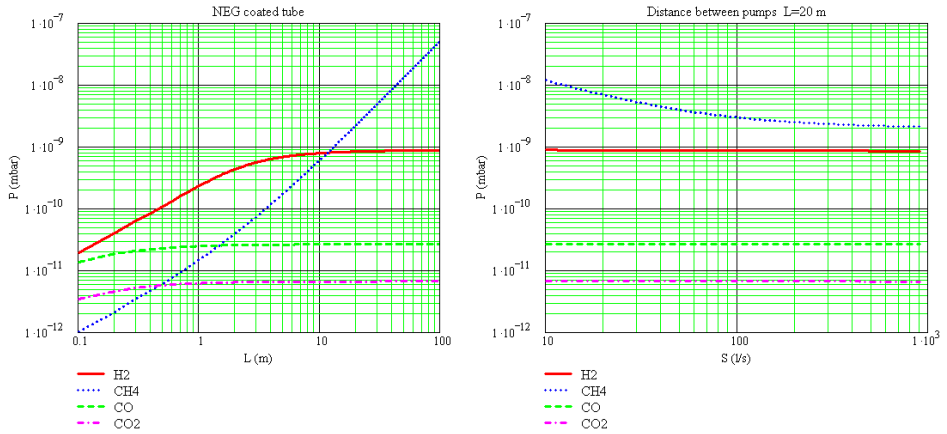

Figure 4.17: Vacuum pressure in the arcs with a TiZrV NEG-coated vacuum chamber activated at 180°C for 24 hours. Left: pressure as a function of distance between pumps at fixed pumping speed. Right: pressure as a function of pumping speed, for fixed distance between pumps.

experimental data are needed before an accurate prediction of the benefit can be made.

Wigglers

The gas pressure in the wigglers is shown in Figures 4.18 – 4.20, for the same three cases (unconditioned chamber; conditioned chamber; NEG-coated chamber) as for the arcs; however, in this case we assumed a copper vacuum chamber, baked at 200°C for 24 hours.

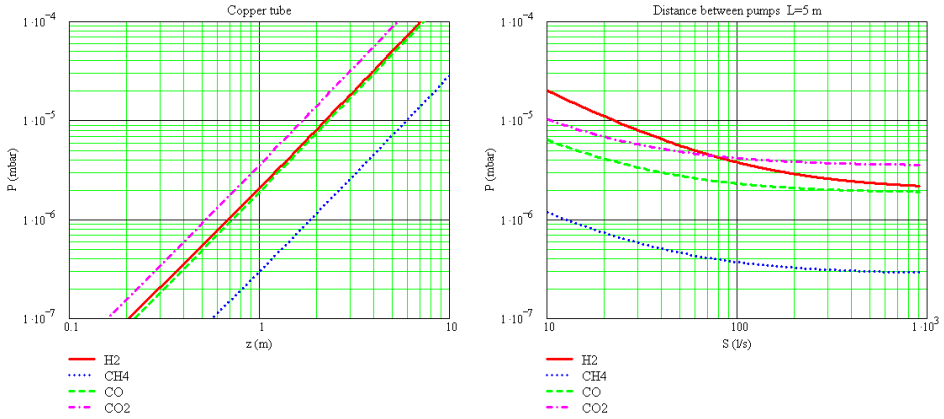

Figure 4.18: Vacuum pressure in the wigglers with a copper vacuum chamber baked at 200°C for 24 hours, but not conditioned – the accumulated photon dose is approximately 10^{21} photons/m. Left: pressure as a function of distance between pumps at fixed pumping speed. Right: pressure as a function of pumping speed, for fixed distance between pumps.

We make the following observations for the case of a copper vacuum chamber in the wiggler sections.

- The photon stimulated desorption is much larger than the thermal desorption.
- Without conditioning, a pressure of 10 ntorr is achieved using pumps with pumping speeds of 1000 l/s every 10 cm – almost distributed pumping.
- After 100 A·hrs conditioning, a pressure of 1 ntorr is achieved using pumps with pumping speeds of 20 l/s every 20 meters.

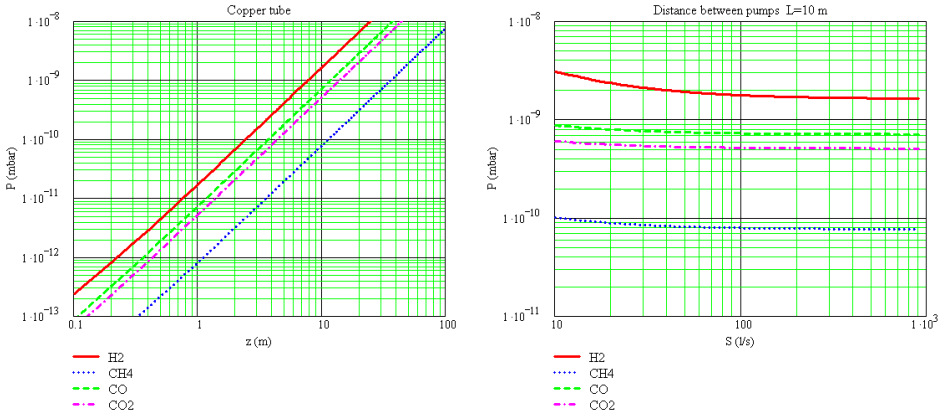

Figure 4.19: Vacuum pressure in the wigglers with a copper vacuum chamber baked at 200°C for 24 hours, after 100 A·hrs beam conditioning. Left: pressure as a function of distance between pumps at fixed pumping speed. Right: pressure as a function of pumping speed, for fixed distance between pumps.

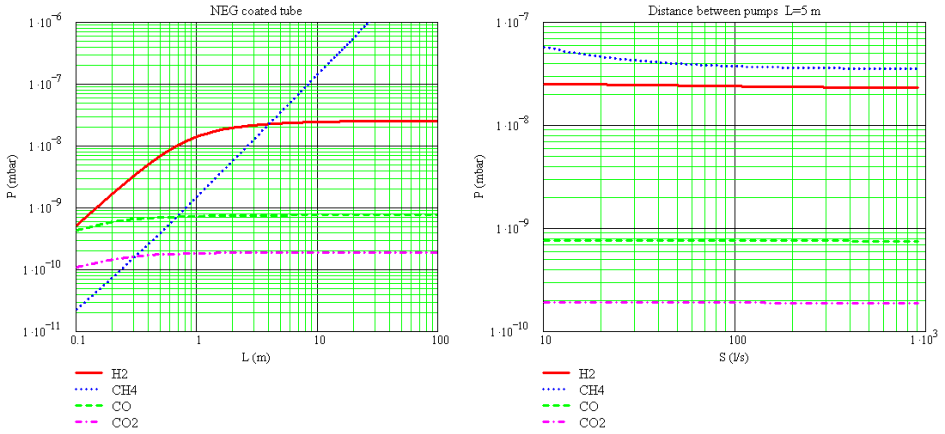

Figure 4.20: Vacuum pressure in the wigglers with a TiZrV NEG-coated vacuum chamber activated at 180°C for 24 hours. Left: pressure as a function of distance between pumps at fixed pumping speed. Right: pressure as a function of pumping speed, for fixed distance between pumps.

As in the case of the arcs, using NEG coating reduces desorption and introduces distributed pumping. An initial pressure of 20 ntorr (mainly H_2 and CH_4 can be achieved using pumps with pumping speeds of 30 l/s every 5 meters (to pump mainly hydrocarbons and noble gases).

Straight Sections

In addition to the usual considerations, the pressure in the straights depends on the distance from the dipoles and the wigglers. Figure 4.21 shows an example of the variation of intensity of synchrotron radiation with distance from a dipole along straight chambers of various diameters. The initial desorption rate will be proportional to the photon flux. During commissioning, parts of the chamber seeing a large photon flux will be conditioned more rapidly than sections seeing few photons; however, after a short conditioning period (of the order of 1 A·hr), even areas that differ in photon flux by a factor of 10^4 will have a difference in outgassing of less than a factor of 10. Desorption yields and fluxes as functions of distance from a dipole and conditioning dose are shown in Figures 4.22 and 4.23.

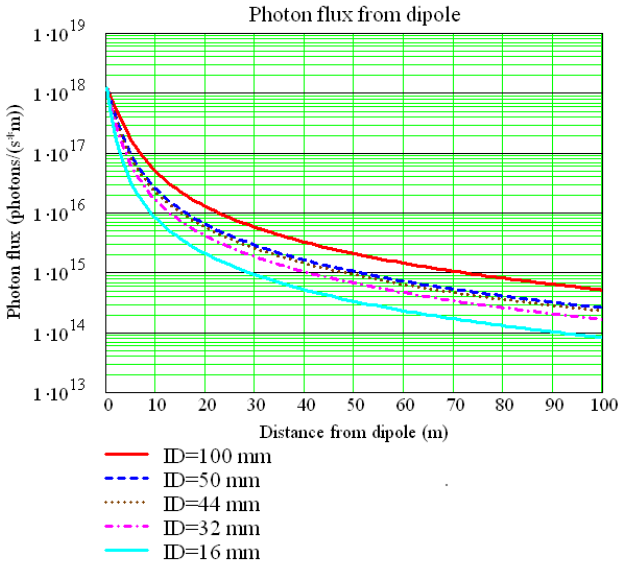

Figure 4.21: Variation in photon flux with distance from a dipole along straight chambers of various diameters.

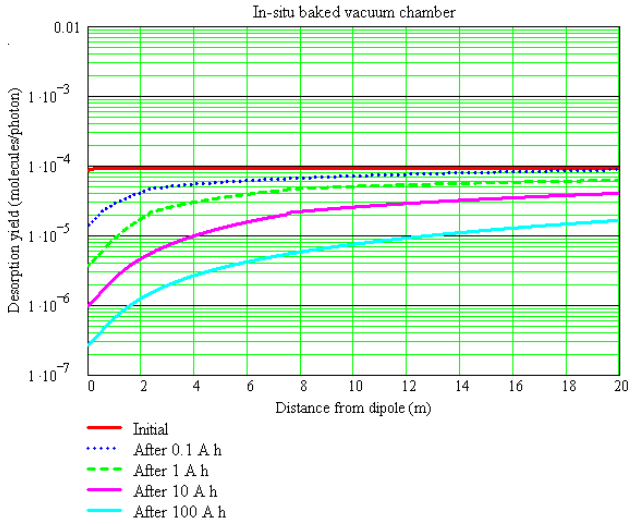

Figure 4.22: Desorption yield as a function of distance from a nearby dipole, for various conditioning doses.

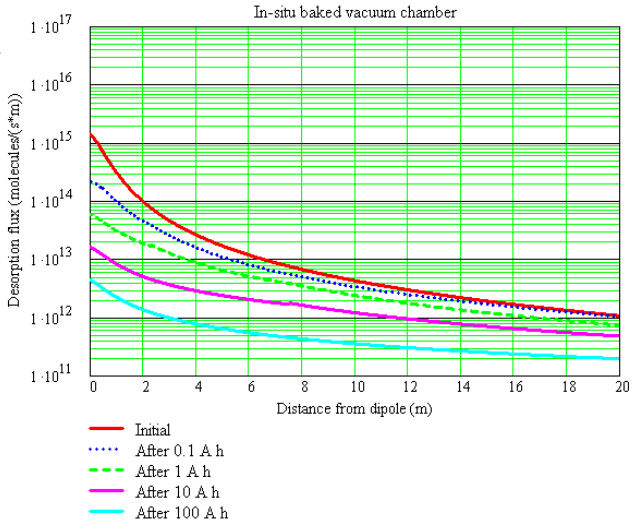

Figure 4.23: Desorption flux as a functions of distance from a nearby dipole, for various conditioning doses.

Where the photon flux is less than 10^{15} photons/m, the thermal desorption is the main source of gas. Gas pressure in the straight section with a photon flux of 10^{15} photons/m (approximately 50 m downstream from a dipole) is shown in Figure 4.24. The vacuum chamber in these areas can be made of a stainless steel tube with a pump having a pumping speed of 30 l/s every 20 – 30 m; this will achieve a vacuum pressure of the order 10 ntorr.

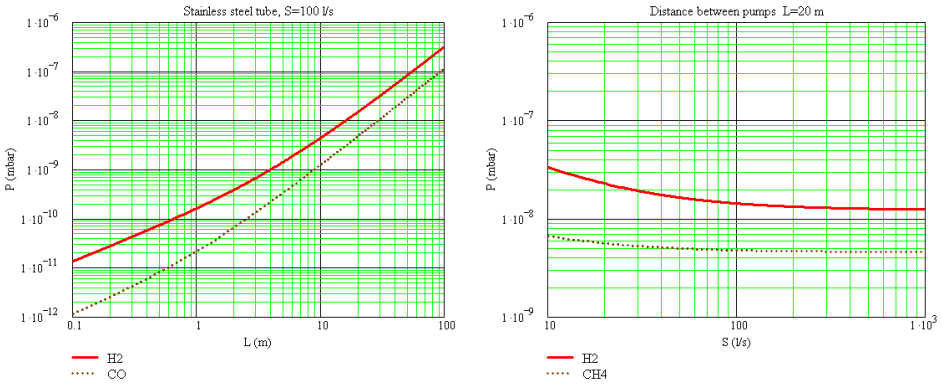

Figure 4.24: Pressure in a straight section 50 m downstream of a dipole. Left: pressure as a function of distance between pumps at fixed pumping speed. Right: pressure as a function of pumping speed, for fixed distance between pumps.

4.3.3 Comments

The results presented here show a preliminary assessment of some of the vacuum issues in the damping rings. The following points should be noted.

- Beam-induced electron multipacting may cause much higher outgassing rates in the positron damping ring. Results from the electron-cloud studies (including the power deposition, electron flux and electron energy distribution) should be included in the design process for the positron damping ring vacuum system.

- An ion-induced pressure instability may cause a sudden very large pressure increase in the positron damping ring. This is a result of residual gas in the chamber being ionized by the beam; the ions are

accelerated to the chamber walls by the field of the beam, where they cause the release of additional gas molecules which can in turn be ionized by the beam. This effect needs further study to ensure that there is sufficient pumping available to avoid an instability.

- The fast-ion instability in the electron damping ring may require a much lower vacuum pressure than the specification assumed here. This will impact the design of the vacuum system.

- The wiggler generates a large amount of synchrotron radiation power. The vacuum chamber design will need to include features to deal with the power. The effect of high synchrotron radiation power on NEG coatings has never been studied: possible issues are the thermal expansion coefficients, film adhesion, and vacuum properties.

- The vacuum chamber in the arcs will require cooling for mechanical stability.

- An antechamber is not necessary from point of view of achieving the vacuum specifications assumed here. However, an antechamber may be necessary to handle the synchrotron radiation power, and/or to suppress beam-induced electron multipacting.

A number of vacuum issues need to be addressed by studies of beam dynamics. These include:

- What is the actual specification of vacuum pressure in the damping rings?

- What are the requirements for avoiding fast-ion instability?

- Are there sections of the ring where the vacuum pressure needs to be better than in other places?

- How much conditioning can be assumed during commissioning?

- Is the impedance of a NEG-coating acceptable (approximately 250 $\mu\Omega$·cm)?

- What is the required vacuum chamber aperture in different sections of the damping ring?

- What are the ionization cross sections for different gas species?

Specifically, studies of electron-cloud are needed to answer the following questions:

- What electron flux on the chamber walls can be expected?
- What is the energy distribution of electrons impacting the chamber walls?
- How much time is necessary for conditioning the chamber surface to reduce the secondary electron yield?
- How does the build-up of the electron cloud vary between different sections, depending (for example) on the presence of magnetic fields or variations in chamber aperture?
- What coating or other treatment of the vacuum chamber is needed to suppress electron cloud?

From our preliminary assessment of the vacuum requirements, we can draw the following conclusions:

- NEG coating of the vacuum chamber in the arcs and the wigglers (and some tens of meters downstream into the straights) looks to be the only possible way to fulfil the vacuum requirements for the damping rings.
- Considering only thermal and photon stimulated desorption, most of the straight sections can be made of stainless steel tube, with pumps having pumping speeds of 30 l/s located every 20-30 m. This will achieve a vacuum pressure of the order of 10 ntorr.
- Including beam-induced electron multipacting is essential in designing the vacuum system. This will be included in future work.
- Specifications set by the fast-ion instability are needed.
- Power dissipation from synchrotron radiation and beam-induced electron multipacting have to be considered.
- The effect of high power synchrotron radiation on NEG coating needs to be studied experimentally.
- A higher current in the damping rings will result in a higher initial pressure because of the higher photon flux; but after sufficiently long conditioning (of the order of 100 A·hrs), the pressure will be relatively insensitive to changes in current.

- A higher current in the damping rings will be more likely to cause ion-induced pressure instability.

4.4 RF System

A detailed analysis of the requirements of the RF system for the damping rings was not performed as part of these studies. Here, we simply note that the principal technology choice is between a superconducting and a normal-conducting RF system. Given the very high voltage required for the damping rings (50 MV or more, in the 17 km lattices), a superconducting system would have some advantages in greater efficiency of energy transfer to the beam.

It is also possible to consider different RF frequencies for the damping rings. 500 MHz RF systems are widely used in electron storage rings (e.g. in third-generation synchrotron light sources), and the RF components are standard. Another possible choice is a 650 MHz system: this may simplify the timing issues (since 650 MHz is half the linac RF frequency), but synchronization with the linac RF is not expected to be a problem for the alternative 500 MHz system. A higher RF frequency provides some advantage in increasing the harmonic number for a given circumference, potentially allowing more flexibility in fill patterns (in particular, allowing ion-clearing gaps), and also leads to a shorter bunch length for a given RF voltage. However, a 650 MHz system would use non-standard RF components, which is likely to be a significant practical disadvantage.

4.5 Instrumentation

High-performance beam instrumentation will be critical to achieving the required beam quality and stability in the damping rings. Most beam instrumentation will serve one of three purposes:

1. to measure beam intensity;
2. to measure beam position;
3. to measure beam phase-space distribution.

In addition to the usual beam position monitors (BPMs) and other relatively conventional instrumentation, special instrumentation will be needed in the damping rings for these purposes. In this section, we list the devices that will likely be required, and comment on their application. In some cases, the

investment is justified as part of a careful attempt to diagnose and correct broadly anticipated difficulties; in other cases, the special devices are part of a tuning or feedback system. Precise specifications of the performance of the diagnostics have not yet been determined; this will be part of the on-going program of damping rings R&D.

4.5.1 Beam Intensity Diagnostics

Beam Lifetime Instrumentation

The machine protection system will require the ability to shut off the downstream beam quickly: this can (in principle) be done without aborting the beam in the damping ring. It is desirable that the rings be kept full and, most importantly, warm at all times, and for this reason, the injector ought to have the capability of providing a positron beam from a low duty-cycle high-power electron beam. This would allow the rings to be kept full while greatly reducing the upstream power, but depends on the beam having good lifetime in the rings, even during nominal operations. In this case, it is important to monitor continuously the beam lifetime so that the back-up "long store" cycles are ready when needed.

Fast Loss Monitors

The beams in the damping rings will have some destructive power. There must be an abort system and associated beam loss monitors. The requirements are similar to other high-power rings.

Collimation Monitoring and Protection

It is likely that sensitive components in the ring will need collimation in order to protect them from poor quality injection. When these devices limit the incoming power, there must be some diagnostic system to provide understanding of the root cause.

4.5.2 Beam Position Diagnostics

Beam Position Monitors

Beam Position Monitors (BPMs) are fundamental to machine commissioning and operation, and to orbit and coupling correction. The need for an ultra-low vertical emittance of 2 pm is likely to drive the performance specifications. High BPM resolution (of the order 1 μm even at low current)

will certainly be needed, but the systematic errors (position offsets, tilts, current and temperature dependencies etc.) must also be well-understood, stable, and kept to as low a level as possible. Basic performance requirements assumed for coupling correction simulations are described in Section 3.2.5. More detailed studies are needed to define the specifications with more completeness and precision.

Extraction Kicker Stabilization

Bunch-to-bunch jitter in the extracted beams from variations in the strength of the extraction kicker may be compensated in the extraction line; this involves a feedback system that measures the position of bunches early in the extraction line, then applies a correction across a "turn-around" in the extraction line. Stabilization will also be needed in the ring itself for bunches that see the trailing edge of an extraction kicker pulse. It is expected that the shape of the kicker pulse will be highly systematic, so a feedforward system can be used, with a kicker (following the main extraction kicker) programmed to cancel the greater part of the effects. There will also be pulse-to-pulse variations, which will require a feedback system similar to the fast feedbacks used to damp multibunch instabilities.

4.5.3 Beam Size Diagnostics

High-Precision Beam Size Monitor

A high-precision beam size monitor, capable of measuring horizontal and vertical beam size and beam tilt, will be fundamental to low-emittance tuning. A laser wire may be appropriate for this purpose.

Bunch-by-Bunch Beam Size Monitor

A precision monitor that can be used to measure the beam size and tilt on a bunch-by-bunch basis will be important for diagnosing collective effects. Such a monitor might be based, for example, on an X-ray synchrotron radiation monitor. While monitors with the required beam size resolution have been made and are currently used (e.g. in the PEP-II LER), none so far have the bandwidth necessary to measure beam parameters bunch by bunch.

Phase-Space Distribution of Injected Beam

Typically, the injected beam is poorly matched to the phase space of a storage ring. In the damping rings, achieving a good match will be important

for injection efficiency, and also to avoid initial emittance increase from filamentation that could delay the start of damping.

Damping Measurements

A monitor with a sufficiently wide dynamic range to monitor damping on the timescale of milliseconds is needed. An X-ray synchrotron radiation monitor may be appropriate.

Fast Coupling Monitor

There may be a need in the machine protection system to be able to couple the beam quickly, so that bunches with nominal charge can be delivered to the downstream systems, but with phase-space volumes large enough to be benign. A fast coupler has its own dangers, and would need monitoring.

4.5.4 Higher Order Beam Diagnostics

Coherent Signal Receivers

Coherent signal receivers will ultimately be used to determine the suitability of the beam for extraction: there should be no detectable coherent motion leading up to extraction. There are few rings in the world that routinely achieve beam stability at a level where no coherent motion can be seen. There may be a need in the damping rings for more than one type of coherent signal monitor. The oscillations of charge distribution associated with the microwave instability require a very high frequency receiver (in the case of the damping rings, in the range of 5 to 10 GHz).

4.5.5 Miscellaneous Instrumentation and Diagnostics

Tune Monitors

Tune monitors are standard instrumentation in storage rings. In the damping rings, the required performance depends on the symptoms of the expected collective effects (e.g. ability to resolve side-bands at the ion frequencies etc.)

Fast Dispersion Measurements

To maintain a very small vertical emittance, vertical dispersion will have to be monitored and corrected continuously. Using a modern BPM system,

it may be possible to make dispersion measurements during a single beam store time, using a very small RF frequency bump.

Chapter 5

Availability

An availability simulation program was used to predict downtimes for different damping ring configurations. The goal of the studies was to determine whether particular configuration options would have a significant impact on the availability of the damping rings. Options that were considered included: different lattice circumferences and styles (represented by the reference lattices); location of the damping rings in the linac tunnels or in separate tunnels; use of two 6 km rings (for either electrons or positrons) in a single 6 km tunnel; and use of superconducting or permanent magnet wigglers.

The Simulation Program

Availsim is a computer program specifically designed for availability studies of the linear collider [52]. Inputs are provided as large "decks" of information about the components of a machine, including the quantity of a specific component, its mean time before failure (MTBF), and its mean time to repair (MTTR). Given this information, the program uses a Monte Carlo simulation to calculate machine availability and to track downtime caused by individual components. The program is very advanced; references [52, 75] contain details about its capabilities and the assumptions used in creating the input decks. Availsim has previously been used for a variety of linear collider availability studies, including: comparisons between warm and cold linacs; comparisons between the one-tunnel and two-tunnels options for the linacs; and comparisons between conventional and undulator-based positron sources. Availsim has also been used to estimate the needed improvements to various components' MTBFs to achieve 75% availability.

The detailed calculation of downtime is complex and involves many input variables. However, to first-order, the downtime resulting from a given type

of component can be calculated as: the number of components, multiplied by the total time until luminosity is recovered after a fault, divided by the MTBF for the component.

The input deck used in these studies, ILC5, is based on the TESLA design. The quantities of components in the ILC5 damping ring are very similar to those in the TESLA reference lattice. ILC5 describes a machine that has two tunnels for the main linac, with minimal equipment in the beamline tunnel, and an undulator source for positron production. This deck includes improved MTBFs to achieve less than 25% downtime. To compare different configuration options for the damping rings, we used downtime percentages simulated from this input deck to calculate the expected downtimes for the various options. Our procedure is described in more detail below.

Damping Ring Beamline Placement

A potentially significant issue for availability is whether the damping ring beamline shares a tunnel with the main linac, or is located in a separate tunnel. Results from studies comparing the two options were presented at the Second ILC Workshop [32]. In the case that the damping ring shared a tunnel with the main linac, the simulation predicted an availability of 78.3%. If the damping ring was in its own tunnel, the availability was 79.0%. The difference between these two cases is not statistically significant, which implies that the availability is not dominated by access and recovery time to the linac and damping rings.

Two 6 km Damping Rings in One Tunnel

A damping ring configuration under consideration is one that has two separate 6 km damping rings (for either electrons or positrons) in one 6 km tunnel. This allows for longer bunch spacing compared to a single 6 km ring. In this configuration, if a component in one of the rings were to break making that ring unusable, the other ring could continue to run, although the machine would be limited to half luminosity. Given the first-order downtime calculation above, two 6 km rings would have twice as many components and twice as much downtime as a single 6 km ring. From the results given below, the average downtime expected for a 6 km ring is about 1.3%. Doubling this and comparing it to the average expected downtime of roughly 1.6% for a 17 km ring, we see that from availability considerations, two 6 km rings in one 6 km tunnel increases the downtime by 1% compared to a 17 km ring. However, the 50% luminosity that may still be provided with

one ring broken could provide a slight advantage over a configuration with a single ring.

MTBF for Kicker Pulsers

The injection and extraction kickers for the damping rings will be challenging, because of the need for fast rise and fall times, large kick amplitude, and high pulse rate. The availability input deck for the damping ring assumes that it is possible to maintain a "hot spare" pulser for the kickers; this effectively eliminates any contribution from the pulsers to the downtime, regardless of the MTBF. For example, in the availability input deck used in these studies, there are 21 kicker pulsers for each injection or extraction kicker, of which only 20 are needed. If each pulser has an MTBF of 35,000 hours, the presence of a spare drops the expected downtime caused by the kicker system from about 1.7% to 0.05%. The MTBF of 35,000 hours was estimated for kicker pulsers for the TESLA damping ring; if a different design is used that has a significantly shorter MTBF, the increased downtime can be mitigated by having more spares.

Superconducting and Permanent Magnet Wigglers

In the availability input deck there are 90 power supplies for 400 m of superconducting wigglers; each power supply has an MTBF of 10^7 hours. The total downtime resulting from failures of the wiggler power supplies is 0.01%. The MTBF of the superconducting wiggler itself should be large enough not to have a significant impact on the availability; the same should be true of a permanent magnet wiggler. Therefore, the wigglers should not have a significant impact on the availability of the damping rings, whether superconducting or permanent magnet technology is used.

Comparison of the Different Reference Lattices

To estimate the downtime for the damping ring reference lattices, we scaled the downtime caused by different components in ILC5 by the relative number of components. To begin with, the components responsible for downtime were divided into two groups. In the first group were those components that appeared in equal quantities in each lattice design. Components in this group included the kicker systems, equipment for the personnel protection system, beam stops and tune-up dumps. In the second group were those components that appeared in different quantities in each lattice design, including dipoles, quadrupoles, RF cavities, etc. The components in

the second group were further classified according to the design parameters that determined their quantities. Table 5.1 shows, for the components that appear in different quantities in different lattices, the design parameter that determines the quantity, the MTBF, the MTTR, and the amount of downtime predicted by the simulation program for the ILC5 deck.

Table 5.1: Components used in availability studies.

Design parameter determining quantity	Component	MTBF [hrs]	MTTR [hrs]	Downtime [%]
Number of bend magnets	bend magnets	2.0×10^7	8	0.046
Number of quadrupoles	quadrupoles	2.0×10^7	8	0.092
	quadrupole flow switches	2.5×10^6	1	0.13
Number of sextupoles	sextupoles	2.0×10^7	8	0.031
Number of correctors	correctors	1.0×10^7	0.5	0.005
	corrector power supplies	4.0×10^5	0.5	0.24
	corrector PS controllers	1.0×10^6	0.5	0.21
Number of bends + quads + sexts	PS for magnet strings	1.0×10^6	4	0.018
	PS controllers	1.0×10^6	1	0.005
Number of bends + quads + sexts + correctors	water pumps	1.2×10^5	4	0.047
	water instrumentation	3.0×10^5	2	0.017
	electricity 0.05-0.5 MW	3.6×10^5	2	0.18
Meters of wigglers	wigglers	1.0×10^7	8	0.015
RF voltage	klystrons	4.0×10^4	8	0.07
	klystron components:			
	power supplies	5.0×10^4	4	0.029
	pre-amplifiers	1.0×10^5	1	0.005
	vacuum gauges	1.0×10^5	1	0.01
	vacuum pump PS	1.0×10^5	1	0.012
	timing controls	3.0×10^5	1	0.005
	other controls	3.0×10^5	1	0.01
	water pumps	1.2×10^5	4	0.023
	water instrumentation	3.0×10^5	2	0.007
	electrical (>0.5 MW)	3.6×10^5	4	0.006
	electrical (0.05-0.5 MW)	3.6×10^5	2	0.007
	RF cavity vacuum pump PS	1.0×10^5	1	0.051
Length of beamline	vacuum valves	1.0×10^6	4	0.097
	vacuum valve controllers	1.9×10^5	2	0.15
	controls backbone	3.0×10^5	1	0.005
	local backbone	3.0×10^5	1	0.18
	timing	3.0×10^5	1	0.002

We then assumed that the downtimes caused by the various components in the ILC5 availability input deck were the same as for the TESLA reference lattice. This assumption is based on the fact that the component quantities in the two cases are very similar. Next, the parameters used to determine

the quantities of the various components, shown in Table 5.2, were found from the reference lattice decks[1]. Finally, component counts relative to the TESLA lattice were calculated and multiplied by the corresponding downtimes for the TESLA lattice to obtain the percentage downtime for each lattice. Table 5.3 shows the results.

Table 5.2: Quantities of components used in availability studies.

	PPA	OTW	OCS	BRU	MCH	DAS	TESLA
Bend magnets	168	64	192	336	336	188	108
Quadrupoles	418	538	684	878	1066	836	946
Sextupoles	112	232	384	504	504	112	304
Correctors	418	538	684	878	1066	836	946
Wigglers [m]	106	160	208	186	468	493	482
RF voltage [MV]	17.8	21.8	19.3	23.2	53.7	48.2	50.0
Circumference [m]	2824	3223	6114	6333	15935	17014	17000

Table 5.3: Percentage downtime for the reference lattices.

	PPA	OTW	OCS	BRU	MCH	DAS	TESLA
Bend magnets (B)	0.072	0.027	0.082	0.140	0.140	0.080	0.046
Quadrupoles (Q)	0.097	0.130	0.160	0.200	0.250	0.190	0.220
Sextupoles (S)	0.011	0.024	0.039	0.051	0.051	0.011	0.031
Correctors (C)	0.200	0.260	0.330	0.430	0.520	0.410	0.460
B+Q+S	0.012	0.014	0.021	0.029	0.032	0.019	0.023
B+Q+S+C	0.120	0.140	0.200	0.270	0.310	0.200	0.240
Wigglers [m]	0.003	0.005	0.006	0.006	0.015	0.015	0.015
RF voltage [MV]	0.085	0.110	0.092	0.110	0.110	0.260	0.230
Circumference [m]	0.071	0.082	0.160	0.160	0.400	0.430	0.430
Total	0.670	0.790	1.100	1.400	2.000	1.600	1.700

The largest difference in percentage downtime between two of the reference lattices is 1.3% (between PPA and MCH) or about two hours per week. While PPA is the lattice with the shortest circumference and the fewest components, MCH is not the lattice with the longest circumference. In this case, the large number of magnets in this lattice is the cause of the relatively high amount of downtime.

[1]The component quantities used for the availability studies are consistent with those used for the cost estimates.

Conclusions

- There is a minimal impact on availability from having the damping ring share a tunnel with the main linac, as opposed to having the damping ring in a separate tunnel.
- Having two 6 km rings (for either electrons or positrons) decreases the availability by 1% compared to a single 17 km ring.
- The effects of failure of the pulsers for the injection/extraction kickers can be mitigated by having a sufficient number of spares.
- The wiggler technology (superconducting or permanent magnet) should have little impact on the overall availability of the damping ring.
- The percentage downtime is correlated with the circumference: the 3 km rings are expected to have the shortest amount of downtime, while the 16-17 km rings are expected to have the longest downtime.
- The largest difference in availability between the reference lattices found in simulation was 1.3%, or two hours per week (between the 3 km PPA lattice and the 16 km MCH lattice). Given the total downtime budget of 25% for the ILC, this could be a significant factor.

Chapter 6

Cost Estimates

A recommendation on the damping rings configuration ought not be made without some attention given to the relative costs of the different options. Here, we present some estimates for the costs of damping rings based on each of the seven reference lattices; while we have attempted to obtain estimates that are reasonably accurate, it is difficult to achieve a high degree of accuracy without detailed engineering designs of the various components and subsystems. Without these designs, a parametric approach is the most appropriate, and while this provides limited accuracy, it does allow a relative comparison of the different options, which is all that is required here.

Two different approaches were taken towards the cost estimates. In the first approach ("bottom-up" or "component-based" cost estimate), tables were compiled of the quantities of the principal components in each of the lattices; then the total cost was obtained by multiplying the quantities by a unit cost for each component, and summing over all types of component. In the second approach ("top-down" or "scaling-based" cost estimate), costs for different sections of the damping rings were estimated from the costs of comparable sections in other machines (for example, PEP-II and the APS), by scaling with the length of the section. The results from one approach can be used to validate the other. The component-based approach provides an estimate from a more detailed model than is used in the scaling-based approach; on the other hand, the scaling-based approach provides an estimate that, in principle, includes a large number of "miscellaneous" items that are not included explicitly in the component-based estimate.

Table 6.1: Component quantities in the reference lattices.

Component type	Unit	PPA	OTW	OCS	BRU	MCH	DAS	TESLA
Dipoles	magnet	168	64	192	336	336	188	108
Quadrupoles	magnet	418	538	684	878	1066	836	946
Sextupoles	magnet	112	232	384	504	504	112	304
Steering	magnet	418	538	684	878	1066	836	946
Septum	magnet	2	2	2	2	2	2	2
Kickers	lot	1	1	1	1	1	1	1
Wigglers	meter	93	163	196	441	441	448	417
Dipole power supplies	PS	21	8	24	42	42	24	14
Quadrupole power supplies	PS	30	30	34	36	38	36	36
Sextupole power supplies	PS	4	8	12	16	16	4	12
Special power supplies	lot	1	1	1	1	1	1	1
Arc vacuum system	meter	2709	1002	5846	3634	3634	3240	2229
Wiggler vacuum system	meter	115	202	268	540	540	560	529
Straights vacuum system	meter	0	2019	0	2159	11761	13214	14242
RF system	MV	18	22	20	23	54	48	50
Dipole supports	support	168	64	192	336	336	836	108
Quad and sext supports	support	530	770	1068	1382	1570	188	1250
Wiggler supports	meter	93	163	196	441	441	448	417
Diagnostics and controls	quad	418	538	684	878	1066	493	946
Tunnel	meter	2824	3223	6114	6333	4174	3800	2758

Component-based (bottom-up) cost estimate

The component counts for the reference lattices are given in Table 6.1. Note that here we cost the positron damping rings; the costs for the electron rings could be a little lower, because a shorter wiggler is needed in the electron rings. For the dogbone rings, we assumed that the length of tunnel required was equal to the length of the arcs, and that the wiggler and straights would share tunnel with the main linacs; for the other lattices, we assumed that a complete new tunnel with length equal to the circumference of the lattice would be needed.

Unit costs for the various component types (which we do not give explicitly here) were taken from various sources. Costs for assembly and installation, engineering design and integration, management and contingency were not included; these may be added as fixed percentages of the hardware costs, and would not change the relative costs of the different options.

Figure 6.1 shows the hardware plus tunnel costs for the reference lattices (positron damping ring), relative to the TESLA lattice. As may be expected, the 3 km lattices are the least expensive, with costs roughly half of those for TESLA. The 6 km lattices are not significantly less expensive than the 17 km lattices: savings in hardware (particularly the vacuum system) are

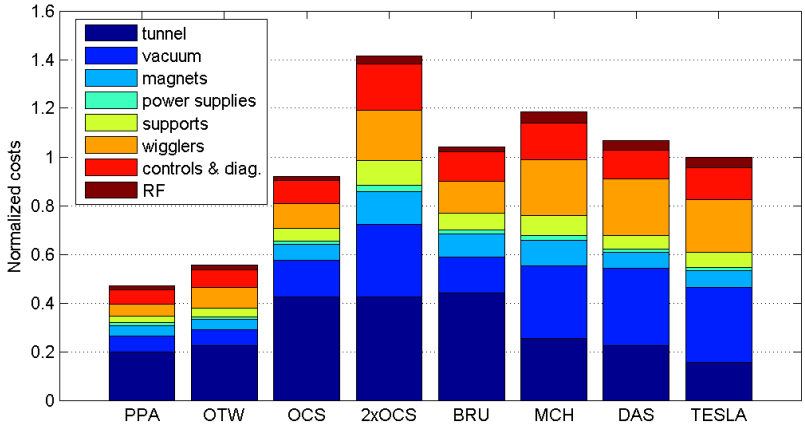

Figure 6.1: Estimated relative costs of the reference lattices, based on component counts.

offset by increased tunnel costs. The TESLA lattice is the least expensive of the 17 km lattices, principally because the arcs in TESLA are somewhat shorter than those in MCH and DAS. Note that the cost of the 2×OCS option (consisting of two independent 6 km rings in a single tunnel) were obtained simply by doubling the number of components in OCS, and using the same tunnel cost.

Figure 6.2 shows the breakdown of the contribution of different categories of components to the overall cost of the lattice in four cases: PPA (3 km lattice), OCS (6 km lattice), 2×OCS (two 6 km rings in a single tunnel), and TESLA (17 km lattice). For the 3 km and 6 km lattices, the tunnel and vacuum system make up nearly two-thirds of the cost. For the TESLA lattice, the tunnel and vacuum make up less than half the cost; but the wigglers contribute about a quarter. In all cases, the magnets, power supplies and RF system each make a relatively small contribution to the cost.

We note that a possible configuration uses a single 6 km ring for one side of the collider (e.g. the electrons) and two 6 km rings in a single tunnel for the other side. In that case, the overall cost may be obtained by averaging (for example) the OCS and 2×OCS options.

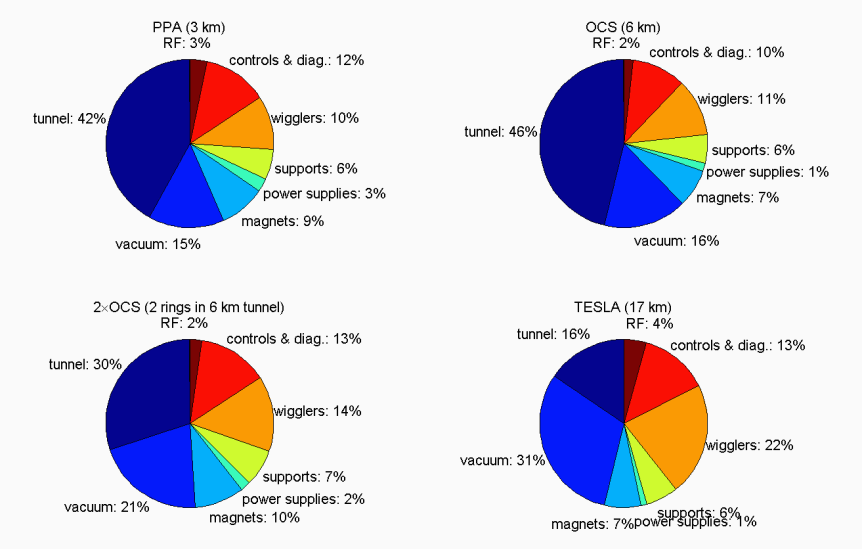

Figure 6.2: Relative contributions of different component categories to the costs of four of the reference lattices.

Scaling-based (top-down) cost estimate

Relative cost estimates from the scaling-based approach are shown in Figure 6.3. The costs are relative to the component-based estimate for the TESLA damping ring. For comparison, the results of the component-based estimate are also shown, with the same vertical scale. Although the scaling-based approach gives a larger cost for a given lattice than the component-based approach, the two approaches lead to a very similar pattern in the cost of one lattice relative to another.

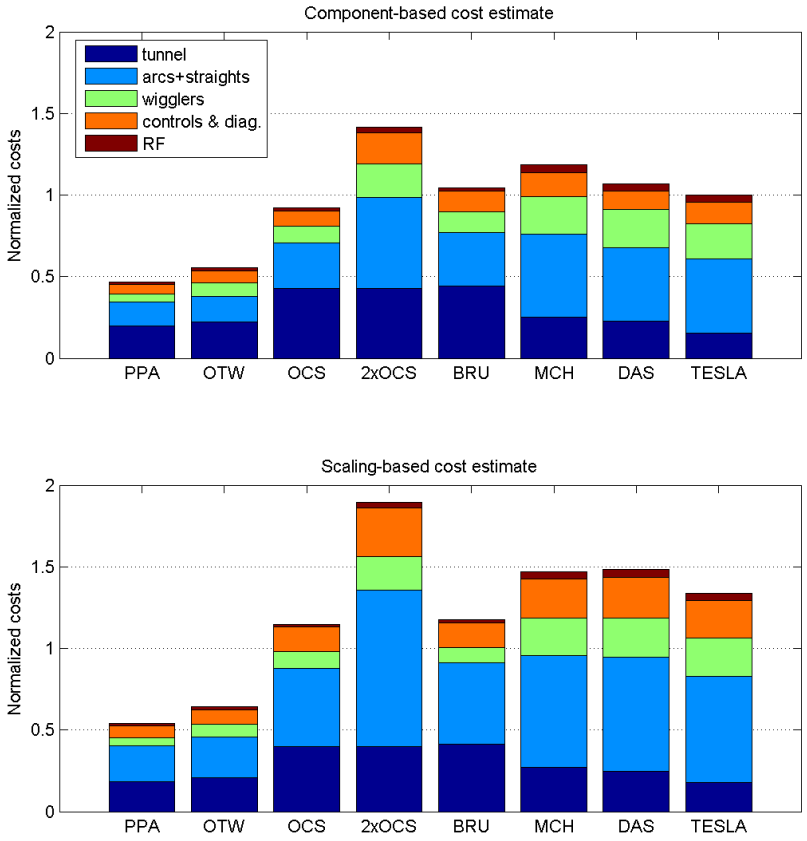

Figure 6.3: Estimated relative costs of the reference lattices, based on scaling from existing machines.

Chapter 7

Configuration Recommendations

The recommendations for the configuration of the ILC damping rings presented in this report are the result of discussions held during a meeting at CERN on November 9–11, 2005. The first part of the meeting was devoted to hearing the results of detailed studies of a range of configuration options, also presented in this report. The studies were carried out over the previous six months by nearly 50 researchers, and the results of the studies form the basis on which the recommendations for the damping rings configuration have been made. In this chapter, we present: a summary of the issues surrounding each configuration item; an assessment of the risks and costs associated with each option for each configuration item; and recommendations for the baseline and alternative configurations.

The studies of the various configuration options were based on nominal parameter and performance specifications for the damping rings: these specifications are given in Section 1.1. The assessments of the significance of the different issues associated with each configuration item, and the risks associated with the various options for each item, were based on a systematic ranking scheme, given in Section 7.1. We should emphasize that although our systematic approach allows a "score table" for the various options for each item to be drawn up, our recommendations were reached through structured discussion, and not by simply adding up the risk scores for the different options. A number of items requiring R&D were identified during the discussions at the CERN meeting: these are given in Section 7.4.

The participants at the CERN damping rings meeting in November 2005 were as follows:

David Alesini (INFN)
Desmond Barber (CI/DESY)
Yunhai Cai (SLAC)
Alex Dragt (UMD)
Eckhard Elsen (DESY)
Louis Emery (ANL)
Jie Gao (IHEP)
George Gollin (UIUC)
Susanna Guiducci (INFN)
Gilbert Guignard (CERN)
Sam Heifets (SLAC)
Eun-San Kim (PAL)
Hyoung Suk Kim (CHEP)
Maxim Korostelev (CERN)
Larisa Malysheva (CI/Liverpool)
Oleg Malyshev (ASTeC)
Fabio Marcellini (INFN)
Chad Mitchell (UMD)
Janice Nelson (SLAC)
Kazuhito Ohmi (KEK)
Yukiyoshi Ohnishi (KEK)
Toshiyuki Okugi (KEK)
Mark Palmer (Cornell)
Mauro Pivi (SLAC)
Ina Reichel (LBNL)
Marc Ross (SLAC)
David Rubin (Cornell)
Daniel Schulte (CERN)
Agoh Tomonori (KEK)
Junji Urakawa (KEK)
Jeremy Urban (Cornell)
Marco Venturini (LBNL)
Rainer Wanzenberg (DESY)
Andrzej Wolski (LBNL)
Guoxing Xia (DESY)

7.1 Ranking of Issues and Risks

The significance of the issues relevant to each configuration item are ranked as follows:

A This issue: is critical to the corresponding item in the configuration decision; has significant technical, operational or cost implications; and is likely to be a key consideration in choosing between the various options.

B This issue is important for the corresponding item in the configuration decision, but should not be considered a decisive factor.

C This issue has only a minor impact on the corresponding item in the configuration decision.

The risks associated with the various options are ranked as follows:

1 The performance requirements of this option have been demonstrated, or studies indicate little risk.

2 Some R&D is required to demonstrate performance requirements, but with a likelihood of successful outcome; or there is low technical risk, and a practical fix will likely be found in the event that a problem occurs.

3 Significant R&D is required to demonstrate performance requirements; or there is a high technical risk, with likelihood to cause ongoing problems.

4 There is unlikely to be an acceptable technical solution.

The cost impacts of the various options are ranked as follows:

1 Lowest cost option, or close to lowest cost.

2 Up to roughly a factor of two greater cost than lowest cost option.

3 Up to roughly a factor of three greater cost than lowest cost option.

4 More than a factor of three greater cost than lowest cost option.

7.2 Configuration Recommendations

7.2.1 Circumference

The choice of ring circumference is strongly coupled to the choices of:

- beam energy: a shorter ring will have a lower space-charge tune shift, that may make a lower energy feasible;
- injected emittance and energy spread: a large energy acceptance can be difficult to achieve in a dogbone lattice;
- bunch train length: if a large number of bunches ($\sim$5600) is needed, a larger circumference will make the injection/extraction kickers easier, and also allow gaps for ion clearing;
- bunch length: a longer bunch reduces the charge density, which will reduce the space-charge tune shift that may be a problem in a 17 km ring;

- injection/extraction kickers: the kickers become more difficult in shorter rings, and other options may become more attractive if a short circumference is chosen;
- wiggler technology: a larger circumference requires a longer wiggler, which can affect the relative cost impact of the different options for the wiggler technology.

Options

Configurations with circumferences of roughly 3 km, 6 km and 17 km have been considered. It is also possible to stack several rings in a single tunnel, dividing the bunch train between the different rings to reduce the average current in any given ring. A further option would be to use RF deflectors to separate alternate bunches down different beamlines for injection and extraction: this would ease the kicker requirements by increasing the bunch spacing locally in the injection/extraction regions, and could be used with any ring circumference.

Rings up to 6 km can be built in (roughly circular) tunnels separate from the main linac. 17 km rings would have a dogbone layout, with long straight sections sharing tunnel with the main linac to reduce costs.

Issues

Electron cloud effect (Significance: A) Shorter rings have a closer bunch spacing, which greatly enhances the build-up of electron cloud. Electron cloud can be difficult to suppress in the dipole and wiggler regions where it is expected to be most severe, and the instabilities associated with electron cloud could significantly affect the performance of the damping rings.

Injection and extraction kickers (Significance: A) Shorter rings have shorter bunch spacing, and place higher demands on the injection and extraction kickers. For rings of 17 km and 6 km circumference, the required rise and fall times are considered achievable, though a full demonstration (including repetition rate, pulse length and amplitude stability) is still required. 3 km rings have a shorter bunch separation requiring faster rise and fall times, so the kickers are more demanding. It may be possible to use RF deflecting cavities to separate bunches between different beamlines for injection and extraction, easing the kicker rise and fall time requirements. Kicker performance is critical to the production of a stable beam from the damping rings.

Acceptance (Significance: A) Given the high average injected beam power, beam losses in the ring could rapidly damage critical components (e.g. the wigglers) and adversely affect diagnostics, making the ring difficult to operate. The design criterion is a lattice that achieves (in simulation) 100% injection efficiency for a nominal injection distribution, including physical apertures and tuning errors. Lattice designs have been developed for 6 km rings that have good acceptance for the baseline positron distribution. The long straight sections in the dogbone damping rings break the lattice symmetry, and generate chromaticity that is difficult to correct locally. As a result, it is difficult to achieve the dynamic aperture needed to accept cleanly the large positron beam from the source.

Cost (Significance: A) A 3 km ring would have rather a lower cost than 6 km or 17 km rings. The additional tunnel in the 6 km rings makes the costs comparable to the 17 km rings. Estimates suggest that using two 6 km rings in a single tunnel is a higher cost than a 17 km ring.

Ion effects (Significance: B) Accumulation of ions in the vacuum chamber can drive instability. Ion effects are complex, particularly in the damping rings where the beam sizes can be very small. Gaps in the fill and very low vacuum levels will be necessary to mitigate ion effects. Present understanding is that the style of lattice, fill pattern and vacuum pressure are more significant than the circumference for the severity of the effects; however, longer rings have a lower current than shorter rings, making it easier to achieve lower vacuum pressures. A larger circumference could help by allowing larger gaps in the fill for a given bunch spacing.

Space-charge (Significance: B) The incoherent space-charge tune shift is proportional to the ring circumference. The coupling bumps used to reduce this effect in the dogbone ring could be some risk for the vertical emittance.

Tunnel layout (Significance: B) Sharing the linac tunnel increases the time taken for commissioning and reduces the availability. Stray fields in the linac tunnel could adversely affect the vertical emittance of the extracted beam (though it may be possible to use feed-forward systems to correct the effects of stray fields). Coupling between the straights in a dogbone lattice is a potential issue.

Availability (Significance: C) The larger number of components in a larger ring is likely to have an adverse impact on reliability.

Classical collective effects (Significance: C) A variety of classical collective effects are of potential concern, including resistive-wall instability, coupled-bunch instabilities driven by higher-order modes, microwave instability, and intrabeam scattering. Studies show that these effects should be manageable in rings with any of the proposed circumference options. The severity of these collective effects tends to be dominated by issues such as bunch charge, bunch length, lattice design (momentum compaction), beampipe diameter etc., rather than by the circumference.

Low-emittance tuning (Significance: C) Achieving the specified vertical beam emittance in the damping rings is important for producing luminosity. However, there is an additive emittance dilution in all the systems downstream of the damping rings; and the luminosity depends on the beam size at the interaction point, which scales with the square root of the emittance. There is little evidence that the circumference of the damping ring in itself has an impact on the emittance sensitivity to misalignments and tuning errors.

Polarization (Significance: C) Studies suggest that depolarization should not be a major issue in any of the configuration options under consideration.

Issues Ranking

Issue	Significance	Risks			
		3 km	6 km	2×6 km	17 km
Electron cloud (e^+ ring)	A	4	3	2	2
Kickers	A	3	2	2	2
Acceptance	A	2	1	1	2
Cost	A	1	2	3	3
Ion effects (e^-) ring	B	3	2	2	2
Space charge	B	1	1	1	2
Tunnel layout	B	1	1	1	2
Availability	C	1	1	1	1
Classical collective effects	C	2	2	2	2
Low-emittanc tuning	C	2	2	2	2
Polarization	C	1	1	1	1

Note: Use of RF deflecting cavities locally to separate alternate bunches

down different beamlines would reduce kicker risks for any of the circumference options, though potentially with some impact on the acceptance.

Baseline Recommendation

The positron damping ring should consist of two (roughly circular) rings of approximately 6 km circumference in a single tunnel. Electron-cloud effects make a single ring of circumference 6 km or lower unattractive, unless significant progress can be made with mitigation techniques. Space-charge effects will be less problematic in a 6 km than in a 17 km ring, and achieving the required acceptance will be easier in a circular ring than in a dogbone ring.

The electron ring can consist of a single 6 km ring, assuming that the fill pattern allows a sufficient gap for clearing ions. The injection and extraction kickers and ion effects are more difficult in a 3 km ring than in a 6 km ring. A 17 km ring could ease ion effects (by allowing larger gaps between minitrains), but would likely be higher cost. We have no recommendation on whether the electron ring needs a separate tunnel from the positron rings.

Although R&D is still required for the injection/extraction kickers for a damping ring with 6 km circumference, it is expected that existing programs will demonstrate a solution.

The exact circumference of the damping rings should be chosen, if possible, to allow flexibility in the fill patterns and number of bunches in a bunch train.

The feasibility of the baseline depends on:

- further progress with developing techniques for suppressing electron cloud (positron rings);
- development of a satisfactory lattice design, e.g. (for electron ring) with properties that mitigate ion effects, etc.
- demonstration of kickers meeting the specifications for rise/fall time, kick amplitude stability and repetition rate.

Alternatives

1. If techniques are found that are sufficiently effective at suppressing the electron cloud, a single 6 km, or possibly smaller, ring can be used for the positron damping ring. This will save costs.

2. If electron cloud mitigation techniques are not found that are sufficient for the baseline positron ring, then a 17 km ring is a possible alternative; this would require addressing space-charge and acceptance issues.

Required R&D

Baseline

- Techniques for mitigating electron cloud to acceptable levels are needed.
- A lattice design is needed that simultaneously satisfies requirements for acceptance and beam stability, and can be tuned easily for low emittance.

Alternative 1 (single 6 km positron ring

- Techniques for mitigating electron cloud to acceptable levels are needed.
- A lattice design is needed that simultaneously satisfies requirements for acceptance and beam stability, and can be tuned easily for low emittance.

Alternative 2 (17 km positron ring

- Techniques for suppressing space-charge tune shifts without driving betatron and synchrobetatron resonances are needed.
- A lattice design is needed that simultaneously satisfies requirements for acceptance and beam stability, and can be tuned easily for low emittance.

General R&D requirements

- Kickers that simultaneously meet specifications on rise/fall time, pulse rate and stability need to be demonstrated.
- Ion instabilities are a concern in the electron ring.
- Ion-induced pressure instabilities in the positron ring need to be addressed.
- A range of classical collective instabilities need to be properly understood, with analysis based on a detailed impedance model.
- The effectiveness of low-emittance tuning techniques need to be assessed.

7.2.2 Beam Energy

The choice of beam energy is strongly coupled to the choices for:

- circumference: a shorter ring will have a lower space-charge tune shift, that may make a lower energy feasible;
- injected emittance and energy spread: lowering the beam energy increases the injected emittance and energy spread, and makes a larger acceptance necessary;
- bunch train length and bunch charge: single bunch collective effects become less severe at lower bunch charge, and may make a lower energy feasible;
- bunch length: a longer bunch length reduces the charge density in the bunch, reduces the severity of single bunch collective effects, and may make a lower energy feasible; wiggler technology: a lower beam energy requires a longer wiggler, which can affect the relative cost impact of the different options for the wiggler technology.

Options

Beams at low energy are sensitive to collective effects. At higher energies, it is difficult to achieve the equilibrium emittances in a lattice of reasonable size. The energy choices are restricted by the need to avoid depolarization resonances, which occur roughly at intervals of 440 MeV. We may consider energies in the range (roughly) 3.7 GeV to 6.8 GeV. Most of the detailed configuration studies have been performed for lattices designed for 5 GeV beam energy. There is also the possibility of bunch spacing resonances affecting the electron cloud effect.

Issues

Longitudinal emittance (Significance: A) An increase in the longitudinal emittance (from an increase in either or both of the bunch length and energy spread) has an impact on the bunch compressors and the spin rotators making their design and operation more difficult. Assuming that the damping wiggler dominates the energy loss of the beam, the equilibrium relative energy spread increases linearly with the beam energy. At 5 GeV, the damping rings will have a natural energy spread of around 0.13% (which is within the nominal value of 0.15% specified for the bunch compressors).

An energy spread of 0.18%, which would be expected in a damping ring at 6.8 GeV, may be acceptable for the spin rotators and (assuming a 6 mm bunch length) for the bunch compressors, but lower values are desirable. The strength needed for the spin rotator solenoid also depends directly on the beam energy: at 5 GeV, this solenoid is already large; an increase in energy would make the solenoid more difficult.

Collective effects (Significance: A) The impact of collective effects (growth rates, thresholds etc.) often scales inversely with the energy: higher energies will reduce growth rates and/or raise thresholds. At a beam energy of 5 GeV, some of the collective effects look challenging (given the baseline circumference). Space-charge problems get worse with lower energy. The emittance growth from intrabeam scattering scales inversely with the fourth power of the energy, and would likely have a significant impact on performance at energies below 5 GeV.

Acceptance (Significance: A) The particle sources produce beams with given normalized emittances and absolute energy spread. Increasing the ring energy provides a benefit from adiabatic damping: the transverse beam sizes scale inversely with the square root of the energy, and the relative energy spread decreases linearly with increasing energy. However, there is a competing effect: a higher energy ring may have a more challenging lattice design to achieve the required equilibrium emittances, which could adversely affect the acceptance.

Transverse emittance (Significance: B) The normalized natural emittance scales with the third power of the energy. An increase in energy can be compensated to some extent by increasing the number of arc cells in the lattice; however, this tends to reduce the momentum compaction, which can lower the thresholds for some collective instabilities. Lattice changes could also adversely affect the acceptance.

Low-emittance tuning (Significance: B) The specification on the extracted vertical emittance applies to the normalized emittance. Reducing the beam energy for a fixed normalized vertical emittance increases the allowed geometric emittance, and would ease the tuning requirements.

Damping rates (Significance: B) Higher energies increase the radiation damping rates, which may allow reduction in wiggler length.

Cost (Significance: B) The construction cost and operating cost of a storage ring generally increase with energy. Although the wiggler length would be reduced at higher energy, the cost savings would likely be offset by higher costs of other systems, including vacuum and RF.

Issues Ranking

Issue	Significance	Risks		
		3.7 GeV	5 GeV	6.8 GeV
Longitudinal emittance	A	1	1	2
Collective effects	A	3	2	1
Acceptance	A	2	1	2
Transverse emittance	B	1	1	2
Low-emittance tuning	B	1	2	3
Damping rates	B	1	1	1
Cost	B	1	1	2

Baseline Recommendation

The damping ring energy should be approximately 5 GeV. A lower energy increases the risks from collective effects; a higher energy makes it more difficult to tune for low emittance, and potentially has an adverse impact on the acceptance.

7.2.3 Injected Emittance and Energy Spread

The specifications for the injected emittance and energy spread are strongly coupled to the choices for:

- circumference: a large energy acceptance can be difficult to achieve in a dogbone lattice;
- beam energy: lowering the beam energy increases the injected emittance and energy spread, and makes a larger acceptance necessary;
- vacuum chamber aperture: a larger transverse emittance requires a larger physical aperture for good injection efficiency;
- wiggler technology: a larger transverse emittance needs a larger physical aperture, which is easier to achieve in some wiggler technologies than others.

Options

	Option I	Option II
Maximum injected betatron amplitude	0.045 m·rad	0.09 m·rad
Injected full-width energy spread	2%	1%

Issues

Acceptance (Significance: A) For a given acceptance, the injection efficiency will improve with smaller injected betatron amplitude and energy spread. With the damping ring lattices considered for the configuration studies, the energy spread was the more important quantity in most cases: a better injection efficiency was found using a simulated positron distribution corresponding to Option II, compared to Option I. The impact on the positron source is not clearly understood at the present time.

Injection systems (Significance: B) A smaller injected emittance allows a narrower aperture in the injection components, which could simplify their design.

Issues Ranking

Issue	Significance	Risks	
		Option I	Option II
Acceptance	A	3	2
Injection systems	B	1	2

Baseline Recommendation

An injected beam with maximum betatron amplitude up to 0.09 m-rad and energy spread up to 1% (full width) is preferred for the damping rings, over a distribution with larger energy spread but smaller betatron amplitude. Achieving good off-energy dynamics in the damping ring lattices is likely to be more problematic than achieving a large on-energy dynamic aperture. A smaller energy spread is likely to improve the margin for the acceptance of the injected beam.

Alternative

If the acceptance issue can be addressed successfully, a larger energy spread on the injected beam (up to 2% full width) could be accommodated.

Required R&D

Baseline Studies of the positron production indicate that an injected full-width energy spread of 1% should be achievable; however, a thorough investigation including realistic models for collimators, energy compressors etc. is still needed.

Alternative A lattice design is needed that shows an energy acceptance with some margin beyond 2% full-width, while satisfying other requirements.

7.2.4 Bunch Train Length and Bunch Charge

The specifications for the bunch train length and bunch charge are strongly coupled to the choices for:

- circumference: if a large number of bunches (∼5600) is needed, a larger circumference will make the injection/extraction kickers easier;
- beam energy: single bunch collective effects become less severe at lower bunch charge, and may make a lower energy feasible;
- bunch length: a longer bunch reduces the charge density, and may make a higher bunch charge possible before reaching limits from collective effects;
- injection/extraction kickers: the kickers become more difficult with a larger number of bunches, which must be packed more closely into the ring;
- RF frequency: the flexibility in the number of bunches in a train depends to some extent on the RF frequency.

Options

	Option I	Option II
Bunch train length	2800	5600
Injected bunch separation	330 ns	165 ns
Injected bunch charge	2×10^{10}	1×10^{10}

Issues

Injection and extraction kickers (Significance: A) It is possible to store 5600 bunches in a ring with approximate circumference 6 km and with

a 4 ns bunch spacing; this bunch spacing is expected to be possible with the proposed baseline kicker technology. However, the kickers do get more difficult as a higher rep rate - with same pulse length - is required. A lower number of bunches (2800) allows gaps between "minitrains" of bunches in the ring, which could provide for a slow fall-time kicker. The gaps get shorter as the number of bunches is increased, and may be reduced to zero with the largest number (5600) of bunches in the ring.

Ion effects (Significance: A) We assume fill patterns for bunch train lengths between 2800 and 5600 bunches, satisfying the following conditions:

- the bunch spacing is independent of the number of bunches (roughly 4 ns in a 6 km ring);
- bunches are arranged in "minitrains" in the ring, with gaps between minitrains;
- additional bunches are accommodated by increasing the number of minitrains, and reducing the gap between minitrains.

The average current is independent of the total number of bunches. In the assumed fill scheme, increasing the number of bunches reduces the gap between minitrains, which could result in the ion effects becoming more severe.

Electron cloud effects (Significance: A) Electron cloud effects are strongly dependent on bunch spacing. To keep these effects under control, it might be necessary always to maintain the largest possible bunch spacing in the positron ring. This means that the number of bunches in each of a pair of 6 km rings may be limited to around 1400, to maintain a bunch separation of 14 ns.

Single-bunch collective effects (Significance: A) Single-bunch effects such as the microwave instability, space-charge tune shifts and emittance growth from intrabeam scattering are mitigated by a lower bunch charge.

Resistive-wall instability (Significance: B) With a fixed average current in the ring, the resistive wall instability will not be significantly affected.

Issues Ranking

Issue	Significance	Risks	
		Option I, 2800 bunches	Option II, 5600 bunches
Injection and extraction kickers	A	2	3
Ion effects (electron ring)	A	2	4
Electron cloud (positron ring)	A	2	3
Single-bunch collective effects	A	2	1
Resistive wall	B	1	1

Baseline Recommendation

A train length of around 2800 bunches is preferred because the kickers, ion effects and electron cloud are easier with a smaller number of bunches. If the electron ring is completely filled with no gaps (as may be the case with around 5600 bunches) the ion effects could be extremely difficult. However, there may well be other acceptable options with numbers of bunches between 2800 and 5600: further studies are needed to specify the gaps in the fill needed to keep ion effects under control.

If the positron rings (total circumference 12 km in our recommended baseline) are uniformly filled with 2800 bunches, the bunch separation is around 14 ns. Studies suggest that because of electron-cloud effects, the bunch separation should not be reduced much below this; this would prevent operation with larger numbers of bunches per train.

It is possible that the fill patterns in the electron and positron rings may need to be different, so as to allow a large bunch spacing between positron bunches (because of electron cloud), and gaps between minitrains of electron bunches (because of ions). This would require electron and positron rings with different circumferences, and would limit flexibility on timing solutions.

Alternative

Increasing the number of bunches beyond 2800 could be possible if electron-cloud and ion effects are found to be manageable, and sufficiently fast kickers can be demonstrated.

Required R&D

Studies are needed to determine:

- the minimum bunch spacing needed to keep electron-cloud effects under control;
- the minimum gap between minitrains needed to keep ion effects under control.

A demonstration is needed of kickers meeting the specifications (appropriate to each option for the number of bunches in a bunch train) for:

- pulse rise and fall times;
- kick repetition rate;
- kick amplitude stability.

7.2.5 Extracted Bunch Length

The specifications for the extracted bunch length are strongly coupled to the choices for:

- circumference: a longer bunch reduces the charge density, which will reduce the space-charge tune shift that may be a problem in a 17 km ring;
- beam energy: a longer bunch length reduces the charge density in the bunch, reduces the severity of single bunch collective effects, and may make a lower energy feasible;
- bunch train length and bunch charge: a longer bunch reduces the charge density, and may make a higher bunch charge possible before reaching limits from collective effects.

Options

The nominal specification on the bunch length has been 6 mm. It is possible to consider bunch lengths up to 9 mm. In principle, the bunch length can be varied independently of other parameters (such as the energy spread) by varying the RF voltage.

Issues

Bunch compressors (Significance: A) For a given energy spread, the bunch compressors get more difficult with increasing bunch length. The following bunch compressor configurations have been considered, and are

deemed practical:

stages of compression	Initial energy spread	Initial bunch length	Final bunch length
Two-stage	0.15%	≤9 mm	300 μm
Two-stage	0.15%	≤6 mm	150 μm
One-stage	0.15%	≤6 mm	300 μm

A two-stage bunch compressor is presently recommended for the ILC baseline configuration, with a one-stage compressor as a lower cost alternative.

Collective effects (Significance: A) Most single-bunch effects become less severe as the bunch length increases (including space-charge tune shifts, microwave instability thresholds, emittance growth from intrabeam scattering). Touschek lifetime benefits from a longer bunch. Many of these effects are of concern in the damping rings, and a 9 mm bunch would therefore provide a potentially useful safety margin over a 6 mm bunch.

Electron cloud (Significance: A) It is possible that electron-cloud effects get worse with increasing bunch length. This issue requires further study.

RF system (Significance: B) The RF voltage needed in a storage ring is inversely proportional to the square of the bunch length. Allowing a longer bunch also allows a larger momentum compaction (which is helpful for suppressing instabilities) for a given voltage. A lower RF voltage reduces costs. However, if the RF voltage is too low, the RF energy acceptance can be small, and this can limit the Touschek lifetime, and the injection efficiency.

Issues Ranking

Issue	Significance	Risks	
		6 mm	9 mm
Bunch compressors	A	1	2
Electron cloud	A	2	2
Collective effects	A	2	1
RF system	B	1	1

Baseline Recommendation

A 9 mm bunch would be helpful for mitigating single-bunch collective effects in the damping rings, but a 6 mm bunch also appears to be a viable option.

Required R&D

Studies of bunch compressors suggest that a 9 mm bunch from the damping ring is acceptable, for a final bunch length of 300 μm. Thorough studies, including tuning simulations for emittance preservation are in progress. Studies of beam dynamics effects in the damping rings with bunch lengths between 6 mm and 9 mm are needed to quantify the benefits (and drawbacks) of longer bunches.

7.2.6 Injection/Extraction Kicker Technology

The choice of technology for the injection/extraction kickers is strongly coupled to the choices for:

- circumference: the kickers become more difficult in shorter rings, and other options may become more attractive if a short circumference is chosen;
- bunch train length: the kickers become more difficult with a larger number of bunches, which must be packed more closely into the ring.

Options

The principal options for the kicker systems are:

- a conventional stripline kicker driven by a fast pulser;
- a "Fourier" kicker, using (for example) a transverse deflecting RF cavity driven by an RF pulse compressed in a highly dispersive waveguide.

RF separators provide a further option that may be combined with either kicker scheme but would more likely be used with the conventional stripline kickers. The RF separators could be used to increase the bunch spacing in the injection/extraction region, by channeling alternate bunches down separate beamlines.

Issues

Rise/fall times and beam stability (Significance: A) The rise and fall times must be sufficiently short as to provide deflection for the target bunch, while not kicking any of the adjacent bunches. The use of RF separators eases the requirements on the rise and fall times. Fast pulsers are available that can provide rise times of around 3 ns. The fall time is likely to be longer; however, the consequences of this may be corrected.

Impedance (Significance: A) The vacuum system of the damping rings will have tight limits on the acceptable impedance, so as to stay below instability thresholds. Systems using RF deflecting cavities potentially add greater impedance than stripline kickers.

Impact on beam dynamics/acceptance (Significance: A) Some studies have shown that the bypass lines associated with RF deflecting cavities may have an adverse impact on the energy acceptance of the damping ring; this issue needs further study.

Kick amplitude stability (Significance: A) There are demanding requirements on the pulse-to-pulse stability of the kick amplitude. It may be possible to design a turn-around in the extraction line, allowing a feedback system to correct bunch-to-bunch extraction jitter. However, this will likely add cost to the machine and will be accompanied by its own set of technical issues.

Kick amplitude (Significance: B) The kickers must be capable of providing sufficient amplitude for clean injection and extraction. Injection of positron bunches sets the amplitude goal, since larger clearance is needed for the large beam from the positron source. In principle, it is possible to use a sequence of kickers, each powered independently, to achieve the required amplitude. The optics of the lattice must be designed to meet the requirements of the injection and extraction components.

Reliability (Significance: C) The kickers must operate reliably. Lifetime is a potential issue for high-power fast pulsers. However, since the number of pulsers required will be limited, it should be possible to maintain a reasonable redundancy in the number of pulsers available at any time.

Cost (Significance: C) The basic stripline kicker scheme uses relatively conventional components. Use of RF separators would incur additional cost because of the extra beamlines required in the damping ring.

Issues Ranking

Issue	Significance	Risks		
		Conventional	Conventional + separators	Fourier
Rise/fall time; beam stability	A	2	1	3
Impedance	A	2	2	2
Beam dynamics	A	1	2	1
Kick amplitude stability	A	3	3	3
Kick amplitude	B	1	1	1
Reliability	C	1	1	1
Cost	C	1	3	3

Baseline Recommendation

The damping ring kickers should be based on "conventional" strip-line kickers driven by fast pulsers, without use of RF separators. The basic technology is available, and is close to a demonstration of most of the performance specifications. Using RF separators has potential cost implications, and could adversely affect the beam dynamics; for these reasons, it is preferred to avoid the need for RF separators if possible.

Alternatives

1. RF separators may prove useful if it is decided to fill the rings with large numbers of bunches, pushing the bunch spacing to small values. Studies should be continued, to understand fully the beam dynamics and engineering issues, and resolve problems.

2. Because Fourier pulse-compression kickers provide a very different approach, it is worthwhile continuing studies to develop a more complete understanding of the benefits and limitations of these systems.

Required R&D

Baseline Kickers need to be demonstrated meeting all specifications for:

- pulse rise and fall times;

- pulse repetition rate;
- kick amplitude stability.

Alternative 1 (RF separators) The beam dynamics and engineering issues associated with the RF separators scheme need to be fully understood, and limitations overcome.

Alternative 2 (Fourier pulse-compression kickers) A more complete understanding is needed of the technical issues involved in Fourier pulse-compression kickers.

Off-Axis Injection The usual operation mode of the damping rings requires on-axis injection, which prevents accumulation of current by stacking charge within RF buckets over many turns. Most conventional storage rings – for example, in synchrotron light sources – use off-axis injection, in which radiation damping is used to merge injected (off-axis) charge with stored (on-axis) charge. The availability of off-axis injection would be of benefit in the damping rings for commissioning and tuning; a high beam current could be stored in the damping rings even with an injector system operating at less than full capacity, or with a separate, low-intensity source.

The possibility of designing the injection system of the damping rings to operate in either on-axis or off-axis mode should be investigated.

7.2.7 Damping Wiggler Technology

The choice of wiggler technology is strongly coupled to the choices for:

- circumference: a larger circumference requires a longer wiggler, which can affect the relative cost impact of the different options for the wiggler technology;
- beam energy: a lower energy requires a longer wiggler, which can affect the relative cost impact of the different options for the wiggler technology;
- injected emittance: a larger transverse emittance needs a larger physical aperture, which is easier to achieve in some wiggler technologies than others;
- vacuum chamber aperture: the wiggler must have sufficient aperture to accommodate the vacuum chamber.

Options

There are three principal options for the damping wiggler technology:

- electromagnetic, normal-conducting (EM/NC);
- electromagnetic, superconducting or superferric (EM/SC);
- permanent magnet with steel poles (hybrid).

Issues

Field quality (Significance: A) A high quality field is needed to achieve the dynamic aperture necessary for good injection efficiency. The field quality depends on the geometry of the wiggler: increasing the gap between the poles, increasing the period, or increasing the pole width can generally improve the field quality. However, increasing the gap and pole width can add considerably to the power consumption for a normal-conducting electromagnetic device, or to the cost of magnetic material for a hybrid device. So far, only a superferric design has been demonstrated that has a satisfactory field quality; however, it is possible that other types of wiggler could be developed into satisfactory designs.

Physical aperture (Significance: A) A large gap is needed to achieve the necessary acceptance for the large injected positron beam. Increasing the gap adds to the power consumption of a normal-conducting electromagnetic device, and to the cost of permanent magnet material in a hybrid device. Acceptance studies indicate that a beam stay-clear of at least 32 mm is required in the wiggler in the positron ring, though a smaller beam stay-clear may be acceptable in the electron ring. A large physical aperture is also desirable from point of view of electron-cloud and resistive-wall effects. So far, only a superferric design has been demonstrated that shows a good physical aperture; however, it is possible that other types of wiggler could be developed into satisfactory designs.

Power consumption/running costs (Significance: A) The operating costs associated with power consumption of the wiggler are an issue. For a hybrid wiggler, the power consumption is essentially zero. For a superconducting device, the power consumption is primarily in the cryogenics. The power consumption of a normal-conducting electromagnetic wiggler is likely to be considerable.

Resistance to radiation damage (Significance: A) The damping rings are likely to be high radiation environments. Permanent magnet materials can be sensitive to radiation, and long-term damage is an issue. Power deposition from radiation can cause quenching of superconducting magnets, but operational experience suggests this may not be a real issue. Normal-conducting electromagnets are generally more resistant to radiation damage, than superconducting or hybrid devices.

Materials and construction costs (Significance: A) Construction of a normal-conducting electromagnetic wiggler is relatively straightforward, and requires no special materials. The cost of the permanent magnet materials in a hybrid wiggler (given the expected pole-width and aperture requirements) may be considerable. The cryogenic systems needed for a superconducting wiggler add to the cost compared to a normal-conducting device.

Requirements for auxiliary systems (Significance: B) Electromagnetic wigglers require power supplies, cooling systems and controls; superconducting wigglers require cryogenics, low-voltage power supplies and controls. Hybrid wigglers require essentially no additional systems.

Flexibility (Significance: B) It may be useful to be able to vary the field strength in the wigglers for tuning and machine studies. The field strength in an electromagnetic (normal-conducting or superconducting) device can be varied easily; a hybrid wiggler would require a mechanism for varying the gap, which would add cost to the device.

Availability (Significance: C) The wigglers are not expected to cause any significant downtime in the damping rings. Hybrid magnets have the advantage of not requiring power supplies, cooling or control systems.

Issues Ranking

Issue	Significance	Risks		
		EM/NC	EM/SC	Hybrid
Field quality	A	2	1	2
Physical aperture	A	2	1	2
Power consumption	A	3	1	1
Resistance to radiation damage	A	1	2	2
Materials and construction costs	A	1	2	3
Auxiliary requirements	B	1	1	1
Flexibility	B	1	1	2
Availability	C	1	1	1

Baseline Recommendation

The damping wiggler should be based on superconducting technology. The requirements for field quality and aperture have been demonstrated in existing designs, and the power consumption is low.

Alternatives

Normal-conducting electromagnetic and hybrid technologies are both viable alternatives. Issues with field quality and aperture can be addressed (at increased cost) in wigglers based on either technology. The power consumption in a normal-conducting wiggler is a concern, though this technology could provide a device with potentially better resistance to radiation damage than the superconducting or hybrid options.

Required R&D

Baseline The CESR-c wigglers have demonstrated the basic requirements for the ILC damping ring wigglers. Designs for a superconducting wiggler for the damping rings need to be optimized.

Alternatives Designs need to be developed with acceptable costs for normal-conducting electromagnetic and hybrid wigglers that meet specifications for aperture and field quality. In the case of a normal-conducting electromagnetic wiggler, the design also needs to show acceptable power consumption.

7.2.8 Main (Non-Wiggler) Magnets Technology

Options

The main magnets (dipoles, quadrupoles and sextupoles) may be electromagnets (EM), or they may be permanent magnets (PM).

Issues

Tunability for beam-based alignment (Significance: A) The challenging goal for vertical emittance makes high-precision beam-based alignment of the quadrupoles essential. Variation of the magnetic center of a quadrupole with magnet strength will contribute to the systematic errors, and limit the accuracy of the results. This is potentially a greater concern with permanent magnets (where variation in field strength generally requires mechanical movement) than in electromagnets.

Flexibility for polarity reversal (Significance: A) It may be desirable to operate the positron damping rings with an electron beam, for example during commissioning, or for e^-e^- collisions. The design of the vacuum chamber (in particular, the location of the photon stops) will likely prevent reversal of the direction of travel of the beam in the ring, so magnet polarities will need to be reversed when switching from a positron beam to an electron beam. This will be more easily achieved with electromagnets than with permanent magnets.

Tunability for optics flexibility and energy variation (Significance: A) It will likely be desirable to have the flexibility to adjust the optics in the damping rings, for example for tuning the emittance and the momentum compaction. Tunability will be more easily achieved with electromagnets than with permanent magnets.

Although the ring energy is nominally fixed in operations, there are circumstances under which it may be useful to vary the energy, perhaps by as much as 10% from the nominal value. Some increase in energy may be helpful to raise the threshold for some collective instabilities, or to increase the damping rates; some reduction in energy may be helpful to reduce the equilibrium emittances. Additionally, although depolarization is not expected to be a significant problem, small adjustments in energy may be necessary to avoid spin resonances. Adjustments in magnet strength to accommodate changes in beam energy may be more easily achieved in electromagnets than in permanent magnets.

Reliability (Significance: B) Failure of a single power supply for an electromagnet will render the damping ring inoperable. Failure of the mechanism for strength adjustment of a permanent magnet will inhibit tuning procedures, but would likely allow operation of the damping ring to continue.

Resistance to radiation damage (Significance: B) Radiation damage is a potential problem for permanent magnets. This issue may be less critical than in the wiggler, since the narrower physical aperture in the wiggler will likely lead to higher radiation levels in that region.

Cost (Significance: C) The cost of permanent magnet materials is high. If the magnet strengths are to be adjustable, then permanent magnet multipoles need precision mechanical tuning systems. Electromagnets need power supplies and cooling systems. Overall, there is unlikely to be any significant difference in cost between the two options.

Issues Ranking

Issue	Significance	Risks	
		EM	PM
Tunability for BBA	A	1	2
Flexibility (polarity reversal)	A	1	4
Tunability (for optics or energy variation)	A	1	2
Reliability	B	2	2
Resistance to radiation damage	B	1	2
Cost	C	1	1

Baseline Recommendation

We recommend that the main magnets in the damping ring be electromagnets. Using electromagnets simplifies tuning issues, and allows polarity reversal, e.g. for storing electrons in the positron ring.

Alternative

Permanent magnets may still be considered as a possibility, if it is decided that polarity reversal is not required.

Required R&D

Baseline Designs for the main damping ring magnets should be straightforward, but still need to be developed.

Alternative The problem of polarity reversal needs to be addressed. A demonstration is needed of a permanent magnet with good tunability and resistance to radiation damage.

7.2.9 RF System Technology

Options

The RF system could, in principle, use either normal-conducting or superconducting RF cavities.

Issues

Higher-order modes (Significance: A) Higher-order modes (HOMs) in RF cavities can have adverse effects on the beam dynamics. Normal-conducting and superconducting cavities can be designed to have HOMs of low amplitudes, but it is still preferable to keep the number of cavities as small as possible. The gap voltage per cell in a normal-conducting RF cavity is typically around 0.7 MV (limited by cooling); in superconducting cavities, voltages as high as 3 MV have been demonstrated. This means that up to four times as many cavities would be needed in a normal-conducting RF system as in a superconducting system.

Power dissipation (Significance: A) In a normal-conducting cavity, the power dissipated in the cavity wall may be as large as the power supplied to the beam. In a superconducting cavity, the power dissipation is negligible; power is required by the cryogenics, but this is still expected to be less than the power dissipated in a normal-conducting cavity.

Phase transients from beam loading (Significance: B) If there are gaps in the fill, variations in beam loading will result in phase transients along each minitrain. The transients depend on the R/Q of the cavities and the total voltage. Since a superconducting RF system would have fewer cavities, the phase transients should be smaller.

Reliability (Significance: C) The superconducting RF system in KEK-B has a trip rate of the order of one trip per day. In PEP-II, the normal-conducting RF system has a trip rate of between three and five trips per day. The system can be designed so that a trip would result in loss of a small number of machine pulses. Trips are not expected to have a significant impact on operation of the damping rings, provided there is some reserve in the amount of RF voltage available.

Cost (Significance: C) The RF system is expected to be a small contribution to the cost of the damping rings. A superconducting system could have some advantage from the smaller number of RF cavities that would be required.

Issues Ranking

Issue	Significance	Risks	
		Normal-conducting	Superconducting
Higher-order modes	A	2	1
Power dissipation	A	2	1
Phase transients	B	2	1
Reliability	C	1	1
Cost	C	1	1

Baseline Recommendation

Each damping ring should use a superconducting RF system. Compared to a normal-conducting RF system, a superconducting RF system requires fewer cavities, (with advantages for cost and keeping HOMs low); the power dissipation is lower; and smaller phase transients are expected.

Alternative

A normal-conducting RF system could still satisfy the requirements for the damping rings.

Required R&D

The basic requirements of the superconducting RF systems for the damping rings have been demonstrated in existing machines, e.g. KEK-B. A full system specification, design and optimization are needed.

7.2.10 RF Frequency

The choice of RF frequency is strongly coupled to the choice of bunch train length: the flexibility in the number of bunches in a train depends to some extent on the RF frequency.

Options

An RF frequency of 500 MHz is a common choice for synchrotron light source storage rings. It is possible to consider other choices, for example 650 MHz.

Issues

Cost (Significance: A) 500 MHz RF systems are standard, and will therefore be lower cost. A 650 MHz system would need to be designed from scratch.

Bunch length (Significance: B) A higher frequency makes it possible to achieve the desired bunch length at a lower voltage. A reduction in voltage has advantages in saving cost; but in the case of the options considered here, the cost savings of the lower voltage of the 650 MHz system compared to the 500 MHz system would be outweighed by the required R&D.

Phase locking with linac RF (Significance: C) The damping ring RF must be phase locked to the linac RF, to ensure that bunches extracted from the damping ring arrive at the correct phase of the main linac RF. An RF frequency of 650 MHz is a simple subharmonic (1/2) of the main linac RF frequency of 1.3 GHz. A 500 MHz RF system is at a more complex subharmonic (5/13). However, either frequency can easily be locked to the main linac RF.

Issues Ranking

Issue	Significance	Risks	
		500 MHz	650 MHz
Cost	A	1	3
Bunch length	B	1	1
Phase locking with linac	C	1	1

Baseline Recommendation

The damping rings RF systems should use an RF frequency of 500 MHz. This is a standard technology; other options would require R&D.

7.2.11 Vacuum Chamber Aperture

The specifications for the vacuum chamber aperture are strongly coupled to the choices for:

- injected emittance and energy spread: a larger transverse emittance requires a larger physical aperture for good injection efficiency;
- wiggler technology: the wiggler must have sufficient aperture to accommodate the vacuum chamber.

Options

The vacuum chamber will have a complicated geometry, and comprehensive studies of issues related to the geometry are not possible without detailed designs. However, it is possible to consider the impact of chambers of different diameters (assuming a circular cross-section) in different sections of the damping rings. We consider three representative cases:

Section	Chamber diameter [mm]		
	Option 44/16/100	Option 50/32/100	Option 50/46/100
Arc	44	50	50
Wiggler	16	32	46
Straight	100	100	100

Issues

Acceptance (Significance: A) The large beam from the positron source needs a large chamber aperture for good injection efficiency. Tracking studies in the reference lattices indicate that in most cases, a diameter of 32 mm in the wiggler would be sufficient, while a diameter of 24 mm would be insufficient. Reducing the beta functions in the wiggler would help with the acceptance, but the beam size varies only as the square root of the beta function, and reducing the beta functions would increase the local chromaticity.

Cost (Significance: A) Increasing the chamber diameter in a storage ring generally increases the cost of the machine, since magnets with larger aperture are required, which are more expensive. In the three options considered here, the difference between 44 mm and 50 mm in the arcs is not likely to be significant. A superconducting wiggler (as in the recommended baseline) can accommodate a chamber with 46 mm aperture; in any case, the wiggler chambers are a relatively small contribution to the cost of the whole vacuum system.

Electron cloud (Significance: A) A larger chamber helps to reduce the build-up of electron cloud from multipacting. With the baseline of two 6 km rings for the positron damping ring, the necessary chamber aperture in the wiggler is likely to be no less than 46 mm. In an alternative 17 km ring, a smaller chamber aperture could be tolerated.

Resistive-wall instability (Significance: A) The resistive-wall wake field drives coupled-bunch instabilities. The strength of the transverse wake is inversely proportional to the cube of the chamber diameter; increasing the diameter by a factor of 2 reduces the wake field by nearly an order of magnitude. Bunch-by-bunch feedback systems can be used to suppress coupled-bunch instabilities, as long as the growth times are above approximately 20 turns. With small chamber diameter (44/16/100), the growth times in the damping rings are of this order; a larger chamber would provide some margin.

Gas conductance (Significance: B) Ion and electron cloud effects place demanding requirements on the residual gas pressure in the vacuum chamber. Increasing the chamber diameter increases the conductance, which helps to achieve a lower average pressure with a given number of pumps; this could be particularly helpful in the wiggler.

BPM performance (Significance: B) Achieving good BPM performance becomes more difficult as the chamber aperture increases.

Issues Ranking

Issue	Significance	Risks		
		Option 44/16/100	Option 50/32/100	Option 50/46/100
Acceptance	A	4	2	1
Cost	A	1	1	1
Electron cloud	A	3	3	2
Resistive-wall	A	3	2	2
Gas conductance	B	2	1	1
BPM performance	B	1	2	2

Baseline Recommendation

A chamber diameter of (not less than) 50 mm in the arcs, 46 mm in the wiggler and 100 mm in the straights is required. The wiggler chamber needs a large aperture to achieve the necessary acceptance, and to suppress electron cloud build-up. The large aperture also reduces resistive-wall growth rates, and eases the requirements on the feedback systems.

Required R&D

Even with a large aperture chamber in the damping rings, a bunch-by-bunch feedback system will be needed in the transverse and longitudinal planes to suppress coupled-bunch instabilities driven by the resistive-wall impedance. Although the required performance of the feedback systems should be within the range of existing technology, studies are needed of the level of residual beam jitter, and possible emittance growth.

7.2.12 Vacuum System Technologies

Options

Vacuum Chamber Material Options for the chamber material are:

- stainless steel;
- copper;
- aluminum.

Treatment for Suppressing Electron Cloud There are several options for treating the chamber to suppress electron cloud, including:

- coating with titanium nitride;
- coating with NEG, e.g. TiZrV;
- using a grooved chamber surface.

Different treatments may be used in different parts of the damping rings.

Pumping Technology Options for pumping technology include:

- use of conventional pumps;
- use of NEG coating.

Antechamber An antechamber may be needed in some sections of the damping ring, and not in others.

In-Situ Baking It may be desirable to have a vacuum chamber that is capable of being baked in-situ.

Baseline Recommendation

Recommendations for the vacuum system for the baseline configuration have not yet been made.

7.3 Summary of Recommendations

7.3.1 Circumference

Baseline

The positron damping ring should consist of two (roughly circular) rings of approximately 6 km circumference in a single tunnel. Electron-cloud effects make a single ring of circumference 6 km or lower unattractive, unless significant progress can be made with mitigation techniques. Space-charge effects will be less problematic in a 6 km than in a 17 km ring, and achieving the required acceptance will be easier in a circular ring than in a dogbone ring.

The electron ring can consist of a single 6 km ring, assuming that the fill pattern allows a sufficient gap for clearing ions. The injection and extraction

kickers and ion effects are more difficult in a 3 km ring than in a 6 km ring. A 17 km ring could ease ion effects (by allowing larger gaps between minitrains), but would likely be higher cost. We have no recommendation on whether the electron ring needs a separate tunnel from the positron rings.

Although R&D is still required for the injection/extraction kickers for a damping ring with 6 km circumference, it is expected that existing programs will demonstrate a solution.

The exact circumference of the damping rings should be chosen, if possible, to allow flexibility in the fill patterns and number of bunches in a bunch train.

The feasibility of the baseline depends on:

- further progress with developing techniques for suppressing electron cloud (positron rings);
- development of a satisfactory lattice design, e.g. (for electron ring) with properties that mitigate ion effects, etc.;
- demonstration of kickers meeting the specifications for rise/fall times, kick amplitude stability and repetition rate.

Alternatives

1. If techniques are found that are sufficiently effective at suppressing the electron cloud, a single 6 km, or possibly smaller, ring can be used for the positron damping ring.
2. If electron cloud mitigation techniques are not found that are sufficient for the baseline positron ring, then a 17 km ring is a possible alternative; this would require addressing space-charge and acceptance issues.

7.3.2 Beam Energy

The damping ring energy should be approximately 5 GeV. A lower energy increases the risks from collective effects; a higher energy makes it more difficult to tune for low emittance, and potentially has an adverse impact on the acceptance.

7.3.3 Injected Emittance and Energy Spread

Baseline

An injected beam with maximum betatron amplitude up to 0.09 m-rad and energy spread up to 1% (full width) is preferred for the damping rings, over a distribution with larger energy spread but smaller betatron amplitude. Achieving good off-energy dynamics in the damping ring lattices is likely to be more problematic than achieving a large on-energy dynamic aperture. A smaller energy spread is likely to improve the margin for the acceptance of the injected beam.

Alternative

If the acceptance issue can be addressed successfully, a larger energy spread on the injected beam (up to 2% full width) could be accommodated.

7.3.4 Bunch Train Length and Bunch Charge

Baseline

A train length of around 2800 bunches is preferred because the kickers, ion effects and electron cloud are easier with a smaller number of bunches. If the electron ring is completely filled with no gaps (as may be the case with around 5600 bunches) the ion effects could be extremely difficult. However, there may well be other acceptable options with numbers of bunches between 2800 and 5600: further studies are needed to specify the gaps in the fill needed to keep ion effects under control.

If the positron rings (total circumference 12 km in our recommended baseline) are uniformly filled with 2800 bunches, the bunch separation is around 14 ns. Studies suggest that because of electron-cloud effects, the bunch separation should not be reduced much below this; this would prevent operation with larger numbers of bunches per train.

It is possible that the fill patterns in the electron and positron rings may need to be different, so as to allow a large bunch spacing between positron bunches (because of electron cloud), and gaps between minitrains of electron bunches (because of ions). This would require electron and positron rings with different circumferences, and would limit flexibility on timing solutions.

Alternatives

Increasing the number of bunches beyond 2800 could be possible if electron-cloud and ion effects are found to be manageable, and sufficiently fast kickers can be demonstrated.

7.3.5 Extracted Bunch Length

A 9 mm bunch would be helpful for mitigating single-bunch collective effects in the damping rings (except, possibly, in the case of electron cloud), but a 6 mm bunch also appears to be a viable option.

7.3.6 Injection/Extraction Kicker Technology

Baseline

The damping ring kickers should be based on "conventional" strip-line kickers driven by fast pulsers, without use of RF separators. The basic technology is available, and is close to a demonstration of most of the performance specifications. Using RF separators has potential cost implications, and could adversely affect the beam dynamics; for these reasons, it is preferred to avoid the need for RF separators if possible.

Alternatives

RF separators may prove useful if it is decided to fill the rings with large numbers of bunches, pushing the bunch spacing to small values. Studies should be continued, to understand fully the beam dynamics and engineering issues.

Because Fourier pulse-compression kickers provide a very different approach, it is worthwhile continuing studies to develop a more complete understanding of the benefits and limitations of these systems.

7.3.7 Damping Wiggler Technology

Baseline

The damping wigglers should be based on superconducting technology. The requirements for field quality and aperture have been demonstrated in existing designs, and the power consumption is low.

Alternatives

Normal-conducting electromagnetic and hybrid technologies are both viable alternatives. Issues with field quality and aperture can be addressed (at increased cost) in wigglers based on either technology. The power consumption in a normal-conducting wiggler is a concern, though this technology could provide a device with potentially better resistance to radiation damage than the superconducting or hybrid options.

7.3.8 Main (Non-Wiggler) Magnets Technology

Baseline

We recommend that the main magnets in the damping rings be electromagnets. Using electromagnets simplifies tuning issues, and allows polarity reversal, e.g. for storing electrons in the positron ring.

Alternative

Permanent magnets may still be considered as a possibility for the main magnets in the damping rings, if it is decided that polarity reversal is not required.

7.3.9 RF System Technology

Baseline

Each damping ring should use a superconducting RF system. Compared to a normal-conducting RF system, a superconducting RF system requires fewer cavities, (with advantages for cost and keeping HOMs low); the power dissipation is lower; and smaller phase transients are expected.

Alternative

A normal-conducting RF system could still satisfy the requirements for the damping rings.

7.3.10 RF Frequency

The damping rings RF systems should use an RF frequency of 500 MHz. This is a standard technology; other options would require R&D.

7.3.11 Vacuum Chamber Aperture

A chamber diameter of (not significantly less than) 50 mm in the arcs, 46 mm in the wiggler and 100 mm in the straights is required. The wiggler chamber needs a large aperture to achieve the necessary acceptance, and to suppress electron cloud build-up. The large aperture also reduces resistive-wall growth rates, and eases the requirements on the feedback systems.

7.3.12 Vacuum System Technologies

Recommendations on the various options for the vacuum system technologies are yet to be made.

7.4 Summary of R&D Requirements

7.4.1 Circumference

Baseline

- Techniques for mitigating electron cloud to acceptable levels are needed.
- A lattice design is needed that simultaneously satisfies requirements for acceptance and beam stability, and can be tuned easily for low emittance.

Alternative 1 (single 6 km positron ring)

- Techniques for mitigating electron cloud to acceptable levels are needed.
- A lattice design is needed that simultaneously satisfies requirements for acceptance and beam stability, and can be tuned easily for low emittance.

Alternative 2 (17 km positron ring)

- Techniques for suppressing space-charge tune shifts without driving betatron and synchrobetatron resonances are needed.
- A lattice design is needed that simultaneously satisfies requirements for acceptance and beam stability, and can be tuned easily for low emittance

General R&D requirements

- Kickers that simultaneously meet specifications on rise/fall time, pulse rate and stability need to be demonstrated.
- Ion instabilities are a concern in the electron ring.
- Ion-induced pressure instabilities in the positron ring need to be addressed.
- A range of classical collective instabilities need to be properly understood, with analysis based on a detailed impedance model.
- The effectiveness of low-emittance tuning techniques need to be assessed.

7.4.2 Injected Emittance and Energy Spread

Baseline

Studies of the positron production indicate that an injected full-width energy spread of 1% should be achievable; however, a thorough investigation including realistic models for collimators, energy compressors etc. is still needed.

Alternative

A lattice design is needed that shows an energy acceptance with some margin beyond 2% full-width, while satisfying other requirements.

7.4.3 Bunch Train Length and Bunch Charge

Studies are needed to determine:

- the minimum bunch spacing needed to keep electron-cloud effects under control;
- the minimum gap between minitrains needed to keep ion effects under control.

A demonstration is needed of kickers meeting the specifications (appropriate to each option for the number of bunches in a bunch train) for:

- pulse rise and fall times;

- kick repetition rate;
- kick amplitude stability.

7.4.4 Extracted Bunch Length

Studies of bunch compressors suggest that a 9 mm bunch from the damping ring is acceptable, for a final bunch length of 300 mm. Thorough studies, including tuning simulations for emittance preservation are in progress. Studies of beam dynamics effects in the damping rings with bunch lengths between 6 mm and 9 mm are needed to quantify the benefits (and drawbacks) of longer bunches.

7.4.5 Injection/Extraction Kicker Technology

Baseline

Kickers need to be demonstrated meeting all specifications for:

- pulse rise and fall times;
- pulse repetition rate;
- kick amplitude stability.

Alternative 1 (RF separators)

The beam dynamics and engineering issues associated with the RF separators scheme need to be fully understood, and limitations overcome.

Alternative 2 (Fourier pulse-compression kickers)

A more complete understanding is needed of the technical issues involved in Fourier pulse-compression kickers.

Off-Axis Injection

The usual operation mode of the damping rings requires on-axis injection, which prevents accumulation of current by stacking charge within RF buckets over many turns. Most conventional storage rings – for example, in synchrotron light sources – use off-axis injection, in which radiation damping is used to merge injected (off-axis) charge with stored (on-axis) charge. The availability of off-axis injection would be of benefit in the damping

rings for commissioning and tuning; a high beam current could be stored in the damping rings even with an injector system operating at less than full capacity, or with a separate, low-intensity source.

The possibility of designing the injection system of the damping rings to operate in either on-axis or off-axis mode should be investigated.

7.4.6 Damping Wiggler Technology

Baseline

The CESR-c wigglers have demonstrated the basic requirements for the ILC damping ring wigglers. Designs for a superconducting wiggler for the damping rings need to be optimized.

Alternatives

Designs with acceptable costs for normal-conducting electromagnetic and hybrid wigglers need to be developed, that meet specifications for aperture and field quality. In the case of a normal-conducting electromagnetic wiggler, the design also needs to show acceptable power consumption.

7.4.7 Main (Non-Wiggler) Magnets Technology

Baseline

Designs for electromagnetic dipoles, quadrupoles etc. should be straightforward, but still need to be developed.

Alternative

The problem of polarity reversal needs to be addressed. A demonstration is needed of a permanent magnet with good tunability and resistance to radiation damage.

7.4.8 RF System Technology

The basic requirements of the superconducting RF systems for the damping rings have been demonstrated in existing machines, e.g. KEK-B. A full system specification, design and optimization are needed.

7.4.9 Vacuum Chamber Aperture

Even with a large aperture chamber in the damping rings, a bunch-by-bunch feedback system will be needed in the transverse and longitudinal planes to suppress coupled-bunch instabilities driven by the resistive-wall impedance. Although the required performance of the feedback systems should be within the range of existing technology, studies are needed of the level of residual beam jitter, and possible emittance growth.

7.4.10 Vacuum System

A number of issues regarding the vacuum system remain to be addressed, including:

- What are the required levels of residual gas pressure needed to avoid ion effects?
- What kind of chamber preparation (NEG coating, TiN coating, grooves etc.) is needed for suppressing electron cloud, and what are the implications e.g. for impedance?
- Can (or should) clearing electrodes be used to suppress electron cloud or ion effects?
- What length of time is allowed by the commissioning schedule for conditioning the vacuum system in the damping rings?

Further studies are needed to resolve these issues.

Bibliography

[1] A. Babayan, D. Melkumyan, V. Nikoghosyan, "Wiggler Magnet Optimization for Linear Collider Damping Ring," unpublished (2005).

[2] K. Bane, "A Simplified Model of Intrabeam Scattering," Proceedings of EPAC 2002, Paris, France (2002).

[3] D. P. Barber, J. A. Ellison and K. Heinemann, "Quasiperiodic Spin-Orbit Motion and Spin Tunes in Storage Rings," Phys. Rev. ST Accel. Beams **7**, 124002 (2004).

[4] D. P. Barber and G. Ripken, in "Handbook of Accelerator Physics and Engineering," eds. A. Chao and M. Tigner, World Scientific 2nd Edition (2002), and 3rd Edition, in preparation.

[5] Y. Batygin, private communication.

[6] Behlke Electronic GmbH, Am Auernberg 4, 61476 Kronberg, Germany. http://www.behlke.de/separations/separation_B3.htm

[7] E. Benedetto *et al*, "Emittance Growth Caused by Electron Cloud Below the Fast TMCI Threshold: Numerical Noise or True Physics?" Proceedings of PAC 2005, Knoxville, Tennessee (2005).

[8] M. Berz *et al*, COSY Infinity. http://www.bt.pa.msu.edu/index_files/cosy.htm

[9] J.D. Bjorken and S.K. Mtingwa, "Intrabeam Scattering," Part. Accel. **13**, 115 (1983).

[10] J. Byrd *et al*, Phys. Rev. Lett. **79**, 79-82 (1997).

[11] Y. Cai, M. Donald, J. Irwin and Y. Yan, SLAC-PUB-7642, (1997).

[12] Y. Cai, "Dynamic Aperture in Damping Rings with Realistic Wigglers," SLAC-PUB-11084 (April 2005).

[13] A. Chao, "Physics of Collective Beam Instabilities in High Energy Accelerators," John Wiley and Sons, New York (1993), p.206.

[14] A. Chao, "Physics of Collective Beam Instabilities in High Energy Accelerators," John Wiley and Sons, New York (1993), p.210.

[15] See, for example, F.S. Crawford Jr, "Waves, Berkeley Physics Course - Volume 3," McGraw-Hill, New York (1968).

[16] A. Curtoni, M. Jablonka, "Study of the TESLA Preaccelerator for the Polarised Electron Beam," TESLA 2001-22 (2001). http://tesla.desy.de/new_pages/TESLA_Reports/2001/pdf_files/tesla2001-22-2.pdf

[17] A. Curtoni, M. Jablonka, K. Floettmann, "Polarized Electron Injector Design for TESLA," presentation at 2nd ILC Workshop, Snowmass (2005). http://alcpg2005.colorado.edu:8080/alcpg2005/program/accelerator/WG3a

[18] W. Decking and R. Brinkmann, "Space Charge Problems in the TESLA Damping Ring," Proceedings of EPAC 2000, Vienna, Austria (2000).

[19] A. Dragt *et al*, Marylie. http://www.physics.umd.edu/dsat/dsatmarylie.html

[20] A. Dragt and C. Mitchell, "Computation of Transfer Maps from Surface Data Using Elliptical Cylinders," Presentation at 2nd ILC Accelerator Workshop, Snowmass, Colorado (2005). http://alcpg2005.colorado.edu:8080/alcpg2005/program/accelerator/WG3b/Presentations/Acceptance/

[21] FID GmbH, Carl-Benz-Strasse 28, Industriepark, 57299, Burbach, Germany. http://www.fidtechnology.com/Products/fastpowergens.htm

[22] H. Fukuma *et al*, "Experimental Observation of the Ion-Related Coupled Bunch Instability in a Bunch Train in TRISTAN AR," Proceedings of PAC 1997, Vancouver, B.C., Canada (1997).

[23] H. Fukuma, "Electron Cloud Effects in KEK-B," Proceedings of ECLOUD'04, Napa, California (2004). CERN-2005-001

[24] M.A. Furman and M.T.F. Pivi, "Simulation of Secondary Electron Emission Based on a Phenomenological Probabilistic Model," LBNL–52807/SLAC–PUB–9912 (2003).

[25] W. Gai, private communication.

[26] G.D. Gollin *et al*, "Studies Pertaining to a Small Damping Ring for the International Linear Collider," FERMILAB-TM-2272-AD-TD (September 2004).

[27] G.D. Gollin, "Studies of Alternative TESLA Damping Ring Designs," http://www.hep.uiuc.edu/home/g-gollin/talks/AAC_damping_rings.pdf (2004).

[28] G.D. Gollin, M.J. Haney, J. Calvey and M. Davidsaver, "Performance Modeling of a Fourier Series Pulse Compression Kicker for the International Linear Collider Damping Rings," (in preparation). http://www.hep.uiuc.edu/home/g-gollin/talks /fourier_series_kicker_technical_memo_draft.doc

[29] G.D. Gollin, M.J. Haney and J.B. Williams, "An Expression of Interest Concerning Investigation of TESLA Damping Ring Kickers Using the A0 Photoinjector Beam" (May 2004).

[30] K. Heinemann, DESY Report 97-166 (1997) and e-print archive: physics/9709025.

[31] K. Heinemann and G. H. Hoffstaetter, "Tracking Algorithm for the Stable Spin Polarization Field in Storage Rings Using Stroboscopic Averaging," Phys. Rev. E **54** (4), 4240 (1996).

[32] T. Himel, "Linear Collider Availability Simulation Results," presented at the Second ILC Workshop, Snowmass (2005). http://alcpg2005.colorado.edu:8080/alcpg2005/program/accelerator /GG3/tom_himel20050812014007.ppt

[33] Y. Honda *et al*, "Achievement of Ultralow Emittance Beam in the Accelerator Test Facility Damping Ring," Phys. Rev. Lett. **92**, 054802-1 (2004).

[34] J. Y. Huang *et al*, Phys. Rev. Lett. **81**, 4388-4391 (1998).

[35] International Linear Collider Technical Review Committee 2nd Report, SLAC-R-606 (2003).

[36] International Linear Collider Technical Review Committee 2nd Report, SLAC-R-606 (2003), p.324.

[37] International Linear Collider Technical Review Committee 2nd Report, SLAC-R-606 (2003), p.327.

[38] International Linear Collider Technical Review Committee 2nd Report, SLAC-R-606 (2003), p.344.

[39] Q. Ji and M. Furman, private communication.

[40] H. Kobayakawa *et al*, Nuclear Instruments and Methods in Physics Research A **248** (1986) 565-568.

[41] G.F. Krebs and M. Holmes, "Measurement of the Radiation Incident on ALS NdFeB Permanent Magnet Insertion Device Structures and a Determination of their Lifetime," Proceedings of PAC 1997, Vancouver, B.C., Canada (1997).

[42] K. Kubo, "Simulation Study of Low Emittance Tuning of the Accelerator Test Facility Damping Ring at KEK," Phys. Rev. STAB **6**, 092801 (2003).

[43] K. Kubo, S.K. Mtingwa and A. Wolski, "Intrabeam Scattering Formulas for High Energy Beams," Phys. Rev. STAB **8**, 081001 (2005).

[44] A. Kulikov, A. Novokhatski and J. Seeman, "Suppression of the Beam Instability Related to Electron Cloud at PEP-II B-Factory," Proceedings of ECLOUD'04, Napa, California (2004). CERN-2005-001

[45] S. Marks, private communication.

[46] K. Ohmi, "Particle-in-Cell Simulation of Beam-Electron Cloud Interactions," Proceedings of PAC 2001, Chicago, Illinois (2001).

[47] K. Ohmi et. al., Phys. Rev. ST-AB, **7**, 104401 (2004).

[48] K. Ohmi, "Electron Cloud Effect in Damping Rings of Linear Colliders," Proceedings of ECLOUD'04, Napa, California (2004). CERN-2005-001

[49] K. Ohmi and F. Zimmermann, Phys. Rev. Lett. **85**, 3821 (2000).

[50] K. Ohmi, F. Zimmermann, E. Perevedentsev, Phys. Rev. E **65**, 16502 (2002).

[51] R. Pasquinelli, private communication.

[52] N. Phinney *et al*, "Reliability Simulations for a Linear Collider," SLAC-PUB-10505 (2004).

[53] F. le Pimpec, F. King, R.E. Kirby, M. Pivi, G. Rumolo, "The Continuing Story of Secondary Electron Yield Measurements from TiN Coating and TiZrV Getter Film," SLAC-TN-04-046 (2004).

[54] A. Piwinski, Proceedings of the 9th International Conference on High Energy Accelerators, Stanford, California (1974), p. 405.

[55] A. Piwinski, "Touschek Effect and Intrabeam Scattering," p.125 in "Handbook of Accelerator Physics and Engineering," eds. A. Chao and M. Tigner, World Scientific (1999).

[56] T. Raubenheimer, "The Generation and Acceleration of Low Emittance Flat Beams for Future Linear Colliders," SLAC Report 387, p.19 (1991).

[57] T. Raubenheimer and F. Zimmermann, Phys. Rev. E, **52**, 5, 5487 (1995).

[58] T. Raubenheimer, "Suggested ILC Beam Parameter Range," http://www-project.slac.stanford.edu/ilc/acceldev/beamparameters.html (February 2005).

[59] D. Rice *et al*, "Production and Testing Considerations for CESR-c Wiggler Magnets," Proceedings of PAC 2003, Chicago, Illinois (2003).

[60] D. Rice, private communication.

[61] G. Rumolo *et al*, "Electron Cloud Studies for KEK-B" Proceedings of PAC 2001, Chicago, Illinois (2001).

[62] SAD (Strategic Accelerator Design), http://acc-physics.kek.jp/SAD/sad.html

[63] D. Sagan, "Bmad Subroutine Library for Relativistic Charged-Particle Simulations," http://www.lns.cornell.edu/ dcs/bmad

[64] K. Satoh and Y. Chin, "Transverse Mode Coupling in a Bunched Beam," Nuclear Instruments and Methods in Physics Research **207** (1983) 309-320.

[65] R. Schlueter and J.-Y. Jung, private communication.

[66] H. Schönbacher and A. Stolarz-Izycka, "Compilation of Radiation Damage Test Data, Part II: Thermosetting and Thermoplastic Resins," CERN 79-08 (1979).

[67] J. Seeman *et al*, "PEP-II and KEK-B Operational Status," Proceedings of PAC 2005, Knoxville, Tennessee (2005).

[68] C. Steier, D. Robin, A. Wolski, G. Portmann, J. Safranek, "Coupling Correction and Beam Dynamics at Ultralow Vertical Emittance in the ALS," Proceedings of PAC 2003, Portland, Oregon (2003).

[69] G.V. Stupakov, T.O. Raubenheimer and F. Zimmermann, Phys. Rev. E, **52**, 5, 5499 (1995).

[70] G.V. Stupakov, Proceedings of the International Workshop on Collective Effects and Impedance for B-Factories, Tsukuba, Japan (1996).

[71] A. Temnykh, "CESR-c: Performance of a Wiggler-Dominated Storage Ring," Proceedings of PAC 2005, Knoxville, Tennessee (2005).

[72] TESLA Technical Design Report, DESY 2001-011 (March 2001).

[73] TESLA Technical Design Report, DESY 2001-011 (March 2001), p. II-149.

[74] M. Tischer, J. Pfluger, W. Decking, "A Compact Damping Wiggler Based on Permanent Magnet Technology for the TESLA Damping Rings," TESLA 2000-20 (2000), and references therein.

[75] US Linear Collider Technology Options Study (2004) http://www.slac.stanford.edu/xorg/accelops/Full/LC_opts_full.pdf

[76] M. Venturini, "Impact of Space Charge on the Beam Dynamics in the ILC Damping Rings," to appear.

[77] M. Venturini and A. Dragt, "Accurate Computation of Transfer Maps from Magnetic Field Data," Nuclear Instruments and Methods in Physics Research A **427** (1999) 387-392.

[78] N.J. Walker *et al*, "Merlin: A C++ Class Library for Performing Charged Particle Accelerator Simulations," http://www.desy.de/∼merlin/

[79] H. Wiedemann, "Particle Accelerator Physics II," p.329, Springer (1995).

[80] S. Wolfram, "The Mathematica Book," Wolfram Media/Cambridge University Press (1999).

[81] A. Wolski and D. Bates, "Spin Tracking Studies for Beam Polarization Preservation in the NLC Main Damping Rings," CBP Tech Note-326 (2004).

[82] A. Wolski, "Lattices with Large Dynamic Aperture for the ILC Damping Rings," LBNL-57045 (February 2005).

[83] A. Wolski, "Alternative Approach to General Coupled Linear Optics," LBNL-59145 (November 2005).

[84] A. Wolski, J. Byrd, D. Bates, "Simulations of Resistive Wall Instability in the ILC Damping Rings," proceedings of PAC 2005, Knoxville, Tennessee (2005).

[85] F. Zimmermann, "Ion Trapping, Beam-Ion Instabilities and Dust," p.130 in "Handbook of Accelerator Physics and Engineering," eds. A. Chao and M. Tigner, World Scientific (1999).